The Functional Roles of the Chemokine CXCL12 in the Progression from Liver Fibrosis to Liver Cancer

Inaugural-Dissertation
to obtain the academic degree
Doctor rerum naturalium (Dr. rer. nat)

submitted to the Department of Biology, Chemistry, Pharmacy
of Freie Universität Berlin

by

Marlene Sophia Kohlhepp

from Tübingen

2023

The following work was conducted from March 2018 until August 2023 at the Department of Medicine III, RWTH-University Hospital Aachen and at the Department of Hepatology and Gastroenterology, Charité University Medicine Berlin under the supervision of Prof. Dr. Frank Tacke.

1st reviewer: Prof. Dr. Frank Tacke

2nd reviewer: Prof. Dr. Sigmar Stricker

Date of defense: 15.12.2023

Statutory declaration

Herewith I, Marlene Sophia Kohlhepp, certify that I have prepared and written my thesis with the subject "The Functional Roles of the Chemokine CXCL12 in the Progression from Liver Fibrosis to Liver Cancer" independently and that I have not used any sources and aids other than those indicated by me.

Table of Contents

Abbreviations

ACKR	Atypical chemokine receptor
AF	Autofluorescence
AF647	Alexa Fluor 647
AF555	Alexa Fluor 555
AF488	Alexa Fluor 488
ALD	Alcohol-associated liver disease
ALT	Alanine aminotransferase
Ang	Angiopoietin
ANOVA	Analysis of variance
APC	Antigen-presenting cell
ARG1	Arginase 1
aSMA	Alpha-smooth muscle actin
B2m	β2-microtubulin
BSA	Bovine serum albumin
CAF	cancer associated fibroblast
cCKR	conventional chemokine receptor
CCL	CC-chemokine ligand
CCR	CC-chemokine receptor
CD	cluster of differentiation
cDNA	complementary DNA
CX3CL	(C-X3-C-motif) ligand
CK19	Cytokeratin 19
CLEC4F	C-Type Lectin Domain Family 4 Member F
CLP	common lymphoid progenitor
CMP c	common myeloid progenitor
CSF-1	colony stimulating factor 1
Ct	cycle treshold
CTGF	connective tissue growth factor
CTLA-4	cytotoxic T-lymphocyte associated protein 4
CX3CR	(C-X3-C-motif) receptor
CXCL	CXC-chemokine ligand
CXCR	CXC-chemokine receptor
DAMP	damage-associated molecular pattern
DDR1	discoidin domain receptor 1
DEN	Diethylnitrosamine
DNA	deoxyribonucleic acid
DPBS	Dulbecco's phosphate buffered saline
ECM	extracellular matrix
EDTA	Ethylenediaminetetraacetic acid
EMT	Epithelial-to mesenchymal transition
FACS	Fluorescence activated cell sorting
FBS	Fetal bovine serum
FFPE	Formalin-fixated paraffin-embedded
FGF	Fibroblast growth factor

Foxp3	Forkhead box P3
FSC	Forward scatter
GAG	Glycosaminoglycan
GBSS	Gey´s balanced salt solution
GLDH	Glutamate dehydrogenase
GRKs	G protein-coupled receptor kinases
h	hour
H/E	Hematoxylin/eosin
HBSS	Hanks' balanced salt solution
HCC	Hepatocellular carcinoma
HGF	Hepatocyte growth factor
HMGB1	High mobility group box 1 protein
HSC	Hepatic stellate cell
i.p	intraperitoneal
i.v.	intravenously
IBA1	Ionized calcium binding adaptor molecule 1
ID1	Inhibitor of DNA binding 1
IF	Immunofluorescence
IFNγ	Interferone gamma
IHC	Immunohistochemistry
IL	Interleukin
iNOS	Inducible nitric oxide synthetase
Kj	Kilojoule
LBR	Liver to body weight ratio
LDH	Lactate dehydrogenase
LPS	Lipopolysaccharid
LSEC	Liver sinusoidal endothelial cells
LYVE-1	Lymphatic vessel endothelial hyaluronan receptor 1
MAPK	Mitogen-activated protein kinase
MCD	Methionine-choline deficient diet
MDSCs	Myeloid-derived suppressor cells
MFI	Mean fluorescence intensity
MHC	Major histocompability complex
MIF	Macrophage inhibitory factor
min	minute
MMP	Matrix metalloproteinase
MoMF	Monocyte-derived macrophages
MPO	Myeloperoxidase
MVD	Microvessel density
NADH	Nicotinamide adenine dinucleotide
NAFLD	Non-alcoholic fatty liver disease
NASH	Non-alcoholic steatoheoatitis
ND	Normal diet
NF-κB	Nuclear factor kappa B
NGS	Normal goat serum
NK cells	Natural killer cells
NKT	Natural killer T cells
PAMP	Pathogen-associated molecular pattern
PD-1	Programmed cell death protein 1

List of contents

Zusammenfassung

Chronische Lebererkrankungen stellen eine erhebliche Belastung für die öffentliche Gesundheit dar und verursachen jährlich zwei Millionen Todesfälle. Diese sind überwiegend auf die Endstadien der chronischen Lebererkrankung, Leberzirrhose und das hepatozelluläre Karzinom (HCC), die häufigste Form von primärem Leberkrebs, zurückzuführen. Das Chemokin (C-X-C-Motiv) Ligand 12 (CXCL12) spielt eine wichtige Rolle bei der Progression von Leberfibrose und primärem Leberkrebs. Zusammen mit seinen beiden Rezeptoren (C-X-C-Motiv) Rezeptor 4 (CXCR4) und atypischer Chemokin Rezeptor 3 (ACKR3) begünstigt CXCL12 sowohl die Bildung von fibrotischem Narbengewebe als auch Wachstum, Progression und Metastasierung von Tumoren. Darüber hinaus steuert CXCL12 die Auswanderung von Immunzellen aus dem Knochenmark und ihre Rekrutierung in den Tumor und begünstigt dadurch eine tumorfreundliche Mikroumgebung.

Ziel dieser Studie war es, die Rolle von CXCL12 bei Leberfibrose und primärem Leberkrebs näher zu untersuchen und zu testen, ob sich die Inhibition von CXCL12 therapeutisch zur Verminderung von Leberfibrose und zur Behandlung von HCC nutzen lässt. Um dies bei der Leberfibrose zu untersuchen, wurde das CXCL12 neutralisierende RNA-Oligomer NOX-A12 in zwei experimentellen Mausmodellen der Leberfibrose eingesetzt, die entweder durch chronische CCl_4-Injektionen oder durch Fütterung mit einer Methionin-Cholin-Mangel-Diät (MCD-Diät) ausgelöst wurde. Um die Wirkung von CXCL12 auf primären Leberkrebs zu untersuchen, wurde NOX-A12 in einem Diethylnitrosamin (DEN)-induzierten Leberkrebsmodell eingesetzt, das entweder mit CCl_4 kombiniert wurde, um ein fibrotisches Milieu zu erzeugen, oder mit einer fett-, zucker- und cholesterinreichen Diät, um eine nicht-alkoholische Fettlebererkrankung (NAFLD) zu induzieren.

Die Inhibition von CXCL12 mit NOX-A12 hatte keinen Einfluss auf den Schweregrad der Leberfibrose, beeinträchtigte jedoch die Entzündungsresolution nach Beendigung der Schadenswirkung. Darüber hinaus verursachte NOX-A12 einen Anstieg der myeloiden Zellen im peripheren Blut, einhergehend mit einem Anstieg von Chemokinen im Blutplasma. In der Leber konnte ein Einfluss von NOX-A12 auf Monozyten abstammende Makrophagen (MoMF) gezeigt werden, was sich durch eine Verringerung von differenzierten CD11c$^+$MHC-II$^+$ MoMF und eine relative Zunahme von unreifen Ly6C$^+$ MoMF äußerte. Darüber hinaus führte die Inhibition von CXCL12 zu einer drastischen Abnahme von Eosinophilen in CCl_4-behandelten Lebern, nicht jedoch in NAFLD-Lebern. Interessanterweise förderte NOX-A12 das Tumorwachstum sowohl im fibrotischen als auch im NAFLD-assoziierten Modell des DEN-induzierten Leberkrebses, obwohl die tumorinfiltrierenden MoMF reduziert und die zytotoxischen CD8$^+$ T-Zellen in Tumoren erhöht waren. Zudem aktivierte NOX-A12 den Umbau von Mikrogefäßen der Tumoren, was sich in einer Hochregulation von CXCR4 auf Endothelzellen und einer verstärkten Genexpression von Angiogenese-assoziierten Markern zeigte. Dies war besonders ausgeprägt bei NASH-HCC nach therapeutischer Behandlung mit NOX-A12. Insgesamt legen die in dieser Studie erhobenen Daten nahe, dass CXCL12 die Entzündungsresolution nach chronischem Leberschaden beeinflusst. Darüber hinaus

deuten die Ergebnisse darauf hin, dass CXCL12 bei primärem Leberkrebs eine wichtige tumorbegrenzende Rolle spielt, die durch eine vielschichtige Beeinflussung des Tumormikromilieus hervorgerufen wird.

Abstract

Liver disease causes two million deaths annually and represents a significant and growing public health burden, with cirrhosis and primary liver cancer accounting for the majority of these deaths. Liver cirrhosis, resulting from chronic inflammation and fibrosis of the liver, is a significant risk factor for the most prevalent type of primary liver cancer, hepatocellular carcinoma. The pleiotropic chemokine (C-X-C motif) ligand 12 (CXCL12) has been implicated in both liver fibrosis and primary liver cancer. By signaling through its two cognate receptors, C-X-C motif receptor 4 (CXCR4) and atypical chemokine receptor 3 (ACKR3), CXCL12 may promote both liver fibrosis and tumor growth, progression, and metastasis. In addition, CXCL12 can also control immune cell egress from the bone marrow and their recruitment to the tumor, which may shape a pro-tumorigenic tumor microenvironment. In this study, the role of CXCL12 on liver fibrosis and primary liver cancer was further investigated, using experimental settings intended to explore CXCL12 inhibition as a potential target for novel interventions in these disease conditions.

To address this in liver fibrosis, NOX-A12, a CXCL12-neutralizing RNA oligomer, was applied in two experimental mouse models, induced either by chronic carbon tetrachloride (CCl_4) injections or by feeding a high fat methionine-choline deficient (MCD) diet. To explore the impact of CXCL12 on primary liver cancer, NOX-A12 was used in a model of diethylnitrosamine (DEN) induced liver cancer combined with either CCl_4 to create a fibrotic environment or with a high-fat, high-sugar, and high-cholesterol Western diet (WD) to induce non-alcoholic fatty liver disease (NAFLD).

CXCL12 inhibition with NOX-A12 had no impact on liver fibrosis but led to a prolonged inflammation after injury cessation. Furthermore, NOX-A12 increased chemokine levels in blood plasma, which was accompanied by an increase of peripheral blood myeloid cells. In the liver, CXCL12 inhibition provoked changes in hepatic monocyte-derived macrophage (MoMF) populations characterized by a decrease of CD11c$^+$MHC-II$^+$ MoMF and a relative increase of immature Ly6C$^+$ MoMF. In addition, CXCL12 inhibition drastically reduced eosinophils in the liver of CCl_4-treated, but not in NAFLD livers. Intriguingly, NOX-A12 promoted tumor growth both in the fibrosis- and in the NAFLD-associated model of DEN-induced liver cancer, despite reducing tumor-infiltrating MoMF and increasing cytotoxic CD8$^+$ T cells in tumor lesions. Moreover, CXCL12 inhibition activated vascular remodeling in tumor microvessels, evident by an upregulation of CXCR4 on endothelial cells and increased expression of angiogenic and anti-angiogenic genes, particularly pronounced in NASH-HCC after therapeutic treatment with NOX-A12. Taken together, these data suggest a role for CXCL12 in chronic inflammation resolution, and in limiting primary liver cancer, mediated by a multi-faceted re-shaping of the tumor microenvironment.

1. Introduction

Liver fibrosis and liver cirrhosis are regarded as major risk factors for hepatocellular carcinoma (HCC) and represent a major and increasing public health burden. Liver disease is responsible for two million deaths annually, with cirrhosis and HCC accounting for the majority of deaths. (1) Etiologies leading to liver fibrosis include viral hepatitis, exposure to environmental toxins, chronic and excessive alcohol consumption, and metabolic diseases. In recent years, non-alcoholic liver disease (NAFLD) resulting from obesity and metabolic disorders is emerging as a major cause of liver fibrosis and cirrhosis. (1, 2) Liver cirrhosis, the most advanced form of liver fibrosis, is a strong risk factor for HCC, independent of the underlying etiology. (3, 4) Although extensive research in the field of liver fibrosis and liver cancer over the past decades has led to a deep understanding of the pathological mechanisms and the identification of many promising drug targets, no effective curative treatment has been approved for the treatment of liver fibrosis and advanced liver cancer. (5) This may be due to previously overlooked complexity and dynamism of the liver microenvironment, where a variety of infiltrating and resident immune cells interact with hepatic stromal and mesenchymal cells. (6) Therefore, a profound understanding of the cellular and immunological mechanisms shaping the tumor-promoting microenvironment in liver fibrosis and HCC is essential for the development of safe and effective new therapies.

1.1 Liver immune homeostasis

1.1.1. The liver architecture

The liver is a vital organ with not only crucial functions in metabolism, detoxification, and immune tolerance but which also possesses remarkable regenerative capacities. Due to its unique anatomical location, the liver receives a dual blood supply, with a large amount of blood coming from the intestines and rich in nutrients as well as gut-derived, food-borne toxic compounds and microbial antigens, making the liver anatomically well positioned for having the role of a crucial immunological gatekeeper for the organism. In the liver, oxygenated arterial blood mixes with the venous portal blood in a ratio of about 20% to 80%, and passes through a network of capillary-like vessels, the sinusoids, before being drained in central veins. These sinusoids are formed by specialized liver sinusoidal endothelial cells (LSECs) and are populated by Kupffer cells, the largest collection of resident macrophages in the body, that are equipped with a multitude of scavenger receptors allowing for an effective clearance of food-derived antigens and aged red blood cells, as well as pathogens and

microbial components. (6-8) The liver sinusoids are fenestrated and organized in so-called sieve plates, forming a selectively permeable barrier that separates the blood stream from the hepatocytes, but also allows for the passage of selected molecules and hepatocyte interactions with immune cells located in the sinusoids. (8) LSECs lack a basement membrane which is accountable for a small gap between sinus endothelium and hepatocytes, called the space of Disse. Within the space of Disse reside the hepatic stellate cells (HSCs) formerly known as Ito cells, a minor cell population of dendritic-shaped pericytes wrapped around the sinusoids. In homeostasis, their main function is the storage of retinoids as well as the production of growth factors and extracellular matrix (ECM). (9) Hepatocytes comprise the main parenchymal cells in the liver with crucial roles in detoxification, metabolism, and protein synthesis, as well as bile production. (7) Bile produced by hepatocytes flows in small ducts formed by hepatocyte membranes, the canaliculi, into bile ducts in the portal areas. These bile ducts are formed by cholangiocytes, specialized epithelial cells that further modify the bile, and ultimately transport it through the biliary tree to the gallbladder and to the intestines. (10)

1.1.2 Hepatic immune cell populations

Despite the constant exposure to a multitude of antigens such as pathogen-associated molecular patterns (PAMPs) including lipopolysaccharides (LPS), the liver is cellular microenvironment generally mediates immunotolerance towards harmless antigens, while also being capable of sensing and eliminating potential threats. Enriched in immune cells of both the innate and the adaptive branch of the immune system, the liver is considered as an immune sentinel. (6)

Innate immunity describes a highly conserved first line of defense against pathogens. Innate immune cells comprise mainly phagocytic myeloid cells, such as macrophages and neutrophils that engulf and remove potential threats to the organism. Phagocytes carry pattern recognition receptors (PRRs) on their surface that bind to signature molecules found on bacteria, fungi, viruses, or parasites, but are also necessary for the phagocytosis of targets tagged by antibodies or certain plasma proteins of the complement system. Adaptive immunity, on the other hand, is a highly specific but slow-responding immune response at first antigen encounter, mainly carried out by T and B cells, lymphocytes that can effectively control and eradicate infections by killing infected cells and producing pathogen-specific antibodies. (11-13)

All blood cells originate from common multipotent hematopoietic stem cells in the bone marrow that give rise to two different lineages of progenitor cells, the common lymphoid progenitors (CLPs) and the common myeloid progenitors (CMPs). While CLPs can generate all types of lymphocytes (i.e., T cells, B cells and NK cells), the myeloid lineage, derived from CMPs, incudes monocytes, granulocytes (neutrophils, eosinophils, and basophils) but also megakaryocytes and erythrocytes. Dendritic cells, on the other hand, can derive from both CLPs and CMPs. (14)

T cells carry highly specific and unique receptors designed to recognize and bind non-self antigens, that are presented to them through certain protein complexes, called major histocompatibility complex (MHC). There are two major classes of MHC with different functions, MHC class I (MHC-I) and MHC class II (MHC-II), which are recognized by two distinct subsets of T cells. MHC-I is present on almost all cells in the body and is used primarily to present intracellular antigens of self or foreign origin, the latter inducing a cytotoxic immune response. Indeed, MHC-I binds to cluster of differentiation (CD)8^{+} T cell receptors on cytotoxic (CD8^{+}) T cells, that, upon stimulation, release cytolytic and cytotoxic molecules and effectively neutralize infected cells. MHC-II, however, is only expressed on professional antigen-presenting cells (APCs), such as macrophages and dendritic cells, and presents to T cells with a CD4 T cell receptor (CD4^{+} T cells) antigens that have been endocytosed and processed. As their primary function is to stimulate and activate other immune cells, CD4^{+} T cells are also known as T helper (Th) cells. (15, 16)

The liver contains several immune cell subsets capable of presenting antigens and activating T cells. (6, 7) Dendritic cells, a rare and heterogeneous population of highly effective professional APCs comprise a small population in the liver. Dendritic cells internalize and present antigens through MHC-II but can also present antigens to CD8^{+} T cells through MHC-I, a mechanism called antigen cross-presentation, making them powerful orchestrators of the immune response. (16, 17) Kupffer cells and LSECs similarly express MHC-II and co-stimulatory molecules and thus, function as professional APCs. Additionally, LSECs have been reported to be able to cross-present to CD8^{+} T cells. (7, 18) Another population of APCs present in the liver are B cells. As antibody-producing cells of adaptive immunity, B cells are key to mount a specific immune response to control infections and acquire immunity. B cells recognize specific antigens through their B cell receptor that contains a distinct membrane-bound antibody, but also express MHC-II through which they present captured antigens to CD4^{+} T cells which in turn activate B cells to produce and secrete large amounts of antibodies. (19, 20)

The liver harbors a large population of natural killer cells (NK cells) and natural killer T cells (NKT cells). (7) NK cells are innate lymphocytes that recognize and eliminate infected or malignant cells. Such cells are detected by NK cells due to their typical downregulation of normal self-molecules such as MHC-I. A lack of MHC-I on target cells, but also inflammatory cytokines activate NK cells to release cytotoxic granules and to eradicate the affected cells. NKT cells are immunomodulatory cells that express both NK cell markers and an α/β T cell receptor (TCR) with a restricted TCR repertoire. Unlike other T cells, NKT cells can recognize and respond to lipid antigens presented through the MHC-I-like molecule cluster of differentiation (CD)1d on APCs. (21) Nonetheless, in homeostasis, the liver displays a state of immune hyporesponsiveness and tolerance due to a constitutive expression of anti-inflammatory cytokines such as interleukin (IL) 10, as well as the presence of T cell inhibitory molecules like programmed death ligand 1 (PD-L1) on Kupffer cells and LSECs. (7)

6

In contrast to the liver resident Kupffer cells, that colonize the fetal liver during development and maintain their number by self-renewal, most macrophages in the body derive from circulating blood monocytes that originate from common myeloid progenitor cells in the bone marrow. (22, 23) Besides the bone marrow-derived monocytes patrolling in the blood, there are also few monocyte-derived macrophages found in the healthy liver, that can mostly be found in the portal areas, where they exert metabolic functions, and in the liver capsule, where they shield the liver from pathogens that might enter from the peritoneal cavity. (24, 25)

1.1.3 Immune cells in liver inflammation and regeneration

Liver injury of any etiology induces liver inflammation initially characterized by a pronounced infiltration of myeloid cells from the circulation. (26) Macrophages are key orchestrators of both initiation and resolution of liver inflammation. Upon injury, damaged hepatocytes release pro-inflammatory molecules, including damage-associated molecular patterns (DAMPs). These endogenous danger signals, among others free DNA, heat shock proteins, or high mobility group box 1 protein (HMGB1) are sensed by PRRs on Kupffer cells and other cells and induce an immune response. (26, 27) Activated Kupffer cells produce a large variety of pro-inflammatory cytokines as well as chemokines that attract neutrophils and monocytes from the circulation to assist in rapid removal of pathogens or dead hepatocytes and to support liver repair. (24, 26) Neutrophils are important first responders in sterile or pathogen-induced inflammation. Following recruitment by Kupffer cell-derived chemoattractants, such as CXC-chemokine ligand (CXCL)1 and CXCL2 that bind to CXC-chemokine receptors (CXCR)1 and CXCR2, respectively, neutrophils phagocytose cell debris or bacteria. However, neutrophils also release inflammatory mediators like reactive oxygen species (ROS) and proteases that can further damage hepatocytes and aggravate inflammation. (24, 28) Furthermore, activated Kupffer cells are an important source of CC-chemokine ligand (CCL)2 that recruits pro-inflammatory CC-chemokine receptor (CCR)2$^+$ monocytes to the liver. (29) Pro-inflammatory monocytes, typically identified by their expression of CD14 in human and Ly6C in murine blood, infiltrate the tissue where they differentiate into pro-inflammatory monocyte-derived macrophages (MoMF) that further promote inflammation by releasing complex and varying mixtures of chemokines and cytokines depending on the environmental cues. (24, 26) Cytokines are small, secreted proteins that serve as signaling molecules between cells and are key orchestrators of inflammatory and developmental processes. Cytokines is a general term that includes many different signaling protein classes such as interleukines (IL), chemokines, interferons (IFN), and growth factors. (30)

Pro-inflammatory and pro-fibrotic cytokines, such as tumor necrosis factor alpha (TNF-α), IL-1β, IL-6, platelet-derived growth factor (PDGF) and transforming growth factor beta (TGF-β), produced by Kupffer cells and infiltrated pro-inflammatory MoMFs, but also DAMPs from dying hepatocytes, result in the activation of HSCs, the key effector cells in hepatic fibrosis. Activated HSCs (aHSCs) proliferate

and transdifferentiate into contractile alpha-smooth muscle actin (αSMA) expressing myofibroblasts that produce large amounts of ECM, especially the fibrillar collagens I and III, and thus lead to scar-formation. (5, 31) However, in mouse models it was demonstrated that once the cause of injury is removed, the liver is highly efficient in resolving inflammation and fibrosis until homeostasis restoration. (27, 31)

MoMFs can both promote fibrosis progression and resolution and thus exert a dual but crucial role in liver fibrosis, as discovered in various experimental mouse models of liver diseases. (24, 26) In mice, it has been shown that pro-inflammatory Ly6C^high MoMF eventually mature in the tissue and downregulate Ly6C expression, while changing their expression profile to adopt an anti-inflammatory, restorative phenotype. Ly6C^low pro-restorative MoMFs do not only terminate inflammation by releasing anti-inflammatory cytokines and clearing the debris by phagocytosis, but also produce ECM-degrading proteins, such as matrix metalloproteinases (MMPs), and growth factors and thus, are crucial for tissue remodeling and repair (Figure 1). (27, 32) Phagocytosis of dead cells (efferocytosis) in combination with exposure to IL-4 and IL-13 are critical cues for the phenotype switch of macrophages. (33)
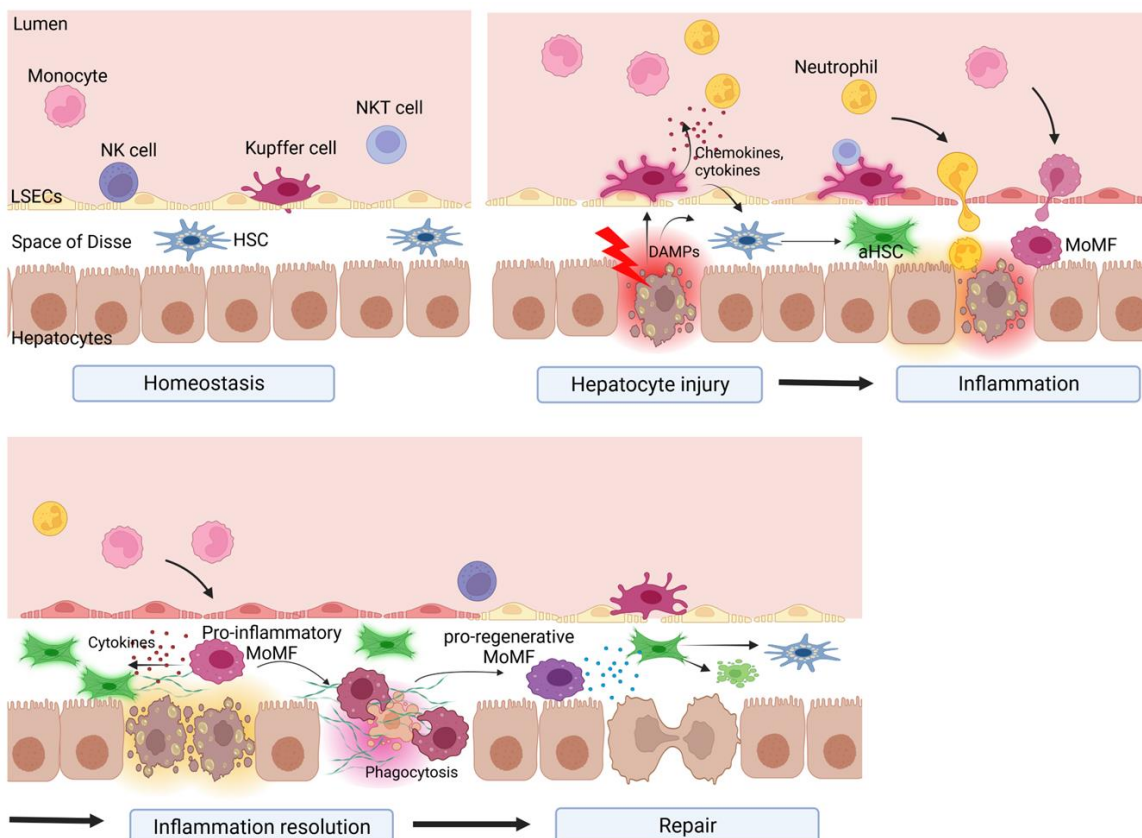
Figure 1: Key immune mechanisms driving liver inflammation initiation and resolution. The healthy liver contains a large population of Kupffer cells, tissue-resident macrophages that are located in the lumen of the blood sinusoids, and exert important homeostatic functions. The sinusoids are lined by liver sinusoidal endothelial cells (LSECs) that separate the blood flow from hepatocytes, the main parenchymal cells in the liver. Between hepatocytes and LSECs is a small

gap, termed space of Disse, in which hepatic stellate cells (HSCs) reside. Natural killer (NK) and natural killer T (NKT) cells patrol the sinusoids, maintaining immunosurveillance. Upon insult, injured and dying hepatocytes release damage-associated molecular patterns (DAMPs) that activate Kupffer cells, LSECs and HSCs to release chemokines and cytokines. HSCs then transdifferentiate into collagen-producing, fibroblast-like activated HSCs (aHSCs). The released cytokines recruit neutrophils and monocytes from the circulation, which elicit an inflammatory reaction, resulting in increased tissue damage. Infiltrating monocytes differentiate into pro-inflammatory monocyte-derived macrophages (MoMF), which release inflammatory and pro-fibrotic cytokines, stimulating further activation of HSCs and production of extracellular matrix (ECM). Phagocytosis of dead material promotes the switch from pro-inflammatory to pro-regenerative MoMFs, which promote tissue repair and degradation of the scar-tissue. Pro-regenerative MoMF can also stimulate aHSCs to undergo apoptosis or return to a quiescent state.

The notion that macrophages can acquire a pro-inflammatory or an anti-inflammatory phenotype and can be polarized *in vitro* by prototypical stimuli has led to the concept of M1 (pro-inflammatory) and M2 (anti-inflammatory) macrophages, based on the Th1 and Th2 paradigm. (34) Although this dichotomy is widely used and still well accepted, it is vastly oversimplified. Over the last years it became increasingly evident, that macrophages display a potent plasticity and diversity, and that their functions as well as marker expression are highly context dependent and versatile. Moreover, macrophages can simultaneously express so-called M1- and M2-markers, making the M1/M2 classification even less relevant in many circumstances. (24, 35)

Still, there are common markers both in mice and in humans that are generally associated with a rather pro-inflammatory, immunogenic macrophage phenotype, such as MHC-II, CD86, inducible nitric oxide synthetase (iNOS) and CD80, while expression of CD206, PD-L1, Arginase 1 (ARG1) and CD301 are indicative of anti-inflammatory, pro-restorative macrophages. (36, 37)

1.2 Liver fibrosis and primary liver cancer

1.2.1 Liver fibrosis as a dynamic hallmark of chronic liver diseases of various etiologies

Liver inflammation and fibrosis are well-organized and protective mechanisms to preserve function and structural integrity of the damaged organ but also support tissue regeneration. However, when the cause of injury persists, as it occurs during chronic infections, autoimmune diseases, cholestasis, or following continuous exposure to metabolic stress or toxins like alcohol, fibrosis becomes progressive and represents a pathological condition. Progressive fibrosis is an aberrant, yet dynamic wound healing process characterized by excessive ECM deposition or scarring, with concomitant matrix remodeling and degradation, and impaired regenerative capacity. Progressive scarring culminates in cirrhosis, the final stage of liver fibrosis, with high risks of liver failure and other life-threatening complications. (5, 27, 31) The pathological manifestations of NAFLD on the other hand range from steatosis, the accumulation of fat in the liver, to steatohepatitis, characterized by ballooning of fat-overloaded hepatocytes and lobular inflammation, to cirrhosis. (38)

1.2.2 The impact of immune cells on liver fibrosis

While the underlying cellular responses resemble the physiological wound healing response, chronic inflammation fails to terminate and deteriorates over time. Senescent hepatocytes, unable to regenerate, accumulate and secrete an array of chemokines, cytokines, and growth factors that further attract immune cells and activate fibroblasts and HSCs. (27, 39) In non-alcoholic steatohepatitis (NASH) and alcohol-associated liver disease (ALD) the chronic inflammatory response was shown to be aggravated by an increased presence of microbial components stemming from a defective intestinal barrier, promoting and amplifying the pro-inflammatory response of macrophages. (27, 40, 41) As in acute inflammation and regeneration, hepatic macrophages can promote both fibrosis progression and resolution. In mice, freshly infiltrating pro-inflammatory Ly6C^{hi} MoMF are attributed pro-fibrotic functions, while matured Ly6C^{low} MoMF are thought to support fibrosis regression and to inactivate aHSCs, that subsequently undergo apoptosis, become senescent or return to a quiescent state. (27, 31)

Various other immune cells participate in chronic liver inflammation, facilitating either fibrosis progression or resolution. Dependent on distinct environmental cues, unstimulated, naïve CD4$^+$ T cells can differentiate into many different effector subtypes that promote different immune responses. For instance, upon stimulation with IL-12, CD4$^+$ T cells differentiate into Th1 effector cells and produce pro-inflammatory cytokines, such as interferon gamma (IFNγ). IFNγ induces the expression of MMPs and is therefore considered to have an antifibrotic effect. Th2 cells on the other hand, are induced upon stimulation with IL-4 and produce IL-4 and IL-13 which are important for wound closure, but also drive fibrosis. (15, 42, 43) IL-4 and IL-13 induce collagen production by fibroblasts but also stimulate macrophages to release growth factors that act on aHSCs, such as fibroblast growth factor (FGF), connective tissue growth factor (CTGF) and platelet-derived growth factor (PDGF). (44) Thus, the balance between Th1 and Th2 adaptive immune responses can skew fibrosis either towards progression or regression. NK cells and $\gamma\delta$ T cells, a small subset of unconventional T cells that is abundant in the liver, eliminate aHSCs and senescent hepatocytes and thus limit fibrosis. (27, 31) The role of NKT cells in liver fibrosis on the other hand, is contradictory. NKT cells secrete cytokines that stimulate TGF-β production in HSCs and therefore play a rather profibrogenic role. However, NKT cells have also been reported to produce IFNγ and to be involved in the removal of senescent hepatocytes. (45, 46)

The unique lipotoxic and inflammatory environment in NAFLD/NASH causes an accumulation of immune cells with a distinct inflammatory signature. Besides an increase in dendritic cells, NAFLD/NASH bear an increased number of metabolically activated CD8$^+$ T cells with an auto-aggressive phenotype inducing hepatocellular death in an MHC-I independent manner. In addition, the

macrophage compartment is expanded by a MoMF population with a unique metabolically activated phenotype, characterized by a high expression of both pro-fibrotic and anti-inflammatory genes, resembling macrophages in lipid tissues. (38, 47-49) Chronic inflammation and fibrosis are characterized by repeated cycles of hepatocyte death and compensatory regeneration together with cellular stress, which facilitates the accumulation of replicative errors and mutations in hepatocytes. (50, 51) As a result, both chronic liver inflammation and fibrosis are strongly predisposing to tumorigenesis, and more than 90% of HCCs develop in the presence of cirrhosis. (4) Figure 2 provides an overview over the inflammatory responses in liver fibrosis.
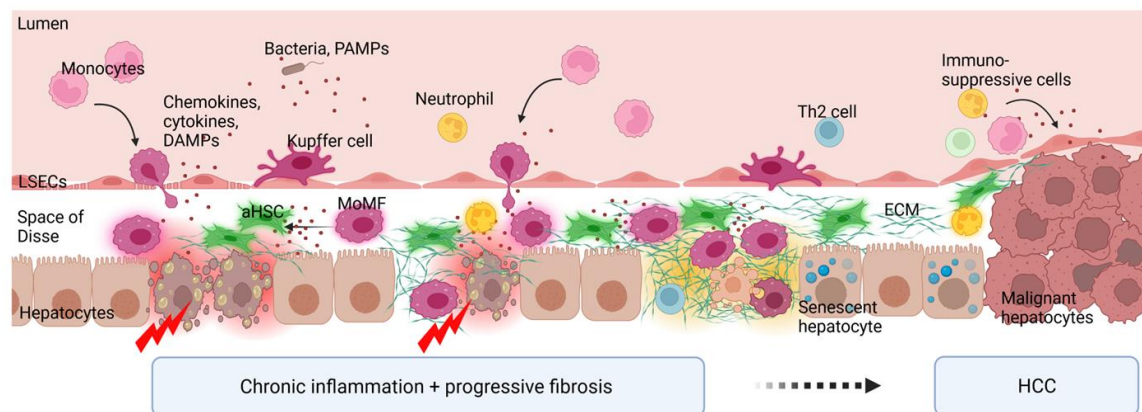
Figure 2: Liver inflammation and fibrosis exacerbation upon chronic injury. Chronic inflammation leads to continuous recruitment of inflammatory cells, activation of hepatic stellate cells (aHSC) and extracellular matrix (ECM) deposition. A defective intestinal barrier, present in some chronic liver diseases, increases bacteria and pathogen-associated molecular patterns (PAMPs) in the portal blood, which further aggravates inflammation. Failure to resolve inflammation and initiate regeneration gradually worsens fibrosis. Over time, functional parenchymal cells are progressively replaced by scar tissue. Chronic inflammation and fibrosis also promote the development and growth of hepatocellular carcinoma (HCC). MoMF, monocyte-derived macrophages; LSECs, liver sinusoidal endothelial cells.

1.2.3 Hepatocellular carcinoma

Primary liver cancers currently rank for the third most common cause of cancer related death worldwide. HCC is the most prevalent form of primary liver cancer and accounts for 80% of all cases, followed by cholangiocarcinoma, a tumor that arises from bile ductular cells, representing about 15% of primary liver cancers. (52) Early-stage HCC is in some cases curable by resection, or ablation, potentially followed by liver transplantation. (4, 53) However, HCC is often diagnosed at an advanced stage and in a cirrhotic liver, when curative treatment is no longer possible. Despite recent advances in palliative treatment options, there is still an unmet need for the therapy of advanced HCC. Although it provides only a small survival benefit of about three months compared with best supportive care and has a high incidence of serious adverse events, the multikinase inhibitor sorafenib has been the standard of care for unresectable HCC for more than a decade. (3) The advent of immune checkpoint inhibitor therapies targeting the programmed cell death protein 1 (PD-1) /PD-L1 axis could significantly

improve overall survival in HCC patients, and a combination therapy of the PD-L1 blocking antibody atezolizumab and the vascular endothelial growth factor A (VEGFA)-neutralizing antibody bevacizumab has recently replaced sorafenib as standard of care in first line therapy for advanced HCC. (4, 54) However, only a small fraction of patients responds to these therapies, for reasons that so far remain unclear. (50)

The cellular origin of HCC is debated. It is assumed that HCC originates from dysplastic mature hepatocytes, although hepatic progenitor cells could also be a source. (55) However, HCC exhibits a high histomolecular heterogeneity, seemingly related to the underlying aetiology and with implications for the prognosis. While mutations in telomerase reverse transcriptase (TERT) are predominant in hepatitis B virus (HBV)-related HCC and result in a poorly differentiated, highly proliferative tumor with a dismal prognosis, mutations in the β-catenin/Wnt pathway, mostly (e.g., in CTNNB1), have a higher prevalence in HCC arising from ALD and a less bad prognosis. Mutations in cell cycle control (TP53) are frequent in both aetiologies. Additionally, there are a multitude of other albeit less frequent, tumor-inducing mutations affecting various tumor-related pathways. (4, 50, 56) However, HCC also has a high intratumoral heterogeneity as well as a variable composition of immune and stromal cells in its microenvironment.

1.2.4 The tumor microenvironment

The tumor microenvironment (TME) describes a dynamic and heterogeneous tumor-specific micromilieu present in tumors that not only supports tumor development and progression, but also provides protection against immune surveillance. The TME comprises both cellular and acellular components. Cellular components include not only tumor cells but also non-malignant cells, like endothelial cells, cancer-associated fibroblasts (CAFs), and other stromal cells, and various immune cells. The acellular components of the TME comprise soluble factors such as cytokines and chemokines, through which the tumor interacts with and reprograms surrounding cells, as well as growth factors and ECM produced by non-malignant cells that promote tumor growth. (57, 58) Thus, the TME creates a complex and dynamic niche with a variable composition depending on tumor type and underlying mutations, but also on the metabolic conditions and the tumor stage. (4, 57, 58)

CAFs, a heterogeneous population of activated fibroblasts, represent a critical tumor-supporting component of the TME. Analogous to activated HSCs in fibrosis, CAFs are activated by TGF-β, PDGF and FGF, upregulate αSMA and acquire a proliferative and secretory phenotype. CAFs produce growth factors and cytokines that recruit and polarize immune cells toward an anti-inflammatory phenotype, thereby creating a tumor-promoting environment. (59) In HCC, activated HSCs promote tumor growth through collagen I production. While collagen I increases matrix stiffness in the tissue surrounding the tumor, thereby promoting tumor progression, degraded collagen I serves as a ligand for discoidin

domain receptor 1 (DDR1) on malignant cells, promoting their proliferation and tumor progression. (60)

HCCs are hypervascular tumors whose rapid growth and progression are highly dependent on angiogenesis. Angiogenesis, the formation of new blood vessels, is normally a finely regulated process that depends on a delicate interplay between proangiogenic and anti-angiogenic factors. (61) In tumors, this balance is dysregulated resulting in a functionally and structurally aberrant vasculature and a poorly oxygenated TME. (62, 63) Out of many pro-angiogenic molecules, the key factors driving tumor neoangiogenesis in HCC are angiopoietin 2 (Ang2) and VEGFA, inducing an altered vasculature in HCC, which is characterized by an increased arterialization of its blood supply along with capillarization of the sinusoidal endothelium. (61, 64)

Tumor-promoting inflammation is an enabling hallmark of cancer, as it can facilitate tumor initiation, promotion and progression, and primary liver cancers are proto-typical inflammation-associated tumors. (57, 65, 66) Chronic, unresolved inflammation results in a tumor-promoting microenvironment that reprograms infiltrating immune cells to an anergic or immunosuppressive phenotype. On the other hand, pro-inflammatory mediators like cytokines can drive tumor development, growth and progression, either by generating reactive oxygen or nitrogen species, that drive mutations in malignant cells, or by activating pathways like nuclear factor kappa B (NF-κB) and signal transducer and activator of transcription 3 (STAT3), that directly promote tumor survival and proliferation and dedifferentiation. (66, 67) Among the tumor-promoting pro-inflammatory cytokines, IL-6 and TNF-α are key drivers of hepatocarcinogenesis, especially in obesity-associated HCC. (68) TNF-α facilitates tumor initiation, but also promotes tumor cell survival and proliferation by activating the NF-κB pathway. IL-6, on the other hand, is a multifunctional cytokine that is regulated by the NF-κB pathway and promotes hepatocyte survival and proliferation through the STAT3 pathway. Although tumor cells themselves produce inflammatory cytokines, stromal cells and immune cells, especially macrophages, are an important source of tumor-promoting inflammatory cytokines. (66, 67)

1.2.5 Immune cells in the tumor microenvironment

The TME of HCC may contain various immune cells that are either actively tumor supportive (e.g., myeloid cells, regulatory T (Treg) cells) or potentially tumoricidal but disabled by the anti-inflammatory environment (e.g., T cells, NKT cells, NK cells). (69) Treg cells are a subpopulation of potent immunosuppressive CD4^{+} T cells, characterized by a constitutive, high expression of CD25 and the transcription factor forkhead box P3 (Foxp3). In normal immune responses, Treg cells are important to limit inflammation and end aberrant immune responses by producing anti-inflammatory cytokines like IL-10, and TGF-β, and the immune checkpoint molecule cytotoxic T-lymphocyte associated protein 4 (CTLA-4) that downregulates the expression of co-stimulatory CD80/CD86 on APCs. In the TME,

however, Treg cells impair anti-tumor surveillance and promote tumor growth and development. (70) In addition to Treg cells, myeloid cells are the main immunosuppressive component of the TME and consist of granulocytes, mainly tumor-associated neutrophils (TANs), tumor-associated macrophages (TAMs) and immature myeloid cells, often referred to as myeloid-derived suppressor cells (MDSCs). (58, 69) Depending on the tumor stage, TANs can either have a pro- or anti-tumorigenic role. TANs recruited during early tumor development release cytotoxic granule proteins and reactive nitrogen and oxygen species (RNS/ROS) that damage malignant cells and promote inflammation. In the TME of advanced tumors on the other hand, TANs secrete anti-inflammatory mediators e.g., prostaglandin E2 (PGE$_2$), matrix remodeling proteins (neutrophil elastase, MMP9), and therefore not only impair anti-tumor responses but also stimulate tumor progression, angiogenesis, and invasion. (71) MDSC is a collective term for immature monocytes and granulocytes with an anti-inflammatory phenotype. In mice, monocytic MDSCs are generally identified by their expression of the surface markers CD11b and Gr1/Ly6C, while granulocytic MDSCs are commonly described as CD11b$^+$ Ly6C^{low} Ly6G$^+$ cells. However, the signature markers for MDSCs are also abundant on regular neutrophils and pro-inflammatory monocytes and additional functional assays are needed to assign these cells without a doubt. (72) TAMs are a major and crucial component of the TME and a high abundance of TAMs in HCC is generally associated with tumor progression and aggressiveness. (73)

1.2.6 The role of tumor-associated macrophages in hepatocellular carcinoma

Most TAMs originate from circulating CCR2$^+$ classical monocytes, and CCL2, produced by malignant cells, CAF, endothelial cells, and other sources, is considered the major route of TAM recruitment. (74, 75) However, there are many other chemokines such as CCL5, CCL3, and CXCL12 and factors e.g., HMGB1, colony stimulating factor 1 (CSF-1) and VEGFA that attract monocytes. (35) Moreover, MoMF can proliferate within the tumor site and Kupffer cells can also contribute to the TAM pool. (76) In addition to classical monocytes, which are often identified in mice by their high expression of Ly6C, there is also a population of non-classical CCR2^{low} Ly6C^{low} CX3CR1^{high} monocytes in the blood. These non-classical monocytes patrol the vessels where they interact with NK cells and play a rather protective role. (37)

Like macrophages in other disease conditions, TAMs can adopt pro-inflammatory and anti-inflammatory phenotypes. TAMs with a pro-inflammatory phenotype are potentially tumoricidal, as they not only directly eliminate tumor cells by phagocytosis but also cross-present tumor antigens to cytotoxic CD8$^+$ T cells and release pro-inflammatory cytokines to induce Th1 cell responses. (34, 77, 78) However, due to their high plasticity and ability to adapt to environmental cues, macrophages are prone to be reprogrammed by the tumor-promoting conditions in the TME. Consequently, the majority of TAMs adopt a phenotype that supports the tumor. (35, 37)

A major role of pro-tumorigenic TAMs is to suppress anti-tumor immunity. TAMs express anti-inflammatory cytokines, such as IL-10 and chemokines, that attract Treg cells and therefore promote an anti-inflammatory TME. (74, 79, 80) In addition, TAMs can directly restrict T cell activity. TAMs express the immune checkpoint ligand PD-L1 that binds to PD-1 on activated cytotoxic CD8$^+$ T cells. (81) Engagement of PD-1 on activated T cells attenuates their cytotoxic activity and induces anergy. (82) Furthermore, TAMs highly express the enzyme ARG1 that catabolizes and thus removes arginine from the microenvironment, an amino acid critical for T cell activation. (83) Besides their inhibitory role, TAMs can also directly support tumor growth and development, and mediate resistance towards anti-tumor therapies. Tumor promoting TAMs produce growth factors, such as hepatocyte growth factor (HGF) that directly facilitate proliferation of HCC, as well as TGF-β which is an important regulator of epithelial-to mesenchymal transition (EMT) of tumor cells, but also release MMPs that activate latent TGF-β and growth factors sequestered in the ECM. (84, 85) Moreover, TAMs accumulate in hypoxic tumor regions and produce factors involved in angiogenesis (e.g., VEGFA, MMP9). (86-88)

Typical conditions in the TME of HCC that influence the activation of tumor infiltrating macrophages include hypoxia, acidosis, and increased free fatty acids and lipid metabolites. As a result of the high energy demand and uncontrolled growth of tumor cells without adequate vascularization and blood supply, the TME becomes increasingly hypoxic and low in nutrients. (89) Hypoxia is defined as a state of pathologically low oxygenation, but it is also a common phenomenon in wounds where it induces angiogenesis and other regenerative responses. Hypoxia is primarily sensed by the transcription factor hypoxia inducible factor 1 subunit alpha (HIF-1α), that induces a multitude of target genes related to regeneration and angiogenesis. (90) In TAMs, hypoxia promotes an anti-inflammatory and pro-angiogenic phenotype, as HIF-1α induces upregulation of PD-L1 and VEGFA. (89)

Malignant cells acquire a specific dysregulated metabolism to adapt to an environment poor in nutrients and oxygen, a phenomenon known as the Warburg effect. (91) The Warburg effect describes the preference of tumor cells to utilize glucose via glycolysis, instead of using the citrate cycle, even under aerobic conditions. (57, 92) Lactate is a side product of aerobic glycolysis, and its accumulation contributes to an acidic microenvironment in the TME. (92) The acidic environment induces immunosuppressive pathways in TAMs and the high lactate concentrations stabilize HIF-1α, which further drives a tumor promoting polarization of TAMs. (93) Moreover, macrophages require glucose for the generation of ROS and inflammatory cytokines. The rapid consumption of glucose by tumor cells makes it unavailable for TAMs and thus impairs an inflammatory response. (94) Due to an increased demand for lipids to build cell membranes and produce lipid mediators, many HCC upregulate genes associated with *de novo* lipogenesis or free fatty acid uptake. (95, 96) This results in an environment enriched in lipids and lipid metabolites, a condition that induces a pro-tumorigenic phenotype in TAM, characterized by the expression of CD206, IL6, VEGFA, MMP9 and ARG. (97)

1.3 The chemokine CXCL12 and its receptors in liver diseases

The inflammatory response is largely orchestrated by chemokines, chemotactic cytokines that may be found in the blood circulation and attract immune cells to sites of inflammation. Thus, chemokines are crucial regulators of inflammatory responses, which makes them promising targets for therapeutic interventions. (98)

1.3.1 Chemokines and chemokine receptors

Chemokines are a large family of small, secreted, chemotactic cytokines, that are key orchestrators of immune cell recruitment and localization. In mice and humans, so far around 50 chemokines are known and can be categorized into four subfamilies according to variations in the configuration of two N-terminal cysteines: CC, CXC, CX3C, and XC. While in CC-chemokines the cysteines are juxtaposed, in CXC-chemokines, an intervening amino acid separates the cysteine residues. In the CX3C-chemokine class, comprising only one member, the cysteines are spatially separated by a sequence of three amino acids. XC-chemokines have only one of the first two cysteines. (98, 99) Chemokines bind to heptahelical surface receptors that can be subdivided into conventional chemokine receptors (cCKR) and atypical chemokine receptors (ACKR). Conventional chemokine receptors are coupled with and transduce signals through activating pertussis toxin sensitive Gαi proteins, as well as through β-arrestin. ACKRs, on the other hand, bind chemokines with a high affinity but typically do not activate signal transduction pathways. Instead, the four known members of the ACKR family are thought to modulate and regulate chemokine abundance and generate gradients by scavenging or transporting chemokines across endothelial cells to the luminal side of blood vessels. Currently, there are 18 known conventional chemokine receptors, that are named after their predominant type of chemokine ligand, CCR, CXCR, CX3CR, and XCR, and numbered in the order of their discovery. (98, 100) Functionally, chemokines can be classified into inflammatory and homeostatic chemokines. Inflammatory chemokine production is inducible, whereas homeostatic chemokines are constitutively expressed. (101)

Chemokines and chemokine receptors are best known for their roles in migration and adhesion of leukocytes, particularly in immune cell localization in homeostasis as well as in immune cell recruitment during inflammation. However, the functions of chemokine receptors go beyond migration as they can also induce pathways that regulate, for example, differentiation, proliferation, survival, or anti-microbial responses. In addition, chemokine receptors can also be expressed on non-immune cells, such as endothelial cells, mesenchymal cells, as well as tumor and tumor stromal cells, where they directly affect angiogenesis, proliferation, and dissemination. (98, 102) The chemokine system is complex, with many pleiotropic but also partially overlapping functions and regulatory

mechanisms, enabling a fine modulation of immune responses. The activity and availability of chemokines is not only regulated through scavenging by ACKRs but also by the chemokines high affinity to bind to glycosaminoglycans (GAGs) on cell surfaces and ECM. (103) While different immune cell types express a different set of chemokine receptors depending on their developmental state and activation, some chemokine receptors are expressed only by distinct immune cell subsets. Most chemokine receptors bind multiple chemokines, and the majority of chemokines can bind to several chemokine receptors. To add another layer of complexity, chemokines can not only bind in their monomeric form, but also form homodimers and heterodimers with other chemokines or other proteins, such as HMGB1. Likewise, chemokine receptors can dimerize with other chemokine receptors and ACKRs, modulating their affinity and receptor functions, respectively. (98)

Of all the chemokines involved in tumor growth and progression, CXCL12 is one of the most potent and versatile, with critical functions in development, homeostasis, and cancer. The CXCL12 chemokine axis has been implicated in over 20 human malignancies, where it is associated with disease progression and poor clinical outcome. (104, 105)

1.3.2 The chemokine CXCL12

CXCL12, formerly called stromal cell-derived factor 1 (SDF-1), holds an extraordinary role in the chemokine system. Together with its two cognate receptors CXCR4 and ACKR3 it is involved in the differentiation, migration, and homing of immune cells in homeostasis, but also plays an essential role in the development of the cardiovascular, nervous, and hematopoietic systems during embryogenesis. (106)

The CXCL12 chemokine axis is essential for life as genetic deletion of either *Cxcl12*, *Cxcr4* or *Ackr3* in mice is perinatal lethal. (107-109) Gain-of-function mutations, on the other hand, most typically result in reduced numbers of neutrophils in the blood, causing an immune disorder known as warts-hypogammaglobulinemia-infections-myelocathexis (WHIM) syndrome, which is characterized by neutropenia, hypogammaglobulinemia, recurrent infections, and a high susceptibility to human papillomavirus infections that manifest as warts. (110) The importance of this chemokine axis is also reflected by the fact that CXCL12 and its receptors are extremely highly conserved in all vertebrates. (106) CXCL12 has six isoforms in humans and three isoforms in mice. All these isoforms are generated by differential C-terminal exon splicing, resulting in different stability and affinities for GAG binding. (101, 106)

CXCL12 is constitutively expressed in many organs, including the primary lymphoid organs (bone marrow and thymus) and secondary lymphoid organs (lymph nodes, spleen, Peyer's patches), as well as in the liver and lung. (98, 106)

CXCR4 (CD184) is a broadly expressed membrane receptor, and CXCL12 is its only known chemokine ligand. (101, 111) First discovered as a cofactor responsible for human immunodeficiency virus (HIV) entry on T cells, CXCR4 is now known to be expressed at varying levels by virtually all leukocyte subsets and their precursors, depending on their maturation or activation. (98, 112) In addition, CXCR4 is expressed by stem cells, endothelial cells, epithelial cells, cells of the neural system, keratinocytes and stromal cells in the lymph nodes, thymus, and bone marrow. (101, 111) Binding of CXCL12 to CXCR4 induces typical heterotrimeric G protein-coupled signal transductions. CXCR4 can not only couple to $G\alpha_i$ G proteins, but also to $G\alpha_q$ and $G\alpha_{12/13}$, resulting in the activation of various signaling pathways. Upon ligand binding, conformational changes in the heptahelical receptor induce the dissociation of the $G\alpha$ and the $G\beta\gamma$ subunits of the coupled G protein, activating a complex cascade of downstream second messenger and signaling pathways, amongst others phospholipase C (PLC), phosphoinositide-3 kinase (PI3K), and Ras pathways that promote migration, adhesion, but also survival and proliferation. (113) Following dissociation of the G proteins, CXCR4 is rapidly desensitized. G protein-coupled receptor kinases (GRKs) phosphorylate the intracellular C-terminus of CXCR4 and recruit β-arrestin that not only sterically blocks binding of G-proteins but also initiates clathrin-dependent internalization and lysosomal degradation of the chemokine-receptor complex. In addition, β-arrestin also activates signaling pathways like p38 mitogen-activated protein kinase (MAPK), which promotes chemotaxis, as well as survival and proliferation. (111, 113, 114) Besides CXCL12, CXCR4 can also bind non-chemokine ligands, including macrophage inhibitor factor (MIF), extracellular ubiquitin and HMGB1. (111, 113)

The atypical chemokine receptor ACKR3, formerly known as CXCR7 or RDC1, is the second receptor of CXCL12 and has CXCL11 as a second ligand. ACKR3 is not coupled to a G protein and functions primarily as a scavenger receptor. ACKR3 binds CXCL12 with a tenfold higher affinity than CXCR4 and is continuously internalized and recycled even in the absence of ligand binding. Thus, ACKR3 sequesters CXCL12 from the environment and plays an important role in modulating CXCR4-dependent migration and other responses. However, ACKR3 can also signal through β-arrestin to induce p38 MAPK signaling pathways. (111, 115) ACKR3 is mainly expressed by neuronal and vascular cells, but also in mesenchymal stromal cells and some immune cell subsets. (116)

CXCL12 is a pleiotropic cytokine that induces a broad range of cellular responses beyond migration and adhesion, such as angiogenesis, survival, and proliferation, therefore it is finely regulated on multiple levels. CXCR4 and ACKR3 can form homo- and heterodimers, each preferentially inducing distinct cellular functions. (98, 101) In addition, CXCR4 can form heterodimers with other receptors. CXCL12 on the other hand can bind in a monomeric or dimeric form to modulate the induced signal, but also forms heterodimers with other chemokines. (105, 117)

In homeostasis, the CXCL12 axis participates in the development, positioning and homing of T cells and B cells in primary and secondary lymphoid organs and regulates the retention of stem cells, progenitor cells and immune cells in the bone marrow. (99, 105, 106) Moreover, CXCL12 is also involved in the regulation of inflammatory responses, wound healing, and tissue repair. During inflammatory responses, CXCL12 synergizes with other chemotactic molecules to potentiate the migration of immune cells to the sites of inflammation. For instance, CXCL12 can form heterodimers with HMGB1 that bind with a high affinity to CXCR4 on monocytes and enhance their infiltration. (118) Both CXCL12 and CXCR4 are upregulated by hypoxia, stress, and vascular injury and mediate the migration of pro-angiogenic immune cells and stem cells to wounds to initiate revascularization and repair. (106, 119-121)

Due to its vital functions in cell migration, survival and proliferation, dysregulation of the CXCL12 axis has been implicated in many inflammatory and autoimmune pathologies, but most notably in cancer. (111, 113, 122, 123) Overexpression of CXCR4, ACKR3 and CXCL12 have been reported in various cancer types, where CXCL12 signaling either directly stimulates proliferation, survival and metastasis of tumor cells or regulates tumor neoangiogenesis and the recruitment of immunosuppressive immune cells and thus facilitates a tumor promoting TME. (113)

1.3.3 The CXCL12 axis in liver fibrosis and liver cancer

CXCL12 is highly expressed in the homeostatic liver, where it is produced by endothelial cells, biliary epithelial cells, HSCs and Kupffer cells. (29, 98, 124) While ACKR3 is predominantly found on liver endothelial cells, CXCR4 can be expressed by most cells in the liver, such as HSCs, hepatocytes, Kupffer cells and other liver resident or cycling immune cells. (120, 124, 125) However, the CXCL12 chemokine axis also plays an important role in liver inflammation, regeneration, and liver cancer (Figure 3). (120, 125) Although CXCL12 participates in the recruitment of inflammatory cells, its role in acute liver injury is rather protective. Both CXCL12 and its receptors are upregulated upon liver damage and interference with either component results in aggravated inflammation and impaired regeneration. Activated HSCs and endothelial cells associated with inflammatory foci secrete increased amounts of CXCL12 in response to hypoxia and hypoxia-induced factors and attract CXCR4^{+} pro-regenerative cells to the site of injury. (120, 125) On LSECs, signaling through ACKR3 induces the hepatoprotective growth factors regulated by the transcription factor Inhibitor of DNA binding 1 (ID1), such as HGF and Wnt2 that promote hepatocyte proliferation and liver regeneration. (126) In addition, liver engraftment with endothelial progenitor cells and mesenchymal and hematopoietic stem cells is controlled by CXCL12 signaling, further supporting regeneration. (127-129)

In chronic liver inflammation and fibrosis, both CXCL12 and its receptors were reported to be upregulated and involved in disease progression. (120, 125) In patients with liver fibrosis of different

etiologies, CXCL12 plasma levels were increased, and CXCL12 was overexpressed in biliary epithelial cells in fibrotic livers. (130) Activated HSCs and myofibroblasts, the key drivers of fibrosis progression, are also an important source of CXCL12 in liver fibrosis. (124, 131, 132) Moreover, HSCs also express CXCR4 and binding of CXCL12 promotes their activation, leading to increased contractility, proliferation, and collagen I production. (131, 133) CXCR4 and to a lesser extent ACKR3 are upregulated in human hepatocytes from ALD and NASH livers in response to inflammatory signals and oxidative stress and implicated to play a role in the formation of Mallory-Denk bodies. (134)
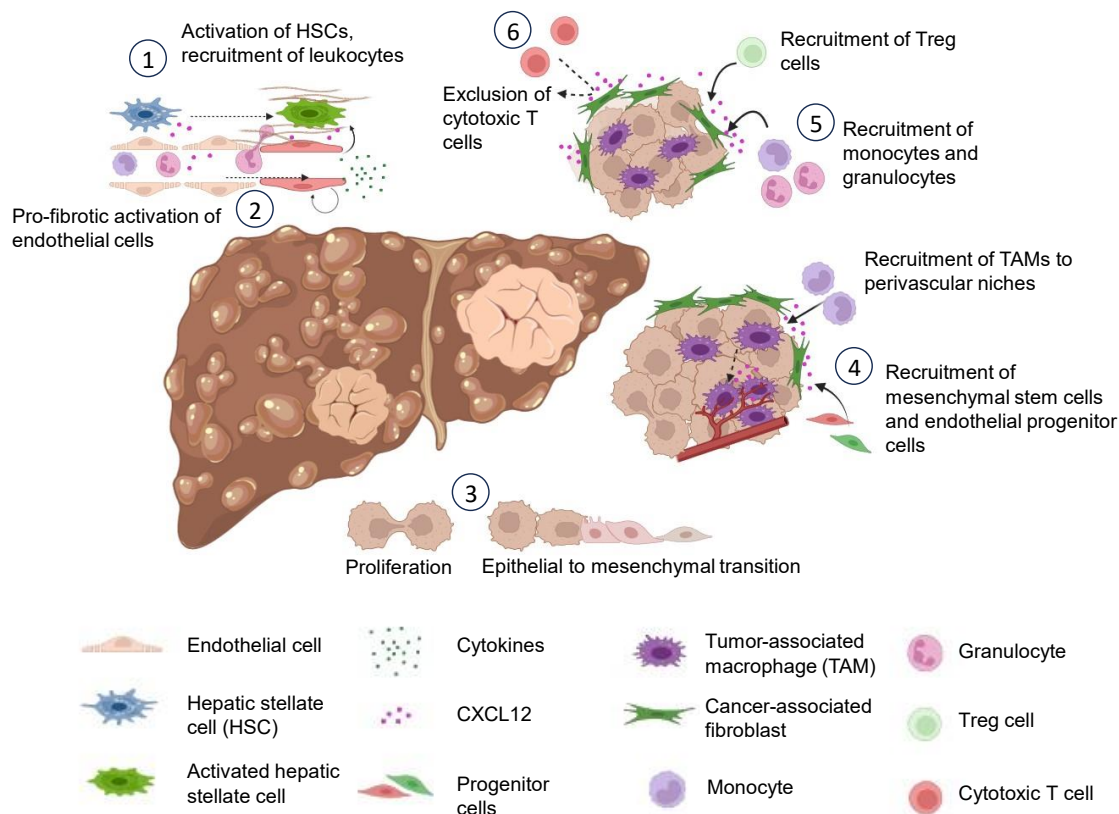
Figure 3: Reported roles of the CXCL12 chemokine axis in liver fibrosis and primary liver cancer.
1) CXCL12-CXCR4 interactions activate HSCs and contribute to fibrosis. 2) Activated LSECs respond to CXCL12 by producing pro-fibrotic mediators. 3) CXCL12-CXCR4 signaling directly induces cell proliferation and dedifferentiation. 4) CXCL12 attracts mesenchymal stem cells and endothelial progenitor cells and pro-angiogenic TAMs that promote tumor vascularization. 5) High CXCL12 concentrations provided by cancer-associated fibroblasts in the tumor and at the tumor margin recruit immunosuppressive immature monocytes, neutrophils, and regulatory T cells (Treg cells) to the tumor, shaping a tumor promoting environment. 6) Cytotoxic T cells are repelled by high concentrations of CXCL12 and thus excluded from the tumor.

On liver endothelial cells, on the other hand, ACKR3 is downregulated during chronic liver injury, whereas the expression of CXCR4 is upregulated. In response to the dominance of CXCR4 over ACKR3 signaling, LSECs downregulate regenerative ID1-dependent genes and acquire a profibrotic phenotype, secreting TGF-β and other factors that promote the activation of HSCs and the progression of fibrosis. (126) The CXCL12 chemokine axis plays a crucial role in regeneration and development; physiological

mechanisms, that are often exploited by tumors. Therefore, the significance of CXCL12 in the growth and advancement of liver cancers is not unexpected. (74) Both CXCR4 and ACKR3 are expressed in the majority of primary liver cancer specimens. (74, 135) CXCR4 has been found to be overexpressed in approximately 50% of HCC, while CXCL12 has been found to be mostly upregulated in the peritumoral region. (74, 135) CXCR4 signaling promotes invasiveness and EMT in hepatoma cell lines. (136, 137) Accordingly, in patients with HCC, high CXCR4 expression is associated with HCC progression and metastasis and predictive of a poor outcome. (135, 136, 138) The prognostic role of ACKR3 in HCC on the other hand, is less clear. Although ACKR3 is overexpressed in advanced and metastatic HCC *in vivo*, and in HCC cell lines with a high invasive potential *in vitro*, promoting tumor growth, angiogenesis, and invasiveness, it appears not to be correlated with patient overall survival. (135, 139, 140)

In the TME, CXCL12 is predominantly expressed by CAFs. (141, 142) However, tumor-associated endothelial cells (TECs), TAMs, and malignant hepatocytes are a source of CXCL12, as well. (29, 143-145) Typical conditions prevailing in the TME, such as hypoxia, high levels of inflammatory cytokines and TGF-β, are known to activate the CXCL12/CXCR4/ACKR3 axis. (57, 146, 147) In addition, mechanical cues have been suggested to influence CXCR4 expression. Matrix stiffness is a major risk factor for HCC development and is involved in several aspects of tumor initiation and progression through the YAP/TAZ pathway. (148, 149) Increased matrix stiffness has been shown to upregulate CXCR4 expression on human HCC cell lines mediating activation of the YAP pathway through downregulation of the ubiquitin-like protein ubiquitin domain containing 1 (UBTD1). (150)

CXCR4 and ACKR3 expression on tumor cells can directly activate pathways, such as the PI3K/AKT, ERK, and MAPK pathway that promote their proliferation, survival, growth, and migration. (113) However, the CXCL12/CXCR4/ACKR3 axis is also important in the TME where it induces angiogenesis and regulates immune suppression, and inflammation. Both ACKR3 and CXCR4 are frequently upregulated on TECs in HCC and their overexpression is associated with increased angiogenesis. (151, 152) During angiogenesis, CXCR4$^+$ endothelial tip cells proliferate and lead new vessel sprouts towards arteries, a mechanism that was shown to be promoted by VEGFA and CXCR4 and tightly regulated by Notch signaling. VEGFA binding on its receptor VEGFR2 on sprouting cells induces upregulation of CXCR4. (153) Neoangiogenesis is crucial for the growth of solid tumors but produces a functionally and structurally abnormal vasculature. (154) CXCR4$^+$ TECs in HCC share functional similarities with tip cells and binding of CXCL12 to CXCR4 on TECs also promotes proliferation and vessel sprouting. (152, 155) ACKR3 on the other hand, promotes survival and migration of endothelial cells. (143) High expression of CXCR4 on TECs is associated with a distinct sinusoidal growth pattern in HCC, called vessels encapsulating tumor clusters (VETC) in which TECs form cobweb-like networks surrounding HCC cell nests which is linked to an aggressive tumor behavior and an increased risk of EMT-independent metastasis. (152, 156-158) The CXCL12/CXCR4 axis also represents an important pathway for the

infiltration of pro-tumorigenic immune cells. Treg cells, one of the most potent anti-inflammatory cell populations, express high levels of CXCR4 and are directed into tumors by CXCL12. (159) CXCL12 signaling also mediates CD4$^+$ T cell differentiation into Treg and promotes their immunosuppressive function. (160, 161) CXCL12 released by CAFs and activated HSCs in the TME attracts monocytes to tumor sites, where they acquire an immunosuppressive phenotype through a mechanism involving IL-6/STAT3 activation or give rise to pro-tumorigenic TAMs. (141, 142, 162) Moreover, pro-angiogenic TAMs are directed by CXCL12 to perivascular areas after chemotherapy in different murine tumor models and promote revascularization and thus chemoresistance. (163) On the other hand, CXCL12/CXCR4 interactions can also impair anti-tumor responses of cytotoxic immune cell populations. While CD8$^+$ T cells are attracted by low concentrations of CXCL12 through CXCR4, they are repelled by high concentrations of CXCL12 as prevalent in the tumor border of HCC (or highly CXCL12 expressing tumors) a phenomenon termed chemorepulsion. (164, 165) In addition, in a model of metastasis of dormant tumor cells into the liver, CXCL12 secreted by activated HSCs has been shown to impair NK cell proliferation and thus limit tumor surveillance. (132)

All in all, the CXCL12/CXCR4/ACKR3 chemokine axis is involved in a variety of physiological and immunological mechanisms that are often exploited by tumors and therefore, represents a tempting potential target for therapeutic interventions. Despite this, there is a lack of understanding of the impact of CXCL12 on the immune microenvironment in the context of liver fibrosis and liver cancer. Given its broad but important roles in the immune system, addressing this research gap might not only answer the question if CXCL12 is a suitable drug target but also provide new insights into the complex role of the immune system in liver diseases.

1.4 Aim of the study

Despite major advances in the understanding of liver diseases in recent years, many aspects of liver fibrosis and liver cancer, in particular the diverse and central roles of the immune system are still incompletely understood, resulting in a paucity of effective therapies.

The chemokine CXCL12 plays a critical role in the initiation and progression of various tumor entities, including primary liver cancer. CXCL12 not only induces tumor-promoting pathways in malignant cells through its two receptors CXCR4 and ACKR3, but also stimulates angiogenesis, and recruits immunosuppressive monocytes and Treg cells, thereby creating a tumor-supportive microenvironment. In the liver, increased expression of CXCR4 or ACKR3 have been associated with tumor growth and aggressiveness in HCC. Furthermore, the CXCL12 chemokine axis has been associated with the activation of HSCs, which are not only the main drivers of liver fibrosis but also contribute to tumor growth. Finally, the CXCL12-CXCR4 axis has been implicated in the recruitment

and activation of various immune cell populations to the liver. However, how this chemokine axis influences tumor growth and immune cells is poorly understood.

Therefore, the aim of this study was to characterize the effect of CXCL12 on immune cell populations in liver fibrosis and primary liver cancer in order to gain a better understanding of how the CXCL12 chemokine axis influences pre-malignant liver fibrosis and cancer and to explore its value as a potential drug target. The central hypothesis of this thesis was that inhibition of CXCL12 might not only interfere with pro-fibrotic and pro-tumorigenic pathways in the liver, but also alter the composition and activation of infiltrating immune cells in favor of tumor-inhibiting cell populations and thus create a less tumorigenic TME. Using experimental mouse models and a pharmacological inhibitor for CXCL12, the following research questions were addressed to test this hypothesis:

- Can inhibition of the CXCL12 chemokine axis attenuate liver fibrosis?
- Does a blockade of CXCL12 influence the composition of liver immune cells during chronic liver injury?
- Can inhibition of CXCL12 attenuate liver tumor growth?
- Does CXCL12 influence the tumor immune and stromal microenvironment?

In order to address these unknowns, we conducted a comprehensive study using several experimental mouse models of liver fibrosis and subsequent cancer, alongside interventional approaches targeting CXCL12 and mechanistic in-vitro experiments. This study aims to investigate the influence of CXCL12 on immune cell composition and activation in chronic liver fibrosis and liver cancer, and the involvement of this chemokine axis in disease progression. Due to its presumed high relevance in liver cancer the CXCL12 axis might represent a target for future therapies. Characterizing the effects of the pharmacological inhibition CXCL12 will contribute to a better understanding of the complex mechanisms that drive tumor growth in the liver and help to develop new therapeutic approaches for patients with HCC in a more targeted manner.

2. Materials and Methods

2.1 Materials

2.1.1 Mouse strains

For the *in vivo* experiments in this study C57BL/6 wild-type mice were used that were either bred and housed under specific-pathogen free (SPF) conditions in the Animal Facility of the University Hospital Aachen or purchased from external animal suppliers (Janvier Labs, France, or Charles River, Germany) at the age of 6-7 weeks and then housed at the Animal Facility of the University Hospital Aachen under SPF conditions or housed under standardized experimental conditions at the "Forschungseinrichtung für experimentelle Medizin" (FEM) of the Charité for at least one week prior to the start of the experiment. All *in vivo* experiments were performed with mice at 8-24 weeks of age under conditions approved by the "Landesamt für Natur, Umwelt und Verbraucherschutz (LANUV)" under the animal grant TVA AZ 84-02.04.2015.A554, or approved by the "Landesamt für Gesundheit und Soziales" (LaGeSo) under the animal grant "Natursubstanzen als Therapie in Leberfibrose"(G0221/20), and were carried out according to the European animal welfare rules and the guidelines of the federation of laboratory animal science associations (FELASA).

2.1.2 Cell lines

Jurkat cells, a human lymphoblast cell line, derived from $CD4^+$ T cells that endogenously express high levels of CXCR4, were kindly provided by the group of Anette G. Beck-Sickinger, Leipzig University and stored in liquid nitrogen.

Table 1: Consumable Materials

Consumable Materials	Company
1 mL Syringe	B. Braun, Sempach, Switzerland
10 mL Syringe	B. Braun, Sempach, Switzerland
5 mL Syringe	B. Braun, Sempach, Switzerland
26 G/27G Needle	B. Braun, Sempach, Switzerland
0.2 mL Strip Tubes	Biozym Scientific GmbH, Hessisch Oldendorf, Germany
0.5 mL Safe-Lock Tubes	Eppendorf, Hamburg, Germany
1.5 mL Safe-Lock Tubes	Eppendorf, Hamburg, Germany
2 mL Safe-Lock Tubes	Eppendorf, Hamburg, Germany
15 mL Falcon	BD Falcon (Corning), Heidelberg, Germany
15 mL Flip-Cap	Greiner Bio-One, Frickenhausen, Germany
50 mL Falcon	BD Falcon (Corning), Heidelberg, Germany

50 mL Flip-Cap	Greiner Bio-One, Frickenhausen, Germany
12-Well Plate	BD Falcon (Corning), Heidelberg, Germany
5 mL Reaction Tube	BD Falcon (Corning), Heidelberg, Germany
6-Well Plate	BD Falcon (Corning), Heidelberg, Germany
APC counting beads	BD Bioscience, New Jersey, US
Cell Strainer	Corning, Corning, US
Costar®Stripette® 10 mL	BD Falcon (Corning), Heidelberg, Germany
Costar®Stripette® 25 mL	BD Falcon (Corning), Heidelberg, Germany
Costar®Stripette® 5 mL	BD Falcon (Corning), Heidelberg, Germany
Costar®Stripette® 50 mL	BD Falcon (Corning), Heidelberg, Germany
Cover Slides	Carl Roth GmbH + Co KG, Karlsruhe, Germany
Cryomold	Sakura Finetek, Leiden, Netherlands
Cryotube	Thermo-Fisher Scientific, Schwerte, Germany
Dako Pen	Dako, Glostrup, Denmark
EDTA Tube	Sarstedt, Nümbrecht, Germany
False bottom tube	Life Technologies (Roche), Darmstadt, Germany
Feather microtome blade R35	pfm medical, Cologne, Germany
Feather Scalpel No.11	Feather, Osaka, Japan
Filter paper MN 640W	Macherey-Nagel GmbH+Co.KG, Düren, Germany
Histogrid	Sarstedt, Nümbrecht, Germany
MicroAmp® Fast 96-Well Reaction Plate (0.1 mL)	Life Technologies, Darmstadt, Germany
MicroAmp® Optical Adhesive Film	Life Technologies, Darmstadt, Germany
Microscope KP slides adhesive	Klinipath B.V. (VWR), Duiven, Netherlands
Petridish (6 cm)	Sarstedt, Nümbrecht, Germany
Pipette filter tip (0.1-20 µL)	Starlab, Hamburg, Germany
Pipette filter tip (1000 µL)	Starlab, Hamburg, Germany
Pipette filter tip (100-1000 µL)	Starlab, Hamburg, Germany
Pipette filter tip (10-200 µL)	Starlab, Hamburg, Germany
Pipette filter tip (200 µL)	Starlab, Hamburg, Germany
Pipette tip (0.1-20 µL)	Starlab, Hamburg, Germany
Pipette tip (100-1000 µL)	Starlab, Hamburg, Germany
Pipette tip (10-200 µL)	Starlab, Hamburg, Germany
Prefilled 2.0 ml tubes, Stainless Steel	Biozym Scientific GmbH, Hessisch Oldendorf, Germany

Table 2: Diets

Diet	Mixture	Manufacturer
Chow diet (standard diet for rodents)	66 kJ % carbohydrates, 23 kJ % protein, 11 kJ % fat	Ssniff-Spezialdiäten GmbH, Soest, Germany
MCD Diet (methionine-choline deficient diet)	64 kJ % carbohydrates, 14 kJ protein, 22 kJ % fat	Ssniff-Spezialdiäten GmbH, Soest, Germany
Western diet (high cholesterol, high fat diet)	43 kJ % carbohydrates, 15 kJ % protein, 42 kJ % fat, + 1.25% cholesterol	Ssniff-Spezialdiäten GmbH, Soest, Germany

Table 3: Chemicals and reagents

Chemicals	Company
2-Mercaproethanol	Thermo-Fisher Scientific (GibcoTM), Schwerte, Germany
4',6-Diamidino-2-Phenylindole (DAPI)	Sigma Aldrich, Munich, Germany
7-Aminoactinomycin D (7-AAD)	Sigma Aldrich, Munich, Germany
Acetic acid	Applichem GmbH, Darmstadt, Germany
Antibody diluent for IHC (B1-31CW)	medac GmbH, Wedel, Germany
Bovine serum albumin (BSA)	Sigma Aldrich, Munich, Germany
Calcium chloride dihydrate ($CaCl_2 \cdot 2H_2O$)	Sigma Aldrich, Munich, Germany
Carbon tetrachloride (CCl_4)	Merck, Darmstadt, Germany
Chloramine T	Sigma Aldrich, Munich, Germany
Citric acid monohydrate ($C_6H_8O_7 \cdot H_2O$)	Sigma Aldrich, Munich, Germany
Collagenase D	Worthington Biochemical Corp., Lakewood NJ, US
DEPC-treated water	Thermo-Fisher Scientific (InvitrogenTM), Schwerte, Germany
Diethylnitrosamine (DEN)	Sigma Aldrich, Munich, Germany
Dimethylaminobenzaldehyde	Sigma Aldrich, Munich, Germany
Disodium hydrogen phosphate dihydrate ($Na_2HPO_4 \cdot 2H_2O$)	Sigma Aldrich, Munich, Germany
Dimethyl sulfoxide (DMSO)	Sigma Aldrich, Munich, Germany
DNase I	Sigma Aldrich, Munich, Germany
Dulbecco's phosphate buffered saline (DPBS)	Pan Biotech, Aidenbach, Germany
Ethylenediaminetetraacetic acid (EDTA) pH 8	Sigma Aldrich, Munich, Germany
Eosin Y solution	Sigma Aldrich, Munich, Germany
Epredia™ DAB Quanto Detection system	Thermo-Fisher Scientific, Schwerte, Germany
Ethanol 99%	Otto Fishar GmbH & Co. KG, Karlsruhe, Germany
Ethanol denatured (70%, 99%)	Carl Roth GmbH & Co. KG, Karlsruhe, Germany

Fetal Bovine Serum (FBS)	Pan Biotech, Aidenbach, Germany
Formalin (4%), methanol stabilized	Sigma Aldrich, Munich, Germany
Glucose ($C_6H_{12}O_6$)	Sigma Aldrich, Munich, Germany
Glucose 5% solution	B. Braun, Sempach, Switzerland
Hanks' balanced salt solution (HBSS)	Pan Biotech, Aidenbach, Germany
Hematoxylin	Dako, Glostrup, Denmark
Hydrochloric acid (HCl) 37%	Applichem GmbH, Darmstadt, Germany
Hydrogen peroxide H_2O_2 30%	Carl Roth GmbH & Co. KG, Karlsruhe, Germany
Hydroxyproline	Sigma Aldrich, Munich, Germany
Image-iT FX Signal Enhancer	Thermo-Fisher Scientific, Schwerte, Germany
immPRESS® HRP Horse Anti-Rabbit IgG Polymer Detection Kit	Vector laboratories, Newark, California, US
InVivoMAb anti-mouse PD-1 Clone RMP1-14	BioXcell, Lebanon NH, US
InVivoMAb rat IgG2a Isotype ctrl	BioXcell, Lebanon NH, US
Isoflurane	AbbVie Deutschland GmbH, Wiesbaden, Germany
Isopropanol	Applichem GmbH, Darmstadt, Germany
LUNARIS^{TM} Mouse 12-plex chemokine Kit	AYOXXA Biosystems GmbH, Köln, Germany
Lysis Buffer (10x)	eBioScience, San Diego, US
Magnesium chloride hexahydrate ($MgCl_2 \cdot 6H_2O$)	Applichem GmbH, Darmstadt, Germany
Magnesium sulfate heptahydrate ($MgSO_4 \cdot 7H_2O$)	Merck, Darmstadt, Germany
Normal goat serum	Thermo-Fisher Scientific, Schwerte, Germany
Normal horse serum 2.5%	Vector laboratories, Newark, California, US
Normal rabbit serum	Invitrogen, Waltham, US
Normal rat serum	Invitrogen, Waltham, US
NOX-A12	Noxxon Pharma, Berlin, Germany
Nycodenz	Axis-Shield, Oslo, Norway
Penicillin Streptomycin	Pan Biotech, Aidenbach, Germany
Perchloric acid ($HClO_4$) 70%	Sigma Aldrich, Munich, Germany
Pharm Lysis Buffer (10x)	eBioscience, San Diego, US
Picric acid ($C_6H_3N_3O_7$) 1.2%	Applichem GmbH, Darmstadt, Germany
Poly-D-Lysin	Thermo-Fisher Scientific, Schwerte, Germany
Potassium chloride (KCl)	Sigma Aldrich, Munich, Germany
Potassium dihydrogen phosphate (KH_2PO_4)	Merck, Darmstadt, Germany
PowerUP SYBR© Green PCR MasterMix	Life Technologies, Darmstadt, Germany
qPCR-Primers	Eurofins Genomics GmbH, Ebersberg, Germany

Recombinant Mouse CXCL12 (SDF-1alpha, carrier-free)	Biolegend
Reverse NOX-A12	NOXXON Pharma, Berlin, Germany
RNASolv® Reagent	Omega Bio-tek, Inc. Norcross, GA, US
Roti® Histokitt	Carl Roth GmbH & Co. KG, Karlsruhe, Germany
RPMI-1640	Pan Biotech, Aidenbach, Germany
Sera from mouse	Sigma Aldrich, Munich, Germany
Sera human	Sigma Aldrich, Munich, Germany
Sirius red F3b	Waldeck GmbH + Co. KG, Münster, Germany
Sodium acetate trihydrate ($CH_3COONa \cdot 3H_2O$)	Sigma Aldrich, Munich, Germany
Sodium chloride (NaCl)	Sigma Aldrich, Munich, Germany
Sodium chloride (NaCl) 0.9%	B.Braun, Sempach, Switzerland
Sodium dihydrogenphosphate hydrate ($NaH_2PO_4 \cdot 2H_2O$)	Sigma Aldrich, Munich, Germany
Sodium dodecylsulfate (SDS) 10%	Rockland Immunochemicals, Inc.Philadeplphia, USA
Sodium hydrogencarbonate ($NaHCO_3$)	Sigma Aldrich, Munich, Germany
Sodium hydroxide (NaOH)	Merck, Darmstadt, Germany
Sodiumazide (NaN_3)	Sigma Aldrich, Munich, Germany
Stacking Gel Buffer (0.5 M Tris HCl, pH 6.8)	Bio-Rad Laboratories Inc., Hercules California, US
Tissue-Tek O.C.T Compound	Sakura Finetek, Leiden, Netherlands
Transcriptor First Strand cDNA Synthesis Kit	Life Technologies (Roche), Darmstadt, Germany
Tween-20	Carl Roth GmbH & Co. KG, Karlsruhe, Germany
Universal HIER Buffer (10X)	Abcam, Cambridge, UK
VectaMount AQ Aqueous Mounting Medium	Vector laboratories, Newark, California, US
Vitroclud	R. Langenbrick GmbH, Emmendingen, Germany
Xylene	Applichem GmbH, Darmstadt, Germany

Table 4: Media and reagents

Buffer / reagent	Ingredients
3% H_2O_2	ddH_2O + 3% H_2O_2
6N HCl	600 mL acetic acid (37%), 40 mL ddH_2O
Acetic acid 0.5%	ddH_2O + 0.5% glacial acetic acid
Antibody stripping buffer	675 µL ddH_2O + 125 µL 0.5 M Tris-HCL pH6.8 + 200 µL SDS (10%)
BB4 (blocking buffer)	1X-DPBS + 2% sera human, 2% sera mouse, 2% normal rat serum, 2% BSA

Buffer A (hydroxyproline assay)	3.4 g NaOH, 3.4 g $C_6H_8O_7 \cdot H_2O$, 12 g $CH_3COONa \cdot 3H_2O$, add 100 mL ddH$_2$O, adjust to pH6
Buffer B (hydroxproline assay)	7.8 mL Buffer A, 12 mL isopropanol, 6.6 mL ddH$_2$O
Chloramine T-solution	0.12 g Chloramine T + 20 mL Buffer B
DAPI (stock solution)	20 mg/mL DAPI in ddH$_2$O
Digestion medium-A	HBSS + 0.1% BSA + 0.1% NaN$_3$
Digestion medium-B	RPMI + 0.1% BSA + 0.1% Penicillin + Streptomycin
Digestion stopping buffer	HBSS + 0.1% BSA + 2 mM EDTA
DNase I	1X-DPBS + 1 mg /mL DNase I
EDTA 100 µM	ddH$_2$O (Millipore) + 0.5 M EDTA
EDTA buffer pH9 (antigen retrieval buffer)	ddH$_2$O + 10 mM TRIS, 1 mM EDTA, 0,05% Tween-20; adjusted to pH9
Ehrlich reagent	1.8 g Dimethylaminobenzaldehyde, 15.6 mL isopropanol, 4.8 mL perchloric acid (50%)
FACS Buffer	1X-DPBS + 0.1% BSA + 2 mM EDTA + 0.1% NaN$_3$
Gey´s balanced salt solution (GBSS)	370 mg KCl, 225 mg $CaCl_2$*2H$_2$O, 991 mg glucose, 30 mg KH_2PO_4, 210 mg $MgCl_2 \cdot 6H_2O$, 70 mg $MgSO_4 \cdot 7H_2O$, 75 mg $NaH_2PO_4 \cdot 2H_2O$, 227 mg NaHCO$_3$, in a final volume of 1 L ddH$_2$O
Lysis buffer	ddH$_2$O + 1/10 10X Lysis buffer
NGS 2%	1X-DPBS + 2% NGS
Nycodenz stock solution	2 g Nycodenz +7 mL GBSS per sample
PBS-1% BSA antibody diluent	1X-DPBS + 1% BSA
PBS-T buffer	1X-DPBS + 0.1% Tween-20
Sirius red staining solution	250 mL picric acid (1.2%) + 0.25 g Sirius red, adjust to pH = 2 with NaOH
Triton-X 0.025% buffer	1X-DPBS + 0.025% (v/v) Triton-X
Universal HIER buffer 1X	ddH$_2$O + 1/10 10X Universal HIER buffer
Washing buffer (immunohistochemistry)	ddH$_2$O + 20 nM Tris + 150 nM NaCl + 0.05% Tween-20

Table 5: Antibodies for flow cytometry

Antibody	Clone	Company	Dilution
anti-mouse CD107a-FITC	1D4B	BD	1:400
anti-mouse B220-PerCp-Cy5.5	RA3-6B2	BD Biosciences	1:400
anti-mouse CD115-PE	AFS98	eBioscience	1:400
anti-mouse CD11b-eFluor 450	M1/70	eBioscience	1:400
anti-mouse CD11b-eFluor BV421	M1/70	eBioscience	1:400

anti-mouse CD11c -BV510	HL3	BD Biosciences	1:400
anti-mouse CD138-BV711	281-1	Biolegend	1:200
anti-mouse CD146-Alexa Fluor 488	ME-9F1	Biolegend	1:400
anti-mouse CD178-PerCp-eFluor710	MFL3	eBioscience	1:400
anti-mouse CD19-FITC	1D3	BD Biosciences	1:400
anti-mouse CD19-Alexa Fluor 700	HK1.4	Biolegend	1:400
anti-mouse CD1d-BV510	1B1	BD Biosciences	1:400
anti-mouse CD25-PerCp-Cy5.5	PC61	BD Biosciences	1:400
anti-mouse CD301-Alexa Fluor 488	MCA2392A488T	BioRad	1:400
anti-mouse CD31-APC	MEC 13.3	BD Biosciences	1:400
anti-mouse CD3-APC	145-2C11	BD Biosciences	1:200
anti-mouse CD4-V450	RM4-5	BD Biosciences	1:400
anti-mouse CD45-APC-Cy7	30-F11	BD Biosciences	1:200
anti-mouse CD45-BV510	30-F11	BD Biosciences	1:200
anti-mouse CD68 unlabeled	FA-11	Biolegend	1:400
anti-mouse CD69-PerCp-Cy5.5	H1.2F3	eBioscience	1:400
anti-mouse CD80-PE	16-10A1	eBioscience	1:400
anti-mouse CD8a-BV711	53-6.7	Biolegend	1:400
anti-mouse CXCR4-PE	L276F12	Biolegend	1:100
anti-mouse F4/80-PE-Cy7	BM8	eBioscience	1:400
anti-mouse γδTCR-APC	GL3	Biolegend	1:400
anti-mouse Gr1 (Ly6C)-PerCp-Cy5.5	RB6.85C	BD Biosciences	1:400
anti-mouse IgD-PE-Cy7	11.26c.2a	Biolegend	1:400
anti-mouse IgM-FITC	eB121-15F9	eBioscience	1:400
anti-mouse Ly6G-Alexa Fluor 700	1A8	BD Biosciences	1:400
anti-mouse MCH-II-FITC	M5/114.15.2	Biolegend	1:400
anti-mouse MHC-II-PE	AF6-120.1	BD Biosciences	1:400
anti-mouse MHC-II-eFluor 450	M5/114.15	Invitrogen	1:400
anti-mouse MHC-II-BV421	M5/114.15.2	Biolegend	1:400
anti-mouse NK1.1-PE	PK136	BD Biosciences	1:400
anti-mouse NK1.1-APC-Cy7	PK136	Biolegend	1:400
anti-mouse PD-1-PE	J43	eBioscience	1:400
anti-mouse PD-L1-PE	NIH5	eBioscience	1:400
anti-mouse SiglecF-BV421	E50-2440	BD Biosciences	1:400
anti-mouse TCRb-PerCp-Cy5.5	H57-597	Biolegend	1:400

anti-mouse TCRb-PE-Cy7	H57-597	eBioscience	1:400

Table 6: Primary antibodies (unconjugated) used in immunohistochemistry

Antigen	Host	Clone	Company	Dilution
αSMA	Mouse	1A4	Agilent	1:400
B220	Rat	RA3-6B2	Biolegend	1:200
CD146	Rat	ME-9F1	Biolegend	1:100
CD4	Rat	4SM95	ThermoFisher	1:400
CD8	Rat	4SM15	ThermoFisher	1:200
CK19	Rat	TROMA-III	Developmental Studies Hybridoma Bank	1:400
CLEC4F	Rat	370901	R&D	1:1000
Collagen I	Rabbit	polyclonal	Abcam	1:500
Collagen IV	Rabbit	polyclonal	Abcam	1:500
CXCR4	Rabbit	EPUMBR3	Abcam	1:500
Desmin	Rabbit	polyclonal	Abcam	1:500
F4/80	Rat	BM8	Dianova	1:200
IBA1	Rabbit	polyclonal	VWR	1:1000
Ki67	Rabbit	SP6	Abcam	1:500
LYVE-1	Rabbit	polyclonal	Abcam	1:200
Myeloperoxidase	Rabbit	EPR20257	Abcam	1:1000
Na:K-ATPase	Mouse	464.6	Abcam	1:400
PCNA	Mouse	PC10	Abcam	1:10000

Table 7: Secondary antibodies (fluorophore-conjugated) used in immunohistochemistry

Antibody	Conjugate	Company
Goat anti-rat	Alexa Fluor 647	Cell Signaling Technology
Goat anti-mouse	Alexa Fluor 488	Cell Signaling Technology
Goat anti-rabbit	Alexa Fluor 555	Cell Signaling Technology
Goat anti-rabbit	Alexa Fluor 647	Cell Signaling Technology
Goat anti-rabbit	Alexa Fluor 750	ThermoFisher

Table 8: Primers

Target	Forward primer (5' - 3')	Reverse primer (5' - 3')

18S	AAC TTT CGA TGG TAG TCG CCG T	TCC TTG GAT GTG GTA GCC GTT T
Acta2	CTT CGT GAC TAC TGC CGA GC	AGG TGG TTT CGT GGA TGC C
Ang1	TTG AGA CCC AGG TAC TAA ATC	TTC ATT TGT CTG TTG GAG AAG
Ang2	TGG CTG ATG AAG CTG GAG	CAA GCT GGT TCC AAT CTC TAT C
B2m	TTC TGG TGC TTG TCT CAC TGA	CAG TAT GTT CGG CTT CCC ATT C
Col1a1	TCT GAC TGG AAG AGC GGA GAG	GGC ACA GAC GGC TGA GTA GG
Cxcl12	CAG CCG TGC AAC AAT CTG AA	GAG CCA ACG TCA AGC ATC TG
Ctgf	GGG CCT CTT CTG CGA TTT C	ATC AGC GCA AGT GCA TTG GTA
Cxcr4	GAG GCC AAG GAA ACT GCT G	GCG GTC ACA GAT GTA CCT GTC
Id1	CCT AGC TGT TCG CTG AAG GC	GTA GAG CAG GAC GTT CAC CT
Il-10	ATA ACT GCA CCC ACT TCC CA	GGG CAT CAC TTC TAC CAG GT
Il-6	GAA CAA CGA TGA TGC ACT TGC	TCC AGG TAG CTA TGG TAC TCC
Ki67	CTG CCT GCG AAG AGA GCA TC	AGC TCC ACT TCG CCT TTT GG
Mmp2	GGC TTC TGT CCT GAC CAA GGA TA	GCT CCT GGA TCC CCT TGA TGT C
Mmp9	GCC GCT CCT ACT CTGCCTGC	CTA CGG TCG CGT CCA CTC GG
Tgfb	GCT CGC TTT GTA CAA CAG CAC C	GCG GTC CAC CAT TAG CAC G
Thbs1	AAA CCG ATT TCC GAC AAT TCC	CAT CAT AAC CTA CAG CAA GTC C
Timp1	TGC AAT GCA GAC GTA GTG ATC AG	GGC CGT GTA GAT AAA CTC GAT GTC
Timp2	CTG CAA CTC GGA CCT GGT CAT A	TGT AGG CGT ACC GGA TAT CTG C
Tnfa	AAT GGC CTC CCT CTC ATC AGT T	CCA CTT GGT GGT TTG CTA CGA
Vegfa	GAG CTC ATG GAC GGG TGA G	CTG GGA CCA CTT GGC ATG G

Table 9: Devices

Device	Company
accu-jet® Pro pipette controller	Brand GmbH & Co. KG Wertheim, Germany
BD LSR Fortessa	BD Biosciences, San Jose, US
Bead bug Microtube homogenizer D1030-E	Benchmark Scientific, Sayreville NJ, US
BioPhotometer	Eppendorf, Hamburg, Germany
Centrifuge 5417 D	Eppendorf, Hamburg, Germany
Centrifuge 5427 R	Eppendorf, Hamburg, Germany
Centrifuge 5810 R	Eppendorf, Hamburg, Germany
Cubis® micro scales	Sartorius, Göttingen, Germany
Cytek Aurora 3	Cytek Biosciences, Fremont, US
Heidolph Polymax	Heidolph Instruments GmbH & CO. KG, Schwabach, Germany

Heracell®	Thermo-Fisher Scientific, Schwerte, Germany
Heraeus™ Megafuge 1.0 R	Thermo-Fisher Scientific, Schwerte, Germany
KS 4000 i control	IKA® -Werke GmbH & CO. KG Staufen, Germany
LabGard ES NU-545 Biosafety Cabinet	NuAire, Plymouth, US
Leica Z16 APO	Leica Microsystems GmbH, Wetzlar, Germany
Microtome RM2255	Leica Biosystems GmbH, Wetzlar, Germany
Multichannel pipette (20-200µL)	Eppendorf, Hamburg, Germany
NanoDrop One/One^C	Thermo-Fisher Scientific, Schwerte, Germany
peqSTAR 2X Thermocycler	Peqlab (VWR), Erlangen, Germany
Pipette (0.1- 2.5 µL)	Eppendorf, Hamburg, Germany
Pipette (0.5-10 µL)	Eppendorf, Hamburg, Germany
Pipette (10-100 µL)	Eppendorf, Hamburg, Germany
Pipette (200-1000 µL)	Eppendorf, Hamburg, Germany
Pipette (20-200 µL)	Eppendorf, Hamburg, Germany
QuantStudioTM 3 Real-Time qPCR System	Thermo-Fisher Scientific, Schwerte, Germany
Quintix® precision scales	Sartorius, Göttingen, Germany
Slide staining set	Bio-Optica , Milano, Italy
StainTray™ Slide Staining System	Simport Scientific, Saint-Mathieu-de-Beloeil, Kanada
Thermomixer F1.5	Eppendorf, Hamburg, Germany
Water bath JULABO TW	JULABO GmbH, Seelbach, Germany
Zeiss Axio	Carl Zeiss Optics, Jena, Germany
Zeiss Axio Observer Z1	Carl Zeiss Optics, Jena, Germany
Zeiss Observer 7	Carl Zeiss Optics, Jena, Germany

Table 10: Software

Software	Version	Provider
Biorender		Biorender, Toronto, Canada
Cell Profiler	4.2.1	Open Source (166)
FIJI (ImageJ)	1.53t	Open Source (167)
BioTek Gen5	3.0	Agilent, Santa Clara, CA, US
Flowlogic	8.7	Inivai Technology, Mentone VIC, Australia
GraphPad Prism	9.5.1	GraphPad Software,Boston, MA, US
Ilastik	1.3.3	Open Source (168)
QuPath	0.4.3	Open Source (169)

| ZEN blue edition | 3.3 | Carl Zeiss, Oberkochen, Germany |

2.2. Methods

2.2.1 Mouse models of liver fibrosis

Chronic CCl_4 injections

Carbon tetrachloride (CCl_4) is a hepatotoxin that causes fulminant liver inflammation and, after repetitive exposure, robust fibrosis in the liver. After injection, CCl_4 is metabolized in hepatocytes leading to the formation of reactive trichloromethyl (CCl_3) radicals. CCl_3 radicals mediate cytotoxic effects and induce a massive demise of hepatocytes. DAMPs released by dying hepatocytes activate local immune cells (e.g., Kupffer cells), which release cytokines and chemokines and trigger an inflammatory response. This is followed by a regenerative phase of hepatocyte proliferation which peaks around 48 h after the CCl_4 injection. The histological manifestation of liver fibrosis can be observed after around 6 weeks of repetitive CCl_4 injections. (170, 171) To induce sterile liver inflammation and fibrosis, male 8-week-old C57BL/6 mice received over a time period of 8 weeks biweekly intraperitoneal (i.p.) injections of 50 µL CCl_4 (0.5 mL/kg bodyweight) diluted in corn oil.

Methionine- and choline-deficient diet (MCD)

Feeding mice a diet deficient in methionine and choline quickly and reproducibly induces steatohepatitis and fibrosis that – regarding certain aspects - resembles the human NASH. The MCD diet contains high amounts of sugar and is moderately enriched in fat, but lacks methionine and choline, which are essential components for the synthesis of phosphatidylcholine. Phosphatidylcholine is a phospholipid involved in the secretion of triglycerides and the formation of very low-density lipoprotein (VLDL), and its absence leads to a strong accumulation of lipids in hepatocytes causing oxidative stress, damage to mitochondrial DNA, and subsequently injury and death of hepatocytes, resulting in liver inflammation. However, the MCD diet does not reflect other important aspects of the human NASH pathology, such as insulin resistance or obesity. (171) Mice were placed on the MCD diet for 7 weeks, starting at 8 weeks of age. The body weight and overall status of the mice were recorded at least once a week during the whole feeding period.

2.2.2 Liver cancer models

DEN model

Diethylnitrosamine (DEN) is a carcinogen widely used to induce HCC in rodents. DEN causes random DNA mutations through DNA alkylation. In addition, metabolic activation of DEN by cytochrome P450 generates ROS that induce cell damage and cell death. When injected into male mice less than 2 weeks of age during a phase of active hepatocyte proliferation, a single dose of DEN is sufficient to induce neoplastic lesions that develop to HCC within 10 months. (172) Male mice were injected intraperitoneally with a single dose of 25 mg/kg bodyweight DEN diluted in saline at an age of 14 days.

<u>DEN + CCl$_4$ model</u>

The majority of human HCC develop in a fibrotic or cirrhotic liver in the presence of chronic liver inflammation. The combination of a single dose of DEN with repeated injections of CCl$_4$ mimics the human etiology of HCC development in an inflamed fibrotic/cirrhotic liver and accelerates tumor growth. (173) To induce liver tumors in a fibrotic/cirrhotic microenvironment, 14-day-old male mice received a single dose of DEN as described above and were subjected to 10 or 16 weeks of biweekly intraperitoneal injections with 50 μL of 0.5 mL/kg bodyweight CCl$_4$ diluted in corn oil, starting at an age of 8 weeks.

<u>DEN + Western diet model</u>

NAFLD and its progredient form NASH are important drivers of HCC, even in the absence of cirrhosis. (4) To induce NAFLD-associated hepatocellular tumors, mice were injected with a single dose of DEN (see above) and, starting at an age of 8 weeks, fed a high-fat, high-sugar, and high-cholesterol Western diet (WD) for 16 weeks. In all tumor models, body weight and overall status were monitored and recorded at least weekly during the additional treatment periods.

2.2.3 Application of NOX-A12 and anti-PD-1

<u>NOX-A12</u>

The Spiegelmer NOX-A12 is a synthetic target-binding oligonucleotide, that binds and neutralizes CXCL12 with high specificity. Designed to bind to a region of the chemokine that does not vary between the different splice variants, it can be assumed that NOX-A12 inhibits all isoforms of CXCL12. (174) Spiegelmers are RNA aptamers that are built from non-natural L-nucleotides, which makes them resistant to nucleases and immunologically passive. An attached polyethylene glycol (PEG)-moiety protects NOX-A12 from rapid renal clearance, resulting in a high, dose-dependent half-life in the circulation of 40-60 hours in humans. (175, 176) Reverse NOX-A12, a nonfunctional aptamer built from the reverse RNA-sequence was used as a vehicle control. NOX-A12 was dissolved in 5% glucose at a concentration of 10 mg/mL and stored at -20 °C until further usage. For *in vivo* treatment, NOX-A12 was administered subcutaneously at a concentration of 20 mg/kg bodyweight 3x per week. The same procedure was followed with reverse NOX-A12.

<u>Anti-PD-1</u>

Anti-PD-1 antibody (clone RMP1-14) was administered intraperitoneally biweekly at a dose of 100 μg diluted in NaCl. An IgG2a isotype was used as control at the same concentration.

2.2.4 Cell isolation and sample preparation

To harvest and investigate the organs, mice were euthanized by an overdose of isoflurane. Cardiac blood was collected by heart puncture and kept in a tube coated with EDTA on ice. The liver was perfused with 1X-DPBS and, for tumor bearing livers, pictures were taken. Liver tissue from the left lateral lobe was preserved in 4% formalin for histopathology, snap frozen in liquid nitrogen for protein and RNA analyses or embedded in Tissue-Tek O.C.T. Compound before freezing and storage at -80 °C. Tumor bearing livers

were cut at representative sites with tumors and preserved in 4% formalin and Tissue-Tek. Tumor tissue from several tumors was pooled and snap frozen for RNA analyses. The remaining liver was weighed, and further used for the isolation of immune cells and flow cytometry analysis.

From the blood, 50 μL was transferred to a 5 mL reaction tube for flow cytometry staining and erythrocytes were lysed by adding 1 mL of lysis buffer and incubating for 10 min at 4 °C. Lysis was stopped with 2 mL cold 1X-DPBS, centrifuged at 450 rcf, and the cell pellet stored at 4 °C until staining. The remaining blood was centrifuged at 10,000 rcf at 4 °C for 10 min. After centrifugation, the supernatant, consisting of blood plasma, was collected. 20 μL of the plasma were diluted with 180 μL cold 1X-DPBS in a false bottom tube and given to the central laboratory of the University Hospital RWTH Aachen for the measurement of several serum markers using standard methods (see 2.2.9.). The remaining blood plasma was stored at -80 ° C.

For the standard hepatic immune cell isolation protocol, the gallbladder was removed, and the liver was placed in 3 mL digest medium-A on ice and cut into small pieces. To dissociate the liver tissue, 300 μL collagenase D were added, followed by an incubation at 37 °C for 40 min. Collagenase D enzyme breaks down the extracellular matrix responsible for cell adhesion in tissues, resulting in the liberation of individual cells. In-between the collagenase digestion, the remaining pieces of liver tissue were mashed by a syringe piston. EDTA-containing digest stopping buffer was added at the end of the incubation time. As collagenase requires Ca^{2+} and Mg^{2+} as co-factors, adding EDTA, a metal-ion chelating agent, inhibits the enzyme and stops the digestion. The digested liver was then gently pushed through a cell strainer using a 10 mL syringe piston to obtain a single cell suspension. The cell suspension was centrifuged at 470 rcf for 5 min at 4 ° C and the supernatant discarded. Afterwards the cells were resuspended in FACS buffer and left for 40 min at 4 °C to allow the larger and heavier hepatocytes to sediment. Subsequently, the supernatant was additionally centrifuged at 18 rcf for 5 min at 4 °C. The supernatant containing the leukocytes was transferred to a new tube and centrifuged at 470 rcf for 5 min at 4 °C. To remove remaining erythrocytes 2 mL of cold lysis buffer was added for 15 min at 4 °C. The lysis process was interrupted by adding 4 mL of 1X-DPBS then performing a 5-minute centrifugation step at 470 g at 4 °C. The supernatant was removed, and the cells were distributed into 5 mL reaction tubes for different staining panels. The tubes were kept at 4 °C before staining.

For the optimized protocol, allowing to isolate LSECs, some changes were made to the original protocol. After removing the gallbladder, the liver was minced and placed in 4.5 mL Digest medium B in a 50 mL Falcon tube. 500 μL collagenase D was added and the mix was incubated at 37 °C for 40 min. After 20 min, 200 μL of a 1 mg/mL DNase I solution was added, and the mix was shaken every 5 min to further dissociate the tissue. The digestion was stopped by adding 5 mL of cold digest stopping buffer and homogenized by repeatedly aspirating with a 10 mL pipette. The dissociated tissue was then flushed through a 70 μm cell strainer into a new 50 mL tube, using a piston to gently push remaining cell aggregates through the mesh. 1X-DPBS was added to up 50 mL and the cell suspension was centrifuged twice at 50 rcf for 1 min at 4 °C,

each time keeping the supernatant and discarding the pellet containing hepatocytes and debris. The supernatant then was centrifuged at 600 rcf for 10 min at 4 °C. The supernatant was removed, and the pellet resuspended in 30 mL cold 1X-DPBS. After another centrifugation step at 470 rcf for 10 min at 4 °C, the cells were purified by a density gradient. For this purpose, the pellet was resuspendend in 6.3 mL of iohexol (Nycodenz) gradient (2 g Nycodenz dissolved in 7 mL GBSS) and filled up to 10 mL with 1X-DPBS to obtain an 18% gradient. The cell-gradient suspension was then carefully underlayered under 6 mL of cold HBSS + 0.1% BSA in a 50 mL Falcon and centrifuged without brake at 1400 rcf for 22 min at 4 °C. After the centrifugation, leukocytes and endothelial cells were condensed in a milky layer at the interphase between the gradient and the top layer, while erythrocytes and hepatocytes were in a pellet at the bottom of the tube. The milky layer was collected, washed with 30 mL cold 1X-DPBS, and spun down at 470 rcf for 10 min at 4 °C, to remove remaining Nycodenz. The supernatant was removed, and the cell pellet resuspended and divided into 5 mL reaction tubes for different staining panels.

Assessment and calculation of the tumor size

To assess tumor growth, macroscopic images of the liver were taken using a Leica Z16 APO microscope. The diameter of visible tumor lesions was manually drawn and measured using the ZEN software.

2.2.5 Flow cytometry

Flow cytometry is a technology used for a multiparametric, high throughput analysis of single cells and particles, allowing for their characterization by size, complexity, and the expression of fluorescently tagged molecules. Cells in a suspension are guided through a fluidic system that creates a thin stream allowing that one cell at a time passes a laser beam at the interrogation point of the flow cytometer's optical system. The optical system includes a laser as the light source. When the laser beam strikes a cell the incident light is scattered. The scattered light can be related to the size of the cell or the granularity of the cell depending on the angle of detection. Detection at an angle of 0° is termed as forward scatter (FSC) and is correlated with the cell size, whereas detection at 90° is termed as side-scatter (SSC) and is correlated with the granularity of the cell. Lasers at different wavelengths can be used to excite multiple fluorophores on a single cell. The emitted signal is collected and focused by lenses, and guided through optical filters that allow only certain wavelengths of light to pass through, enabling the detection of a specific signal out of a spectrum of light by detectors. After detection, the flow cytometry's electronics multiply and digitize the signal, which is then saved for further analysis. Each detected signal can be analyzed using the area, width, or height of the voltage peak. Fluorophore-labeled antibodies against specific markers on cells are commonly used to distinguish cell types and explore their activation status, however, many immune cells can be differentiated using FSC and SSC alone. A list of the antibodies used in this project is provided in Table 6. Unless indicated otherwise, the antibodies were used at a concentration of 0.25 µL per sample (dilution 1:400) and prepared as a mix in BB4 blocking buffer. 20 µL of antibody mix were then added to the cell suspension and incubated for 20 min at 4 °C protected from light, then 7-AAD was added and

incubated for further 5 min. When unlabeled primary antibodies together with a secondary fluorescent antibody were used, they were incubated in two separate steps and washed in-between and before the antibody mix was added with 2 mL FACS buffer, centrifugation at 470 x rcf, for 5 min at 4 °C. Cells were then washed once with 2 mL cold FACS buffer, centrifuged at 470 x rcf, for 5 min at 4 °C and kept on ice until measurement at the LSR Fortessa flow cytometer. To determine absolute cell numbers, 10 µL APC counting beads were added to each tube. The analysis was done using the software FlowLogic v8.7. Different gating strategies were used to distinguish between distinct subsets of immune cells in the blood and liver (Figure 4).
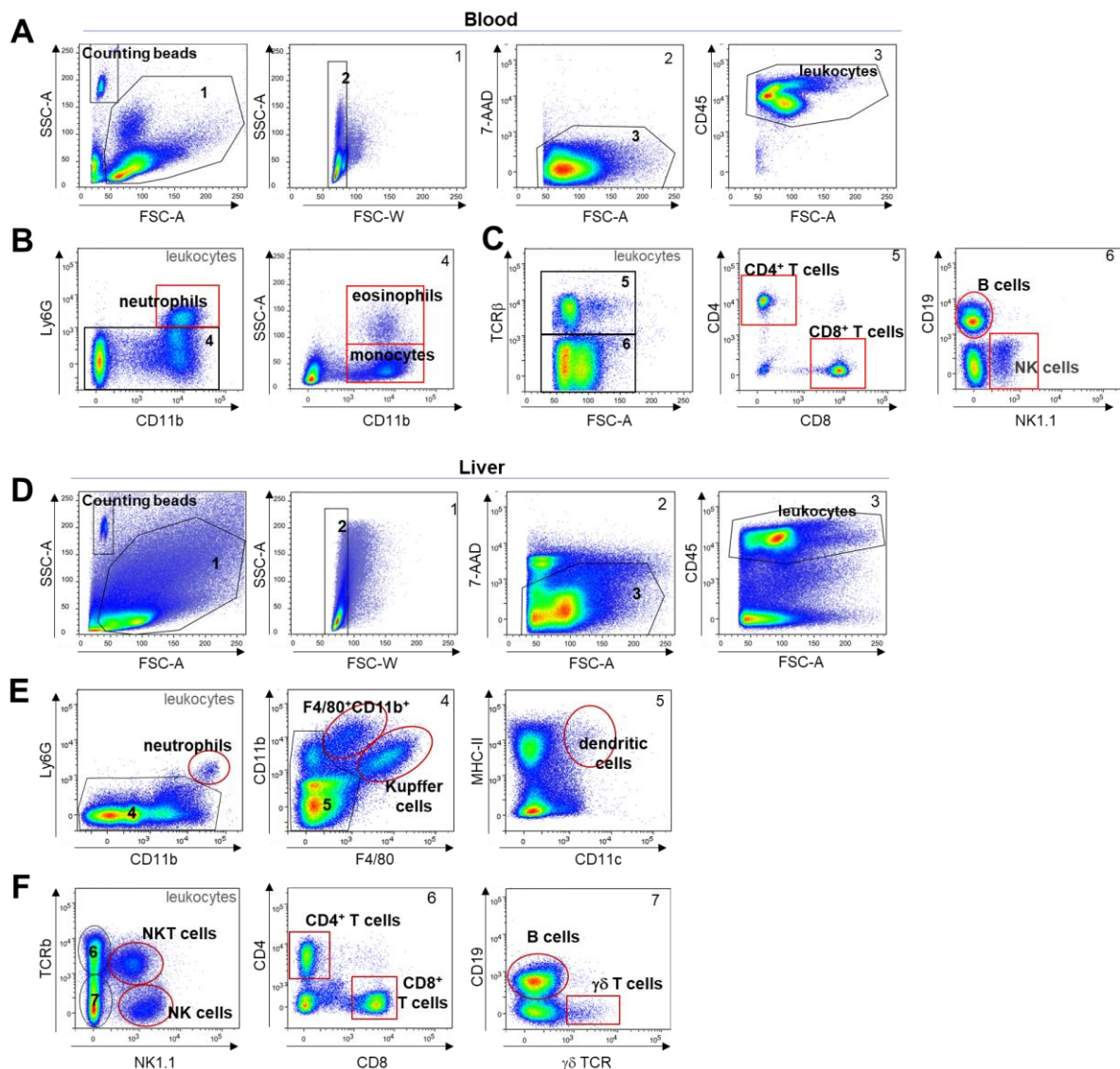
Figure 4 : General gating strategy for the identification of leukocytes isolated from blood and liver. A) Blood cells were gated according to their size (FSC-A) and granularity (SSC-A) (1). Doublets were excluded by their high width (FSC-W). Dead cells were identified using the DNA intercalating dye 7-AAD. From the living cells, leukocytes were identified by their positivity for the pan-leukocyte marker CD45. **B**) Gating strategy for myeloid cells. Among live, single leukocytes, neutrophils were identified by their expression of Ly6G and CD11b. Monocytes are classically defined as CD11b$^+$ Ly6G$^-$ cells. Eosinophils are also CD11b$^+$ Ly6G$^-$ leukocytes but can be distinguished from monocytes by their high granularity. **C**) Gating strategy for lymphocyte populations. T cells (5) are identified by TCRb staining and are further subdivided into CD8$^+$ cytotoxic T cells and

CD4$^+$ T helper cells. Within the TCRb$^-$ population (6), B cells were identified by CD19 expression and NK cells by NK1.1 expression. **D**) Liver cells (1) were gated according to their size (FSC-A) and granularity (SSC-A). Doublets were excluded by their width (FSC-W). Dead cells were excluded, and leukocytes were identified by their positivity for CD45. **E**) Among leukocytes, neutrophils were identified by their expression of Ly6G and CD11b. Infiltrated hepatic macrophages are defined as Ly6G$^-$ F4/80$^+$ cells. While Kupffer cells typically express high levels of F4/80 and intermediate levels of CD11b, infiltrating monocyte-derived macrophages express intermediate to high levels of F4/80 but high levels of CD11b. Within the F4/80$^-$ population, dendritic cells were identified by their high positivity for CD11c and MHC-II. Monocytes were defined as F4/80$^-$ CD11b$^+$ cells. **F**) Gating strategy for lymphocyte populations. NK cells and NKT cells express the NK cell marker NK1.1 and can be distinguished by their expression of the T cell receptor beta (TCRb). NK1.1$^-$ TCRb$^+$ T cells can be further divided into T helper cells (CD4$^+$ T cells) and cytotoxic T cells (CD8$^+$ T cells). Among the TCRb$^-$ cells, B cells are identified by their expression of CD19. Gamma delta T cells (γδT cells) express a γδTCR instead of the more common αβTCR and were therefore defined as TCRb$^-$ γδTCR$^+$ cells.

2.2.6 Hydroxyproline assay

Hydroxyproline is a major component of collagen and can be measured in a colorimetric assay to quantify collagen deposition. (177) Frozen liver tissue samples were thawed, weighed, and transferred into a 2 mL safe-lock reagent tube. 10 µL 6 N HCl per mg liver tissue were added and the samples incubated at 110 °C for 16 h. In this step, the polypeptides contained in the sample were hydrolytically cleaved into their individual amino acids. After cooling down, the homogenized sample was filtered through a folded filter saturated with 6N HCl. From each sample, 15 µL was used in duplicate and mixed with 15 µL methanol in 1.5 mL safe-lock reagent tube. The samples were then concentrated in a vacuum centrifuge at 1300 rpm, for 1 h at 50 °C. A standard series was prepared in 50% in triplicates to determine the concentration. The concentrated samples were resuspended in 50 µL of 50% isopropanol. The crystals of the samples were resuspended with 50 µL of 50% isopropanol. Then 100 µL of 0.6% chloramine-T solution was added to all samples including the standards, mixed on and incubated for 10 min at room temperature. During this step, hydroxyproline is oxidized to pyrrole. The addition of Ehrlich's reagent results in a yellow-orange coloration of the solution after 45 min incubation at 50 °C under agitation, allowing the pyrrole concentration to be determined by colorimetry. All samples were then pipetted onto a 96-well plate and the absorbance was measured at a wavelength of 570 nm using a spectrophotometer with Gen5 version 3.0 software. After subtracting the blank value, a linear regression line was generated with the values of the standard series. From this, the hydroxyproline concentration of the samples were extrapolated.

2.2.7 RNA Isolation

RNA was isolated from snap-frozen liver tissue using the guanidine isothiocyanate-phenol-chloroform method, which is based on the differential solubility of RNA, DNA, and other biomolecules in a biphasic emulsion. The chaotropic salt guanidine isothiocyanate denatures proteins and inhibits RNases, which otherwise would rapidly digest the RNA. A ready-to-use phenol-guanidine isothiocyanate solution (RNAsolv® Reagent) was used. Small pieces of liver tissue were transferred into a tube containing metal beads and phenol and allowed to thaw on ice. Then, the tissue was lysed using a tissue homogenizer at a speed 4000 for 2x each 30 s, and the lysate transferred into a 2 mL safe-lock tube. 200 µL chloroform were

added and the samples were vortexed vigorously for 15 s, followed by an incubation for 10 min on ice. Subsequently, the samples were again vortexed for 15 s and the emulsion centrifuged at 12.000 rcf for 15 min at 4 °C. Thereby, the mixture separates into two distinct phases, a lower organic phase and an upper aqueous phase, separated by an interphase. While proteins and lipids remain in the organic phase, RNA dissolves in the aqueous phase. DNA accumulates in the interphase. 500 µL of the upper RNA-containing phase were carefully pipetted into a new 2 mL safe-lock tube, avoiding the interphase, and placed on ice. 500 µL isopropanol were added to the RNA solution and the sample was inverted to gently mix it. Isopropanol is used to precipitate and recover the RNA. The samples were incubated for 10 min and then centrifuged at 12.000 rcf for 10 min at 4 °C. The supernatant was removed, and the RNA pellet washed with 1 mL 80% ethanol followed by a centrifugation at 7500 rcf for 5 min at 4 °C. The supernatant was discarded. This step was repeated and, after removing the remaining ethanol, the pellet dried at room temperature for 10 min. The pellet was then dissolved in 100 µL RNase-free water and transferred into a fresh tube. The RNA concentration was determined using a NanoDrop.

2.2.8 Quantitative reverse transcription PCR

Reverse transcription quantitative polymerase chain reaction (RT-qPCR or qPCR) is used to detect and quantify RNA. This method is based on reverse transcription of RNA by the enzyme reverse transcriptase into complementary DNA (cDNA), which allows amplification of selected targets by PCR. During PCR, double-stranded DNA (dsDNA) is amplified in repeated cycles, and the amount of DNA synthesized can be measured indirectly using fluorescent reporter dyes. 1 µg RNA were transcribed into cDNA using random hexamer primers. The resulting cDNA was diluted with 200 µL nuclease-free water and used for qPCR using primer pairs designed to specifically bind and amplify target gene sequences. SYBR™ green, a dsDNA binding reporter dye was used for the detection and quantification of the amplified DNA during each qPCR cycle. To determine the relative expression of target genes, the house-keeping genes *B2m* (encoding for β2-microglobulin) and *18S* (part of ribosomal RNA) were used as internal controls. House-keeping genes are genes that are needed for the maintenance of cells and are therefore constitutively expressed and ideally unaffected by different conditions.

Depending on the abundance of mRNA in the tissue, the cDNA contains a higher or lower number of transcribed copies. During qPCR, the target sequences are amplified exponentially. Depending on the number of copies of cDNA, a threshold for detection is reached after a certain number of cycles. This number of cycles required for the fluorescence signal to cross the detection threshold is defined as the Ct (cycle threshold) value. The Ct values can be used for semi-quantitative analyses. The Ct of the target gene (x) is normalized to the sample mass by comparing it to the Ct of the housekeeping gene from the same sample (hkg) resulting in a ΔCt value ($\Delta Ct = Ct_{(x)} - Ct_{(hkg)}$) and allowing for the comparison of experimental (exp) to control (ctrl) group samples. The relative change in gene expression can be calculated by using the ΔΔCt formula: $2^{-(\Delta Ct(exp) - \Delta Ct(ctrl))}$.

2.2.9 Measurement of serum transaminases

Measurement of serum activity and serum marker concentrations was performed by the central diagnostic laboratories of the University Hospital RWTH Aachen, using an assay that measures the absorbance of nicotinamide adenine dinucleotide (NADH) at 340 nm. Alanine aminotransferase (ALT) converts L-alanine and α-ketoglutarate to pyruvate and L-glutamate. Pyruvate is used by the enzyme lactate-dehydrogenase (LDH) to oxidize NADH and H+ into lactate, NAD+ and H_2O. The declining concentration of NADH can be determined by measuring the absorbance at 340 nm, and the final concentration of ALT is quantified using a standard curve. The measurement of GLDH activity and cholesterol concentration is based on an enzymatic reaction that reduces the tetrazolium salt 3-(4,5-dimethylthiazol-2-yl)-2,5-diphenyltetrazolium bromide (MTT), resulting in a color change of reduced MTT that can be measured at 565 nm.

2.2.10 Multiplex chemokine assay

Serum chemokines were analyzed with a 12-plex chemokine kit using a LUNARIS™ biochip. The LUNARIS™ system integrates a bead-based multiplexing technique in a plate-based format with an image-based analysis. Antibody-coated beads are immobilized in a distinct pattern on a planar biochip. After binding of their respective analyte, secondary antibodies and a fluorescent label are added, and the fluorescence is detected. (175) The assay was performed according to the LUNARIS™ Mouse 12-Plex chemokine Kit Handbook Version 07_2018.

2.2.11 Histology

Histology is used to visualize the microscopic anatomy of biological tissues and to examine pathological changes on preserved tissue. Tissue samples were fixated with 4% formalin for 48 h, and subsequently dehydrated with ethanol, and finally with the hydrophobic solvent xylene. This step was performed by the Interdisziplinäres Zentrum für Klinische Forschung (IZKF) facility of the University Hospital RWTH Aachen. After dehydration, the samples were embedded in paraffin for conservation. For histological analyses, 1-2 μm thick sections were cut from the paraffin-embedded tissue and were placed on a microscopy slide.

2.2.12 Hematoxylin and Eosin staining

Hematoxylin and eosin staining (H/E) is used to visualize the histomorphology of tissues, as it can display both cellular and extracellular components. Hematoxylin is a basic dye that stains acidic structures like DNA-containing nuclei blue, while the acidic dye eosin stains basic or acidophils structures, such as cytoplasmic proteins, pink. For H/E staining, sections were pre-warmed for 45 min at 37 °C and then incubated 3x 10 min in xylene for deparaffinization. The sections were then rehydrated by successive dips in 100% (2x), 96% (2x), 70% ethanol and deionized water each for 15 s. The slides were then immersed for 5 min in hematoxylin solution and blued in running tap water for 5 min. Then, the sections were counterstained with eosin solution for 3 min, submerged to 0.5% acetic acid for 3 s and dehydrated by

successive immersion for 15 s in 70% (2x), 96% (4x) and 100% ethanol. Slides were incubated for 5 min in xylene and then mounted with hydrophobic mounting medium (Roti Histokitt) and a cover glass. Microscopic images were obtained by using the Axio® Observer Z1 microscope in the brightfield mode, with a 10x objective. From fibrotic tissues 4x4 tiles of a representative area were acquired at a 10x magnification. From tumor-bearing livers, the whole sections were scanned.

2.2.13 Sirius red

Sirius red staining is used to visualize and quantify fibrotic changes in a tissue. Sirius red dye binds to the triple helix structure of collagens, resulting in a strong red stain. Under polarized light, type I collagen fibers appear yellow-orange and type III collagen fibers appear greenish. (178) 2 µm thick formalin-fixated paraffin-embedded (FFPE) sections were deparaffinized in xylene for 2x 5 min. Then the slides were submerged to 100% ethanol 2x for each 5 min and rehydrated in a series of graded alcohols, 2x 96%, 70%, and deionized water, each 5 min. The sections were covered with Sirius red staining solution (1 mg/mL Sirius red in 1.2% picric acid, pH 2) and incubated for 1h at room temperature. The sections were then immersed in 0.5% acetic acid for 15 seconds and dehydrated in a graded alcohol series of 96% ethanol for 2 min, 100% ethanol 2 x 5 min, and xylene 2 x 5 min. The sections were mounted with Roti Histokitt and a cover glass. From each section 4x4 tiles of a representative area were acquired at 10x magnification, in bright field and polarized light, and the positive area of Sirius red was quantified using ImageJ software. Large vessels were excluded from the analyzed area.

2.2.14 Immunohistochemistry and immunofluorescence

Immunohistochemistry (IHC) and immunofluorescence (IF) are both immunostaining methods that use antibodies to detect and visualize antigen targets in tissues. The ability to see the target of interest in a tissue sample while preserving the spatial context and tissue architecture is the major advantage of immunostaining. IHC is oftentimes performed on FFPE tissue, as this procedure preserves the tissue architecture and FFPE tissue can be easily cut into very thin sections. However, as fixation with formalin causes cross-linking of proteins and masks epitopes for antibody binding, tissue sections must be unmasked before staining. This step, called antigen retrieval, is usually performed with boiling or heated buffers at different pH values. Secondary and sometimes tertiary antibodies, designed to bind to the primary (or secondary) antibody, are often used in IHC and IF because they provide flexibility and signal amplification. While IHC uses chromogens, IF uses fluorophores to visualize the target.

IHC-staining of Ki67

For IHC staining the slides were deparaffinized in xylene for 3x 10 min and then rehydrated by immersion in a series of ethanol (2x 100%, 2x 96%, 1x 70%) each 5 min, followed by 5 min in deionized water. The

slides were then transferred into pre-warmed EDTA buffer pH 9 in a plastic staining cuvette and placed in a water bath for 30 min at 98 °C, followed by a cooldown for 30 min on the bench. The sections were outlined with Dako pen and immersed in deionized water. To inactivate endogenous peroxidases the slides were incubated in 3% H_2O_2 for 10 min and then washed in washing buffer for 3x 5 min. Subsequently, the sections were blocked with 2.5% normal horse serum and incubated overnight with anti-Ki67 antibody, diluted 1:2000 in antibody diluent, in a staining chamber.

The following day, the slides and anti-rabbit ImmPRESS reagent were equilibrated to room temperature. The slides were immersed in washing buffer 3x 5 min and then incubated with anti-rabbit ImmPRESS reagent for 30 min at room temperature. The ImmPRESS reagent contains a secondary antibody conjugated to peroxidase micropolymers. Adding a chromogen substrate results in the development of a staining signal around the bound antibodies. 3,3'Diaminobenzidine (DAB) chromogen was diluted in DAN substrate (1 drop /mL) and applied to the sections for about 60 s and then placed in deionized water. The slides were washed in deionized water 3x for 2 min. Then the slides were dipped twice in hematoxylin solution and blued in running lukewarm tap water for 2.5 minutes. Subsequently, the slides were immersed in a series of ascending ethanol concentrations for each 5 min (1x 70%, 2x 96%, 2x 100%) and incubated in xylene for 3x 5 min. The slides were mounted with Vitroclud and a cover glass. After hardening of the mounting media, the sections were scanned with the Axio® Observer Z1 microscope in the brightfield mode, with a 10x magnification. Ki67$^+$ nuclei from hepatocytes were counted semi-automatically using QuPath v0.4.3.

<u>Immunofluorescence</u>

For conventional immunofluorescence staining, slides were treated as detailed below (2.2.17); however, the protocol was stopped after the first image acquisition. Stained areas were segmented using Ilastik and FIJI was used for stained area calculation.

2.2.17 Sequential immunofluorescence

Multiplex immunostaining allows for the characterization of the composition and spatial relationships of immune cells and other cell types on a single FFPE tissue section. Here, a sequential immunostaining protocol was used that was established and further optimized for the investigation of several cell markers on individual tumors on liver sections. The technique is based on sequential cycles of immunostaining, imaging, and chemical removal of the antibodies, followed by digital processing and analysis of the acquired images (Figure 5). (179)

The multiplex immunostaining protocol was performed on 2 µm thick FFPE sections, that were deparaffinized in xylene for 2x 10 min, followed by successive immersions in 2x 96% ethanol, 80% ethanol, 70% ethanol and 50% ethanol and deionized water for 5 min each. Antigen retrieval was performed in pre-heated 1X universal buffer for 25 min at 98 °C. After a 30-minute cool-down at room temperature, the sections were encircled with Dako pen to build a hydrophobic barrier, and rinsed in 1X-DPBS, 3x 2 min. To reduce autofluorescence, one to two drops of Image-iT FX Signal Enhancer were applied on each section

and incubated in a staining chamber at room temperature for 30 min. The slides were rinsed in 1X-DPBS for 3x 2 min, placed in a staining chamber and blocked with 2% normal goat serum (NGS) for 1 h at room temperature. Primary antibodies from different host species were diluted in 1X-DPBS + 1% BSA at the indicated concentrations (Table 7) and 100 µL of the antibody mix was applied on each section and incubated in a staining chamber over night at 4 °C.

The next day, the slides were rinsed in 1X-DPBS, 3x 2 min, a mix of secondary antibodies diluted in 1X-DPBS + 1% BSA was applied and incubated in a staining chamber for 1 hour at room temperature. Next, the sections were rinsed once in PBS-T for 5 min, followed by 1X-DPBS 2x 3 min. 100 µL DAPI, diluted 1/1000 in PBS, were applied and incubated for 5 min at room temperature, followed by submerging the slides in deionized water for 3x 2 min. The slides were kept in deionized water then mounted with aqueous mounting medium, and a cover slide 3 min before imaging. The sections were scanned using a Zeiss Axio Observer Z1 microscope. After imaging, the slides were immersed in deionized water until the coverslips were detached from the slides. 100 µL antibody stripping buffer were applied to each section and incubated in a hybridization oven at 56 °C for 1 hour. Subsequently, the slides were washed in PBS-T for 3x 20 min, followed by an antigen retrieval in 1X universal buffer for 15 min at 94 °C. After a 30-minute cooldown at the bench the slides were washed in 1X-DPBS 3x 2 min and then blocked with 2% NGS for 30 min. A primary antibody mix was applied (see above) and incubated in a staining chamber overnight at 4 °C. The same procedure was repeated on the following days. An overview of the staining panel on each day is provided in Table 12.

Table 11: Staining panel for sequential multiplex immunofluorescence. Secondary antibodies against the primary antibody host species were used in the indicated colors: purple = Alexa Fluor (AF)750, red = AF647, orange = AF555, green = AF488, blue=DAPI.

Host species	Cycle 1	Cycle 2	Cycle 3	Cycle 4	Cycle 5	Cycle 6	Cycle 7
Mouse		Na:K-ATPase			αSMA	PCNA	
Rabbit	CXCR4	Ki67	Collagen I	IBA-1	β-Catenin	MPO	Collagen IV
Rat	F4/80	B220	CD8	CLEC4F		CD4	CK19
-	DAPI	DAPI	DAPI	DAPI	DAPI	DAPI	DAPI

The scanned images from each day were further processed. Using the ZEN software, a shading correction and tile stitching was applied to all images and the pictures were exported as grayscale TIFF images. With the FIJI software the single images from each day were then combined in a hyperstack and the hyperstacks from each day were concatenated and registered with the FIJI plugin HyperstackReg V5.6. using the DAPI signal from each day as a reference. The aligned single stain pictures were saved separately. For analysis binary masks for each marker were generated using the trainable classification software Ilastik. (179) Tumor regions were identified by merging cytokeratin 19 (CK19), αSMA, collagen I and collagen IV images.

44

While collagen I and IV are abundant in the fibrotic non-tumor tissue, they are virtually absent or distorted within neoplastic tissue. (60, 180) As tumors and dysplastic nodules have an abnormal vasculature, resulting from arterial blood supply, they lack portal fields that can be easily identified by CK19^{+} bile ducts next to αSMA[+] arteries. (64) Tumor masks were drawn manually in FIJI and converted into binary masks. CellProfiler v3.1.9 was used for cell identification, counting, localization, and staining intensity measurements in each tumor and non-tumor tissue.
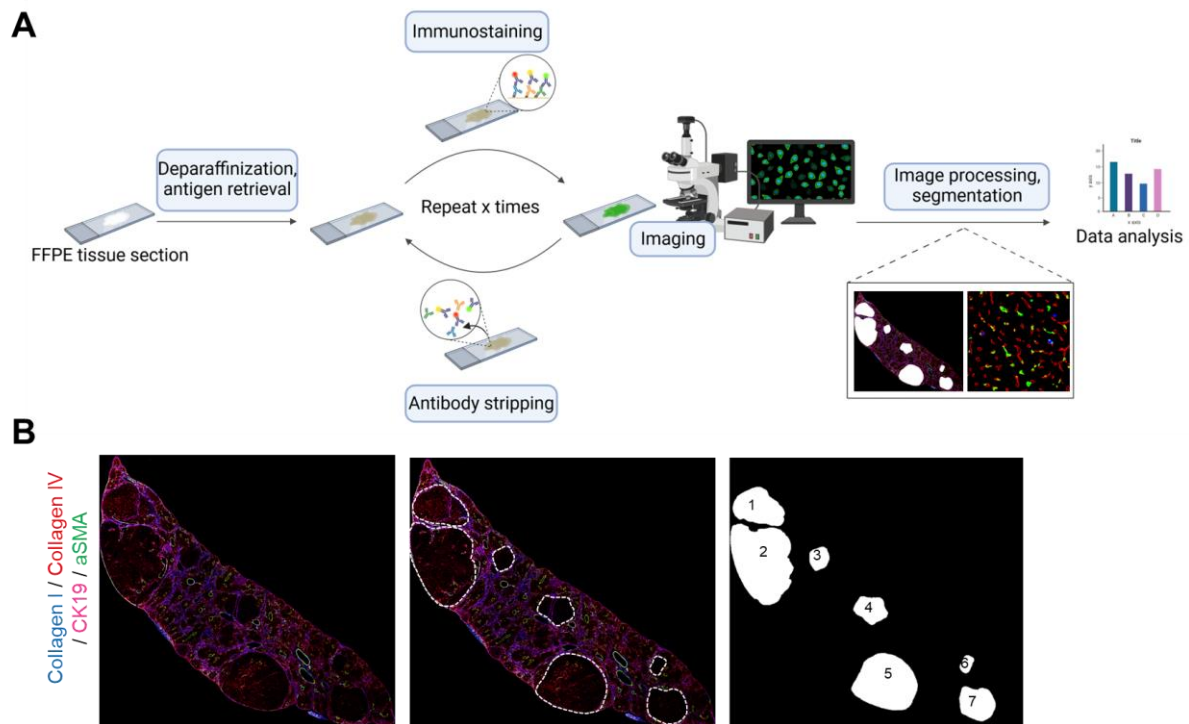
Figure 5: Multiplex immunostaining workflow. A) Formalin-fixed paraffin-embedded (FFPE) liver sections were deparaffinized, followed by antigen retrieval and immunostaining. After image acquisition, the bound antibodies are stripped off and the slide can be stained with a set of additional markers. During the following image processing the images from every step are aligned. Using a semi-automated approach, the positively stained areas are identified and further analyzed. **B**) Example of how the tumor regions were defined in DEN + CCl$_4$ tumor samples, using collagen I, collagen IV, CK19 and αSMA.

2.2.15 Cell culture and *in vitro* assays

Cell culture of Jurkat cells

Jurkat cells were stored in RPMI1640 + 10% DMSO + 40% FBS (heat inactivated) in liquid nitrogen. After thawing, Jurkat cells were cultured in RPMI1640 + 10% FBS at 37 °C at 95% humidity and 5% CO$_2$.

CXCR4 activation assay

Cover slides were placed in a 12-well plate and coated with Poly-L-lysin (0.1 mg/mL, 30 min) and washed twice with 1X-PBS. 4.5 x 10^5 Jurkat cells in RPMI1640 + 5% FBS were added to each well and allowed to

settle overnight. CXCL12 (SDFα), NOX-A12, and CXCL12 together with NOX-A12 were pre-incubated for 30 min at 37 °C and then added to the cells. After 15 min incubation at 37 °C, cells were placed on ice and fixated with 1% formalin for 30 min. The cover slides were washed gently with 1X-DPBS (3x 5 min) and permeabilized with 0.025 Triton-X in 1X-DPBS for 15 min. After blocking non-specific antibody binding with 2% normal goat serum (NGS), a phospho-sensitive anti-CXCR4 antibody clone (EPUMBR3), binding only to unphosphorylated but not activated and hence phosphorylated CXCR4, was applied (1:500 in 1X-DPBS+1% BSA) for 1 h at room temperature. After washing in 1X-DPBS (3x 5 min) cells were stained with a secondary antibody (goat anti-rabbit, AF647 conjugated), 1 h at room temperature. The cells were washed (3x 5 min 1X-PBS) and counterstained with DAPI for 5 min. After carefully rinsing twice with deionized water, 1 drop aqueous mounting medium was applied to each cover glass and the cover glass was transferred to a slide. After drying of the mounting medium, the slides were imaged with the Zeiss Observer 7 microscope with a 20x magnification.

2.2.16 Statistical analyses

Statistical analyses were done by using the software GraphPad Prism v9.5.1. The data for each group were presented as scatter plots with a bar indicating their mean value, and the standard deviation (SD) was indicated by positive error bars. The statistical significance of the difference between two groups was analyzed by a two-tailed unpaired Student's t-test. For multiple group comparisons significance between groups was analyzed by a one-way ANOVA with Tukey's correction for post-hoc analysis. Significances were marked in the diagrams as follows: $*$ = p <0.05; $**$ = p <0.01; $***$ = p <0.001, $****$=p <0.0001.

3. Results

The following section presents a detailed description of the results obtained. While in the first part, comprising paragraphs 3.1 -3.4, the role of CXCL12 in chronic liver fibrosis is evaluated, the second part includes sections 3.5 - 3.7 and addresses how inhibition of CXCL12 alters the stromal and immune environment of primary liver cancer in a setting of chronic liver disease. In the third section, the impact of the CXCL12 inhibitor NOX-A12 on liver fibrosis in a toxin- and a diet-induced model of liver injury is investigated. Subsequently, the impact on immune cells in both conditions is evaluated. The fourth section briefly describes the influence of CXCL12 inhibition on early recovery after chronic liver injury. Section five evaluates the overall impact of NOX-A12 on liver tumor growth using two models of inflammation-driven carcinogenesis that reflect on tumor progression in both a fibrotic/cirrhotic liver and a diet-induced fatty liver. The impact of CXCL12 inhibition on the fibrotic/cirrhotic tumor-associated immune milieu is further explored in section six. In section seven, the impact of CXCL12 inhibition on immune cells and the microenvironment in early NAFLD/NASH-associated tumors is examined.

3.1 Investigation of the impact of NOX-A12 on chronic liver inflammation and fibrosis

3.1.1 NOX-A12 effectively neutralizes CXCL12 and does not induce liver injury

Prior to any in-depth analyses, the functionality of the Spiegelmer NOX-A12 as a CXCL12 neutralizing agent was confirmed in an *in vitro* internalization assay. Jurkat cells were incubated for 15 minutes with either 20 nM CXCL12, 50 nM NOX-A12 or 20 nM CXCL12 together with 50 nM NOX-A12. Binding of CXCL12 to CXCR4 was assessed by using a phospho-sensitive anti-CXCR4 antibody that only binds unphosphorylated CXCR4. Stimulation with CXCL12 resulted in a rapid phosphorylation and internalization of CXCR4, which was reflected by a reduced surface staining. This effect was abrogated in the presence of NOX-A12 (Figure 6 A). To further confirm the *in vivo* functionality and safety of NOX-A12, healthy 6-week-old C57BL/6J wildtype (WT) mice were injected subcutaneously with either 20 mg/kg body weight NOX-A12 or non-functional reverse NOX-A12 (revNOX-A12) three times per week. Mice were sacrificed after four weeks, and liver and blood serum were harvested for further analysis (Figure 6 B). In the serum of NOX-A12 treated animals highly increased serum levels of CXCL12 were detected, while CXCL12 serum levels in revNOX-A12 treated mice were comparable to untreated controls (Figure 6 C, D). To ensure that CXCL12 inhibition by NOX-A12 does not have adverse effects, liver histology after treatment with NOX-A12 or revNOX-A12 was assessed by hematoxylin and eosin (H/E) staining and this showed no sign of inflammation, injury, or altered microarchitecture (Figure 6 E). Serum levels of alanine aminotransferase (ALT) and glutamate dehydrogenase (GLDH) were unchanged, indicative of an overall good tolerance of NOX-A12 by the liver

(Figure 6 F). We thus concluded that NOX-A12 can be used as a CXCL12-neutralizing agent for *in vivo* experiments in mice.
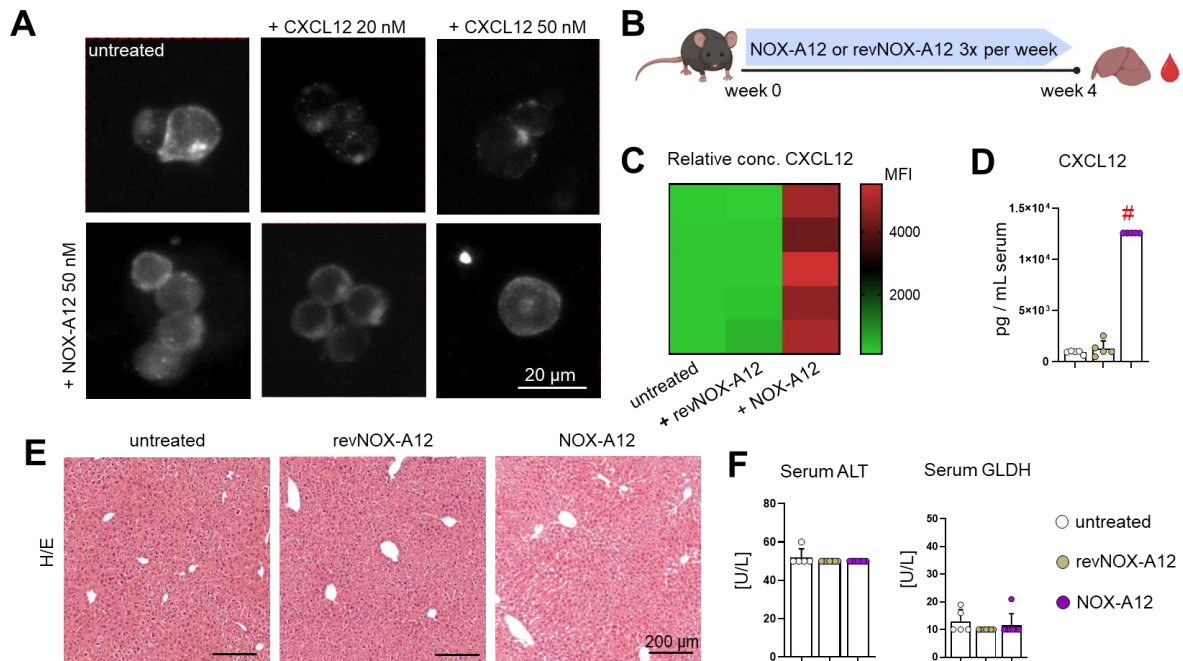
Figure 6: NOX-A12 effectively neutralizes CXCL12 and does not induce liver injury. A) The ability of NOX-A12 to prevent CXCR4 internalization was assessed. Staining of CXCR4 on Jurkat cells after stimulation with CXCL12, NOX-A12 or CXCL12 + NOX-A12. Representative images from multiple experiments. **B**) Experimental outline. Healthy six-week-old mice were treated with NOX-A12 or reverse NOX-A12 (revNOX-A12) three times per week for four weeks. Mice were euthanized and liver and blood serum were collected. **C-D**) Serum levels of CXCL12 were analyzed using a protein chip microarray. Heatmap of the mean fluorescence intensity of CXCL12 (C) and quantification of the CXCL12 serum concentrations (D). # Note: In some samples, the serum CXCL12 concentration exceeded the concentration of the highest reference control, therefore values were limited to the highest calculable concentration. **E**) Hematoxylin and eosin (H/E) staining of liver sections from untreated mice or mice subjected to four weeks NOX-A12 or revNOX-A12 treatment. **F**) Serum levels of alanine aminotransferase (ALT) and glutamate dehydrogenase (GLDH). Error bars represent mean +/- S.D. As some data points were either above or below detection limits no statistical analysis was performed.

3.1.2 NOX-A12 does not affect overall chronic liver inflammation and fibrosis induced by CCl$_4$ injections or MCD diet.

To investigate the effects of CXCL12 inhibition and the potential therapeutic value of NOX-A12 in chronic liver disease, two experimental models of liver inflammation were used: a model of toxic liver injury and fibrosis induced by repeated injections of the hepatotoxin carbon tetrachloride (CCl$_4$), which recapitulates several aspects of human liver fibrosis, and a methionine-choline-deficient diet (MCD) model, which reflects characteristics of NASH. (171)

8-week-old C57BL/6 wildtype mice were subjected to biweekly intraperitoneal injections with CCl$_4$ for eight weeks. Over this time course, NOX-A12 or revNOX-A12 was administered subcutaneously three times per week and mice were sacrificed two days after the last CCl$_4$ injection and one day after the last NOX-A12 or revNOX-A12 injection. The liver and blood were collected (Figure 7 A). Untreated mice served as a control.

H/E staining of liver sections revealed typical signs of chronic liver inflammation after CCl_4 exposure such as a slightly distorted microarchitecture, without apparent differences between revNOX-A12 and NOX-A12 treated livers (Figure 7 B). Serum ALT and GLDH, reflective of liver damage, were increased upon chronic CCl_4 treatment (Figure 7 C). Also, the number of leukocytes in the liver, as determined by flow cytometry was elevated in CCl_4 treated mice, indicative of liver inflammation (Figure 7 D). However, there were no clear differences between NOX-A12 treated and revNOX-A12 treated mice. Liver fibrosis was assessed by Sirius red staining of liver sections and by analysis of the hydroxyproline content in liver tissue. Chronic CCl_4 treatment caused extensive collagen deposition and an increase in hydroxyproline, but no effect of CXCL12 inhibition on fibrosis was observed (Figure 7 E, F). The number and activation of HSCs was assessed by immunofluorescence staining of αSMA and desmin, revealing an increase after chronic injury but no difference between NOX-A12 and rev-NOX-A12 treated groups (Figure 7 G).

These findings were confirmed on the transcriptional level in liver
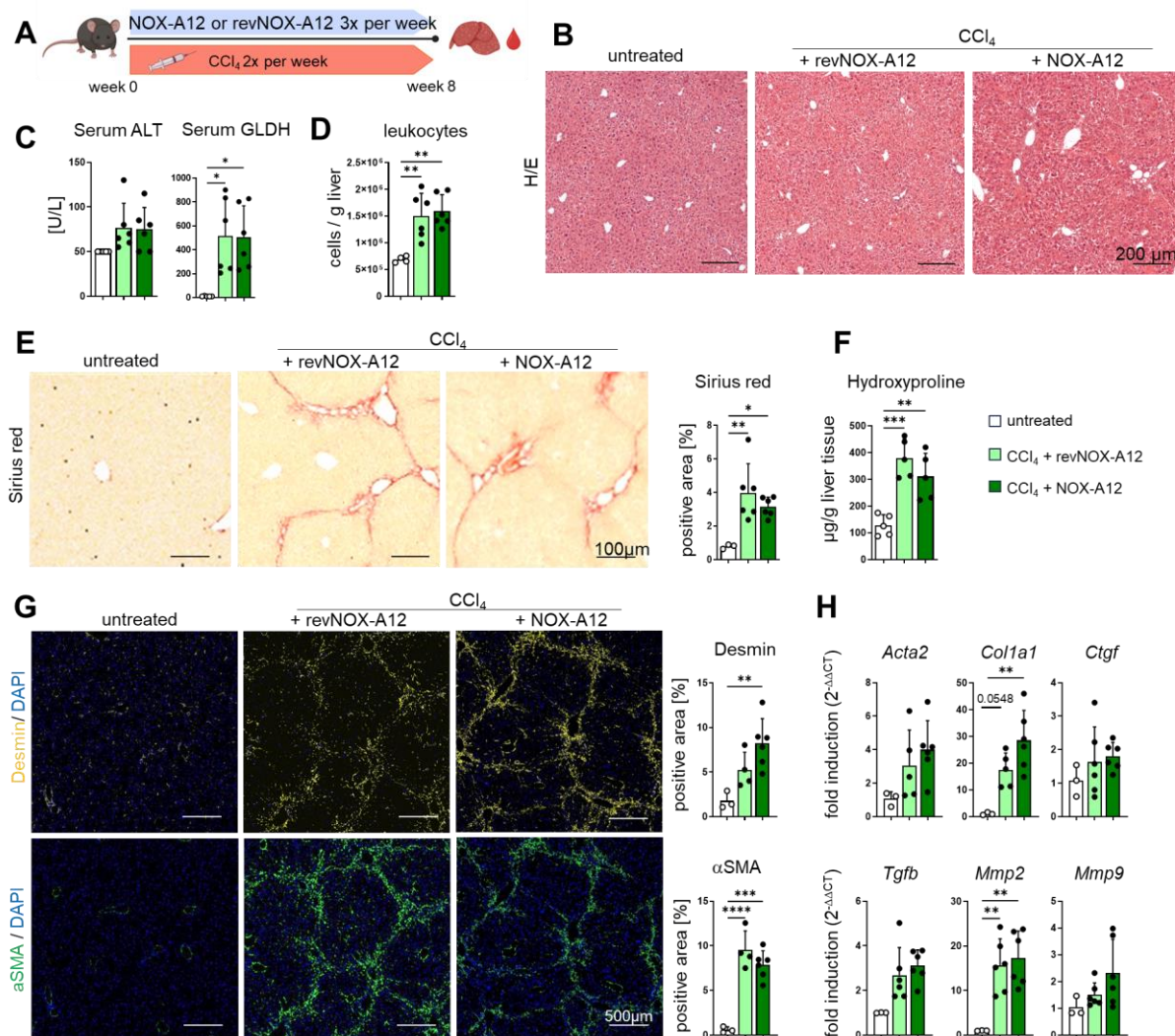
Figure 7: CXCL12 inhibition does not impact CCl_4-induced chronic liver injury and fibrosis A) Experimental setup: eight-week-old mice were subjected to biweekly injections of 0.5 mL/kg body weight of CCl_4 over an eight-week period. NOX-A12 or revNOX-A12 was administered subcutaneously three times per week. Mice were sacrificed approximately 48 h after the last CCl_4 injection. Untreated age-matched mice served as a control. **B**) H/E staining of liver sections from untreated healthy

mice and mice subjected to chronic CCl₄ treated with NOX-A12 or revNOX-A12. **C**) Serum levels of ALT and GLDH. **D**) The number of liver leukocytes was assessed by flow cytometry. **E**) Collagen deposition in the liver from mice subjected to chronic CCl₄ injections and NOX-A12 or revNOX-A12, or from healthy controls was assessed by Sirius red staining. Representative pictures and quantification of the Sirius red as positive area per analyzed region. **F**) Hydroxyproline content of liver tissue was measured. **G**) Immunofluorescence staining of desmin and αSMA, representative images and quantification of desmin and αSMA positive area. **H**) Quantitative real-time PCR of fibrosis related genes was performed on liver homogenates. Housekeeping genes: 18S + B2m. Error bars represent mean +/- S.D. One-way ANOVA followed by Tukey's multiple comparison test was performed. *p<0.05; **p< 0.01; ***p< 0.005; ****p< 0.0001.

homogenates. Gene expression of *Acta2* was not affected by CXCL12 inhibition, similar to other HSC activation markers (*Col1a1*, *Ctgf*). Furthermore, the gene expression of neither the pro-fibrotic factor *Tgfb* nor the metalloproteinases *Mmp2*, and *Mmp9* were affected by NOX-A12 treatment (Figure 7 H).

To assess the impact of CXCL12 inhibition by NOX-A12 on metabolic dysregulation-driven liver inflammation, mice were fed a methionine-choline deficient (MCD) diet for seven weeks, combined with NOX-A12 or revNOX-A12 treatment (Figure 8 A). MCD diet induced a pronounced steatohepatitis, characterized by large fatty vacuoles and accumulation of inflammatory cells in both treatment groups, as assessed by H/E staining (Figure 8 B). Serum ALT and GLDH levels and the number of leukocytes in the liver were strongly increased after MCD diet with no differences between NOX-A12 or revNOX-A12 treated groups (Figure 8 C, D). Liver fibrosis, as determined by Sirius red staining and hydroxyproline measurement, was not affected by NOX-A12 (Figure 8 E, F). Also, the activation and number of HSCs assessed by immunofluorescence staining of αSMA and desmin, (Figure 8 G) as well as the expression of several fibrosis-associated genes (*Acta2, Col1a1, Ctgf, Tgfb, Mmp2, Mmp9*) (Figure 8 H) was unaltered.
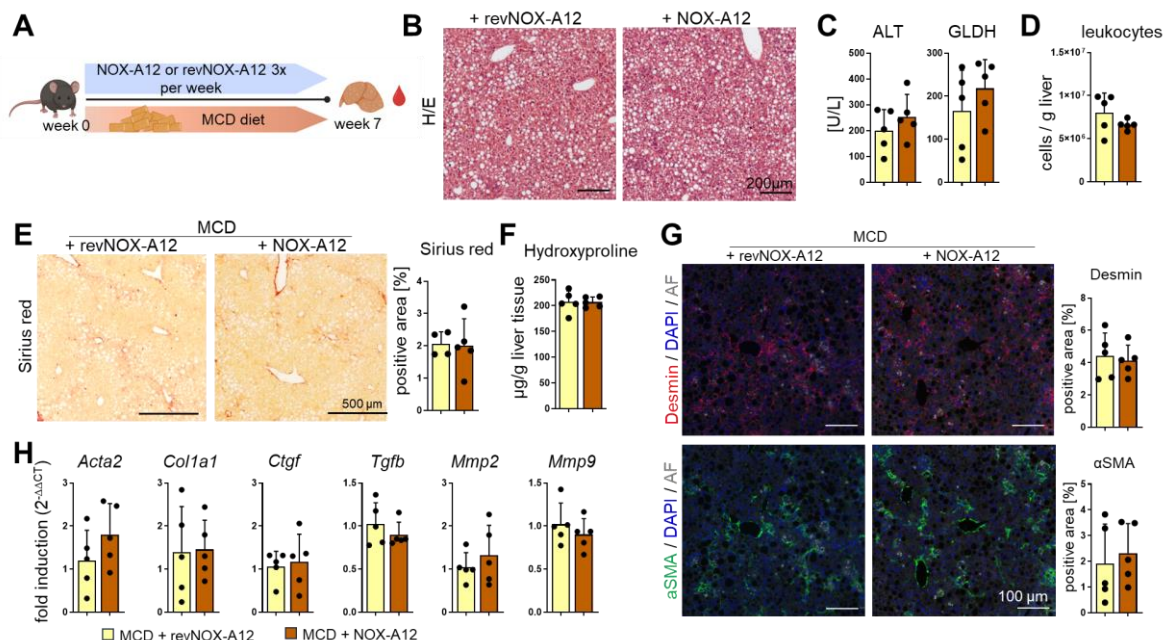
Figure 8: CXCL12 inhibition has no effect on MCD diet-induced liver injury and fibrosis. A) Mice were fed a methionine-choline deficient (MCD) diet for 7 weeks. NOX-A12 was administered three times per week during the whole period of MCD diet. A control group received revNOX-A12 for 7 weeks. **B**) HE staining of MCD-fed mice treated with NOX-A12 or revNOX-A12. **C**) Serum levels of ALT and GLDH. **D**) The number of liver leukocytes was assessed by flow cytometry. **E**) Collagen deposition in MCD-fed mice, treated with NOX-A12 or revNOX-A12 visualized by Sirius red staining. Representative pictures and quantification of the Sirius red as positive area per analyzed region. **F**) Hydroxyproline content of liver homogenates was

analysed. **G**) Desmin and αSMA immunofluorescence staining. Representative images and quantification of desmin and αSMA positive area. AF, autofluorescence. **H**) Quantitative real-time PCR of different fibrosis related genes was performed on liver homogenates. Housekeeping genes: *18S + B2m*. Error bars represent mean +/- S.D. Unpaired Student´s t-test was conducted. *p<0.05; **p< 0.01; ***p< 0.005; ****p< 0.0001.

Overall, these data show that NOX-A12 does not alter tissue injury or fibrogenesis in these two mouse models of liver disease. Nevertheless, CXCL12 neutralization is expected to affect immune cell mobilization and recruitment, so we next sought to characterize the immune status of these mice.

3.2 Evaluation of the effect of CXCL12 inhibition on immune cells during CCl₄-induced chronic liver inflammation

3.2.1 Study of the effects of NOX-A12 on circulating immune cells in CCl₄-induced chronic liver inflammation

To characterize the systemic effects of NOX-A12 during CCl$_4$-induced chronic liver disease, blood leukocytes and serum content were analyzed. The total number of blood leukocytes was not altered in mice after chronic CCl$_4$ injury, however significantly increased in the group that received both CCl$_4$ and NOX-A12 treatment (Figure 9 A). Differential analysis of blood leukocyte populations by flow cytometry (according to the fluorescence activated cell sorting (FACS) gating strategy detailed in Figure 4) showed increased absolute numbers of neutrophils, monocytes, and eosinophils after NOX-A12. The relative numbers of monocytes (percentage of leukocytes) were significantly increased during chronic liver inflammation compared to healthy controls, which was even more pronounced in the NOX-A12 treated group (Figure 9 B). A subtype analysis of the monocyte population revealed a strong accumulation of Ly6C$^+$ monocytes in CCl$_4$ treated animals, which was further increased upon NOX-A12 treatment, both in absolute numbers and in the proportion of monocytes (Figure 9 C, D). The number of lymphocytes in the blood was unchanged between all groups, both in relative and in absolute numbers, except for a decrease in the relative amount of NK cells (Figure 9 E). In addition, serum levels of a variety of inflammatory and homeostatic chemokines were analyzed, using a multiplex protein microarray. The inflammatory chemokines CCL4 and CCL2 were significantly upregulated in the serum of CCl$_4$-treated animals in comparison to healthy controls, but were not influenced by CXCL12 inhibition, whereas there was a strong increase in the levels of CCL3, CCL5 and CXCL10 after NOX-A12 treatment. Whilst a tendency towards increased levels of CXCL1 is visible, CCL11 remained unaffected (Figure 9 F, G). The serum concentrations of the dual chemokines CCL20 and CCL22, as well as of the homeostatic chemokines CCL19 and CX3CL1 were not substantially elevated during chronic liver inflammation, however, significantly elevated upon CXCL12 inhibition (Figure 9 H, I).

Collectively, these data demonstrate that NOX-A12 affects the circulating immune cell compartment and chemokine levels, which may either reflect or drive changes in the local immune microenvironment in the liver.
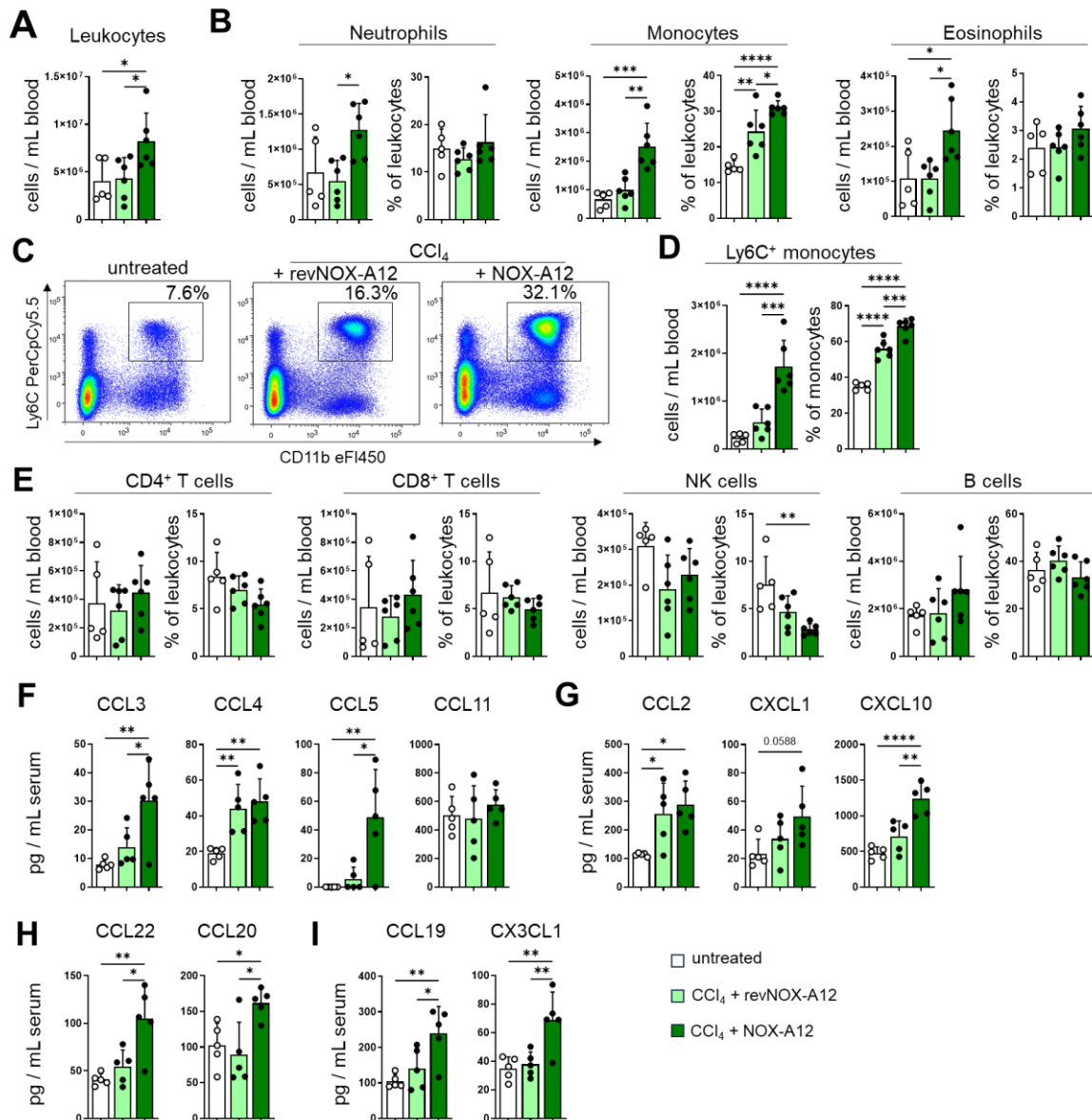
Figure 9: NOX-A12 increases blood leukocytes and serum chemokines in a model of CCl₄-induced chronic liver injury. Blood immune cell populations of healthy (untreated) mice and mice subjected to chronic CCl₄ injections that received either NOX-A12 or revNOX-A12 were analyzed by flow cytometry. **A**) Number of leukocytes per mL of blood. **B**) Absolute (cells per mL blood) and relative (percent of leukocytes) numbers of neutrophils, monocytes, and eosinophils. **C**) Representative FACS plots. **D**) Quantification of Ly6C⁺ monocytes (absolute numbers and proportion of monocytes). **E**) Absolute and relative numbers of lymphoid immune cell populations. F-I) Serum chemokine levels were measured using a multiplex protein microarray. **F-G**) Serum levels (pg/mL) of inflammatory chemokines with (F) redundant receptor affinities or (G) currently known to bind to individual receptor affinities **H**) Serum levels of chemokines involved in homeostatic and inflammatory processes. **I**) Serum levels of homeostatic chemokines. Error bars represent mean +/- S.D. One-way ANOVA followed by Tukey's multiple comparison test was performed. *p<0.05; **p< 0.01; ***p< 0.005; ****p< 0.0001.

3.2.2 Influence of NOX-A12 on hepatic immune cell recruitment and phenotype in CCl₄-induced chronic liver fibrosis

In parallel to blood leukocytes, liver leukocytes were analyzed by flow cytometry, as detailed in Figure 4. No clear changes were observed in the absolute numbers of most hepatic lymphocyte subsets analyzed, except for a decrease in the number of NKT cells in the injury models compared to healthy controls, which was also reflected in the relative abundance. Furthermore, chronic CCl₄ treatment provoked an increase in the relative amount of NK cells and B cells. While NK cells were unaffected by CXCL12 blockade, there was a significant decrease in the relative number of hepatic B cells in NOX-A12 treated animals compared to the revNOX-A12 vehicle control (Figure 10 A). Next, the activation status of NK cells, CD8⁺ T cells and CD4⁺ T cells was examined. Both NK cells and CD8⁺ T cells displayed strongly increased levels of surface CD107a in CCl₄ + revNOX-A12 treated animals, in comparison to cells from untreated animals. However, the percentage of CD107a⁺ cells was significantly decreased in both NK cells and CD8⁺ T cells upon CXCL12 inhibition (Figure 10 B, C). CD25 expression was strongly increased in hepatic CD4⁺ T cells during chronic CCl₄ + revNOX-A12 treatment, but drastically reduced in the CCl₄ + NOX-A12 treated group (Figure 10 D).
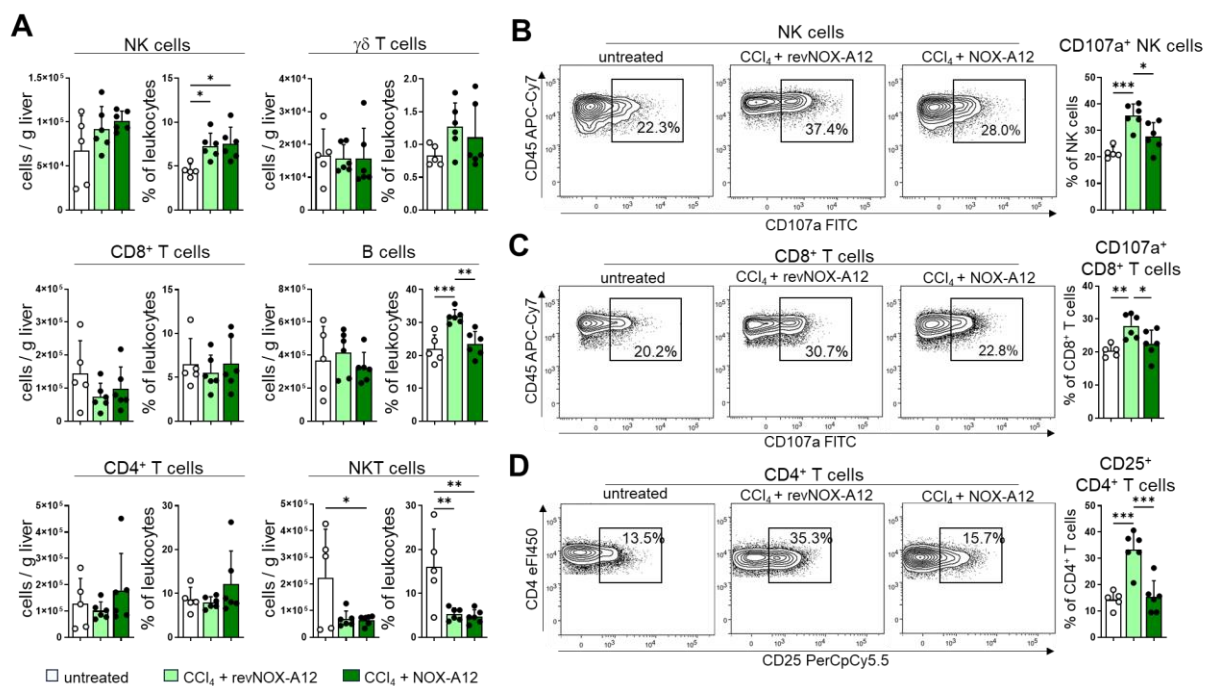
Figure 10: NOX-A12 influences lymphocyte activation in chronic CCl₄ induced liver inflammation. A) Absolute (cells per gram liver tissue) and relative (percent of leukocytes) numbers of lymphoid cells from the liver of untreated mice or chronically CCl₄ injected mice treated with revNOX-A12 or NOX-A12, were investigated by flow cytometry. **B-C)** Representative FACS plots and quantification of CD107a surface staining on hepatic NK cells (B) and CD8⁺ T cells. **D**) CD25 expression on CD4⁺ T cells. Representative FACS plots and quantification Error bars represent mean +/- S.D. One-way ANOVA followed by Tukey's multiple comparison test was performed. *p<0.05; **p< 0.01; ***p< 0.005; ****p< 0.0001

In addition, myeloid hepatic immune cell populations were analyzed by flow cytometry. The numbers of neutrophils and dendritic cells were unchanged by CCl_4 treatment. However, the relative proportion of dendritic cells was significantly reduced by NOX-A12 (Figure 11 A). In contrast, the hepatic macrophage compartment undergoes drastic changes upon CCl_4 treatment. While the number of liver resident Kupffer cells, which can be gated as $CD11b^{int} F4/80^{hi}$ cells (red outline), decreases, there is a dramatic increase in the number of infiltrating macrophages, which are often gated as $Ly6G^- CD11b^+ F4/80^{int/+}$ cells (yellow outline, here named: $CD11b^+F4/80^+$ cells). [181] The absolute cell counts and relative numbers of macrophages did not change with CXCL12 inhibition. (Figure 11 A, B). To validate the results obtained by flow cytometry and to investigate whether NOX-A12 influences the spatial distribution of macrophages, immunofluorescence staining was performed for C-Type Lectin Domain Family 4 Member F (CLEC4F) as a marker for Kupffer cells and for ionized calcium-binding adaptor molecule 1 (IBA1) as a pan-monocyte/macrophage marker. In the healthy liver, Kupffer cells ($CLEC4F^+ IBA1^+$) were rather evenly distributed in the sinusoids, while MoMF ($CLEC4F^- IBA1^+$) were mainly located perivascular in the portal areas. In chronically injured livers there was a pronounced accumulation of MoMF around periportal areas. While the staining also showed a clear reduction of Kupffer cells and increase in MoMF in chronic CCl_4 injured livers, there was no obvious difference between the revNOX-A12 and NOX-A12 treated groups (Figure 11 C).
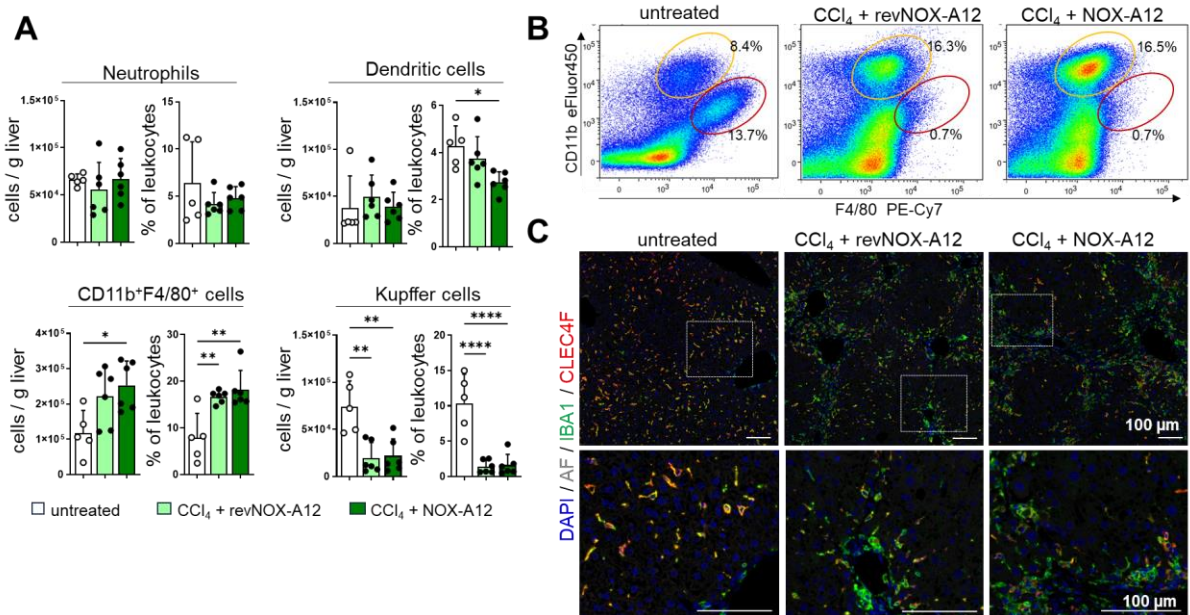
Figure 11: NOX-A12 has moderate effects on major myeloid hepatic immune cell populations in CCl_4 induced chronic liver disease. Myeloid immune cell populations from livers subjected to chronic CCl_4 + revNOX-A12 or NOX-A12, and untreated controls were analyzed by flow cytometry. **A**) Absolute (cells per gram liver tissue) and relative (percent of leukocytes) numbers of infiltrating myeloid cells, Kupffer cells, dendritic cells, and neutrophils. **B**) Representative FACS plots showing the classical gating for monocyte derived macrophages (here named $CD11b^+F4/80^+$ cells, yellow outline) and Kupffer cells (red outline). **C**) Liver macrophage populations were further analyzed by immunofluorescence staining of IBA1 and CLEC4F. Nuclei were stained with DAPI. An autofluorescence (AF) channel was used to visualize the background. Error bars represent mean +/- S.D. One-way ANOVA followed by Tukey's multiple comparison test was conducted. *$p<0.05$; **$p< 0.01$; ***$p< 0.005$; ****$p< 0.0001$.

3.2.3 Investigation of the effect of NOX-A12 on hepatic macrophages

Further analysis of macrophage subpopulations revealed a distinct population of SSC^{hi} cells within the classical CD11b$^+$ F4/80$^{int/+}$ MoMF gate (for clarity here named: CD11b$^+$F4/80$^+$ cells), that was strongly expanded during chronic CCl$_4$ injury, but drastically reduced by CXCL12 inhibition (Figure 12 A). In another set of experiments, using mice that received eight weeks repetitive injections of CCl$_4$ and were sacrificed 36 h after the last CCl$_4$ injection, this population was shown to be most likely comprised of eosinophils, as about 90% of this cell population expressed the eosinophil specific marker SiglecF. This was observed both in healthy liver and during chronic CCl$_4$ injury (Suppl. Figure 1 B). SSC was plotted against MHC-II, which is upregulated on activated macrophages, to distinguish eosinophils (blue outline) from MoMF (red outline) (Figure 12 B). In the healthy liver, eosinophils made up almost 20% of the CD11b$^+$F4/80$^+$ cells, while during chronic liver injury, they accounted for approximately 30%. NOX-A12 reduced the proportion of eosinophils in the CD11b$^+$F4/80$^+$ gate to about 12% (Figure 12 C).
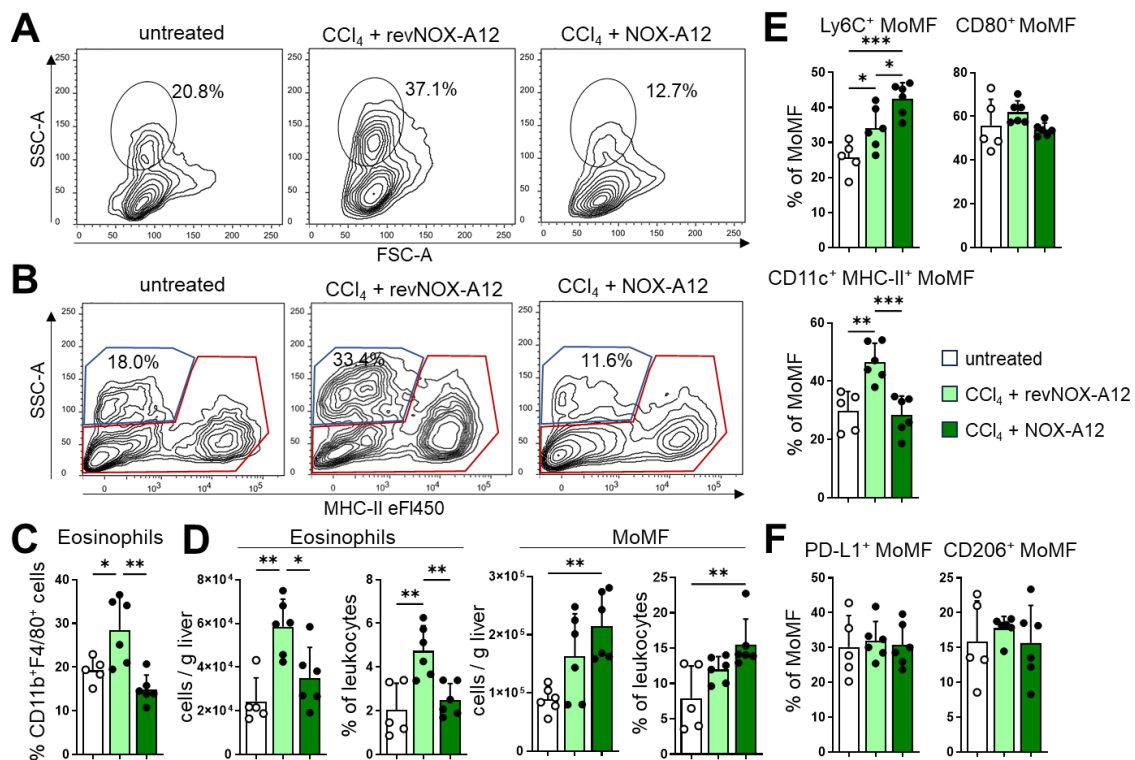
Figure 12: Investigation of subpopulations within infiltrating myeloid cells identifies eosinophils affected by CXCl12 inhibition in chronic CCl$_4$-induced liver inflammation. Infiltrating myeloid cells from untreated controls, and mice chronically treated with CCl$_4$ and NOX-A12 or revNOX-A12, were investigated by flow cytometry. **A)** Representative FACS plots of a distinct SSC^{high} population within the infiltrating myeloid cells (Ref. Supplemental figure 1). **B)** Gating strategy used to distinguish eosinophils (blue outline) from infiltrating monocyte-derived macrophages (MoMF) (red outline). **C)** Percentages of eosinophils present within CD11b$^+$F4/80$^+$ cells. **D)** Absolute (cells per g liver tissue) and relative (percent of leukocytes) numbers of eosinophils and monocyte-derived macrophages (MoMF). **E)** Proportion of Ly6C$^+$, CD11c$^+$ MHC-II$^+$ and CD80$^+$ MoMF. **F)** Percentage of PD-L1$^+$ and CD206$^+$ MoMF. Error bars represent mean +/- S.D. One-way ANOVA followed by Tukey's multiple comparison test was conducted. *p<0.05; **p< 0.01; ***p< 0.005; ****p< 0.0001.

The absolute and relative numbers of eosinophils and MoMF as determined above (3.2.3) were evaluated. Both absolute and relative numbers of eosinophils were significantly increased after chronic CCl_4-induced injury but decreased in the NOX-A12-treated group. The absolute numbers of MoMF were also increased in CCl_4-treated animals compared to healthy controls, with a trend toward a more pronounced increase in the NOX-A12-treated group, which was significantly increased compared to healthy controls, while in the revNOX-A12-treated group, the MoMF did not reach significance. The relative numbers of both treatment groups were significantly increased compared to healthy controls (Figure 12 D). The activation of MoMF was further investigated. Chronic liver injury induced an increase in pro-inflammatory $Ly6C^+$ MoMF which was even more elevated in the NOX-A12 treatment group. While no clear effect was observed for the expression of the co-stimulatory molecule CD80 on MoMF, a subset of $CD11c^+MHC-II^+$ MoMF accumulated after CCl_4-induced injury in the vehicle group but was strongly reduced under inhibition of CXCL12 (Figure 12 E). The anti-inflammatory markers CD206 and PD-L1 were not regulated on MoMF (Figure 12 F). As there were not enough Kupffer cells for a reliable analysis in the CCl_4 treated groups, liver resident macrophages were not further analyzed in this model.

At the site of inflammation, $Ly6C^+$ infiltrating monocytes upregulate MHC-II and mature to pro-inflammatory macrophages which finally differentiate into $Ly6C^-$ restorative macrophages. (32) In order to distinguish freshly infiltrating immature macrophages from maturated pro-inflammatory and differentiated pro-restorative macrophages, the MoMF population was plotted according to their expression of Ly6C and MHC-II, resulting in four distinct populations (Figure 13 A).

Freshly infiltrating MoMF ($Ly6C^+MHC-II^-$) expressed low levels of F4/80, CD11c and PD-L1, and intermediate levels of CD206 compared to the other macrophage populations. $Ly6C^+MHC-II^+$ MoMF expressed intermediate levels of F4/80, and PD-L1, and displayed the highest proportion of CD206 positive cells. CD11c was highly expressed, however not on the entire cell population. $Ly6C^- MHC-II^+$ MoMF on the other hand expressed intermediate levels of F4/80 as well but were mainly CD11c positive and expressed lower levels of CD206. Most of the population expressed PD-L1, however there was also a PD-L1 negative fraction. A fourth population, negative for both Ly6C and for MHC-II was additionally characterized by low F4/80 expression and intermediate to low CD11c. This population was predominantly negative for CD206 but expressed high levels of PD-L1 (Figure 13 A). The absolute cell numbers and their relative contributions to the MoMF pool was determined for each of the populations in untreated conditions and after chronic CCl_4 injury, together with NOX-A12 or revNOX-A12. In steady state, $Ly6C^-$ MoMF (both $MHC-II^+$ and $MHC-II^-$) comprised the largest proportion of the MoMF population in the liver, each representing about 30% of the whole population, while the proportion of $Ly6C^+ MHC-II^+$ MoMF was below 5%. Except for the $Ly6C^- MHC-II^-$ population, the numbers of all MoMF subsets were elevated upon chronic liver inflammation ($Ly6C^+ MHC-II^+$ MoMF, CCl_4 + revNOX-A12 vs. untreated p=0.08). The relative proportions were shifted towards a

dominance of Ly6C$^+$ MHC-II$^+$ and Ly6C$^-$ MHC-II$^+$ MoMF in CCl$_4$ treated animals compared to healthy controls, while the proportion of Ly6C$^-$ MHC-II$^-$ MoMF decreased. The percentage of freshly infiltrating Ly6C$^+$ MHC-II$^-$ MoMF remained stable. Inhibition of CXCL12 during chronic CCl$_4$-induced liver inflammation resulted in an additional prominent increase in Ly6C$^+$ MHC-II$^-$ freshly infiltrating MoMF and a moderate increase in the absolute number of Ly6C$^-$ MHC-II$^-$ MoMF. However, the relative proportion of Ly6C$^-$ MHC-II$^+$ MoMF was significantly reduced compared to the revNOX-A12-treated group (Figure 13 B).
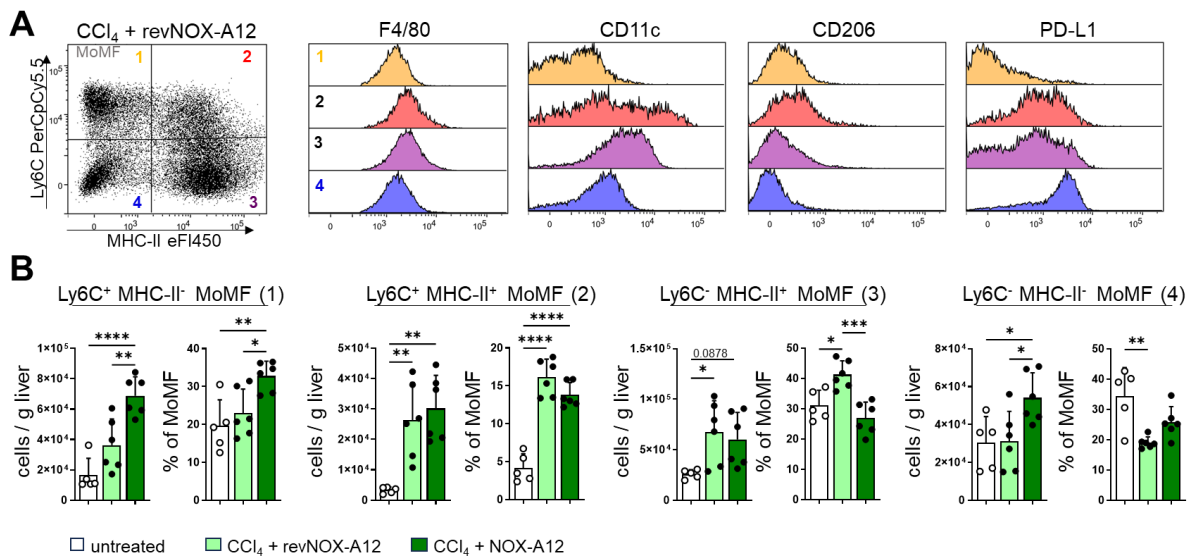
Figure 13: NOX-A12 increases the ratio of immature versus mature macrophages in CCl$_4$ induced liver injury. MoMF from untreated controls and mice treated with CCl$_4$ and NOX-A12 or revNOX-A12 were further analyzed by flow cytometry. **A)** Gating of MoMF subpopulations based on their expression of Ly6C and MHC-II and representative histograms indicating expression of different macrophage activation markers on the indicated MoMF subpopulations. **B)** Relative proportion (percent of MoMF) and absolute numbers (cells per gram liver tissue) of different macrophage subpopulations, distinguished by their MHCII and Ly6C expression. Error bars represent mean +/- S.D. One-way ANOVA followed by Tukey multiple comparison test was performed. *p<0.05; **p< 0.01; ***p< 0.005; ****p< 0.0001

In summary, relative proportions of MoMF were shifted towards an overrepresentation of freshly infiltrating Ly6C$^+$ MHC-II$^-$ MoMF and a relative decrease in mature, Ly6C$^-$ MHC-II$^+$ MoMF upon CXCL12 inhibition in the chronic CCl$_4$ model. We next sought to determine whether those observations were general or could be dependent on the injury model.

3.3 Characterization of the influence of CXCL12 inhibition on immune cells in MCD-diet-induced NASH

As the immunological landscape in NASH differs from toxic-induced metabolic liver diseases, the impact of CXCL12 inhibition on liver immune cells was also investigated in the MCD-diet induced NASH model. (38, 47)

3.3.1 Assessment of systemic effects of NOX-A12 during MCD-diet induced NASH

First, the impact of CXCL12 inhibition on blood leukocyte composition during MCD-diet induced NASH was explored. Upon NOX-A12 treatment, total leukocyte numbers were only marginally increased without reaching statistical significance (Figure 14 A). Absolute and relative numbers of neutrophils and monocytes were not altered. The relative numbers of eosinophils were reduced in the NOX-A12 treated group, however there was no significant change in the absolute numbers (Figure 14 B). Although the number of monocytes was unaffected, the amount of Ly6C$^+$ monocytes was strongly elevated after NOX-A12 treatment compared to the revNOX-A12 treated group (Figure 14 C, D). While the numbers of CD4$^+$ T cells, CD8$^+$ T cells and NK cells were not changed, there was a strong increase in both absolute and relative B cells in the blood of NOX-A12 treated animals (Figure 14 E). The analysis of a set of different inflammatory
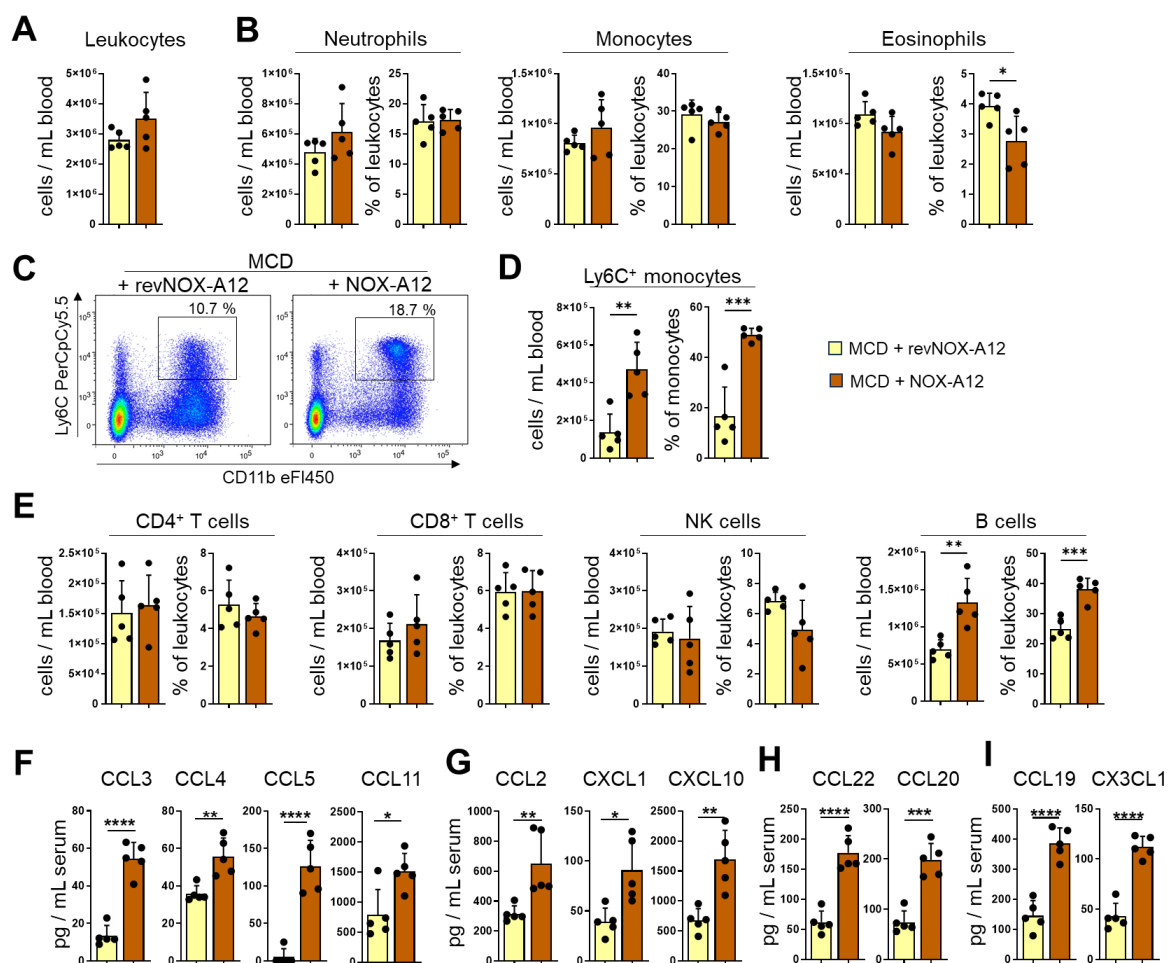
Figure 14: NOX-A12 affects immune cell composition and increases chemokines in the circulation during MCD-diet induced NASH. Leukocyte populations from the blood of mice fed with MCD and treated with revNOX-A12 or NOX-A12 were analysed by flow cytometry. **A)** Calculated number of total leukocytes per mL blood. **B)** Absolute (cells per mL blood) and relative numbers (percent of leukocytes) of neutrophils, monocytes, and eosinophils. **C)** Representative FACS plots of Ly6C$^+$ monocytes. **D)** Calculation of Ly6C$^+$ monocytes. Absolute numbers and proportion of monocytes. **E)** Absolute and relative numbers of CD4$^+$ and CD8$^+$ T cells, NK cells and B cells. **F-G)** Serum chemokine levels were measured using a multiplex protein microarray. Serum levels (pg/mL) of inflammatory chemokines with (F) redundant receptor affinities or (G) currently known to bind to individual receptor affinities. **H)** Serum levels of chemokines involved in homeostatic and inflammatory processes. **I)** Serum levels of homeostatic chemokines. and inflammatory processes. **I)** Serum levels of homeostatic chemokines. Error bars represent mean +/- S.D. Unpaired Student´s t-test was conducted. *p<0.05; **p< 0.01; ***p< 0.005; ****p< 0.0001.

and homeostatic chemokines in the serum revealed a global upregulation of all tested chemokines upon NOX-A12 treatment (Figure 14 F-I), with a particularly pronounced effect on the inflammatory chemokines CCL3 and CCL5 (Figure 14 F), as well as on the dual chemokines CCL20 and CCL22 (Figure 14 H) and the homeostatic chemokines CCL19 and CX3CL1 (Figure 14 I). Overall, NOX-A12 treatment changed circulating blood immune cell composition and chemokine concentrations, which could either reflect or drive local immune changes in the liver.

3.3.2 Examination of the influence of CXCL12 inhibition on hepatic immune cells in MCD-diet induced NASH

In parallel, immune cells were isolated from livers of MCD-diet fed mice that had received either revNOX-A12 or NOX-A12 and analyzed by flow cytometry. Treatment with NOX-A12 caused only minor changes in lymphoid immune cell populations. The absolute number of B cells was reduced without significance (p = 0.0549) in NOX-A12 treated animals, while there was no clear difference in the relative numbers. The relative number of NKT cells, on the other hand, was slightly increased, while there was no difference in the absolute numbers (Figure 15 A). Although not increased in number, NK cells and CD8$^+$ T cells from NOX-A12 treated mice showed an increased positivity for the cytotoxicity marker CD107a in the MCD model. Surface CD107a was slightly but not significantly (p = 0.0750, unpaired Student´s t-test) elevated on NK
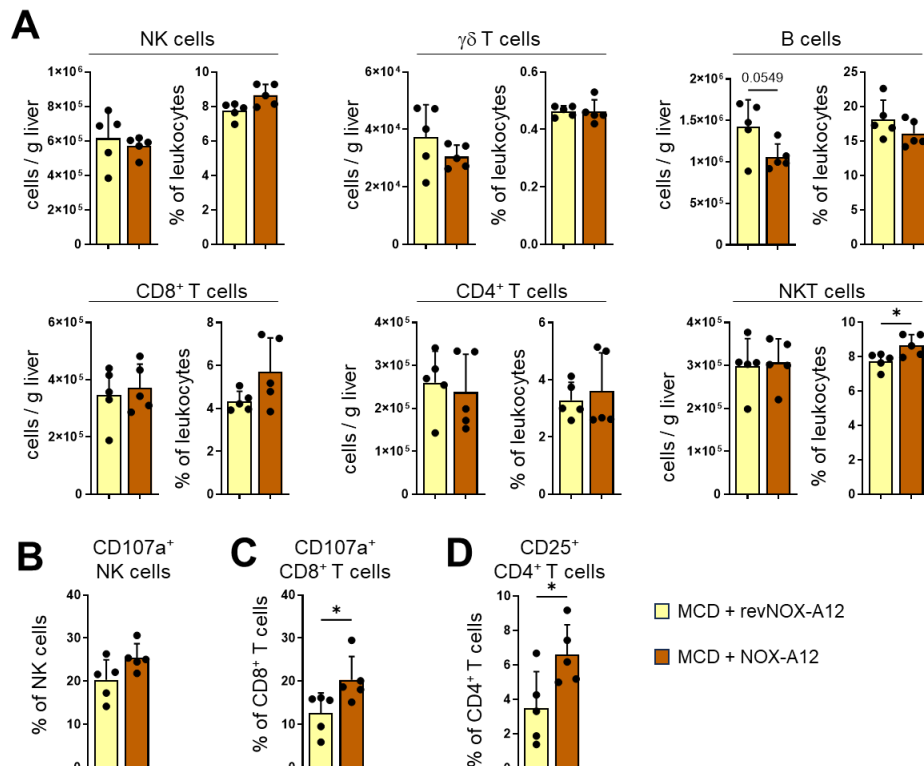
Figure 15: NOX-A12 has moderate effects on hepatic lymphoid cells in MCD-diet induced NASH. Lymphoid liver immune cells from MCD-fed mice treated with NOX-A12 or revNOX-A12, were assessed by flow cytometry. **A)** Absolute (cell counts per gram liver tissue) and relative (percent of leukocytes) numbers of different lymphoid immune cell populations. **B-C)** Surface CD107a on NK cells (B) and CD8$^+$ T cells (C) was analyzed. **D)** CD25 expression on CD4+ T cells was assessed. Error bars represent mean +/- S.D. Unpaired Student´s t-test was conducted. *p<0.05; **p< 0.01; ***p< 0.005; ****p< 0.0001.

cells and significantly increased on CD8+ T cells compared to cells from revNOX-A12 treated mice (Figure 15 B, C). Moreover, there was a small, yet significant rise in CD25+ cells within CD4+ T cells following NOX-A12 treatment (Figure 15 D).

The accumulation of infiltrating myeloid cells, neutrophils and dendritic cells induced by MCD diet, was not affected by NOX-A12 treatment, neither was the number of Kupffer cells (Figure 16 A, B). The localization of Kupffer cells and MoMF assessed by IF staining of CLEC4F and IBA1, showed an accumulation of large aggregates of MoMF distributed in the tissue, however there were no obvious differences between the treatment groups (Figure 16 C).
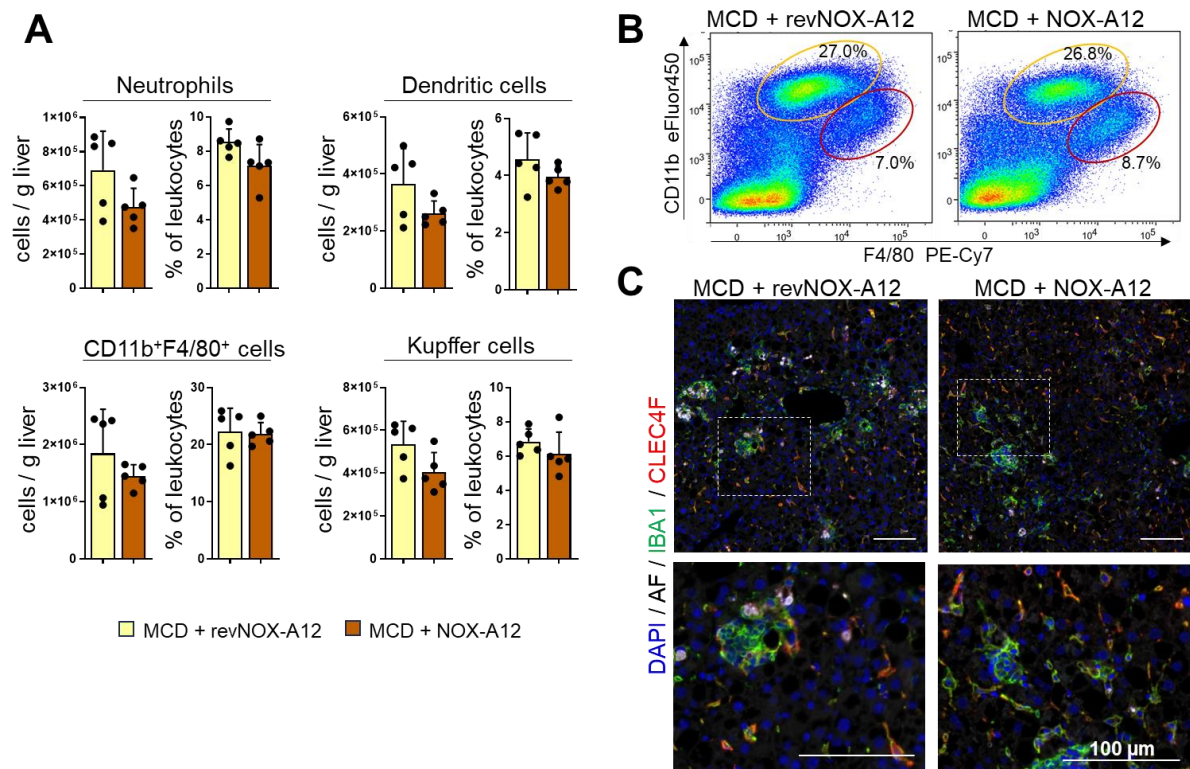
Figure 16: NOX-A12 does not influence major myeloid immune cell populations in MCD-diet induced NASH. Myeloid hepatic immune cells from MCD diet-fed mice treated with revNOX-A12 or NOX-A12 were analysed by flow cytometry. **A)** Absolute counts (cells per g liver tissue) and relative proportions (percent of leukocytes) of CD11b+F4/80+ cells, Kupffer cells, neutrophils and dendritic cells. **B)** Representative FACS plots of CD11b+F4/80+ (yellow outline) and Kupffer cells (red outline). **C)** Representative pictures of immunofluorescence staining of MoMF (IBA1+/CLEC4F-) and Kupffer cells (IBA1+/CLEC4F+) on liver tissue. Autofluorescence (AF) signal was used to visualize the liver structure. Error bars represent mean +/- S.D. Unpaired Student´s t-test was performed. *p<0.05; **p< 0.01; ***p< 0.005; ****p< 0.0001.

Eosinophils comprised only a minor fraction of the CD11b+F4/80+ cells (Figure 17 A). While the proportion of eosinophils in the CD11b+F4/80+ gate was not significantly changed, the absolute number of eosinophils was significantly decreased after NOX-A12 treatment. Although the relative numbers of eosinophils did not differ significantly, there was a strong trend (p= 0.0564) towards a reduction in the NOX-A12 treated group. The number of MoMF was unchanged (Figure 17 B). Also, the expression of pro-inflammatory and anti-inflammatory markers of MoMF was unchanged upon CXCL12 inhibition (Figure 17 C, D).

In addition, changes in the Kupffer cell pool were evaluated by flow cytometry. In response to CXCL12 inhibition, there was a slight increase in CD206$^+$ Kupffer cells. Since markers such as PD-L1, MHC-II and CD80 are expressed on normal Kupffer cells, mean fluorescence intensity (MFI) was measured to identify changes in the expression levels. The overall amount of PD-L1, MHC-II and CD80 positive Kupffer cells was not statistically changed, however, there was a slight increase in the MFI of PD-L1 (p = 0.0516) and CD80 (Figure 17 E).
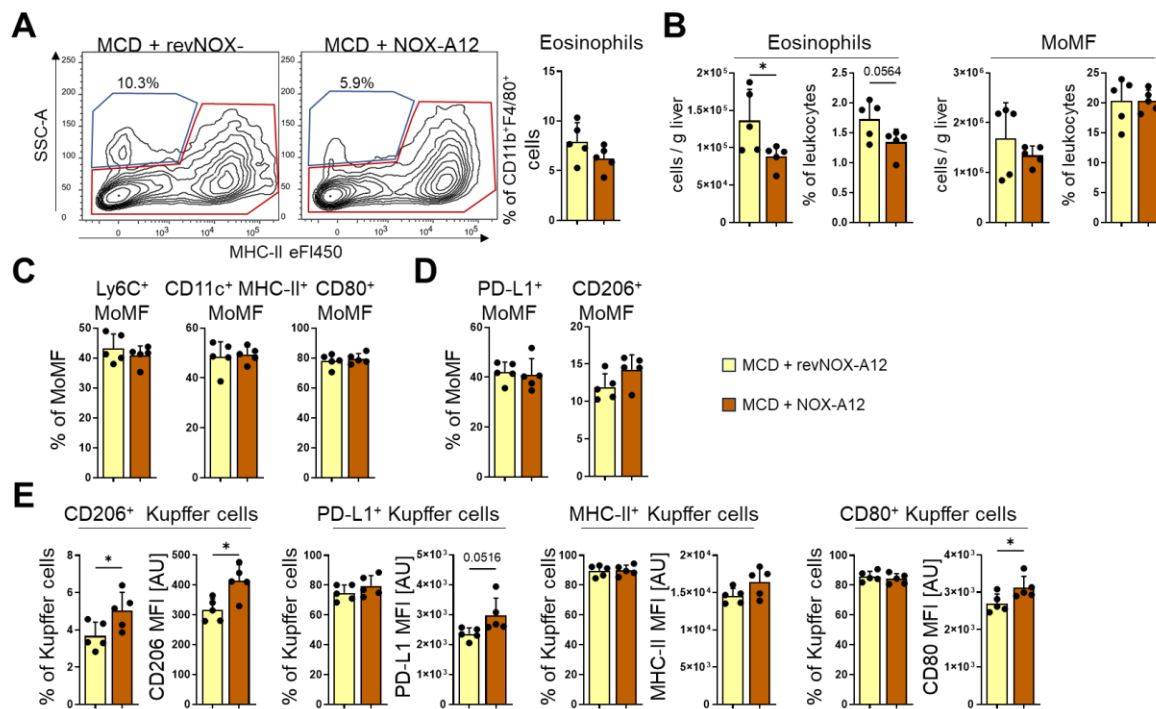
Figure 17: NOX-A12 moderately affects hepatic macrophage activation in MCD-diet induced NASH. MoMF and Kupffer cells isolated from livers of MCD-fed mice treated with NOX-A12 or revNOX-A12 were analyzed by flow cytometry. **A**) Proportion of eosinophils (blue outline) within the CD11b$^+$F4/80$^+$ gate, representative images and quantification. The remaining MoMF (red outline) were further analyzed. **B**) Absolute (cells per gram liver tissue) and relative numbers (percent of leukocytes) of eosinophils and MoMF. **C**) Proportions of MoMF positive for Ly6C, CD11c and MHC-II, and CD80. **D**) Percentage of PD-L1 and CD206 expressing MoMF. **E**) Mean fluorescence intensity (MFI) of CD206 and PD-L1, , MHC-II and CD80 on Kupffer cells. Error bars represent mean +/- S.D. Unpaired Student´s t-test was performed. *p<0.05; **p< 0.01; ***p< 0.005; ****p< 0.0001.

MoMF subpopulations distinguished by their expression of Ly6C and MHC-II were further analyzed. Although the expression profiles of F4/80, CD11c, CD206 and PD-L1 largely resembled the expression profiles of these subsets in CCl$_4$ treated animals, the Ly6C$^+$MHC-II$^+$ MoMF were markedly expanded during MCD-diet and displayed an increased expression of CD11c (Figure 18 A, B). Treatment with NOX-A12 did not alter the absolute numbers or proportions of any macrophage subpopulation (Figure 18 B).
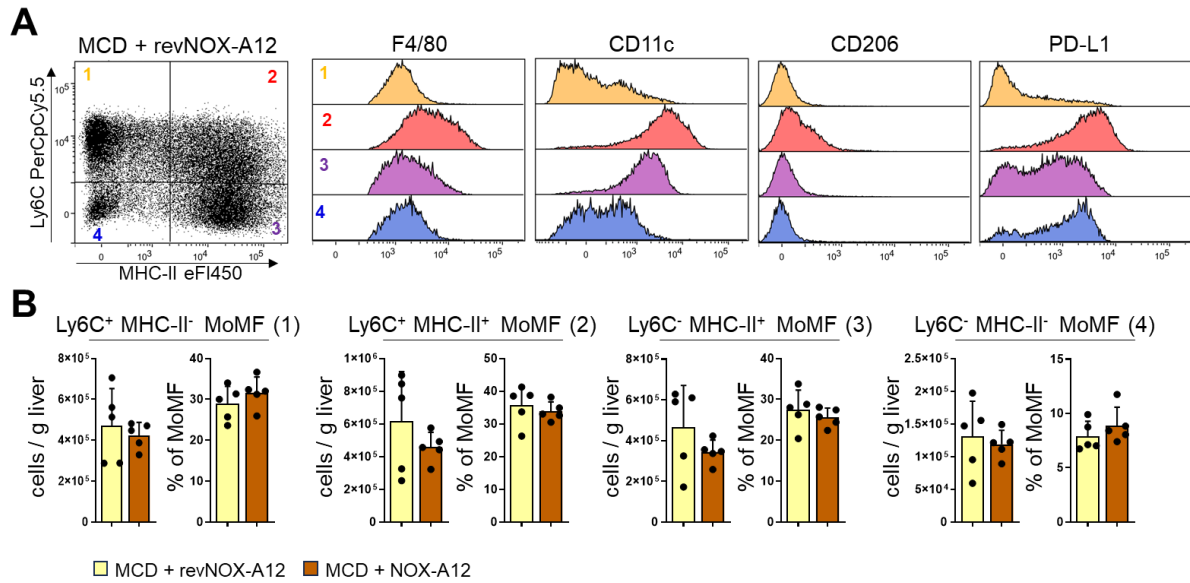
Figure 18: NOX-A12 does not impact influence macrophage infiltration in MCD-diet induced NASH. MoMF from mice treated with MCD and either revNOX-A12 or NOX-A12 were further analyzed based on their expression of Ly6C and MHC-II. **A)** Gating of MoMF subpopulations, and representative histograms of different macrophage activation markers on each subpopulation. **B)** Absolute number (cells per gram liver tissue) and relative amount (percent of MoMF) of the indicated MoMF subpopulation. Error bars represent mean +/- S.D. Unpaired Student´s t-test was performed. *p<0.05; **p< 0.01; ***p< 0.005; ****p< 0.0001.

3.4 Examination of the impact of CXCL12 inhibition on liver recovery after CCl_4-induced chronic liver inflammation.

As the CXCL12 chemokine axis is a critical regulator of liver regeneration, the impact of CXCL12 inhibition on early recovery from chronic liver inflammation and fibrosis was investigated using chronic CCl_4-induced liver injury as prototypical model. Eight-week-old mice were subjected to biweekly CCl_4 injections for eight weeks and were sacrificed 96 h after the last CCl_4 injection to allow the liver to terminate the inflammation and start regeneration. NOX-A12 or revNOX-A12 were administered three times per week during the whole period of CCl_4 injections with the last injection taking place one day before the mice were analyzed (Figure 19 A). Untreated, age- and sex-matched animals served as control.

3.4.1 Investigation of the influence of NOX-A12 on recovery from chronic CCl_4-induced injury

H/E staining of liver tissue showed that immune cell infiltrates were still present in the liver 96 h after the last CCl_4 dose, both in revNOX-A12 and NOX-A12 treated animals (Figure 19 B). While serum ALT levels were close to baseline levels, GLDH was significantly increased in the group that received NOX-A12 (Figure 19 C). The cell count of leukocytes per gram liver tissue was evaluated by flow cytometry. While the number of leukocytes was only slightly increased in mice that received the non-functional revNOX-A12, leukocytes were significantly elevated in response to CXCL12 inhibition (Figure 19 D). Liver fibrosis was assessed by Sirius red staining and hydroxyproline measurement. Four days after the last injury, severe liver fibrosis remained, which was unaltered by CXCL12 inhibition (Figure 19 E, F). Desmin and αSMA

immunofluorescence staining was performed on liver sections. Both desmin and αSMA were increased on recovering livers compared to healthy liver, however the analysis of the desmin or αSMA positive area did not reveal significant differences between treatment with NOX-A12 or revNOX-A12 (Figure 19 G). The expression of several genes associated with fibrogenesis (i.e., *Acta2, Col1a1, Timp1, Timp2*) and fibrosis resolution (*Mmp2, Mmp9*) was performed on liver tissue lysates. The mRNA levels of all analyzed genes
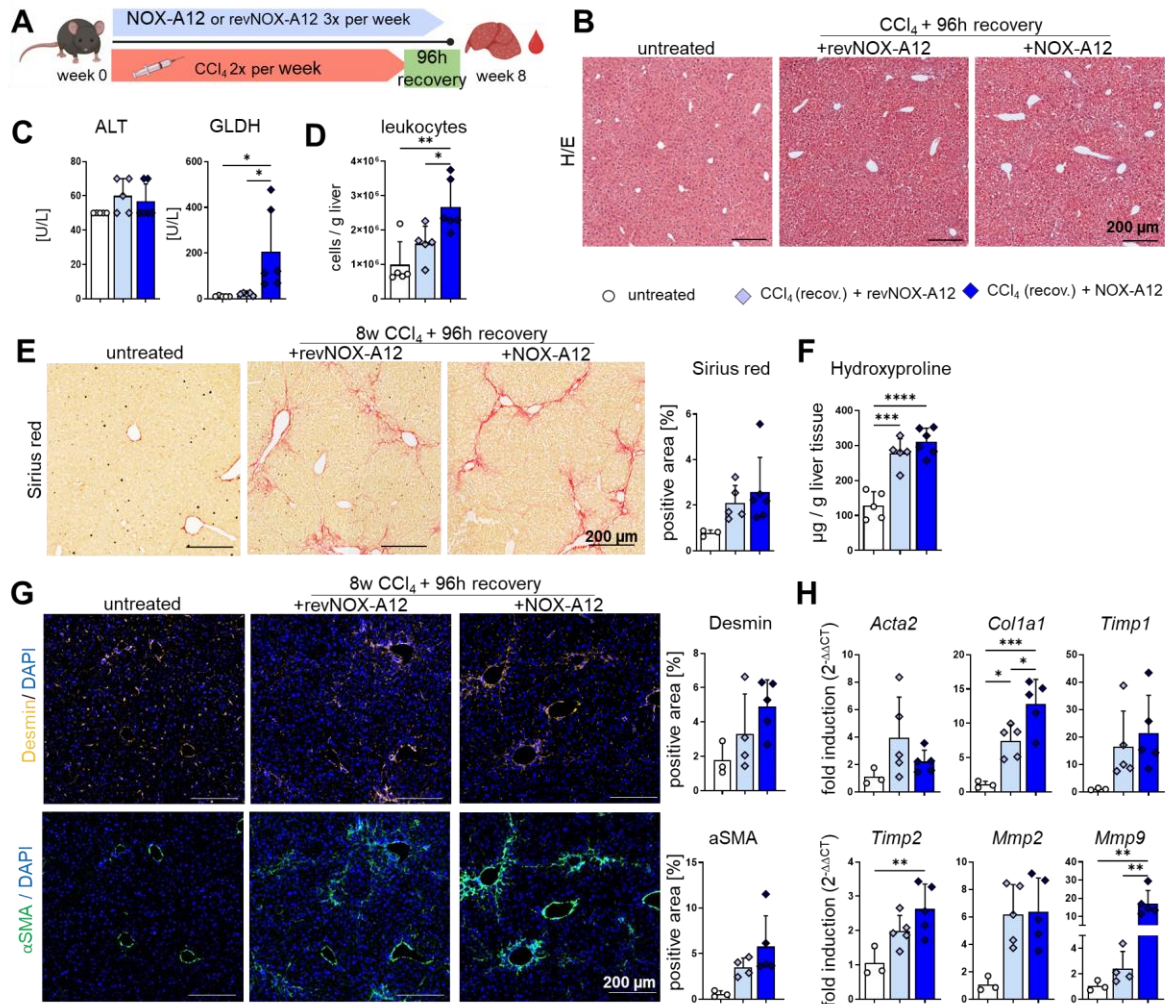
Figure 19: Investigation of the influence of NOX-A12 on recovery from chronic CCl₄ injury. A) Mice were treated with CCl₄ twice a week for eight weeks and allowed to recover for 96 h. NOX-A12 or revNOX-A12 was administered three times per week throughout the time course, with the last injection one day prior to analysis. Healthy, untreated mice served as controls. **B**) H/E staining on representative liver sections. **C**) Serum levels of ALT and GLDH. **D**) The number of leukocytes in the liver was evaluated by flow cytometry. **E**) Sirius red staining was performed on liver sections. Representative images and quantification of the Sirius red positive area. **F**) Hydroxyproline content of liver tissue was measured. **G**) Immunofluorescence staining of desmin and αSMA, representative images and quantification of the desmin and αSMA positive area. **D**) QPCR of fibrogenesis-related and fibrosis resolution-associated genes was performed on liver homogenates. Housekeeping genes: *18S rRNA + B2m.* Error bars represent mean +/- S.D. One-way ANOVA followed by Tukey's multiple comparison test was conducted. *$p < 0.05$; **$p < 0.01$; ***$p < 0.005$; ****$p < 0.0001$.

were still increased during early recovery after chronic liver fibrosis. However, upon CXCL12 inhibition both *Col1a1* and *Mmp9* were significantly upregulated compared to the revNOX-A12 treated group (Figure 19 H).

3.4.2 Characterization of the impact of NOX-A12 on immune cell composition during recovery

Next, the composition of the liver immune cells during recovery from chronic liver injury in NOX-A12 and revNOX-A12 treated mice was explored by flow cytometry. The absolute numbers of B cells, CD4$^+$ T cells, and CD8$^+$ T cells were significantly increased after NOX-A12. There was also a trend toward increased absolute numbers of NKT cells. The relative numbers, however, were unchanged or decreased as in the case of NK cells (Figure 20 A). While the number of Kupffer cells was unaffected by NOX-A12, the absolute and relative number of neutrophils and MoMF was significantly enhanced. Eosinophils were increased in absolute cell counts; however, the relative numbers were not changed compared to the revNOX-A12 treated group (Figure 20 B).
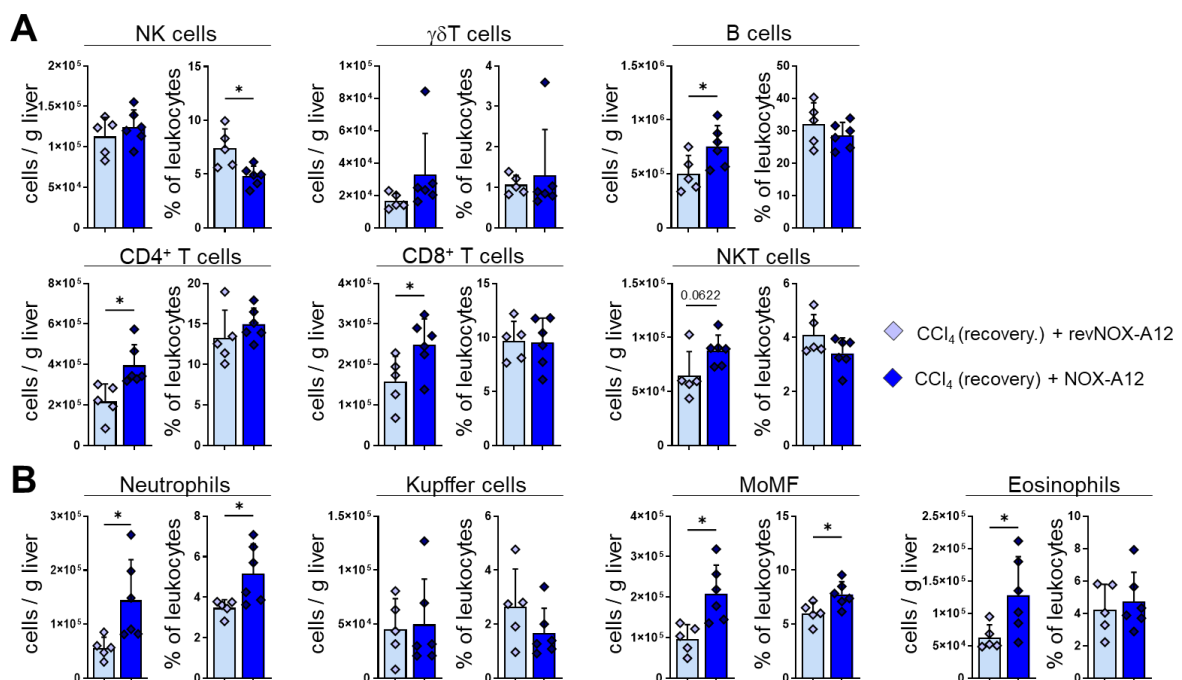
Figure 20: NOX-A12 increases immune cells during recovery from chronic CCl$_4$ injury. Hepatic immune cell populations were isolated from mice recovering from chronic CCl$_4$ induced liver inflammation, treated with NOX-A12 or revNOX-A12, and analysed by flow cytometry. **A**) Absolute (cells per gram liver tissue) and relative (percent of leukocytes) numbers of lymphoid immune cell populations. **B**) Absolute and relative numbers of myeloid immune cell populations. Error bars represent mean +/- S.D. Unpaired Student´s t-test was performed. *p<0.05; **p< 0.01; ***p< 0.005; ****p< 0.0001.

3.4.3 NOX-A12 influences liver regeneration after chronic liver injury.

To investigate the impact of NOX-A12 on regeneration and compensatory proliferation from chronic liver injury, IHC staining of Ki67 was performed on liver sections from each treatment group. The number of Ki67$^+$ hepatocytes was counted semi-automatically. 96 h after the last insult, the number of proliferating hepatocytes in the revNOX-A12 treated group was back on the level of a healthy liver, while there was still a high number of Ki67$^+$ hepatocytes present in the liver of mice that were treated with NOX-A12 (Figure 21

A). Gene expression analysis performed on liver lysates also showed a clear and strong upregulation of *Mki67*, the gene encoding Ki67, after NOX-A12 treatment (Figure 21 B). In contrast, 48 h after the last CCl_4 injection following chronic injury, the number of proliferating hepatocytes was not significantly different between revNOX-A12 and NOX-A12 treated animals as assessed by IHC staining for Ki67 (Figure 21 C), which was also reflected by *Mki67* gene expression in liver tissue (Figure 21 D). The number of Ki67 hepatocytes and the expression of *Mki67* in total liver tissue were also not altered by NOX-A12 in MCD diet-induced NASH (Figure 21 E, F).
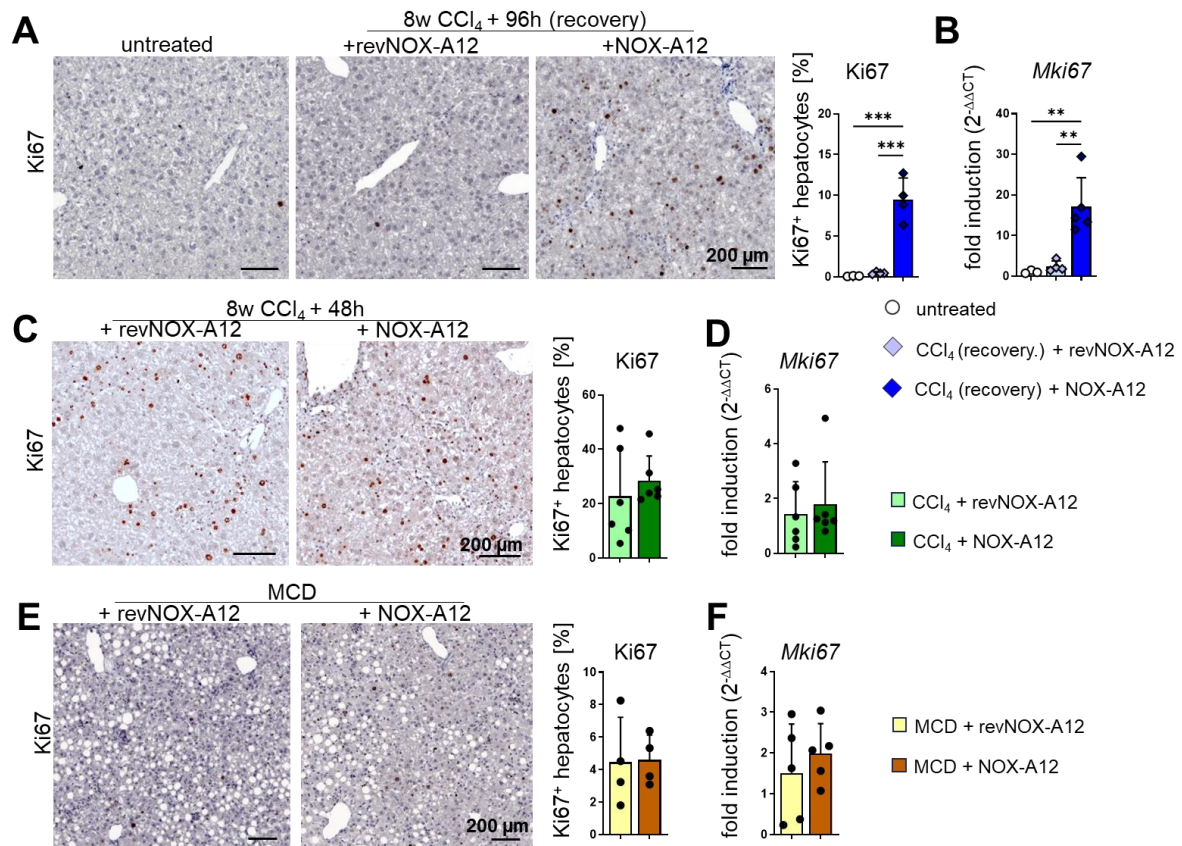
Figure 21: NOX-A12 increases hepatocyte proliferation during recovery from chronic CCl_4 induced liver injury. **A**) IHC staining of Ki67 on liver sections. Mice were subjected to eight weeks of repetitive CCl_4 injections while treated with NOX-A12 or revNOX-A12, followed by a recovery phase of 96 h. Untreated, healthy animals served as controls. Representative pictures and quantification of Ki67+ hepatocytes. **B**) QPCR analysis of Ki67 expression in liver tissue lysates. **C**) Ki67 IHC staining on liver tissue from mice that were subjected to eight weeks CCl_4 and treated with revNOX-A12 or NOX-A12 and euthanized 48 h after the last CCl_4 injection. Representative pictures and quantification of Ki67+ hepatocytes. **D**) *Mki67* expression in liver tissue lysates was analyzed by qPCR. **E**) IHC staining of Ki67 was performed on liver sections from MCD-diet fed mice that were treated with revNOX-A12 or NOX-A12. Representative images and quantification of Ki67+ hepatocytes. **F**) *Mki67* expression in total liver tissue was explored by qPCR. Housekeeping genes: *18S rRNA + B2m*. Error bars represent mean +/- S.D. One-way ANOVA followed by Tukey's multiple comparison test was conducted for A, B. Unpaired Student´s t-test was performed for C-E. *p<0.05; **p< 0.01; ***p< 0.005; ****p< 0.0001.

3.5 Investigation of the impact of CXCL12 inhibition on liver tumor growth.

3.5.1 Evaluating two different models of DEN-induced chronic inflammation-driven liver cancer.

A large body of evidence suggests that the CXCL12 axis promotes the development and progression of HCC. Therefore, the impact of CXCL12 inhibition on hepatocellular primary liver cancer was investigated using a model of DEN-induced liver tumors.

Firstly, the influence of a high fat and high cholesterol diet (Western diet, WD) on DEN-induced liver tumor growth was evaluated and compared to DEN alone and to DEN in combination with chronic CCl_4 injections. Male mice were injected with a single dose of DEN at an age of 14 days. At an age of 8 weeks, mice were put on a WD diet, or subjected to biweekly injections with 0.5 mL/kg CCl_4 for 16 weeks or left on normal diet (ND) without any further interventions and then sacrificed for further analysis (Figure 22 A). While DEN without any further injury only induced very few, small tumor lesions, 16 weeks of CCl_4 treatment resulted in a massive outgrowth of large tumor nodules. WD fed mice, on the other hand, exhibited more tumor nodules than mice on ND, however, these tumors were much smaller and fewer than in the CCl_4 treated group (Figure 22 B). The liver to body weight ratio (LBR) is often used as an indicator of tumor load. However, while the LBR was significantly increased upon WD and CCl_4 treatment in comparison to the group that received DEN only, it did not reflect the large differences in tumor size and number between WD and CCl_4 treated livers (Figure 22 C). Immune cell infiltration into the liver indicative of inflammation was assessed by flow cytometry. While the number of leukocytes was elevated in both the DEN + WD and the DEN + CCl_4 model compared to DEN + ND, there was only a slight and not significant increase in leukocyte numbers upon chronic CCl_4 injury compared to WD (Figure 22 D).
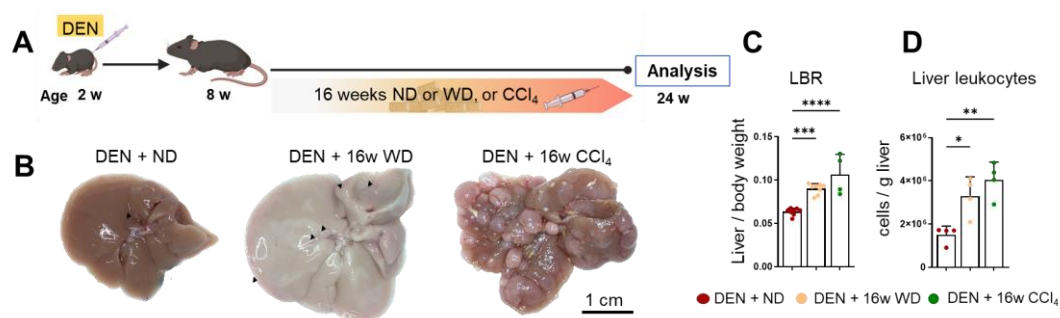
Figure 22: DEN-induced tumor growth is accelerated by chronic liver inflammation. A) Experimental setup. 14 days-old mice were injected with diethylnitrosamine (DEN) and at an age of 8 weeks, were either left on normal diet (ND) without any further treatment, fed a Western diet (WD), or subjected to biweekly injections with CCl_4 for 16 weeks. **B)** Representative images of tumor bearing livers following the indicated treatment, arrows indicate small tumor lesions. **C)** Liver to body weight ratio (LBR). **D)** The number of leukocytes per gram liver tissue was assessed by flow cytometry. Error bars represent mean+/- SD. One-way ANOVA, followed by Tukey´s multiple comparison test was performed. *p<0.05; **p< 0.01; ***p< 0.005; ****p< 0.0001.

3.5.2 Assessment of the influence of NOX-A12 on DEN-induced liver tumor growth

To investigate the impact of CXCL12 inhibition on tumor growth in a fibrotic/cirrhotic environment the DEN + CCl_4 model was employed. As this model caused very large tumors after 16 weeks of CCl_4 treatment, a group of mice was treated for ten weeks with biweekly injections of CCl_4 together with NOX-A12 or revNOX-A12 three times per week, to be able to assess early to intermediate stages of tumor growth (Figure 23 A). After ten weeks CCl_4 treatment liver tumors were clearly detectable, without overgrowing the whole liver (Figure 23 B). Mice treated with NOX-A12 developed larger tumors, as indicated by increased LBR and more tumor nodules larger than 1 mm. To reduce variability due to differences in liver size, tumor burden was determined as the cumulative tumor diameter of all macroscopically visible tumors normalized to liver weight. Tumor burden was also increased in animals treated with NOX-A12 (Figure 23 C). Next, the impact of NOX-A12 on advanced tumors was explored in DEN-treated mice that were subjected to 16 weeks of repetitive CCl_4 injections combined with NOX-A12 or revNOX-A12 (Figure 23 D).
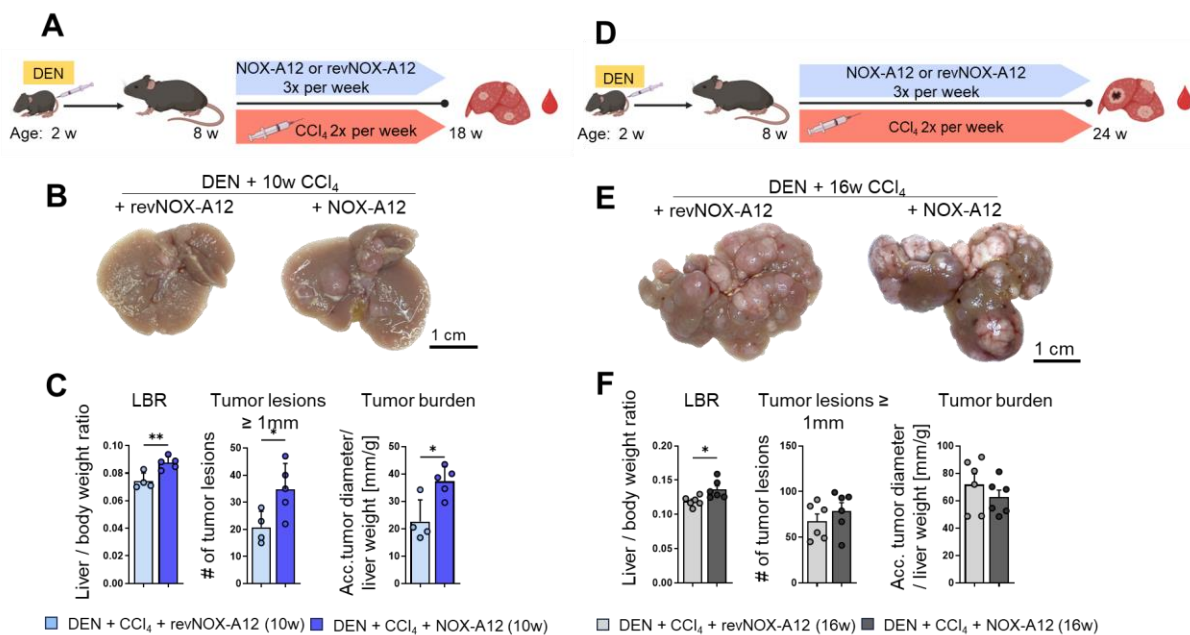
Figure 23: CXCL12 inhibition with NOX-A12 promotes liver tumor growth in a DEN + CCl_4-induced fibrosis-associated tumor model. The impact of CXCL12 inhibition on tumor development was studied in early and advanced fibrosis/cirrhosis-associated tumors. **A)** Schematic representation of the experimental setup for early tumor development. Fourteen days-old male mice were injected with a single dose of DEN and then subjected to biweekly CCl_4 injections for ten weeks, starting at week eight. NOX-A12 or revNOX-A12 was administered three times per week during the entire period of CCl_4 injections. **B)** Representative macroscopic images of tumor-bearing livers after the indicated treatment. **C)** Tumor growth was assessed by liver to body weight ratio (LBR), and the number of grossly visible tumor lesions ≥ 1mm diameter. Accumulated diameters of grossly visible tumors were evaluated and normalized to liver weight to determine tumor burden. **D)** Experimental setup for the investigation of advanced liver tumors. Mice were treated with DEN, CCl_4 and NOX-A12 or revNOX-A12 and subjected to 16 weeks of CCl_4 and revNOX-A12 or NOX-A12. **E)** Macroscopic pictures of representative tumor-bearing livers after 16 weeks of treatment with CCl_4 and revNOX-A12 or NOX-A12. **F)** LBR, number of tumor lesions ≥ 1mm diameter, and tumor burden were analyzed. Error bars represent mean +/- S.D. Unpaired Student´s t-test was performed. *$p<0.05$; **$p< 0.01$; ***$p< 0.005$; ****$p< 0.0001$.

This treatment regimen resulted in many big tumors covering large portions of the liver surface (Figure 23 E). However, while the LBR of NOX-A12 treated animals was higher than the LBR of revNOX-A12 treated mice, no difference could be detected in the numbers of tumors larger than 1 mm or the tumor burden (Figure 23F). Next, the effect of CXCL12 inhibition by NOX-A12 on carcinogenesis was investigated in NAFLD/NASH associated liver tumors. Two-week-old mice received a single dose of DEN and were fed WD from the age of 8 weeks and for 16 weeks. NOX-A12 or revNOX-A12 was administered three times per week while feeding the diet (Figure 24 A). As NOX-A12 and revNOX-A12 are dissolved and administered in glucose, another group treated with DEN + WD served as a control to detect effects of the vehicle on tumor growth. While there were only a few small tumors in both the DEN + WD and DEN + WD + revNOX-A12 groups, NOX-A12 induced a strong increase in tumor growth (Figure 24 B). This was also reflected in the analysis of the tumor load. There were no significant changes in LBR, tumor number and tumor burden between DEN-treated mice that received WD and revNOX-A12 and mice that only had been fed WD, while the tumor burden and counts of visible tumors were clearly increased upon NOX-A12 treatment. The LBR was significantly increased compared to DEN + WD group but did not reach statistical significance compared to the revNOX-A12-treated group (p=0.0757) (Figure 24 C). To further investigate if CXCL12 inhibition rather
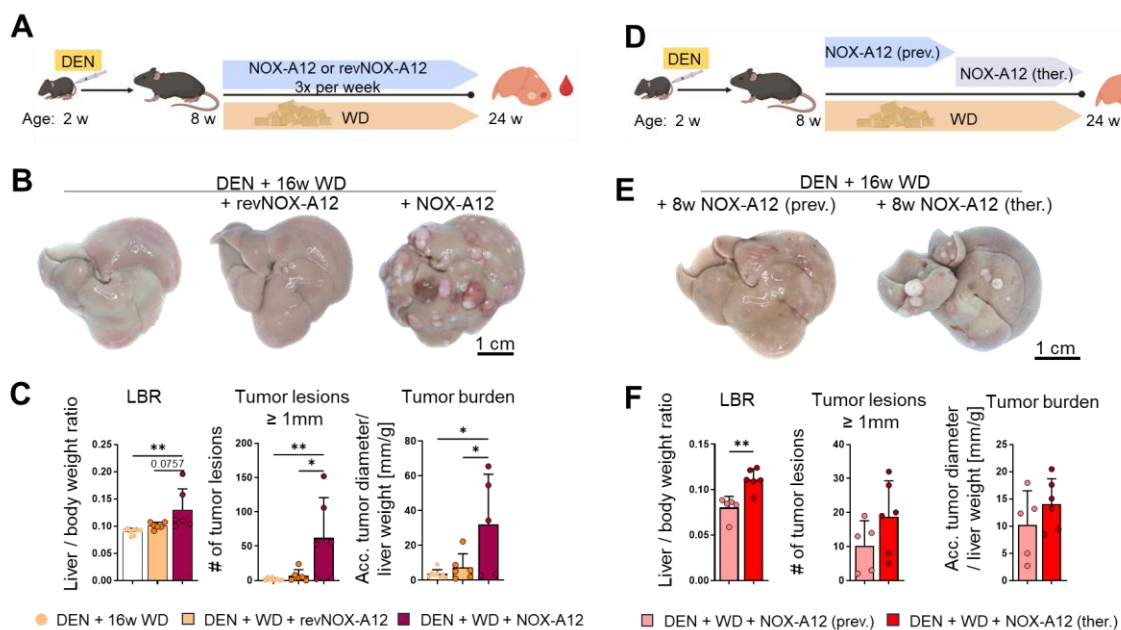
Figure 24: CXCL12 inhibition with NOX-A12 accelerates tumor growth in WD-induced NAFLD. A) Experimental setup. Mice were treated with DEN at an age of two weeks and put on a Western diet (WD) for 16 weeks starting at an age of 8 weeks. NOX-A12 or revNOX-A12 was administered 3x per week from week 8 -16. Mice that were subjected to DEN + 16 weeks WD served as a control. **B**) Macroscopic images of representative tumor bearing livers. **C**) Tumor growth was assessed by liver to body weight ratio (LBR) and number of grossly visible tumor lesions larger than 1 mm. The accumulated diameters of grossly visible tumors were normalized to the liver weight to assess the tumor burden. **D**) Mice were treated with DEN and put on a Western diet for 16 weeks. NOX-A12 was either administered preventively (prev.) during either the first eight weeks of diet or therapeutically (ther.) during the last eight weeks of diet. Mice were sacrificed after 16 weeks. **E**) Macroscopic pictures of representative tumor bearing livers subjected to the indicated treatments. **F**) LBR, number of tumor lesions larger than 1 mm, and calculated tumor burden of mice treated with DEN + WD and NOX-A12 preventively or therapeutically. Error bars

represent mean +/- S.D. One-way ANOVA followed by Tukey´s multiple comparison test (C), or unpaired Student´s t-test was performed (F). *p<0.05; **p< 0.01; ***p< 0.005; ****p< 0.0001.

impacts tumor growth during early onset of tumor development or during tumor promotion in established tumors, mice were subjected to DEN + 16 weeks of WD and treated with NOX-A12 during the first 8 weeks (preventively) or during the last 8 weeks (therapeutically) of WD (Figure 24 D). Although there was no statistically significant difference in the number of tumor lesions that reached 1 mm or more in diameter or tumor burden, there was a slight trend toward an increase in the therapeutic treatment group, which also had a significantly increased LBR in comparison to the preventive treatment group (Figure 24 E, F).

3.5.3 Combination therapy with anti-PD-1 does not rescue the NOX-A12 induced phenotype

Although CXCL12 inhibition alone promoted tumor growth instead of showing anti-tumor effects, checkpoint inhibitors had been shown to be more effective in combination with CXCL12 inhibition. (165, 182, 183) Therefore, to test in a small pilot study whether PD-1 blockade could reverse the tumor-promoting effect observed with NOX-A12 alone, or whether PD-1 effects could be strengthened by NOX-A12, n=4 mice per group were subjected to DEN followed by 16 weeks of WD and treated therapeutically (i.e., the last eight weeks of the WD diet) with an anti-PD-1 antibody, in combination with NOX-A12. Control mice were treated with either an unspecific isotype antibody (n=3) or with the isotype together with NOX-A12 (n=4) (Figure 25 A). The anti-PD-1-treated group did not differ significantly from the isotype group, while NOX-A12 increased the LBR of both isotype and anti-PD-1-treated animals. The number of tumors and tumor burden were also increased in the NOX-A12 treated groups but did not reach statistical
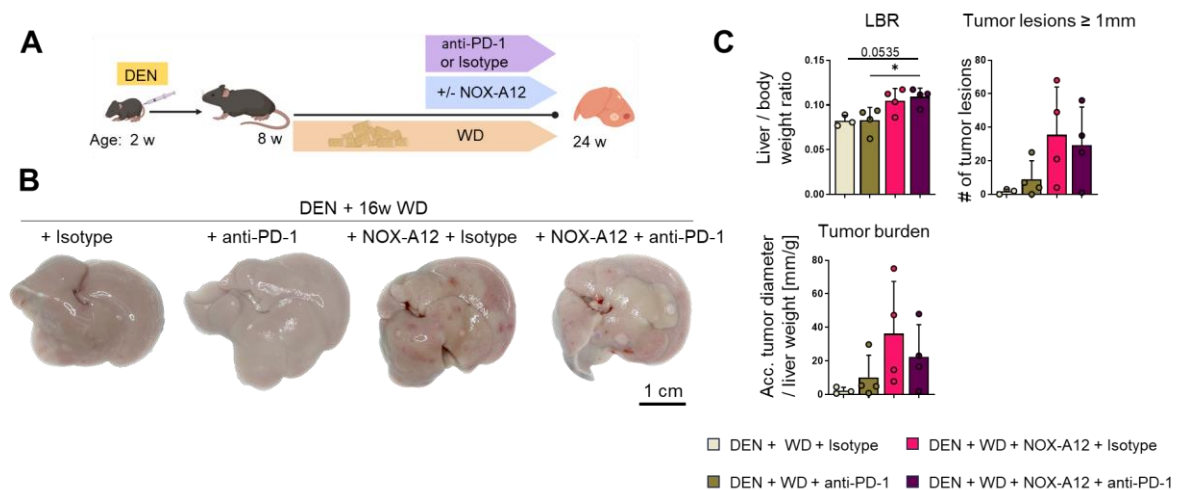
Figure 25: Combination therapy of NOX-A12 and anti-PD-1 does not rescue the NOX-A12 induced phenotype in the DEN + WD tumor model. A) Experimental setup: 14 days-old mice received a single dose of DEN. At an age of 8 weeks, they were put on a Western diet (WD) for 16 weeks. After 8 weeks on WD, mice were given twice a week an anti-PD-1 antibody or an isotype control intraperitoneally, in combination with NOX-A12 subcutaneously three times per week, or without any further intervention. Mice were sacrificed at an age of 24 weeks and analyzed. **B**) Macroscopic pictures of representative tumor bearing livers subjected to the indicated treatments. **C**) Tumor growth was assessed by liver-to-body ratio (LBR), and the

number of tumor lesions with a size of 1 mm or more. Tumor burden (accumulated tumor diameter/liver weight) was analyzed. Error bars represent mean +/- S.D. One-way ANOVA followed by Tukey's multiple comparison test was performed. *p<0.05; **p< 0.01; ***p< 0.005; ****p< 0.0001.

significance (Figure 25 B, C). In both the anti-PD-1 and anti-PD-1 + NOX-A12-treated groups, one mouse developed visible fibrosis that was associated with increased tumor growth (data not shown). In the NOX-A12 + isotype group, two out of four mice had visible fibrosis together with an increased tumor load (Suppl. Figure 4 A).

3.6 Characterization of the effect of CXCL12 inhibition on the TME of fibrosis - associated HCC

3.6.1 Analysis of the systemic effects of NOX-A12 in mice with fibrosis associated HCC

In light of the observed influence of NOX-A12 on tumor growth, the next aim was to evaluate whether CXCL12 inhibition led to immune microenvironment changes that could explain the phenotype. Starting with the model of DEN + CCl_4 induced fibrotic/cirrhotic HCC, the systemic effect on blood immune cell populations during both intermediate (10 weeks CCl_4) and progredient stages of tumor development (16 weeks CCl_4) was assessed. For in-depth analysis of blood leukocytes by flow cytometry, the dendritic cells markers MHC-II and CD11c were included in the antibody panel. CD11b, frequently used as marker for myeloid cells, is not exclusively expressed on granulocytes, eosinophils, and monocytes, but can also be upregulated on B cells and NK cells. (184, 185) Therefore, an antibody against the M-CSF receptor (CD115) was added to the analysis to more robustly identify the monocyte population (Figure 26 A). Noteworthy, the total blood leukocytes were slightly but not significantly increased upon CXCL12 inhibition at both time points (Figure 26 B).

During early tumor growth (10 weeks CCl_4), neutrophils in the blood NOX-A12 treated mice showed a trend towards an increased absolute number, while during advanced tumor growth (16 weeks CCl_4), neutrophils were equally elevated in both treatment groups. The relative numbers of neutrophils revealed a significant increase in the proportion of neutrophils in the control group (revNOX-A12) with advanced tumors. The small population of dendritic cells did not show clear differences. Eosinophils, on the other hand, were increased upon NOX-A12 both during early and advanced tumor growth, however failed to reach statistical significance. The absolute and relative numbers of CD115^{+} monocytes on the other hand, showing a trend towards increased numbers after NOX-A12 in the early treatment group, were strongly elevated after 16 weeks of NOX-A12 treatment (Figure 26 C).
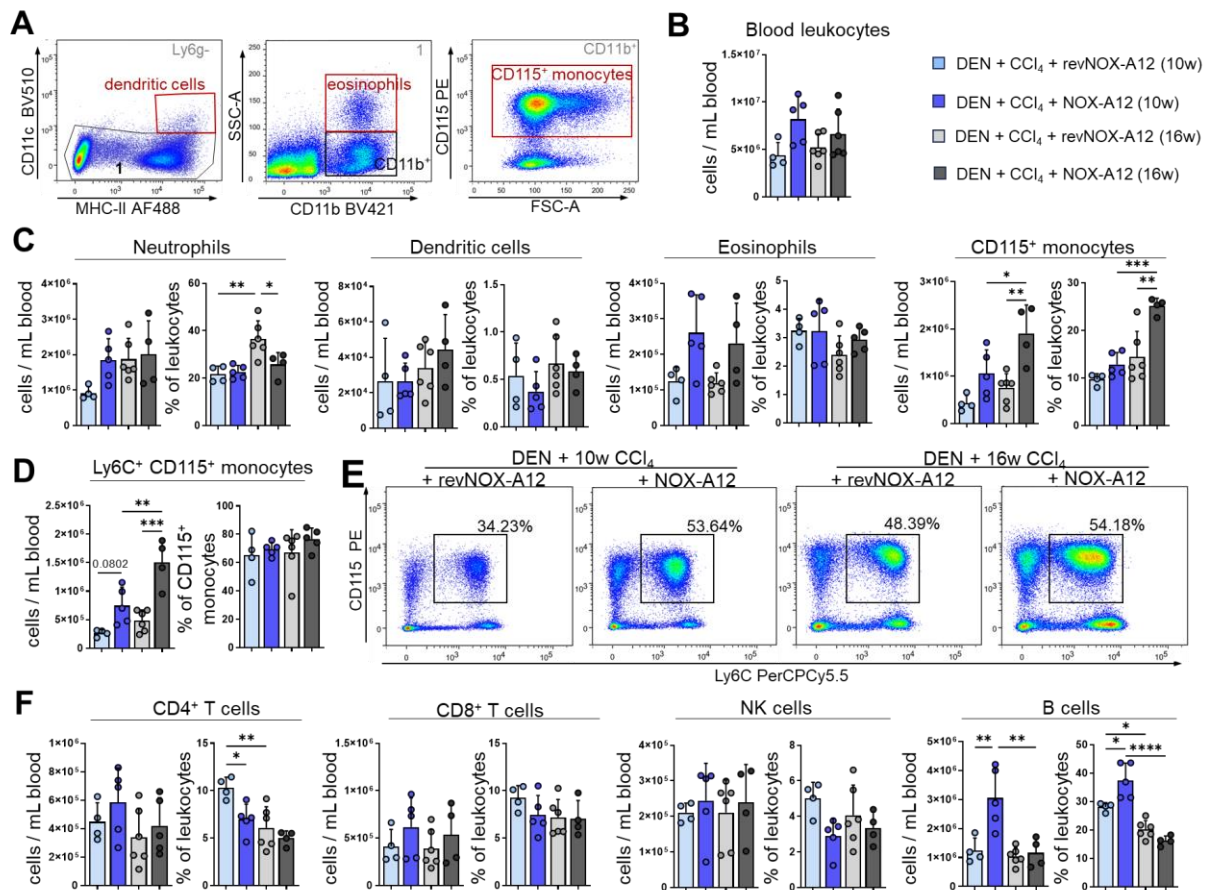
Figure 26: Influence of NOX-A12 on blood immune cells in the DEN + CCl₄ liver cancer model. Blood leukocytes from tumor bearing mice (DEN + 10 or 16 weeks CCl₄) treated with revNOX-A12 or NOX-A12, were analyzed by flow cytometry. **A)** Extended gating strategy to include dendritic cells in the analysis. An antibody against CD115 (CSF1R) was used to separate monocytes from other CD11b⁺ cells. **B)** Total number of leukocytes per mL of blood. **C)** Absolute numbers (cells per mL blood) and relative proportion (percent of leukocytes) of myeloid immune cell populations. **D)** Absolute and relative numbers of Ly6C⁺ monocytes. **E)** FACS plot showing CD115 and Ly6C expressing monocytes within the CD11b⁺ population. **F)** Absolute and relative numbers of lymphoid immune cells. Error bars represent mean +/- S.D. One-way ANOVA followed by Tukey' multiple comparison test was performed. *$p<0.05$; **$p< 0.01$; ***$p< 0.005$; ****$p< 0.0001$.

While the absolute number of Ly6C⁺ monocytes was increased upon CXCL12 inhibition, the proportion of Ly6C⁺ cells within the monocytes was unchanged between the different groups, indicating an increase of monocytes instead of a selective accumulation of a certain subpopulations (Figure 26 D). Using CD115 as an additional marker for monocytes revealed that within the CD11b⁺Ly6G⁻SSC^low monocyte population, only a proportion of cells expressed CD115, and a considerable population of CD115⁻ cells also expressed Ly6C (Figure 26 E). The absolute numbers of CD4⁺ and CD8⁺ T cells as well as NK cells in the blood were not affected by NOX-A12, nor by the tumor stage. Still, there was a significant decrease in the relative numbers of CD4⁺ T cells upon NOX-A12 treatment during the early time point and with increased tumor load. The number of B cells was increased upon CXCL12 inhibition, both in absolute and relative numbers after 10 weeks of CCl₄, while after 16 weeks of CCl₄ there was no difference between the revNOX-A12 and the NOX-A12 treated group (Figure 26 F). In addition, the serum levels of several chemokines were analyzed. The

concentrations of the inflammatory chemokines CCL3 and CCL5 were slightly, but not significantly, increased in the NOX-A12 treated group, but were not influenced by the increased tumor burden present at the late time point. CCL11 also showed a trend towards increased levels in the NOX-A12 treated groups. Although not significantly changed, serum levels of CCL4 were slightly elevated in animals with advanced tumors compared to groups with early tumors and significantly increased in NOX-A12 treated animals after 16 weeks of CCl_4 treatment (Figure 27 A). The serum concentration of CCL2 was raised by NOX-A12 treatment after both 10 weeks and 16 weeks of CCl_4. CXCL1, on the other hand, increased with disease progression but was unaffected by CXCL12 inhibition. Serum levels of CXCL10 showed a trend toward increased levels after 16 weeks compared to 10 weeks of CCl_4 treatment, although the changes were not significant (Figure 27 B). The homeostatic chemokines CCL19 and CX3CL1 as well as the dual chemokines CCL20 and CCL22 were upregulated following CXCL12 inhibition, but not affected by disease progression (Figure 27 C, D).
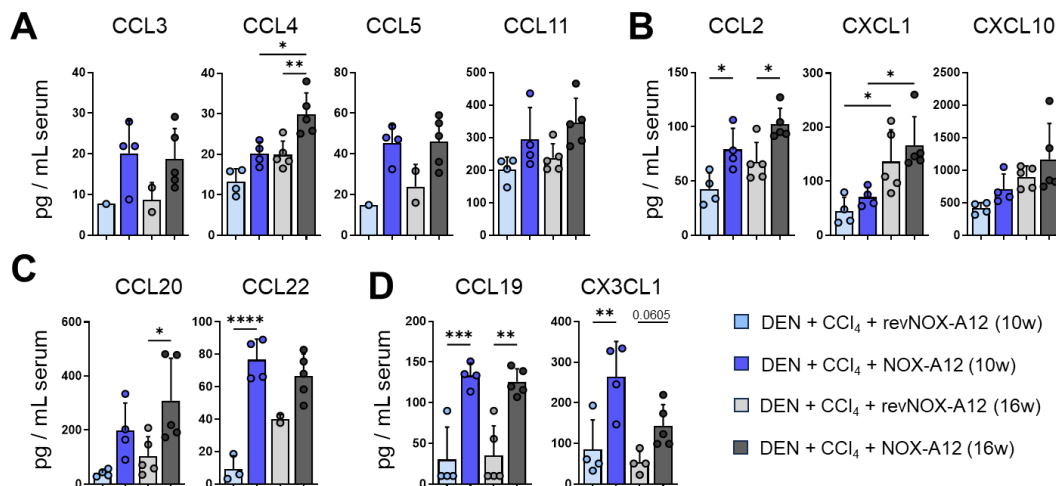
Figure 27: NOX-A12 increases serum chemokine levels in DEN + CCl_4 treated mice. Serum chemokines of tumor bearing mice, treated 10 weeks or 16 weeks with CCl_4 and NOX-A12 or revNOX-A12 were measured using a multiplex protein microarray. **A-B)** Serum levels (pg /mL serum) of inflammatory chemokines with affinity to several (A) or to single (B) chemokine receptors. **C)** Serum levels of chemokines involved in both homeostatic and inflammatory processes. **D)** Serum levels of homeostatic chemokines. Values below or above the assay's threshold were excluded. Error bars represent mean +/- S.D. One-way ANOVA followed by Tukey's multiple comparison test was performed. *$p<0.05$; **$p< 0.01$; ***$p< 0.005$; ****$p< 0.0001$.

## 3.6.2 Characterization of the tumor immune microenvironment in mice with fibrosis-associated HCC

Next, the impact of CXCL12 inhibition on the TME of fibrosis/cirrhosis-driven liver tumors was explored. The liver histology of tumor bearing mice was assessed by H/E staining. After 10 weeks of CCl_4 treatment together with NOX-A12 or revNOX-A12, singular tumor nodules were present in the liver surrounded by normal fibrotic tissue with large immune cell infiltrates in the fibrotic areas. However, no obvious histologic

differences were observed (Figure 28 A). Following 16 weeks of CCl_4 treatment, large proportions of the area in liver sections consisted of tumor tissue, while the remaining non-tumoral parenchyma was remodeled into fibrotic tissue, with islets of hepatocytes surrounded by scar tissue.

Within the normal tissue of revNOX-A12 treated mice, swollen hepatocytes and eosinophilic anuclear areas were abundant. This phenomenon seemed to be much less pronounced in livers from NOX-A12 treated mice (Figure 28 B, Suppl. Figure 4 B). While serum ALT levels did not differ clearly between the groups, there was a tendency towards decreased GLDH after 16 weeks of NOX-A12 treatment. Serum LDH was unchanged between the NOX-A12 and the revNOX-A12 treated group during early tumor stages. After 16 weeks of CCl_4 treatment, there was a clear trend toward increased serum lactate dehydrogenase (LDH) after NOX-A12 treatment while LDH levels in the serum of revNOX-A12 treated mice did not differ from the levels measured in the 10 week-treated groups (Figure 28 C). In order to evaluate the impact of NOX-A12 on tumor promoting inflammation, the number of leukocytes was analyzed by flow cytometry, using an optimized isolation protocol (see section 3.6.3). The number of leukocytes was not significantly altered between the different groups (Figure 28 D). Furthermore, gene expression of *Cxcr4* and a set of genes associated with tumor-promoting inflammation (i.e., *Tnfa*, *Il-6*, *Il-10*) was assessed in total non-tumor liver tissue and tumor tissue from tumor-bearing mice and compared to healthy controls. *Cxcr4* transcription levels were significantly upregulated in fibrotic non-tumor and in tumor tissues compared to healthy liver tissues. *Tnfa* expression was moderately but not statistically significantly upregulated in early tumors and strongly induced in advanced tumors. There were no detectable changes in *Il-6* expression between healthy and fibrotic tissues, but *Il-6* was slightly upregulated in tumor tissues, with no further increase in advanced tumors. *Il-10*, on the other hand, was differentially expressed only in advanced tumor tissue, showing a significant but moderate increase compared to the other conditions (Figure 28 E). Next, the effect of NOX-A12 on the expression of the above-mentioned genes in tumor tissue and normal tissue distant from the tumors was evaluated. In non-tumor tissue of mice subjected to DEN and 10 weeks of CCl_4, *Cxcr4*, *Tnfa* and *Il-10* expression was not clearly different between revNOX-A12 and NOX-A12 treated samples, however, the expression of *Il-6* was significantly downregulated in the NOX-A12 treated group (Figure 28 F). Gene expression measured in tumor samples from each treatment group was compared to tumor tissue from mice treated with DEN + 10w CCl_4 and revNOX-A12. *Cxcr4* mRNA levels were significantly increased in tumors from NOX-A12 treated animals, regardless of tumor stage, while *Tnfa, Il-6* and *Il-10* were not differentially expressed in revNOX-A12 and NOX-A12 treated tumors (Figure 28 G).
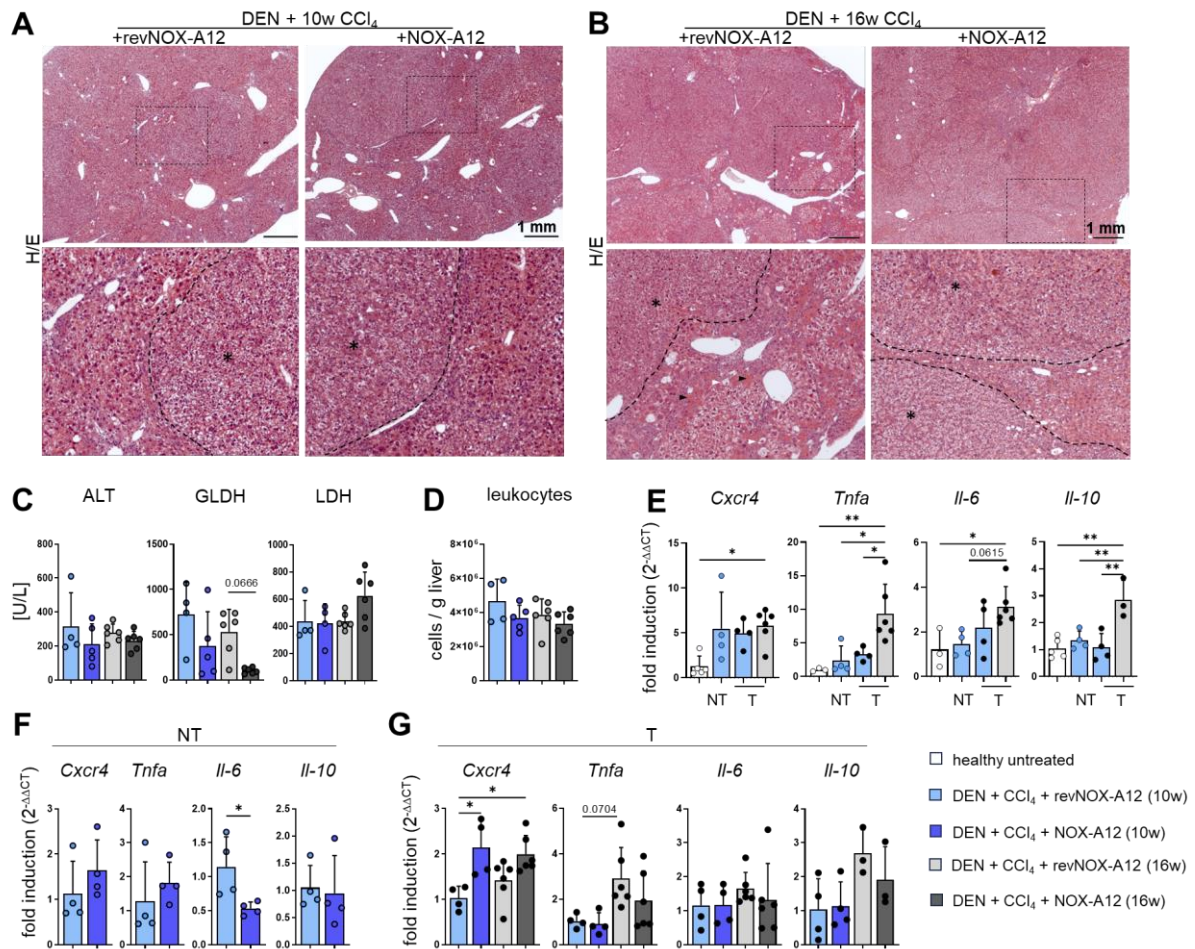
Figure 28: Assessment of the impact of CXCL12 inhibition on liver injury and inflammation in fibrotic/cirrhotic tumor-bearing livers. Livers of DEN + CCl$_4$ treated mice (for 10 and 16 weeks) that had received NOX-A12 or revNOX-A12 were further analyzed. **A**, **B**) Representative H/E pictures of liver histology at indicated time points and enlarged images of tumor margins (* tumor area; white arrows: swollen hepatocytes; black arrows: eosinophilic area). **C**) Serum levels of ALT, GLDH and LDH. **D**) Absolute numbers (cells per gram liver) of liver leukocytes. **E**) Quantitative RT-PCR was used to measure the fold induction of genes linked to tumor-promoting inflammation in healthy liver tissues, compared to fibrotic non-tumor (NT) and tumor (T) tissues of mice that received treatment with DEN + CCl$_4$ + revNOX-A12. **F**) Differential gene expression of *Cxcr4*, *Tnfa*, *Il-6* and *Il-10* in liver NT homogenates from mice after treatment with DEN + 10w CCl$_4$ and NOX-A12 or revNOX-A12. **G**) The gene expression of *Cxcr4*, *Tnfa*, *Il-6* and *Il-10* was analyzed in tumor tissue from the indicated treatment groups and compared to the expression in tumor tissue from samples treated with DEN+10w CCl$_4$ + revNOX-A12. Housekeeping genes: *18S rRNA + B2m*. Error bars represent mean +/- S.D. One-way ANOVA followed by Tukey's multiple comparison test was performed (C, D, E, G). Unpaired Student´s t-test was performed (F) *p<0.05; **p< 0.01; ***p< 0.005; ****p< 0.0001.

3.6.3 Investigating the impact of NOX-A12 on tumor angiogenesis

CXCR4 has been reported to be upregulated on endothelial cells during tumor neoangiogenesis. (152, 155) To investigate the impact of NOX-A12 on angiogenesis, endothelial cells were isolated from fibrotic tumor-bearing livers and analyzed by flow cytometry. As the standard isolation protocol used so far did not allow to isolate endothelial cells in a sufficient quantity and quality for an analysis especially from fibrotic tissue, the isolation protocol was optimized for a gentler digestion, resulting not only in better yields of LSECs but

also of Kupffer cells (Suppl. Figure 2 A, B). LSECs isolated from total liver were gated as CD45$^{int/-}$ cells, double positive for CD31 and CD146. On this population the CXCR4 positive fraction was determined (Figure 29 A). Only few CXCR4$^+$ LSECs were present in healthy liver, whereas a strong increase in CXCR4$^+$ LSECs fibrotic, tumor-bearing livers was observed. After 10 weeks of CCl$_4$ the amount of CXCR4$^+$ LSECs did not clearly differ upon revNOX-A12 treatment compared to NOX-A12 treatment. While there was a trend towards an increase of CXCR4$^+$ LSECs with disease severity in revNOX-A12 treated animals, NOX-A12 caused a strong increase in CXCR4$^+$ LSECs after 16 weeks of CCl$_4$. (Figure 29 B, D). Similarly, the protein levels of CXCR4 within the CXCR4$^+$ gated LSEC population, measured as MFI were increased in fibrotic tumor-bearing livers,
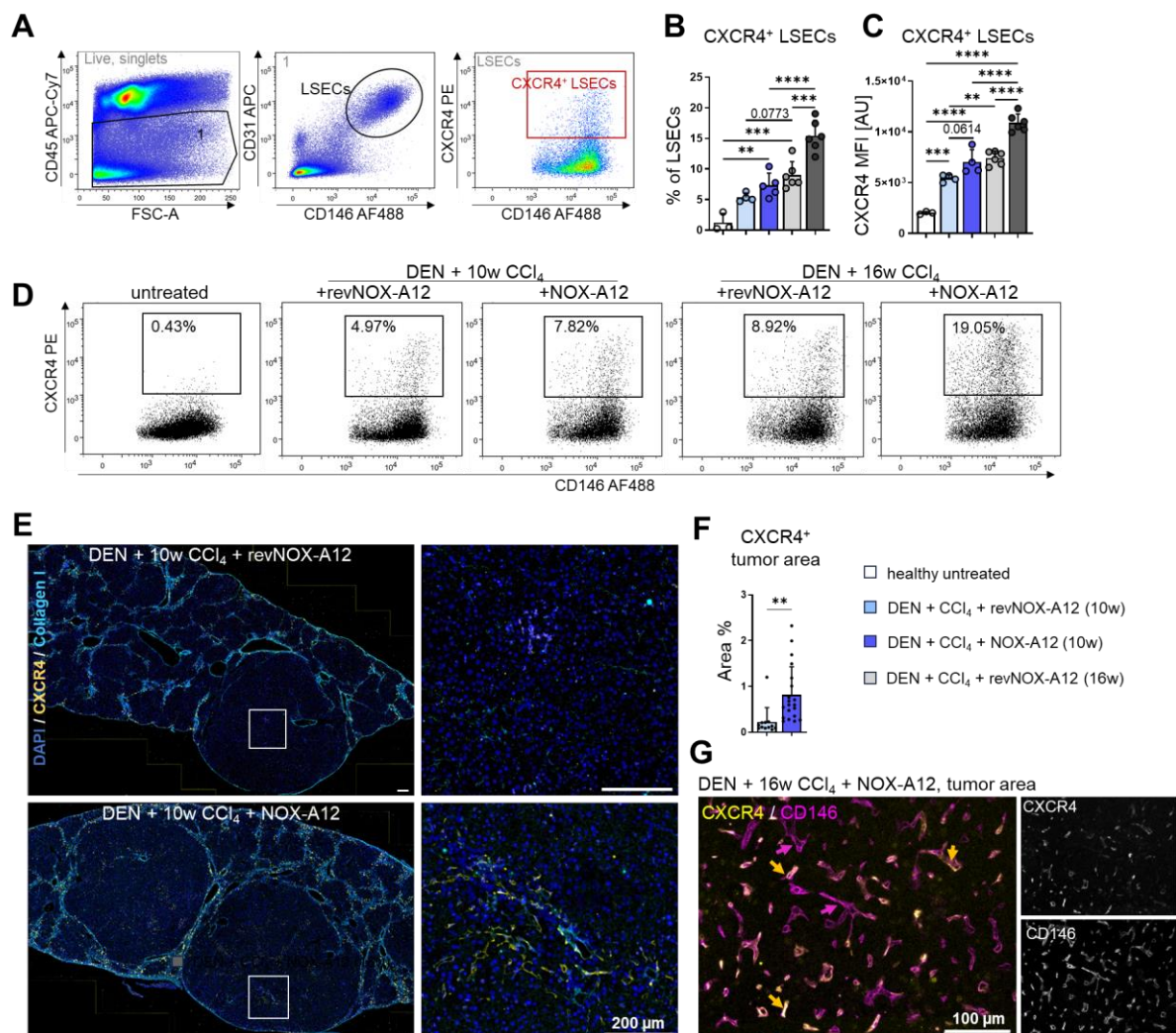
Figure 29: Intratumoral endothelial cells increase CXCR4 expression upon CXCL12 inhibition. A) Gating strategy used to identify LSECs by flow cytometry. **B**) The percentage of CXCR4$^+$ LSECs in mice subjected to DEN and CCl$_4$ together with NOX-A12 or revNOX-A12 (10 and 16 weeks) was determined by flow cytometry. **C**) CXCR4 expression levels (mean fluorescence intensity, MFI) on CXCR4$^+$ LSECs. **D**) Representative plots of CXCR4$^+$ LSECs in the indicated treatment groups. **E**) Immunofluorescence staining of CXCR4 was conducted on liver section from mice subjected to DEN and 10w CCl$_4$, treated with revNOX-A12 or NOX-A12. Collagen-I staining is shown to distinguish the tumor area from fibrotic non-tumor tissue. **F**) Quantification of the CXCR4$^+$ area in individual tumors from DEN+10w CCl$_4$ treated mice, treated with NOX-A12 or revNOX-A12. **G**) Co-staining of CXCR4 and CD146 on a representative tumor area after DEN + 16w CCl$_4$ + NOX-A12 treatment. Orange arrows indicate CXCR4$^+$ CD146$^+$ double positive tumor endothelial cells (TECs), pink arrows indicate CD146$^+$ single positive

TECs. Error bars represent mean +/- S.D. One-way ANOVA followed by Tukey's multiple comparison test was performed. *p<0.05; **p< 0.01; ***p< 0.005; ****p< 0.0001.

and further increased in livers with advanced tumors but were highly upregulated after NOX-A12 treatment (Figure 29 C). Immunofluorescence staining of CXCR4 on FFPE liver sections showed that CXCR4 was selectively increased on cells with an endothelial-like shape in the tumors of NOX-A12 treated mice, while positive stained area was much lower or absent in tumors after revNOX-A12 treatment (Figure 29 E). This was also reflected by the quantification of the CXCR4$^+$ area within individual tumors (Figure 29 F). In non-tumor areas, positive CXCR4 staining was mostly found in macrophages in the vicinity of scar tissue (Suppl. Figure 4 C). The identity of the CXCR4$^+$ cells in the tumor was determined by co-staining with the endothelial marker CD146, which confirmed a specific increase in CXCR4 after NOX-A12 treatment on a subset of TECs (Figure 29 G).

In light of these findings, the impact of NOX-A12 on tumor vascular cells was further explored. Lymphatic vessel endothelial hyaluronan receptor 1 (LYVE-1) is a marker of lymphatic vessels and LSECs but not expressed on other endothelial cells, while CD146 is expressed on all endothelial cells in the murine liver except lymphatic endothelium. (186, 187) Co-staining of LYVE-1 and CD146 on tumor tissue revealed a distinct intratumoral zonation of LYVE-1$^+$ and LYVE-1$^-$ endothelium, while CD146 was expressed on all endothelial cells (Figure 30 A). Tumor neoangiogenesis is characterized by an increase of small vessel density. (188) Therefore, the CD146$^+$ area was assessed to determine the microvessel density (MVD) of tumors in NOX-A12 versus revNOX-A12 treated fibrotic livers (n=3 per group). Due to the high level of intertumoral heterogeneity, both histologically and immunologically, that was observed in the DEN-induced tumors, all tumors were analyzed as individual samples (Suppl. Figure 3). However, no obvious changes in MVD were observed (Figure 30 B). The LYVE-1$^+$ area was analyzed, showing a reduction in advanced tumors in the control group (revNOX-A12). While there was no difference in the LYVE-1$^+$ area between NOX-A12 and revNOX-A12 treatment after 10 weeks of treatment, in advanced tumors, the LYVE-1+ area was slightly increased after NOX-A12 treatment compared to revNOX-A12 (Figure 30 C). The expression of both CD146 and LYVE-1 were enhanced on tumor endothelium (Figure 30 D). To investigate if CD146 or LYVE-1 expression was altered on protein level in response to NOX-A12, their MFI on CD146$^+$ cells was measured. In the revNOX-A12 treated group, CD146 MFI was increased in advanced tumors, while there were no significant differences observed for LYVE-1. NOX-A12 induced an increase in MFI of CD146 and LYVE-1 during the early timepoint, however after 16 weeks of CCl$_4$ in advanced tumors no differences between the vehicle group and NOX-A12 treatment were detected (Figure 30 E). Overexpression of CXCR4 in response to CXCL12 inhibition was found to be associated with LYVE-1$^-$ TECs (Figure 30 F). Next, expression levels of genes associated with angiogenesis and vascular remodeling were analyzed by qPCR

in total non-tumor liver and tumor tissue. In control groups *Cxcl12* expression was reduced in fibrotic tissue, as well as in tumors compared to healthy liver tissue.
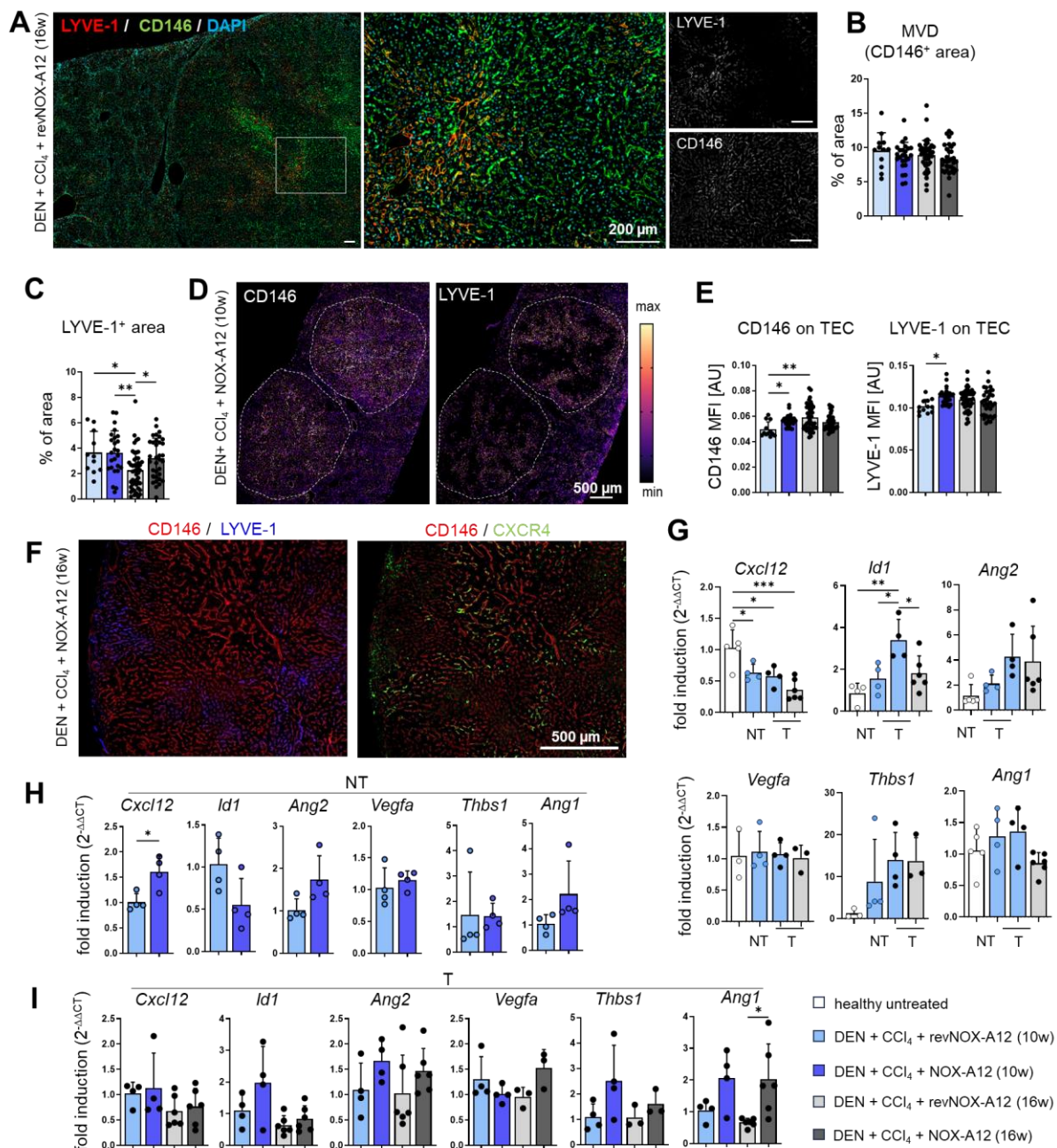
Figure 30: Investigation of the influence of CXCL12 inhibition on tumor vasculature. A) Representative image of CD146 and LYVE-1 staining in an advanced fibrosis-associated liver tumor (DEN + 16w CCl$_4$ + revNOX-A12). Overview and enlarged image of the tumor center. **B**) Microvessel density (MVD) was determined by measuring the CD146$^+$ area in different tumors from n=3 samples per group. **C**) LYVE-1 positive area in individual tumors (n=3 samples per group) **D**) LUT (look-up-table) was used to show differential staining intensities of CD146 and LYVE-1 on representative single channel images on a liver from a DEN+10w CCl$_4$ + NOX-A12 treated mouse. Tumors were circled manually (white dashes). **E**) Mean fluorescence intensity (MFI) of CD146 and LYVE-1 on CD146$^+$ tumor endothelial cell (TEC) clusters. (n=3 mice per group). **F**) Immunofluorescence staining of CD146 and LYVE-1, and CD146 and CXCR4 on sequential sections from a DEN + 16w CCl$_4$+NOX-A12 treated liver. **G-I**) Expression levels of genes associated with vascular remodeling and angiogenesis were determined by qPCR. **G**) Differential gene expression in total fibrotic non-tumor liver (NT) and tumor tissue (T) from DEN + CCl$_4$ + revNOX-A12 treated mice

compared to healthy controls. **H**) Gene expression levels in NT tissue of NOX-A12 treated mice compared to revNOX-A12 treated animals after DEN + 10w CCl$_4$ treatment. **I**) Gene expression levels in tumor tissue from NOX-A12 or revNOX-A12 treated mice after 10 or 16 weeks of CCl$_4$ treatment, compared to tumor tissue after DEN + 10w CCl$_4$ + revNOX-A12 treatment. Housekeeping genes: *18S rRNA + B2m.* Error bars represent mean +/- S.D. One-way ANOVA followed by Tukey's multiple comparison test was performed (B, C, E, G, I). Unpaired Student's t-test was performed (H). *$p < 0.05$; **$p < 0.01$; ***$p < 0.005$; ****$p < 0.0001$.

The pro-angiogenic transcription factor *Id1* was increased on mRNA level in early tumors but decreased in advanced tumor samples. *Ang2* was slightly increased in fibrotic liver and even more in tumors, however without reaching statistical significance, while *Vegfa* expression was unchanged between all groups. Although not statistically significant, *Thbs1* was strongly upregulated in normal fibrotic tissue and in tumor tissue. *Ang1*, on the other hand, remained unchanged between healthy and diseased tissues of the control groups (Figure 30 G). NOX-A12 upregulated CXCL12 expression in fibrotic non-tumor tissue of mice subjected to DEN and 10 weeks of CCl$_4$. While there was a trend towards reduced expression levels of *Id1*, the other genes were not differently expressed in non-tumor tissue of both treatment groups (Figure 30 H). In addition, altered gene expression was evaluated in tumor tissue, compared to tumors from mice treated with CCl$_4$ + revNOX-A12 for 10 weeks. Although there was a trend toward increased *Id1* and *Thbs1* in early tumors after NOX-A12 treatment, most of the genes analyzed were not differently expressed in response to CXCL12 inhibition. The exception was *Ang1*, which was slightly but significantly upregulated in advanced tumors after NOX-A12 treatment. While this trend was also observed in less advanced tumors after 10 weeks of treatment, it did not reach statistical significance (Figure 30 I).

3.6.4 Evaluation of the influence of NOX-A12 on the immune microenvironment

Next, the influence of CXCL12 inhibition on immune cells in the fibrotic/cirrhotic tumor-bearing liver was investigated. As DEN in combination with CCl$_4$ induced small tumors alongside fibrotic and cirrhotic nodules, it was not applicable to dissect separate smaller, in-tissue tumors from fibrotic tissue in a time frame that would allow for further lengthy analysis of fresh cells.

Hence, for some samples depending on the model and duration of treatment, there was not enough material of either normal tissue or tumor tissue for FACS analysis. Therefore, for FACS analyses the entire tumor-containing tissue was used, allowing a comprehensive analysis of global changes. This was complemented by a spatial analysis using multiplex immunofluorescence.

The number of lymphoid cells in tumor-bearing livers after DEN and 10 or 16 weeks of CCl$_4$ treatment combined with NOX-A12 or revNOX-A12 was evaluated. Although CD8$^+$ T cells were not changed by NOX-A12 treatment, there was a slight but insignificant trend toward increased absolute and relative numbers after 16 weeks compared to 10 weeks of CCl$_4$ treatment. The CD4$^+$ T cell population showed no obvious changes in absolute cell numbers. However, the relative number of CD4$^+$ T cells was reduced by NOX-A12

after 10 weeks and increased after 16 weeks of CCl_4. The NK cell population was unaffected. The absolute numbers of NKT cells were low and did not show any changes, but the relative contribution of NKT cells to the leukocyte pool was doubled after 16 weeks of CCl_4 and NOX-A12 compared to the revNOX-A12 treated groups and compared to the 10-week treated group. No significant changes were observed in the absolute numbers of $\gamma\delta$ T cells, but the relative numbers were increased in the revNOX-A12 treated group after 16 weeks CCl_4 treatment compared to 10 weeks. The absolute numbers of B cells, on the other hand, decreased with disease progression. Although there was only a trend toward reduced B cell numbers following CXCL12 inhibition in absolute numbers and no difference in relative numbers, there was a significant additional reduction of B cells by NOX-A12 after 16 weeks of CCl_4, which was reflected in both absolute and relative numbers (Figure 31).
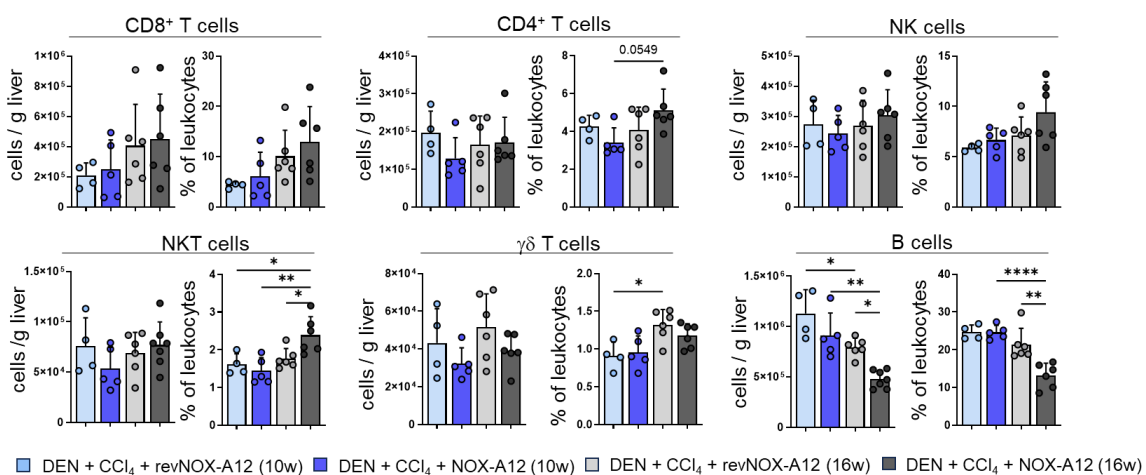
Figure 31: NOX-A12 reduces B cells in fibrotic/cirrhotic tumor-bearing livers. Absolute (cell per gram liver) and relative (percent of leukoytes) numbers of different lymphocyte populations retrieved from total liver tissue after DEN + 10 or 16 weeks CCl_4 + NOX-A12 or revNOX-A12 treatment. Error bars represent mean +/- S.D. One-way ANOVA followed by Tukey's multiple comparison test was conducted. *p<0.05; **p< 0.01; ***p< 0.005; ****p< 0.0001.

To further investigate the differences in B cell numbers observed by flow cytometry, immunofluorescence staining was performed on sections of tumor –bearing livers after 10 weeks of CCl_4 and NOX-A12 or revNOX-A12, using B220 as a B cell marker. In fibrotic non-tumor tissue of revNOX-A12-treated animals, B cells were found to cluster near vessels in scar tissue, which was absent or greatly reduced in NOX-A12-treated animals (Figure 32 A). Semi-automated analysis of B220$^+$ cell density showed a significant reduction of B cells in both normal and tumor tissue after NOX-A12 treatment. Although no B220$^+$ cell clusters were observed in tumor tissue, the overall density of B cells in tumors was not appreciably lower than in the corresponding normal fibrotic tissue (Figure 32 B). Similar clusters were observed in normal tissue of control mice (revNOX-A12) after 16 weeks of CCl_4, which were also largely reduced by NOX-A12. However, B cells were not proliferating in these clusters as confirmed by the absence of Ki67 staining (Figure 32 C).

To determine whether a specific B cell subset was reduced by CXCL12 inhibition, B cells isolated from livers
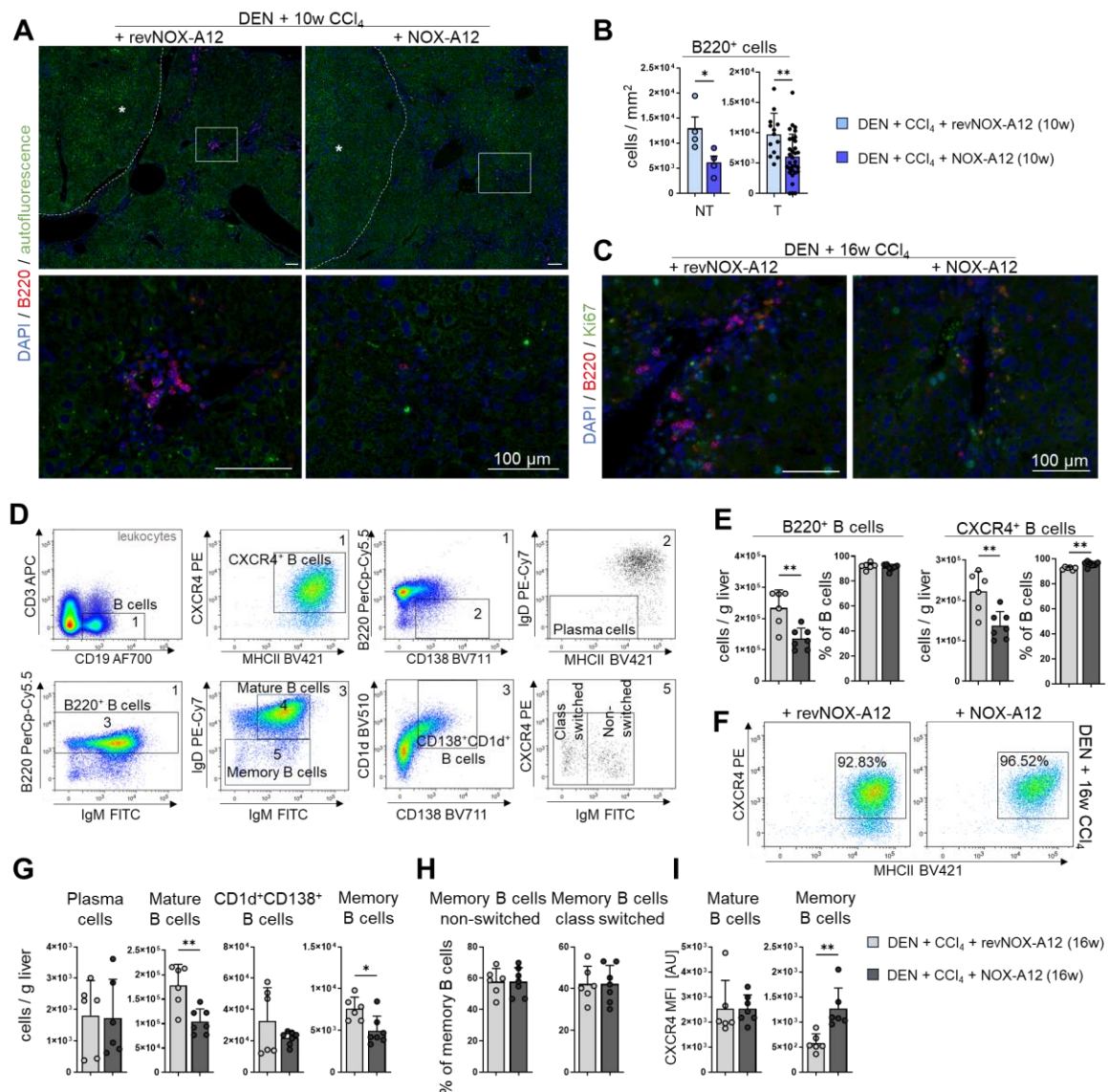
Figure 32: NOX-A12 reduces mature B cells and memory B cells in fibrotic/ cirrhotic tumor-bearing livers. A) Immunofluorescence staining of B220 on liver sections from mice subjected to DEN and 10w CCl_4 combined with NOX-A12 or revNOX-A12 treatment. Tumor area (*) and fibrotic non-tumorous tissue. **B)** Quantification of B220+ cells per mm^2 tissue in non-tumor liver tissue (NT) and tumors (T), from n=4 mice. **C)** Representative images of B220+ cells in NT tissue after treatment with DEN and 16w of CCl_4 together with NOX-A12 or revNOX-A12. **D)** Gating strategy used to identify different B cell subsets by flo4w cytometry in mouse livers with advanced fibrosis/cirrhosis-associated tumors treated with NOX-A12 or revNOX-A12. **E)** Absolute (cells per gram liver tissue) and relative (percent of B cells) numbers of B220+ B cells and CXCR4+ positive B cells. **F)** Representative FACS plots of CXCR4+ B cells. **G)** Absolute numbers of plasma cells, mature B cells, CD1d+CD138+ B cells and memory B cells. **H)** Proportion of unswitched and class switched memory B cells. **I)** CXCR4 expression (mean fluorescence intensity, MFI) on mature B cells and memory B cells. Error bars represent mean +/- S.D. Unpaired Student´s t-test was performed. *p<0.05; **p< 0.01; ***p< 0.005; ****p< 0.0001.

subjected to DEN and 16 weeks of CCl_4 and treated with NOX-A12 or revNOX-A12 were further analyzed by flow cytometry. B cells were identified as CD19+ CD3- leukocytes cells, that were predominantly positive for MHC-II and CXCR4 in the liver. Antibody secreting plasma cells were identified as CD138 positive cells with low expression of B220 and no expression of MHC-II or IgD. B220+ B cells were further subdivided into

mature B cells, which are positive for both IgD and IgM, while IgD negative cells were denoted as memory B cells. Memory B cells were further subdivided according to their expression of IgM into non-switched and class-switched memory B cells. Within the mature B cells a subset positive for CD1d and CD138 was identified (Figure 32 D). While the absolute numbers of B220$^+$ B cells were decreased following NOX-A12 treatment, the relative proportion of B220$^+$ cells within the B cell population were unchanged (Figure 32 E). While the absolute numbers of CXCR4$^+$ B cells was reduced in the NOX-A12-treated group, there was a slight but significant increase in the relative amount of CXCR4$^+$ B cells (Figure 32 E, F). An analysis of B cell types showed that mature B cells and memory B cells were reduced by CXCL12 inhibition. Plasma cells were very rare in the liver however their number was not influenced by NOX-A12. Also, the absolute number of CD1d$^+$CD138$^+$ B cells did not clearly differ between NOX-A12 and revNOX-A12 treated animals (Figure 32 G). Although the total number of memory B cells was reduced by NOX-A12, the proportion of non-switched to class-switched memory B cells was unchanged (Figure 32 H). Lastly, the surface CXCR4 on mature B cells and memory B cells was analyzed. While the protein level of CXCR4 was unaffected on mature B cells, it was increased on memory B cells upon CXCL12 inhibition (Figure 32 I).

The absolute numbers of CD4$^+$ and CD8$^+$ T cells as well as NK cells were not significantly changed upon NOX-A12 treatment. Nevertheless, the influence of NOX-A12 on T and NK cell activation was further investigated by flow cytometry. On CD8$^+$ T cells, the activation marker CD69 was increased in livers with advanced tumors, but not impacted by NOX-A12 treatment. A similar trend was observed for PD-1. In contrast, surface CD107a was reduced after 16 weeks of CCl$_4$ treatment compared to after 10 weeks, which was also unchanged by NOX-A12 treatment. CD178 was expressed at low levels on CD8$^+$ T cells in livers with early tumors after 10 weeks of CCl$_4$ treatment with no detectable effect of NOX-A12 treatment. However, CD178 was strongly upregulated in livers with advanced tumors, with an additional increase in the NOX-A12 treated group (Figure 33 A). On CD4$^+$ T cells, the expression of CD25 was decreased in mice treated with CCl$_4$ for 16 weeks compared to 10 weeks of treatment, while CD69 was not changed. There was no clear effect of NOX-A12 although after 16 weeks of CCl$_4$ there was a subtle trend towards increased CD25 levels on CD4$^+$ T cells after NOX-A12 treatment compared to revNOX-A12 (Figure 33 B). Similarly, neither NOX-A12 treatment nor tumor burden caused clear differences in the expression of CD69 on NK cells. However, the percentage of CD107a$^+$ NK cells was strongly reduced with disease progression. Although not significant, there was a slight trend toward higher levels of CD107a on NK cells in advanced tumors exposed to NOX-A12 compared to the revNOX-A12 treated group (Figure 33 C).

Increased levels of CXCL12 at the tumor border have been reported to prevent T cells from infiltrating tumors. (165) Therefore, the localization of CD4$^+$ T cells and CD8$^+$ T cells was evaluated using IF staining on tumor-containing sections from livers treated with DEN and 10 weeks CCl$_4$ combined with NOX-A12 or revNOX-A12. An antibody directed against CD4 was used to identify CD4$^+$ T cells while CD8$^+$ T cells were identified with an anti-CD8 antibody. Collagen I immunostaining was used to localize the tumor border (Figure 33 D). In the control group, CD4$^+$ and CD8$^+$ cells were mainly located in fibrotic areas and at the

tumor margin, with few CD4+ cells within tumors. In the liver of NOX-A12 treated animals CD8+ and CD4+ cells also accumulated predominantly at the tumor margin and in fibrotic structures, but there were also increased numbers of CD8+ cells abundant in tumors, while the distribution of CD4+ cells was not affected (Figure 33 D, E, F).
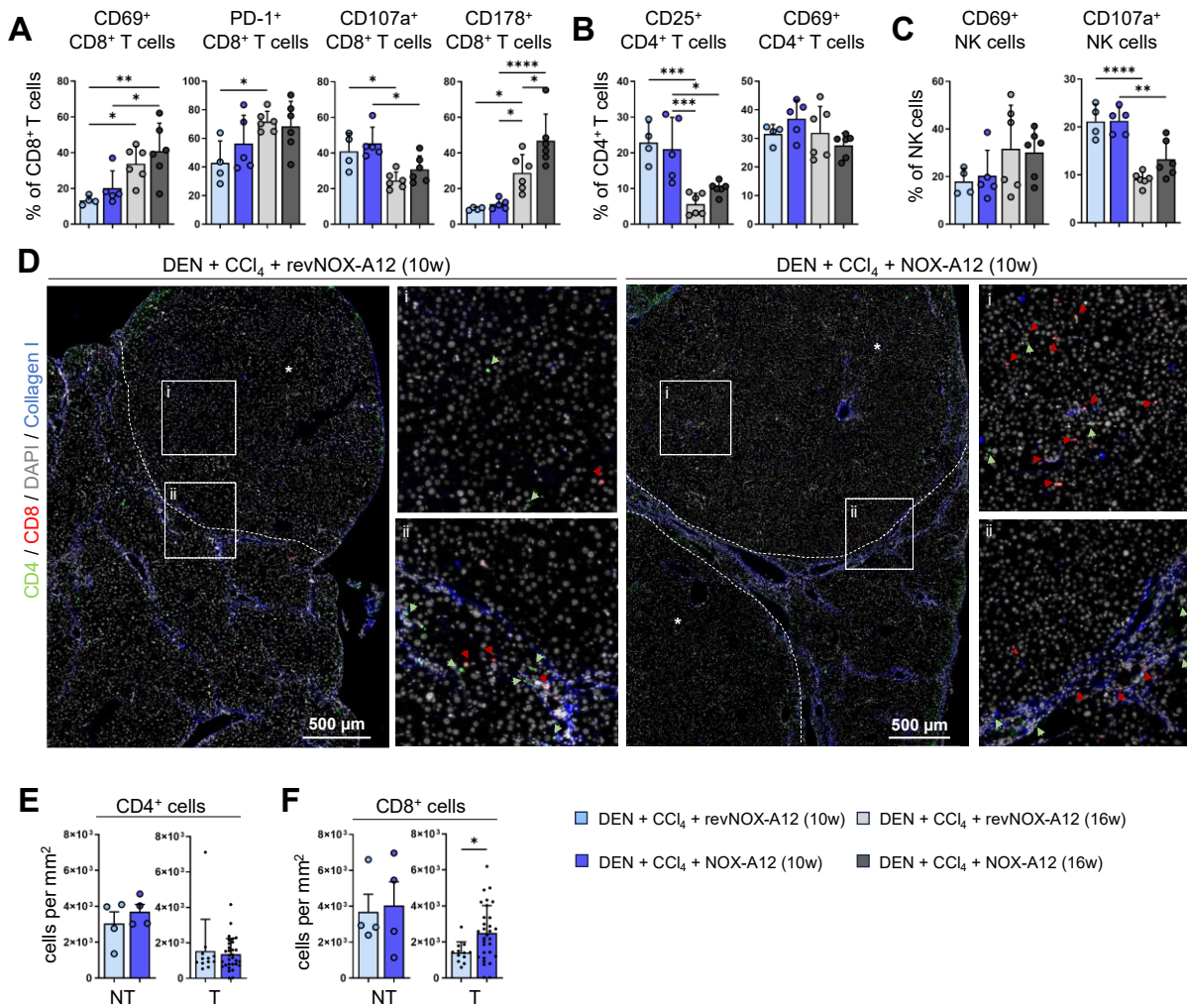
Figure 33: Effects of NOX-A12 on T cell activation and localization in DEN + CCl₄ treated tumor-bearing liver. The impact of CXCL12 inhibition on T cell and NK cell activation in tumor-bearing fibrotic liver was evaluated by flow cytometry. A-C) Markers of activation and cytotoxicity were assessed on CD8+ T cells (A), CD4+ T cells (B), and NK cells (C). D) The localization of CD8+ T cells (CD8+ cells) and CD4+ T cells (CD4+ cells) was explored by immunofluorescence on non-tumor (NT) and tumor (T) tissue (*) of DEN-treated livers after 10 weeks of CCl₄ and revNOX-A12 or NOX-A12. Representative pictures, with enlarged pictures of tumor area and tumor margin; Green arrows: CD4+ cells; red arrows: CD8+ cells. E-F) Semi-automated quantification of CD4+ and CD8+ cells per mm² in normal tissue (NT) and tumor (T) regions. Error bars represent mean +/- S.D. One-way ANOVA followed by Tukey's multiple comparison test was performed (A-C). Unpaired Student´s t-test was performed (E-F) *$p < 0.05$; **$p < 0.01$; ***$p < 0.005$; ****$p < 0.0001$.

In addition, the impact of NOX-A12 on myeloid cells over the course of fibrosis-associated tumor progression was investigated. The major hepatic myeloid immune cell populations were analyzed by flow cytometry. Neutrophils comprised only a small fraction of hepatic leukocytes and were not changed between the different conditions. Dendritic cells showed a slight trend toward lower absolute numbers after NOX-A12 and with disease progression, however the relative numbers were not clearly changed

(Figure 34 A). The absolute and relative numbers of Kupffer cells were reduced after 16 weeks CCl_4 treatment compared to 10 weeks. However, the reduction of Kupffer cells was less pronounced in the NOX-A12 treated group. Both the absolute and relative amounts of $CD11b^+F4/80^+$ cells were strongly reduced in the NOX-A12 treated group after 10 weeks of CCl_4 and after 16 weeks of CCl_4. However, after 16 weeks of treatment there was no detectable additional decrease of $CD11b^+F4/80^+$ cells by NOX-A12 (Figure 34 A, B). The population of $CD11b^+F4/80^+$ cells identified by flow cytometry (see Figure 34 A, B), was further subdivided into eosinophils and MoMF (Figure 34 C). After 10 weeks of CCl_4 treatment, eosinophils represented a major proportion of approximately 60% of $CD11b^+F4/80^+$ cells from tumor-bearing livers, which was largely reduced by NOX-A12. Also, the proportion of eosinophils was reduced after 16 weeks of CCl_4 treatment in livers with larger tumors, with a strong trend toward an additional reduction in NOX-A12 treated samples (Figure 34 D).
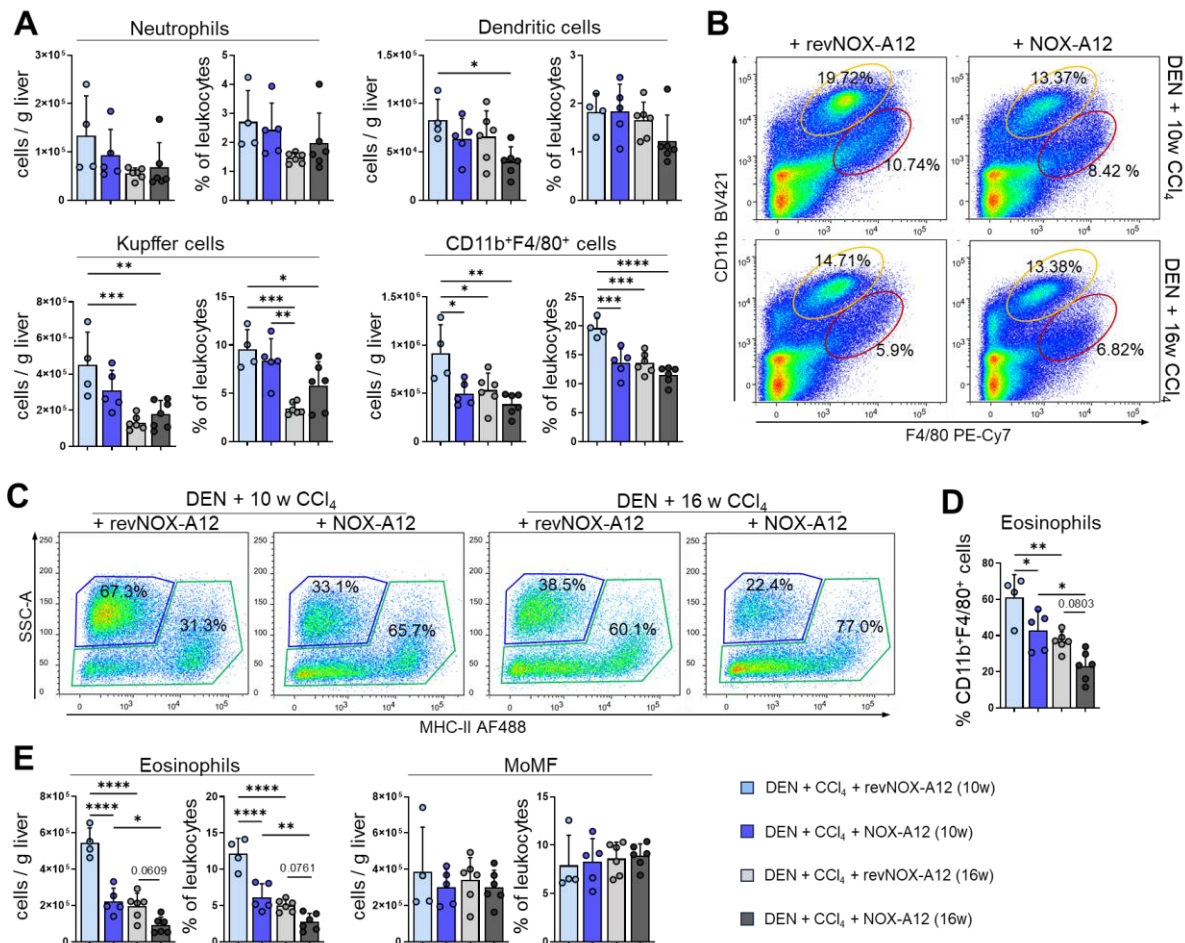
Figure 34: NOX-A12 reduces eosinophils in DEN + CCl_4-induced fibrotic/cirrhotic tumor-bearing liver. Immune cells were isolated from total liver tissue of mice treated with DEN + CCl_4 + NOX-A12 or revNOX-A12 (10w and 16w) and were analyzed by flow cytometry. **A**) Absolute (cells per gram liver tissue) and relative (percent of leukocytes) numbers of major myeloid immune cell populations. **B**) Representative FACS plots of liver macrophages ($CD11b^+F4/80^+$ cells, yellow outline; Kupffer cells, red outline) after indicated treatments. Representative values for the percentage of each sub-gate within the parent gate are shown. **C**) Representative FACS plots of eosinophils (blue outline) and MoMF (green outline) within $CD11b^+F4/80^+$ cells, values indicate percent of parent. **D**) Proportion of eosinophils within the $CD11b^+F4/80^+$ population. **E**) Absolute and

relative numbers of eosinophils and MoMF. Error bars represent mean +/- S.D. One-way ANOVA followed by Tukey's multiple comparison test was performed. *p<0.05; **p< 0.01; ***p< 0.005; ****p< 0.0001.

This shift in the ratio of eosinophils to MoMF was caused by a drastic decrease in eosinophils rather than a change in the MoMF population. While the absolute number of cells and the relative amount of MoMF within the leukocytes were largely unaffected by NOX-A12, both the absolute and relative numbers of eosinophils were decreased with disease progression and by NOX-A12 (Figure 34 E).

Next, the influence of NOX-A12 on liver macrophage activation in fibrosis- and cirrhosis-associated tumor liver was evaluated by flow cytometry. The proportion of $Ly6C^+$ MoMF was increased in livers with advanced tumors. There was a slight trend towards an increase in response to NOX-A12. The amount of $CD80^+$ MoMF was marginally reduced after 16 weeks of CCl_4 compared to 10 weeks but was not influenced by NOX-A12 treatment (Figure 35 A). The fraction of $MHC-II^+CD11c^+$ MoMF was not only significantly reduced in livers with advanced tumors, but also reduced upon NOX-A12 treatment (Figure 35 A, B).
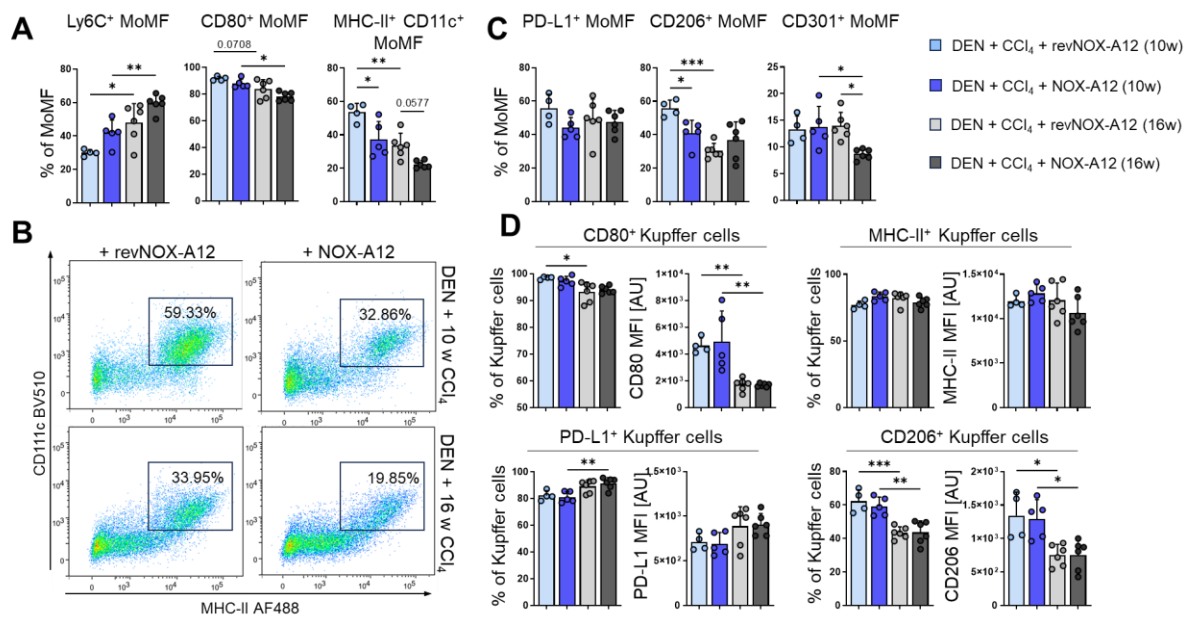
Figure 35: CXCL12 inhibition influences MoMF activation in tumor bearing fibrotic/cirrhotic livers. Several markers of macrophage activation were assessed by flow cytometry. **A**) Relative proportion (percent of MoMF) of macrophages expressing markers associated with inflammation and immune responses. **B**) Representative FACS plots of $MHC-II^+CD11c^+$ MoMF from the indicated treatment groups. **C**) Relative proportion of MoMF expressing anti-inflammatory markers. **D**) Relative proportion and protein expression level (mean fluorescence intensity, MFI) of selected activation markers on Kupffer cells. Error bars represent mean +/- S.D. One-way ANOVA followed by Tukey's multiple comparison test was performed. *p<0.05; **p< 0.01; ***p< 0.005; ****p< 0.0001.

The protein expression level of PD-L1 on MoMF was not significantly altered between the different groups. The amount of $CD206^+$ MoMF was decreased in NOX-A12 treated mice after 10 weeks of CCl_4 and reduced after 16 weeks CCl_4 compared to 10 weeks. However, in livers with advanced tumors, NOX-A12 treatment did not provoke changes in CD206. The proportion of CD301+ MoMF was significantly dereased in NOX-A12 treated mice with advanced tumors, while not changed in the other treatment groups (Figure 35 C).

Also, changes in Kupffer cell activation were evaluated. As Kupffer cells highly expressed most of the analyzed markers the MFI was determined to assess changes in the expression level. While there was only a small decrease in the fraction of CD80+ Kupffer cells, the expression level of CD80 was clearly reduced after 16 weeks of CCl_4 treatment compared to 10 weeks. However, no effect of NOX-A12 treatment was detected. MHC-II, on the other hand was unchanged on Kupffer cells regardless of the respective treatment. While the relative number of PD-L1$^+$ Kupffer cells was slightly increased in mice with advanced tumors irrespective of NOX-A12 treatment, the overall expression of PD-L1 was not significantly changed. The relative amount of CD206$^+$ Kupffer cells was significantly reduced after 16 weeks of CCl_4 compared to 10 weeks, which was also reflected in the MFI (Figure 35 D).

In addition, to assess changes in freshly infiltrated and mature MoMF, the MoMF population was stratified by the expression of Ly6C and MHC-II and subdivided into four populations (Figure 36 A). Although the absolute numbers of immature (Ly6C$^+$MHC-II$^-$) MoMF tended to increase with disease progression, there
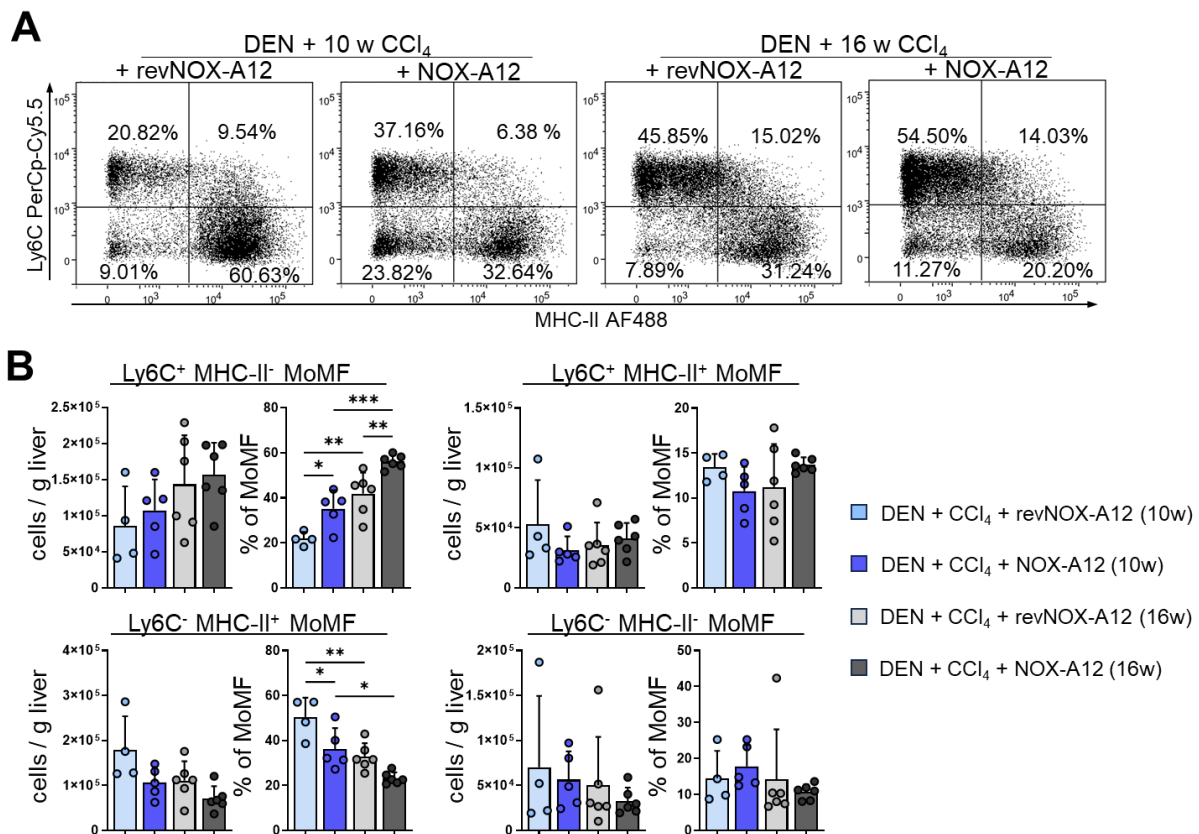
Figure 36: NOX-A12 increases infiltrating Ly6C$^+$ MoMF and decreases mature MoMF in fibrosis-associated tumor-bearing livers. A) MoMF subpopulations were subdivided based on their expression of Ly6C and MHC-II. Representative FACS plots of the indicated treatment groups are shown. **B)** Absolute numbers (cells per gram liver tissue) and relative proportions (percent of MoMF) of different MoMF subpopulations, distinguished by their MHC-II and Ly6C expression. Error bars represent mean +/- S.D. One-way ANOVA followed by Tukey's multiple comparison test was performed. *p<0.05; **p< 0.01; ***p< 0.005; ****p< 0.0001.

was no difference between NOX-A12 and revNOX-A12 treatment. The relative proportion of Ly6C$^+$ MHC-II$^+$ MoMF on the other hand, was significantly increased after 16 weeks of treatment compared to 10 weeks

as well as in response to NOX-A12 treatment. MoMF double positive, as well as MoMF double negative, for Ly6C and MHC-II were not considerably changed. Ly6C$^-$ MHC-II$^+$ MoMF on the other hand, showed a tendency towards a decrease in absolute numbers, both upon NOX-A12 treatment and in livers with advanced tumors (Figure 36 B).

The localization of Kupffer cells and infiltrating macrophages in response to NOX-A12 was evaluated by sequential immunofluorescence staining on liver sections from mice subjected to DEN and 10 weeks of CCl$_4$ in combination with NOX-A12 or revNOX-A12, using antibodies against the pan monocyte/macrophage marker IBA1, F4/80, and the Kupffer cells specific marker CLEC4F. Macrophages largely accumulated in inflamed regions of non-tumor tissue, where they were mainly comprised of IBA1$^+$ CLEC4F$^-$ MoMF with varying F4/80 expression, while they were less dense and more scattered within tumors. While IBA1$^+$CLEC4F$^+$F4/80$^+$ Kupffer cells were relatively rare in non-tumor regions as compared to the homeostatic conditions, TAMs with a Kupffer cell-like phenotype were highly abundant in some, but not in all tumor regions, independent of CXCL12 inhibition (Figure 37 A). F4/80$^+$ cells, comprising both Kupffer cells and MoMF, were less abundant in tumors compared to normal tissue, however there was no difference between NOX-A12 and revNOX-A12 treated animals. While their density was increased in some of the tumors compared to normal tissue, the overall amount of CLEC4F$^+$ IBA1$^+$ Kupffer cells was unchanged by NOX-A12.

Although the density of MoMF was only minimally reduced in normal fibrotic tissue by CXCL12 inhibition, the spatial analysis revealed a significant reduction of TAMs with a MoMF-like phenotype by NOX-A12 (Figure 37 B). In addition, the localization of neutrophils was investigated, using an antibody against MPO. While neutrophils tended to be reduced in normal liver tissue of NOX-A12 treated mice, there was no difference in the number of tumor infiltrating neutrophils (Figure 37 C). In normal tissue, neutrophils were found predominantly in fibrotic areas, whereas in tumors they were found dispersed or focally accumulated (Figure 37 D).
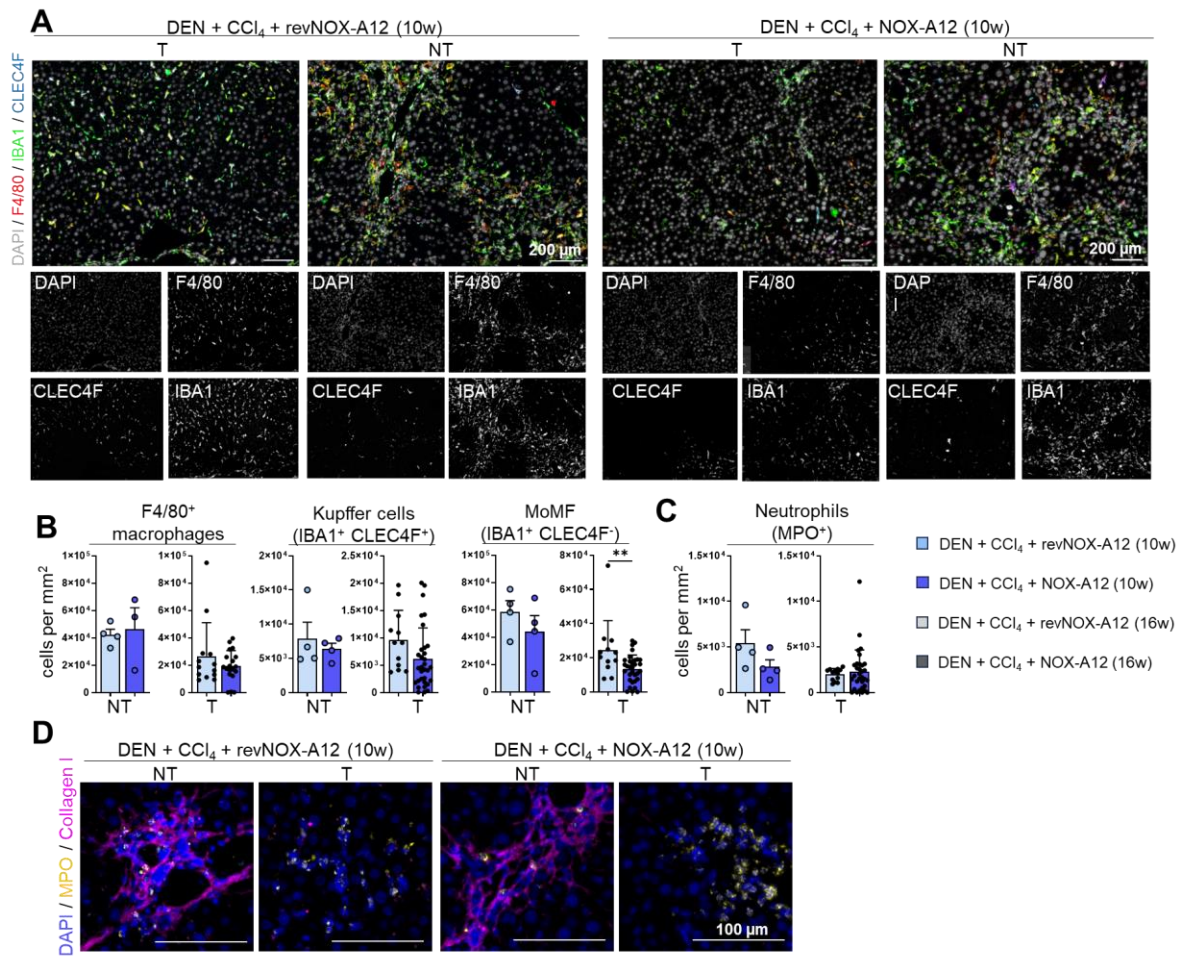
Figure 37: NOX-A12 reduces infiltrating MoMF in DEN + CCl₄-induced liver tumors. A) The spatial distribution of MoMF (IBA1⁺, CLEC4F⁻, F4/80⁺/⁻) and Kupffer cells (IBA⁺ CLEC4F⁺F4/80⁺) in livers from animals treated with DEN + 10w CCl₄ + NOX-A12/revNOX-A12 was investigated by sequential multiplex immunofluorescence. Representative images of tumor and non-tumor areas and grayscale images of individual markers. **B**) The number of all macrophages (F4/80⁺) (n=3), MoMF, and Kupffer cells (n=4) per mm² was analyzed in non-tumor and tumor tissue. **C**) The number of neutrophils (MPO⁺ cells) was quantified in non-tumor and tumor tissue. **D**) Representative pictures of MPO⁺ neutrophils in fibrotic non-tumor tissue and tumor tissue. MPO = myeloperoxidase. Error bars represent mean +/- S.D. Mann-Whitney U test was performed *p<0.05; **p< 0.01; ***p< 0.005; ****p< 0.0001. NT = non-tumor area, T = tumor area

Using sequential immunofluorescence allowed to stain a set of multiple different markers on the same liver slides (Figure 38 A). The densities of different immune cells obtained by sequential immunofluorescence were then calculated for each individual tumor and correlated using Spearman's correlation coefficient. Generally, while the density of all immune cells was positively correlated, a high density of immune cells also correlated with an increased density of proliferating cells, however, not with a higher rate of proliferation (percent of Ki67⁺ nuclei). The density of B cells (B220⁺) strongly and significantly correlated with the density of TAMs (both Kupffer cell-like and MoMF-like). NOX-A12 treatment positively correlated with an intratumoral CXCR4⁺ area and CD8⁺ T cell density, however showed a negative correlation with proliferation as well as B cells and MoMF-like TAMs (Figure 38 B).
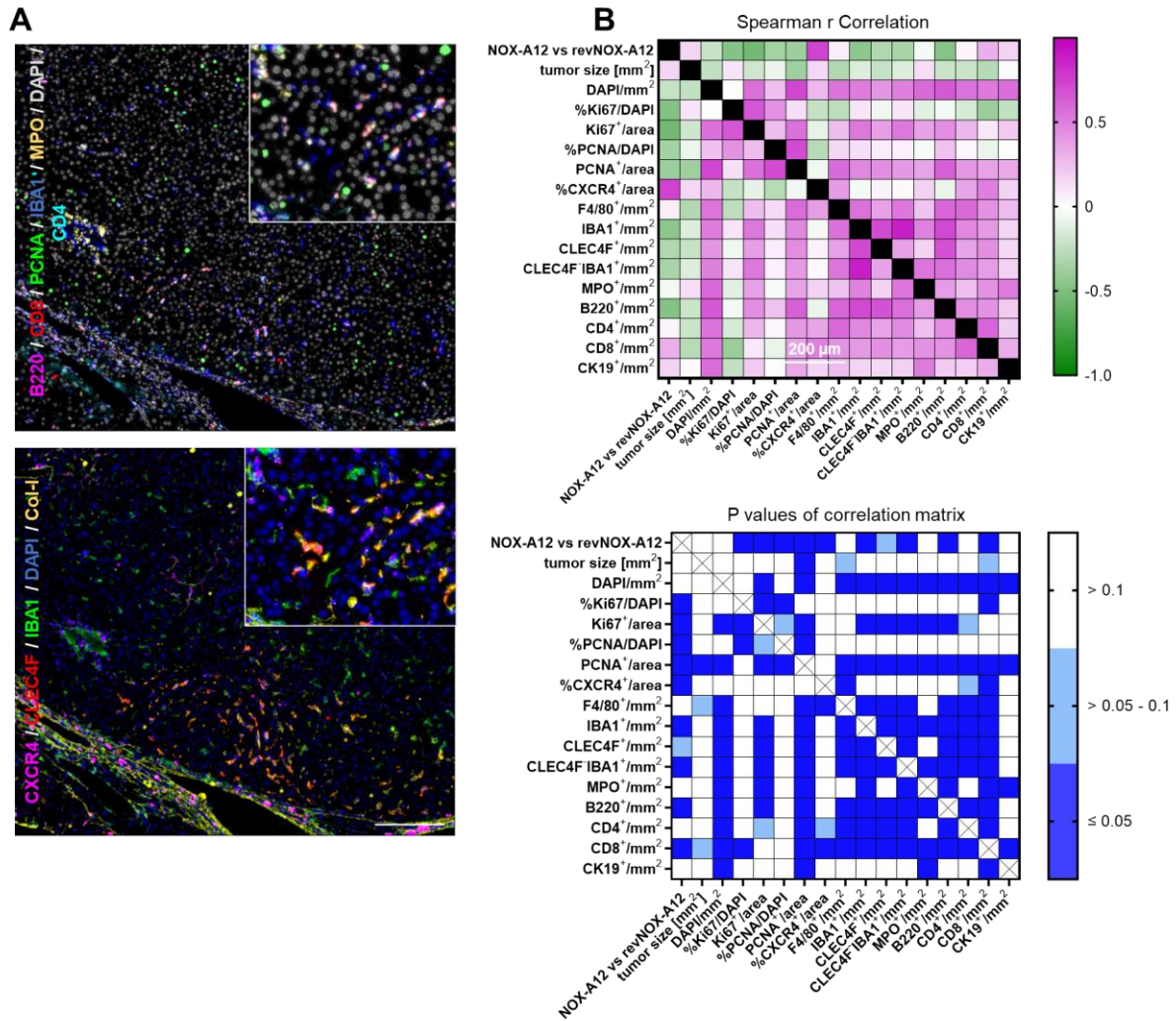
Figure 38: Spearman's correlation matrix reveals concomitant inflammatory and tumorigenic processes in individual tumors. Data obtained by sequential multiplex immunofluorescence staining of liver tumors after DEN + 10 weeks CCl_4 and revNOX-A12 or NOX-A12 treatment (n= 4 mice per group) were correlated for individual tumors using Spearman's correlation coefficient. **A**) Staining of multiple markers on the same slide using sequential multiplex immunofluorescence. Representative picture showing a tumor margin in a DEN + 10w CCl_4 + NOX-A12 treated liver. **B**) Spearman's correlation matrix and respective p values of different parameters, stained on individual tumors.

3.7 Evaluation of the impact of CXCL12 inhibition on the TME in NAFLD/NASH-associated HCC

While feeding a WD for 16 weeks only mildly promoted DEN-induced tumor growth, CXCL12 inhibition by NOX-A12 had a strong tumor promoting effect in this model. To further investigate this phenomenon, liver and blood were analyzed from WD-fed mice with DEN-induced liver tumors, treated either long-term or therapeutically with NOX-A12, or with revNOX-A12 as a control (Figure 39 A).

3.7.1 Investigation of the systemic effects of NOX-A12 in mice with NAFLD-associated HCC

As a first step, the influence of NOX-A12 on circulating leukocytes in a setting of NAFLD-associated liver tumor was analyzed. The absolute numbers of leukocytes were significantly increased after CXCL12 inhibition compared to revNOX-A12 (Figure 39 B). A differential blood analysis showed a trend toward increased neutrophils and clear expansion of CD115$^+$ monocytes and eosinophils after treatment with NOX-A12, that was also reflected in the relative numbers. Although not significant, this tendency was also present after therapeutic treatment with NOX-A12. Dendritic cells, which represent a small fraction of circulating blood leukocytes, were significantly reduced after NOX-A12, both in the long-term and in the therapeutic treatment group (Figure 39 C). The absolute number of classical Ly6C+ monocytes was also increased, however the proportion of Ly6C$^+$ cells within the monocyte population was not altered between
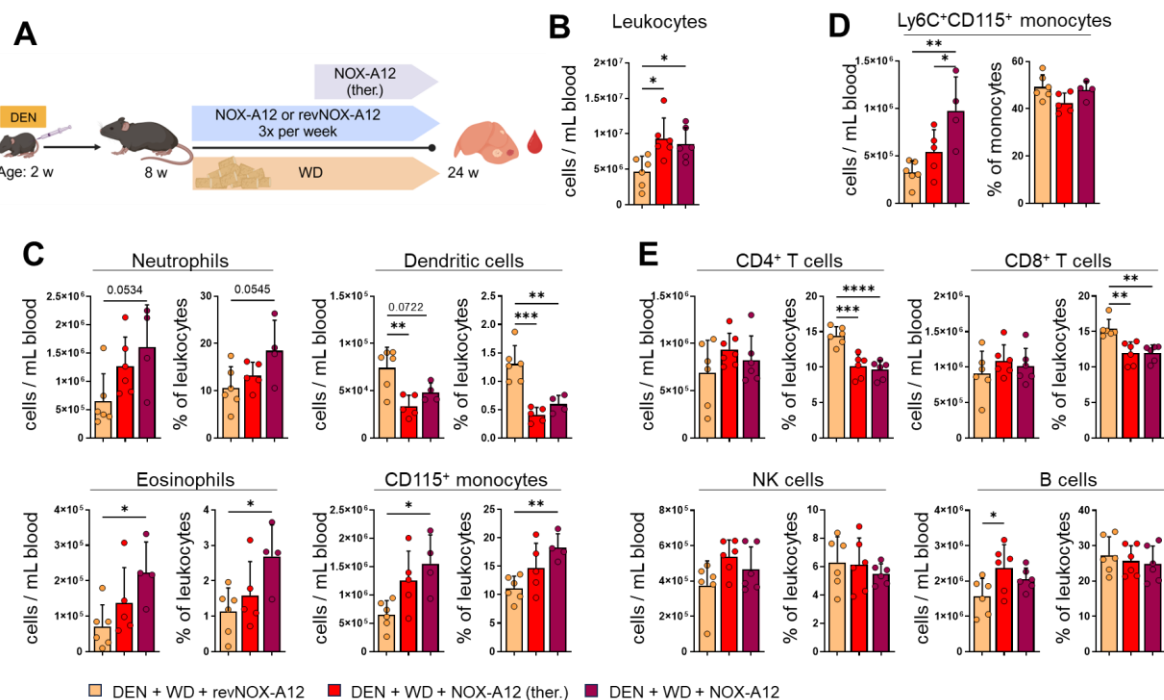
Figure 39: CXCL12 inhibition influences the composition of blood leukocytes of mice with DEN-induced NAFLD-associated liver cancer. A) DEN-injected mice were fed WD for 16 weeks and were treated during this time with revNOX-A12 or NOX-A12 (16 weeks, or 8 weeks therapeutically). Liver and blood immune cell populations were analyzed by flow cytometry. **B)** Number of leukocytes per mL blood. **C)** Absolute (cells per mL blood) and relative (percent of leukocytes) numbers of myeloid cell populations. **D)** Ly6C$^+$CD115$^+$ monocytes, absolute cell counts and proportion of monocytes. **E)** Absolute and relative numbers of lymphoid immune cell populations. Error bars represent mean +/- S.D. One-way ANOVA followed by Tukey's multiple comparison test was performed. *p<0.05; **p< 0.01; ***p< 0.005; ****p< 0.0001.

revNOX-A12 and NOX-A12 treated groups (Figure 39 D). The absolute numbers of both CD4^{+} and CD8^{+} T cells were not changed between the different groups, while the relative numbers were diminished upon NOX-A12 treatment. Both absolute and relative numbers of NK cells were not clearly changed.

The absolute counts of B cells were increased after therapeutic application of NOX-A12, however not after long-term treatment. The proportion of B cells in blood leukocytes was unchanged (Figure 39 E).

In addition, the levels of chemokines in the serum of mice subjected with DEN, 16 weeks of WD and revNOX-A12 or NOX-A12 were analyzed. Serum from untreated mice served as control.

Out of the inflammatory chemokines analyzed, CCL4, CCL2 and CXCL1 were increased in DEN + WD treated mice compared to healthy controls, while CCL5, CCL11 and CXCL10 were largely unaffected (Figure 40 A, B). While most chemokines were not affected by NOX-A12 in the DEN + WD model, there was a strong trend towards decreasing levels of CCL2 in the serum after NOX-A12 (Figure 40 B). The serum levels of the homeostatic and dual chemokines CCL20, CCL22, CCL19 and CX3CL1 were not changed in DEN-treated, WD-fed mice (Figure 40 C, D).
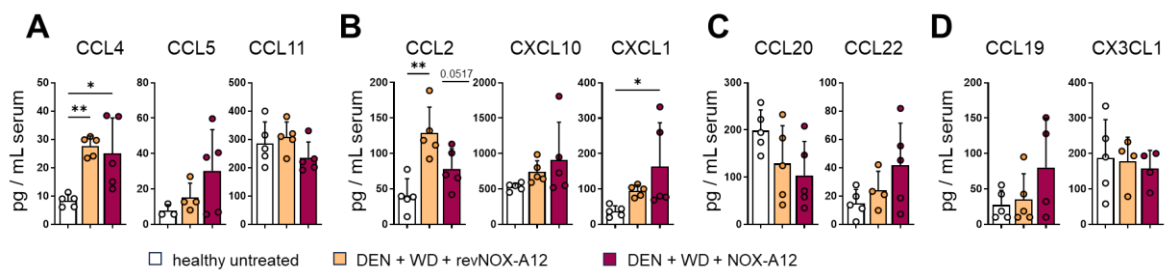
Figure 40: Serum chemokine levels are moderately affected by NOX-A12 in WD-fed tumor-bearing mice. Chemokine levels in the serum of DEN treated mice, that were fed WD for 16 weeks and were treated during this time with NOX-A12 or revNOX-A12 were measured using a multiplex protein microarray. Serum of healthy mice was used as control. **A-B**) Serum levels (pg /mL serum) of inflammatory chemokines with affinity to several (A) or to single (B) chemokine receptors. **C**) Serum levels of chemokines involved in both homeostatic and inflammatory processes. **D**) Serum levels of homeostatic chemokines. Values below or above the assay´s threshold were excluded. Error bars represent mean +/- S.D. One-way ANOVA followed by Tukey's multiple comparison test was performed. *$p<0.05$; **$p< 0.01$; ***$p< 0.005$; ****$p< 0.0001$.

3.7.2 Investigation of the influence of NOX-A12 on the steatotic microenvironment

Regarding the liver, a single injection with DEN followed by a WD for 16 weeks mainly induced microvesicular steatosis with small neoplastic lesions, partially with large lipid vacuoles within the malignant hepatocytes. The tumor lesions were considerably larger following NOX-A12 treatment compared to revNOX-A12 treatment (Figure 41 A). The serum levels of ALT and GLDH, indicative of liver injury, as well as the total number of liver leukocytes, indicative of inflammation, were unchanged between revNOX-A12 and NOX-A12 treated groups (Figure 41 B, C).
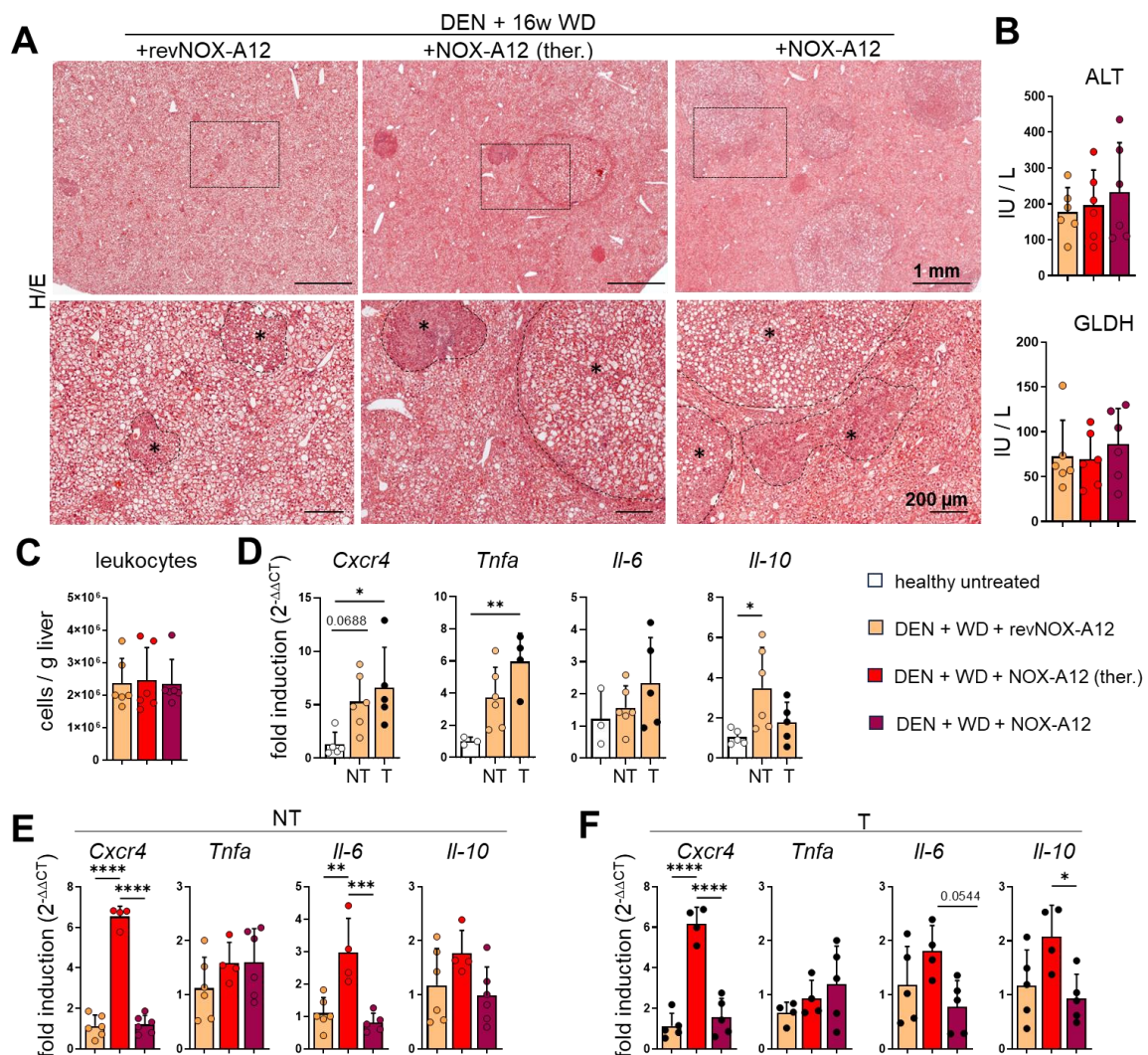
Figure 41: Therapeutic treatment with NOX-A12 induces expression of inflammatory genes in tumor-bearing steatotic livers. A) Representative images of H/E staining on liver tissue from mice treated with DEN, 16 w WD and revNOX-A12 or NOX-A12 (long-term and therapeutically). Overview and enlarged images of regions with tumors (*). **B)** Serum levels of ALT and GLDH. **C)** Absolute numbers (cells per gram liver) of liver leukocytes were assessed by flow cytometry. **D-F)** Gene expression levels of *Cxcr4*, *Tnfa*, *Il-6* and *Il-10* in total tissue from non-tumor areas (NT) and tumors (T) were measured by qPCR. **D)** Gene expression levels in tumor and non-tumor liver tissue from DEN + WD + revNOX-A12 treatment were compared to healthy liver tissue. **E)** Differential gene expression in non-tumor liver tissue between revNOX-A12 and NOX-A12 (long-term or therapeutically) treated mice. **F)** Differential gene expression in tumors from mice subjected to DEN, WD and NOX-A12 (long-term or therapeutic) compared to revNOX-A12. Housekeeping genes: *18S rRNA + B2m.* Error bars

represent mean +/- S.D. One-way ANOVA followed by Tukey's multiple comparison test was performed. *p<0.05; **p< 0.01; ***p< 0.005; ****p< 0.0001.

In addition, gene expression of *Cxcr4* and a panel of cytokines associated with tumor-promoting inflammation (i.e., *Tnfa, Il-6, Il-10*) was assessed in total non-tumor liver tissue and tumor tissue from DEN injected mice after 16 weeks of WD together with revNOX-A12 and compared to healthy controls. mRNA transcript levels of *Cxcr4* and *Tnfa* were increased after DEN + WD both in non-tumor and in tumor tissue. The expression levels of *Il-6* were not changed between healthy and steatotic liver, but moderately upregulated in tumor tissue. *Il-10* was significantly upregulated in non-tumor tissue after WD, but not increased in tumor tissue (Figure 41 D). While long-term NOX-A12 treatment did not change the expression of *Cxcr4*, *Tnfa*, *Il-6* and *Il-10* in steatotic non-tumor liver tissue compared to revNOX-A12, therapeutic treatment with NOX-A12 strongly induced the expression of *Cxcr4* and *Il-6*. *Tnfa* and *Il-10* on the other hand, were not clearly changed (Figure 41 E). Similarly, in total tumor tissue, the expression levels of the afore-mentioned genes did not differ significantly between revNOX-A12 and NOX-A12 long-term treatment. Therapeutic treatment with NOX-A12 however, markedly induced *Cxcr4* expression in tumors, while *Il-6* and *Il-10* were moderately but significantly upregulated. *Tnfa* gene expression was unaffected (Figure 41 F).

3.7.3 Assessment of the effect of NOX-A12 on angiogenic factors in tumor-bearing fatty liver

The amount of CXCR4$^+$ LSECs in tumor-bearing steatotic livers as assessed by flow cytometry was moderately increased after NOX-A12 treatment compared to revNOX-A12 treatment without reaching statistical significance (Figure 42 A). Immunofluorescence staining of CXCR4 on liver tissue demonstrated a significant increase in the expression of CXCR4 on a fraction of cells with a vascular shape within tumor nodules following treatment with NOX-A12. However, this phenomenon was not evident in all tumor nodules (Figure 42 B). This was also confirmed by measuring the CXCR4-positive area per tumor. The results demonstrated a significantly increased CXCR4$^+$ area after therapeutic NOX-A12 treatment compared to revNOX-A12, whereas the CXCR4$^+$ area in the long-term NOX-A12-treated group was not statistically significantly increased (Figure 42 C). Gene expression analysis of angiogenesis-associated genes was performed by qPCR on non-tumor and tumor tissue lysates from mice exposed to DEN and fed WD along with revNOX-A12-injections as a vehicle control and compared to liver tissue from healthy controls. The mRNA expression of *Cxcl12* was significantly decreased in steatotic liver tissue and tumors, whereas *Ang2* was distinctly upregulated. While *Id1*, *Vegfa*, as well as *Ang1* were not clearly changed, *Thbs1* was upregulated in steatotic non-tumor tissue and strongly increased in tumor tissue (Figure 42 D). Next, the influence of NOX-A12 on the expression of these genes on NAFLD/NASH associated liver tumor was evaluated by comparing non-tumor and tumor tissue the respective revNOX-A12 treated samples. In non-

tumor liver tissue, long-term NOX-A12 treatment did not provoke obvious changes in the expression of most of the genes, except for a trend towards increased *Ang1*. Therapeutic application of NOX-A12 moderately induced *Cxcl12* and *Ang1* expression and strongly increased *Vegfa* and *Thbs1*. *Id1* and *Ang2* were not clearly changed (Figure 42 E). Similarly, in tumor tissue, long-term treatment with NOX-A12 did not induce clear differences in angiogenesis-related genes in comparison to revNOX-A12 treatment. In contrast, therapeutic NOX-A12 treatment significantly upregulated the expression of *Cxcl12*, *Id1*, *Vegfa*, *Thbs1* and *Ang1*, while *Ang2* expression was not differentially regulated (Figure 42 F).
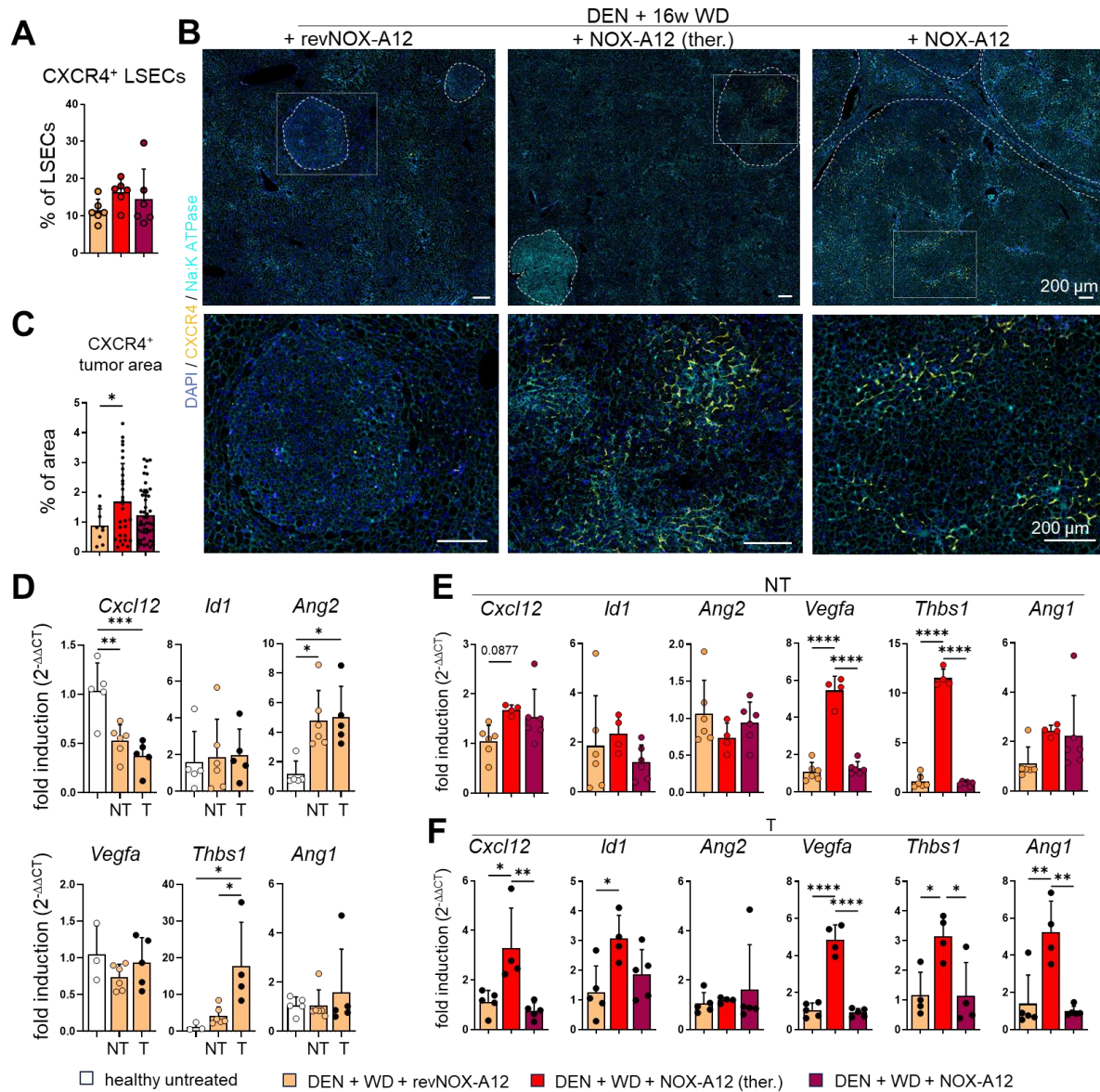
Figure 42: Evaluation of the influence of CXCL12 inhibition on tumor angiogenesis in NAFLD-associated liver cancer. A) The relative amount of CXCR4+ LSECs in tumor-bearing fatty liver after treatment with NOX-A12 or revNOX-A12 was determined by flow cytometry. **B)** Representative immunofluorescence pictures of CXCR4+ cells in liver tumors of revNOX-A12 and NOX-A12 treated animals. **C)** Quantification of the CXCR4+ area within individual tumors (n=4 per group). **D-F)** The expression of genes associated with vascular remodeling and angiogenesis was determined by qPCR in total non-tumor (NT) and tumor tissue (T) from mice subjected to DEN and 16 weeks of WD, treated with revNOX-A12 or NOX-A12. **D)** Gene expression levels in non-tumor and tumor tissue of revNOX-A12 treated mice in comparison to healthy controls. **E)** Differential gene expression

in steatotic non-tumor tissue between mice treated with revNOX-A12 and mice treated with NOX-A12 (long-term and therapeutic). **F**) Differential gene expression in tumor tissue between revNOX-A12-treated and NOX-A12-treated samples (long-term and therapeutic). *18S rRNA + B2m* were used as references. Error bars represent mean +/- S.D. One-way ANOVA followed by Tukey's multiple comparison test was performed. *$p<0.05$; **$p<0.01$; ***$p<0.005$; ****$p<0.0001$.

3.7.3 Investigating the effect of NOX-A12 on the immune cells in steatotic tumor-bearing liver.

To determine the influence of CXCL12 inhibition on immune cells in a lipotoxic tumor environment, leukocytes were isolated from total liver tissue and analyzed by flow cytometry. With the exception of NKT and γδ T cells, which increased significantly both in absolute and in relative numbers after long-term NOX-A12 treatment, there were no major changes in the numbers of most lymphocyte populations between NOX-A12 and revNOX-A12 treated samples (Figure 43 A). On the other hand, NOX-A12 induced a significant decrease in the proportion of CD25$^+$ CD4$^+$ T cells, with the most prominent effect after long-term treatment (Figure 43 B). While PD-1 and CD107a as marker for T cell activation and cytotoxicity on CD8+ T cells were not affected by therapeutic NOX-A12 administration, long-term treatment with NOX-A12 significantly upregulated PD-1 whilst reducing CD107a (Figure 43 C). Surface CD107a expression on NK cells was unaltered by CXCL12 inhibition (Figure 43 D).
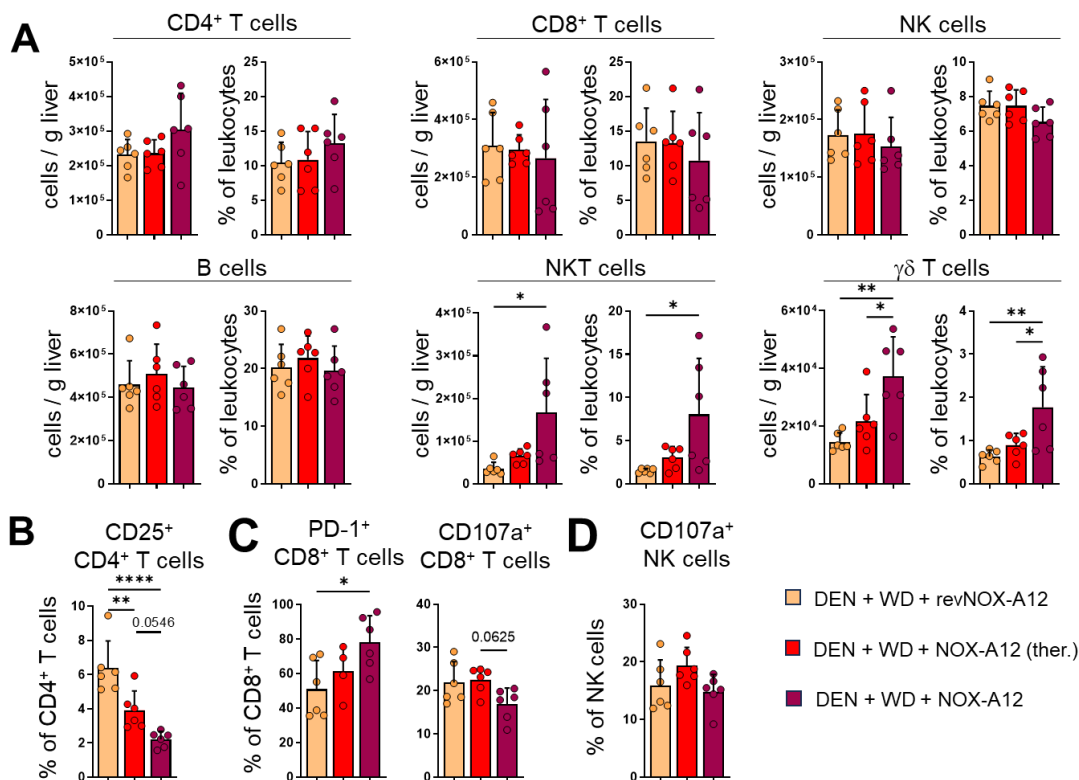
Figure 43: Impact of NOX-A12 on lymphoid immune cells in tumor-bearing steatotic liver: Lymphoid immune cells from tumor-bearing steatotic livers treated with revNOX-A12 or NOX-A12 (long-term and therapeutically) were analyzed by flow cytometry. **A**) Total (cells per gram liver tissue) and relative (percent of leukocytes) numbers of different lymphoid cell populations. **B**) Analysis of the proportion of CD25$^+$ cells within CD4$^+$ T cells. **C**) The proportion of CD8$^+$ T cells expressing

markers of T cell activation and cytotoxicity was analyzed. **D**) Surface CD107a on NK cells was assessed. Error bars represent mean +/- S.D. One-way ANOVA followed by Tukey's multiple comparison test was performed. *p<0.05; **p< 0.01; ***p< 0.005; ****p< 0.0001.

The absolute as well as relative numbers of major hepatic myeloid immune cell populations were unchanged between NOX-A12 and revNOX-A12 treated mice (Figure 44 A). Eosinophils constituted only a minor proportion of CD11b⁺F4/80⁺ cells and total leukocytes while the population of MoMF expanded. NOX-A12 did not affect either eosinophils or MoMF (Figure 44 B, C).
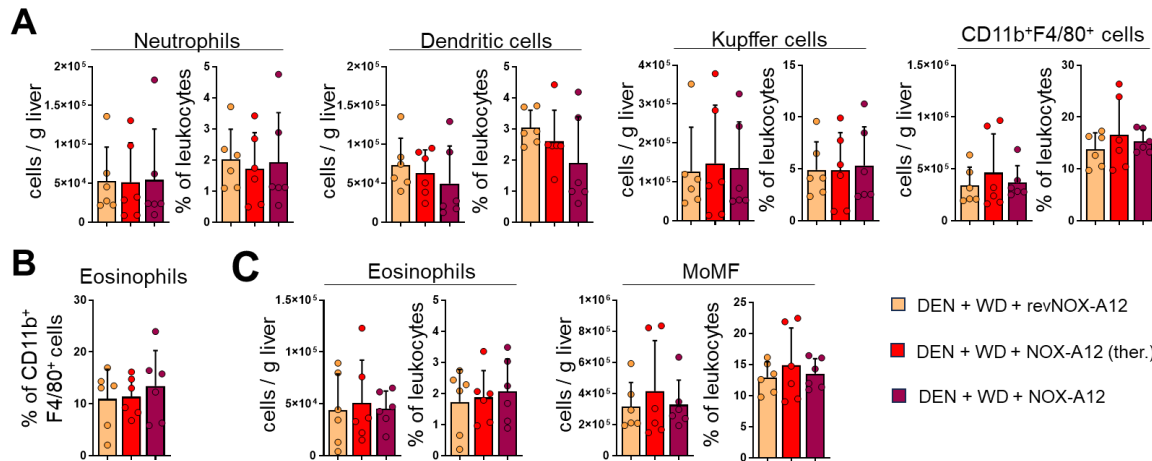
Figure 44: The numbers of hepatic myeloid immune cells are not affected by NOX-A12. Hepatic myeloid immune cells from liver subjected to DEN and 16 weeks of WD, treated with revNOX-A12 or NOX-A12 were analyzed using flow cytometry. **A**) Absolute (cell per gram liver) and relative (percent of leukocytes) numbers of the main myeloid immune cell populations in the liver. **B**) Proportion of eosinophils within the CD11b⁺F4/80⁺ population. **C**) Absolute and relative numbers of eosinophils and macrophages. Error bars represent mean +/- S.D. One-way ANOVA followed by Tukey's multiple comparison test was performed. *p<0.05; **p< 0.01; ***p< 0.005; ****p< 0.0001.

The activation status of hepatic macrophages in response to CXCL12 inhibition was further evaluated using flow cytometry. The expression of CD206, PD-L1, and CD80 on Kupffer cells was not affected by NOX-A12 treatment. However, there was a tendency towards decreased expression levels of MHC-II after long-term NOX-A12 treatment (Figure 45 A). While the more pro-inflammatory markers Ly6C and CD80 were not significantly altered, NOX-A12 treatment decreased the relative amount of MHC-II⁺ CD11c⁺ MoMF (Figure 45 B, C). The amount of PD-L1⁺ MoMF was not affected by NOX-A12 treatment. Nevertheless, there was a noticeable reduction in the proportion of CD206⁺ MoMF following therapeutic NOX-A12 administration, but not after long-term treatment. The relative number of CD301⁺ MoMF decreased after NOX-A12 regardless of the treatment duration (Figure 45 D, E). Additionally, MoMF were gated for MHC-II and Ly6C expression to distinguish between immature and more differentiated MoMF (Figure 45 F). Although no clear difference in absolute numbers was observed between treatment groups, there was a distinct shift in proportions towards increased immature Ly6C⁺MHC-II⁻ MoMF and decreased Ly6C⁻MHC-II⁺ MoMF following NOX-A12 treatment. Furthermore, the fraction of Ly6C⁻MHC-II⁻ was expanded after therapeutic NOX-A12 treatment (Figure 45 F).
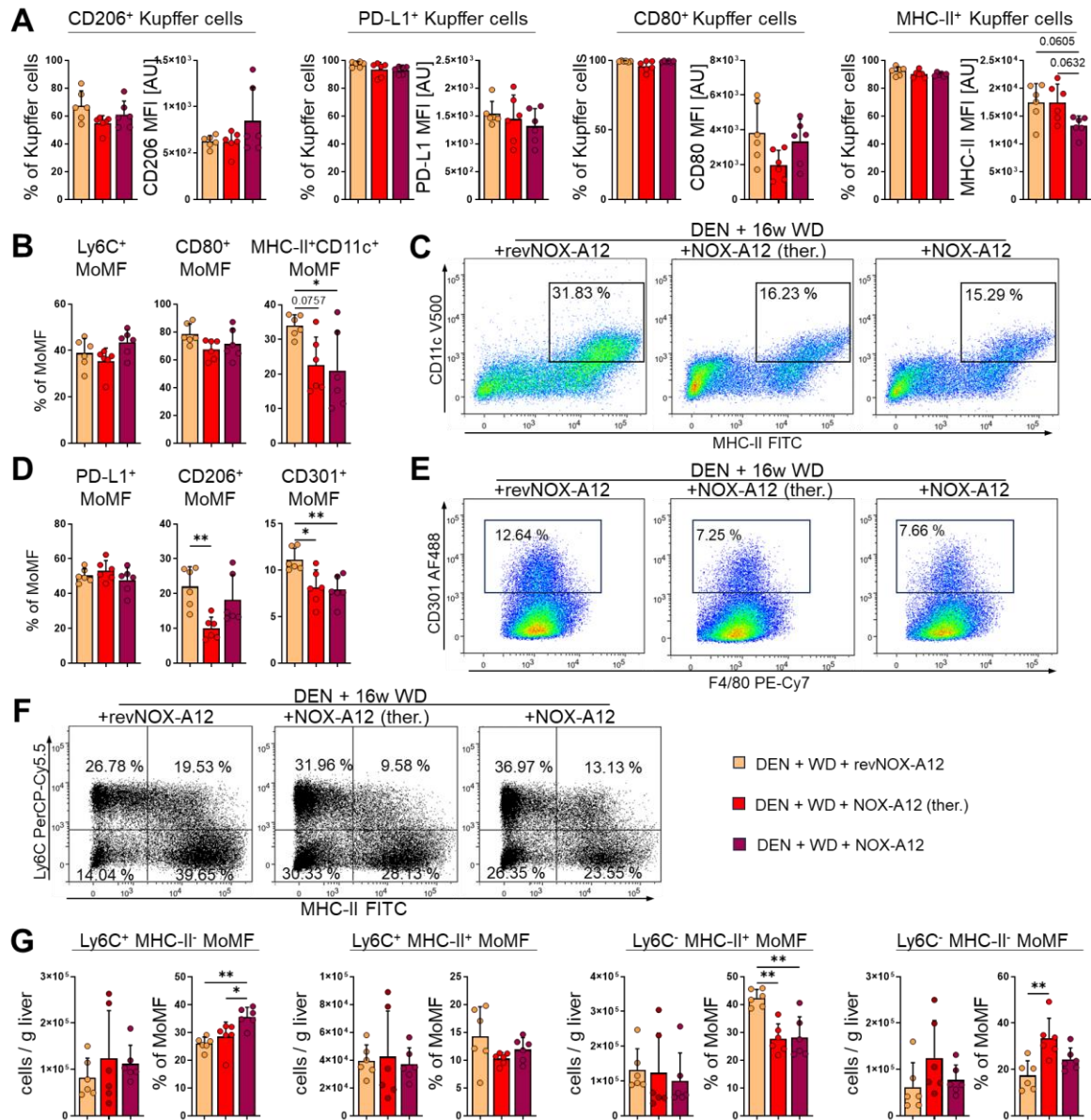
Figure 45: MoMF in tumor-bearing NAFLD livers are differentially activated by NOX-A12 treatment. The expression of activation markers on hepatic macrophages after exposure to DEN, WD and revNOX-A12 or NOX-A12 (long-term and therapeutically) was assessed by flow cytometry. **A**) Analysis of the positive fraction and mean fluorescence intensity (MFI) of a panel of activation markers on Kupffer cells. **B**) Proportions of MoMF expressing markers associated with inflammation and immune responses. **C**) Representative FACS plots displaying MHC-II⁺CD11c⁺ MoMF from the indicated treatment groups. **D**) Proportion of MoMF expressing anti-inflammatory markers. **E**) Representative FACS plots of CD301⁺ MoMF from the indicated treatment groups. **F**) Representative FACS plots of MoMF subpopulations after indicated treatments are presented according to their expression of Ly6C and MHC-II. **G**) Absolute (cells per gram liver tissue) and relative (proportion of MoMF) numbers of the different MoMF subpopulations. Error bars represent mean +/- S.D. One-way ANOVA followed by Tukey's multiple comparison test was performed. *p<0.05; **p< 0.01; ***p< 0.005; ****p< 0.000

4. Discussion

The final stages of chronic liver diseases, namely liver cirrhosis and hepatocellular carcinoma, represent a significant healthcare burden that still lack effective therapeutic options, despite years of extensive research and many potential drug targets having been identified. Due to its proposed pathogenic relevance in liver fibrosis and liver cancer, the CXCL12 chemokine axis is one of such potentially relevant drug targets. (74, 120, 125) However, the effects of CXCL12 on the complex immunological micromilieu of the liver are poorly characterized. Therefore, we aimed at better understanding those effects using established mouse models of liver diseases. To investigate the roles of CXCL12 in liver fibrosis and liver cancer, the CXCL12-neutralizing Spiegelmer NOX-A12, also known as olaptesed pegol, was used. While most inhibitors of the CXCL12/CXCR4/ACKR3 chemokine axis only target one of the receptors, NOX-A12, the inhibitor used in this study, uses an alternative approach. By neutralizing CXCL12, it disrupts signal transduction through both ACKR3 and CXCR4. (174) Due to its safety, tolerability and efficacy in preclinical studies for several cancer types, NOX-A12 is currently evaluated in clinical trials for the treatment of colorectal and pancreatic cancer alone or as combination therapy with the anti-PD-1 antibody Pembrolizumab (NTC03168139) and of glioblastoma under radiotherapy in combination with bevacizumab, an anti-VEGF antibody (NCT04121455).

Here, treatment of healthy mice with NOX-A12 dramatically increased plasma levels of CXCL12. Due to their unique properties, Spiegelmers such as NOX-A12 are stable in plasma and protected from renal clearance, which results in an accumulation of complexes of the inactivated target chemokines bound to Spiegelmers in the circulation (174, 189-191). Nevertheless, and as part of this thesis, the functionality of NOX-A12 was confirmed by testing the ability of NOX-A12 to prevent CXCR4 activation by CXCL12 on Jurkat cells. After binding its ligand, CXCR4 is rapidly phosphorylated and then internalized. (114) Using a phospho-sensitive anti-CXCR4 antibody it was confirmed that NOX-A12 prevented the phosphorylation of CXCR4 by CXCL12. Therefore, the increase in plasma levels of CXCL12 indicates an efficient target engagement in our *in vivo* experiments.

Main findings from our comprehensive study in complementary mouse liver disease models demonstrate that the *in vivo* inhibition of CXCL12 using NOX-A12:

- neither prevents nor increases liver fibrosis in CCl$_4$- and MCD diet-induced chronic liver injury;
- delays inflammation resolution after cessation of injury;
- alters the composition and activation of infiltrating leukocytes in the diseased liver;
- promotes DEN-induced inflammation-driven tumor growth;
- induces a tumorigenic microenvironment by shifting macrophage activation phenotypes and by inducing vasculature remodeling.

4.1 The intricate influence of the CXCL12/CXCR4 axis on liver fibrosis and injury

CXCL12 has been shown to promote liver fibrosis through CXCR4 either by directly activating HSCs or by inducing secretion of profibrotic factors in activated LSECs. (126, 131, 133) However, we did not find indications of an impact of NOX-A12 on fibrosis or HSC activation in two experimental models of liver fibrosis.

Similarly, earlier studies showed that blockade of CXCR4 failed to improve hepatic fibrosis and to attenuate HSC activation following chronic CCl_4 injections. While one study reported that CXCR4 inhibition with AMD070 did not influence HSC activation and liver fibrosis after chronic CCl_4, in another study administration of AMD3100 with an osmotic pump during chronic CCl_4 injections exacerbated liver fibrosis and promoted HSC activation as determined by increased mRNA levels of *Col1a1* and *Acta2*, and inflammation as assessed by increased infiltration of immune cells, especially neutrophils in mice. (192, 193) Similar results were reported for conditional *Cxcr4* knock-out mice. Here, deficiency for *Cxcr4* resulted in increased liver damage after chronic CCl_4, together with worsened fibrosis, and upregulated mRNA levels of *Col1a1* and *Asma*. (194) Similarly, in a mouse model of LPS-induced endotoxemia CXCR4 inhibition by AMD3100 impaired the health status of the mice while enhancing inflammation and parenchymal injury in the liver. (195)

Using NOX-A12, specifically and solely neutralizing CXCL12, we did not observe an aggravation of liver damage, fibrosis, or inflammation after chronic CCl_4 or MCD diet. However, CXCL12 is not the sole ligand of CXCR4. CXCR4 is strongly upregulated in severely stressed hepatocytes (196) and might be important for receiving survival signals and avoiding cell death. CXCR4 also binds CXCL14 as well as non-chemokine mediators, e.g., extracellular ubiquitin (197) or MIF (198). While CXCL14 and extracellular ubiquitin are considered antagonists of CXCL12-CXCR4 interactions, (197, 199) MIF can trigger CXCR4-dependent pathways. (200, 201) MIF is a pleiotropic inflammatory cytokine that interacts with CXCR4 and several other receptors, such as CXCR2, CD74/CD44 and ACKR3. (202) In liver fibrosis, MIF was suggested to play a hepatoprotective role, as MIF or CD74 deficiency exacerbated CCl_4-induced fibrosis in mice. (203) Interestingly, CXCR4 and CD74 can form a functional receptor complex. Although MIF can also signal through each individual receptor, MIF-induced responses were shown to be amplified by co-expression of CD74 and CXCR4, as found on HSCs. (200, 201, 203, 204) Thus, antifibrotic and hepatoprotective pathways triggered by other ligands than CXCL12 may be impaired by CXCR4 receptor blocking agents, but still permitted after CXCL12 neutralization. In contrast, enhanced CXCL12-ACKR3 signaling appears to play an anti-fibrotic role in the liver via LSECs. Pharmacological activation of ACKR3 has been shown to attenuate CCl_4-induced liver fibrosis. (126, 205) Although other factors might be involved, this might provide an explanation why NOX-A12, which blocks both CXCL12-CXCR4 and CXCL12-ACKR3 pathways, failed to ameliorate fibrosis.

4.2 Effect of CXCL12 inhibition on recovery after chronic CCl₄-induced liver injury

Interestingly, we observed a delayed inflammation resolution in NOX-A12-treated mice during recovery from chronic CCl₄-induced liver inflammation. Although the CXCL12/CXCR4/ACKR3 axis is known to play an important role in wound healing, its role in liver regeneration remains controversial. In addition, most studies focus on liver regeneration after acute injury, while the impact of CXCR4 and ACKR3 on recovery after chronic injury is less described. Therefore, we investigated the effect of CXCL12 inhibition on hepatocyte proliferation during peak fibrosis and during early recovery from chronic CCl₄-induced liver inflammation and fibrosis. While during active fibrogenesis and inflammation in the CCl₄ and MCD diet models, the number of proliferating hepatocytes as well as the overall expression of *Mki67* were unaffected by CXCL12 inhibition, we observed increased hepatocyte proliferation under NOX-A12 treatment at 96 hours after the last CCl₄ injection.

The CXCR4-CXCL12 axis is considered to play a hepatoprotective role during regeneration. Progenitor cells, such as hematopoietic and mesenchymal stem cells, have a great regenerative potential and are recruited to the liver through the CXCL12/CXCR4 axis after acute injury. (128, 206) However, during chronic injury and stress, increased glucocorticoid levels downregulate CXCR4 expression on mesenchymal stem cells. This results in an impaired engraftment to the liver and thus an overall low contribution to regeneration in chronic liver fibrosis. (207) Ding et al. demonstrated a bivalent role for CXCL12 signaling in liver regeneration after acute and chronic damage. After acute liver injury, CXCL12 signaling through ACKR3 in LSECs induced HGF and WNT2 promoting liver regeneration, whereas in response to chronic liver injury, activated LSECs upregulated CXCR4, while ACKR3 was downregulated. CXCL12 stimulation of CXCR4-overexpressing LSECs induced the secretion of pro-fibrotic factors, such as TGFβ. (126)

On the other hand, Wilson et al. reported that CXCR4 inhibition with AMD3100 increased hepatocyte proliferation and reduced necrotic areas after ischemia/reperfusion (I/R) in mice, whereas application of CXCL12 reduced regeneration. After partial hepatectomy, a non-inflammatory model of liver regeneration, neither CXCR4 blockade nor CXCL12 application affected regeneration, suggesting that inflammatory or injury-related mechanisms caused the increased proliferation after I/R. (208)

Following chronic CCl₄-induced fibrosis, 96 hours after the last insult, the liver undergoes a phase of inflammation resolution, during which maximum scar removal and elimination of activated HSCs occur. (32) While we found the amount of fibrosis and HSCs unaffected by NOX-A12 treatment at this time point, we observed an increase in immune cell infiltration together with increased levels of *Col1a1, Mmp9* expression and GLDH in the plasma, indicative of still ongoing inflammation, HSC activation and hepatocyte damage. Serum ALT levels on the other hand, were unchanged. This discrepancy can be explained by the higher sensitivity and persistence of GLDH in the serum compared to ALT. (209) All in all, these results

suggest an impaired resolution of inflammation and a prolonged phase of compensatory proliferation rather than a more effective regeneration upon CXCL12 inhibition.

4.3 The influence of CXCL12 inhibition on chronic liver inflammation

In this thesis project, we particularly aimed at drawing attention to how the inhibition of CXCL12 affects the composition and activation of immune cells during chronic inflammation and liver cancer. Indeed, the CXCL12/CXCR4 axis is crucial for immune cell trafficking, and liver inflammation has been shown to impact every stage of liver disease initiation and progression. We found that NOX-A12 profoundly changed the composition of immune cells both in the circulation and in the diseased liver.

4.3.1 Changes in peripheral immune cell mobilization

It is well established that the CXCL12/CXCR4 chemokine axis regulates leukocyte retention in and egress from the CXCL12-enriched bone marrow, and inhibition of either CXCL12 or CXCR4 results in an increase in peripheral blood leukocytes. (99, 176, 192, 193, 210-212) In good agreement with this, we found blood leukocytes moderately but consistently increased after NOX-A12 treatment in all liver injury models. In healthy humans, a single dose of NOX-A12 induced a strong increase in blood neutrophils, lymphocytes and to a lesser extent monocytes. (176) Similarly, a single dose of AMD3100 was shown to mobilize large numbers of T cells besides neutrophils and monocytes, both in healthy humans and healthy mice. (212) However, we did not observe increased numbers of T cells. Interestingly, we observed differences in the composition of NOX-A12-mobilized leukocytes between the different liver injury models used. CXCL12 inhibition predominantly resulted in increased myeloid cell numbers after CCl_4 injections, similar to the effect reported with AMD3100. (193) In the MCD model, however, the amount of B cells was increased, while the numbers of other immune cell populations were unchanged.

Not only does the CXCL12 chemokine axis mediate the release of leukocytes from the bone marrow, but it also mediates homing back to the bone marrow and infiltration into other organs, which is also regulated by a variety of other chemokines with redundant functions that could partially compensate for the missing CXCL12 signaling. (98, 99, 213-216) Indeed, we found several inflammatory and homeostatic chemokines increased in the serum of NOX-A12 treated animals. As the high selectivity of NOX-A12 for CXCL12 has been previously demonstrated in a competitive assay against 23 human chemokines an increase in chemokine levels due to non-specific chemokine binding to the inhibitor can be excluded. (217) The affected chemokines also varied strongly between the different models. While in the CCl_4 model distinct chemokines were increased, for example CXCL10, CCL19 and CX_3CL1, in the MCD model, all measured chemokines were upregulated, further supporting a highly context-dependent role of CXCL12 in inflammatory liver diseases.

The above-described differences in chemokine levels and peripheral blood leukocytes were also observed in the tumor models. In DEN + CCl$_4$ treated mice, NOX-A12 differently influenced the composition of blood leukocytes and the plasma chemokine levels even between mice with intermediate (DEN + 10w CCl$_4$) versus high (DEN + 16w CCl$_4$) tumor burden. Interestingly, CXCL12 inhibition in mice treated with DEN + WD displayed increased myeloid cell subsets but fewer peripheral dendritic cells, while the serum levels of the measured chemokines were largely unaffected. Although dendritic cells were reported to be mobilized into the blood by CXCR4 inhibition (218), an *in vitro* study showed that dendritic cells from the monocytic lineage require CXCR4 engagement for maturation and survival, (219) which could be a reason for their decrease. However, this was not investigated in more depth in this study.

A common observation for all models we used was higher numbers of Ly6C$^+$ monocytes in the blood, indicative of an increased release of immature monocytes from the bone marrow. Chong et al., identified two different subpopulations of Ly6C$^+$ monocytes in the bone marrow that expressed different levels of CXCR4 (CXCR4^{hi} and CXCR4^{lo}), with CXCR4^{lo} monocytes displaying a more inflammatory phenotype and increased levels of CCR2, proposing CXCR4^{hi} monocytes in the bone marrow as precursors of classical monocytes. (211) Indeed, monocytes in the bone marrow downregulate CXCR4 expression upon interaction of CCL2 with its receptor CCR2, resulting in an egress of monocytes into the blood. (220) Although the expression level of CXCR4 was not assessed, it can be assumed that the population of Ly6C$^+$ monocytes in the NOX-A12 treated animals might also contain both inflammatory and pre-mature monocytes. Conversely, in MCD-fed mice, the increase in Ly6C$^+$ monocytes represented rather a shift in the proportion of Ly6C$^-$ to Ly6C$^+$ monocytes, as the total number of monocytes was unchanged, suggesting a more complex influence of CXCL12 on monocytes in this setting.

However, CD11b is not an exclusive marker for monocytes. (185) In the tumor models, using CD115 as additional marker for monocytes, it became evident that both Ly6C$^+$ and Ly6C$^-$ monocytes were increased in the blood. Previous studies showed that CXCR4 inhibition not only releases leukocytes from the bone marrow but also mobilizes marginated immune cells from the lung and possibly other reservoirs, resulting in a concomitant accumulation of mature and immature monocytes. (211, 213) Moreover, we observed a population of so far unidentified Ly6G$^-$ CD11b$^+$ CD115$^-$ Ly6C$^+$ cells, which were seemingly increased in the blood of mice with a high tumor load. Although we did not further explore this population, a recent publication described the presence of Ly6G$^-$ CD11b$^+$ CD115$^-$ Ly6C^{hi} myeloid precursor cells in tumor bearing mice with the ability to differentiate into polymorphonuclear cells with an immunosuppressive phenotype. (221)

Taken together, we observed that NOX-A12 mobilized peripheral blood leukocytes, but the composition of the affected leukocyte populations varied between the different liver disease models. The increase of leukocytes was concomitant with changes in plasma chemokine levels, indicating an intricate and etiology-dependent role for the CXCL12 chemokine in liver diseases.

4.3.2 The impact of NOX-A12 on immune cells in chronic liver inflammation

To investigate the impact of CXCL12 inhibition on immune cell activation, we performed a comprehensive FACS analysis. As expected, we found the number of Kupffer cells reduced in CCl_4-treated mice compared to healthy controls, while the population of infiltrating $CD11b^+$ $F4/80^+$ phagocytes was increased. (32, 222) In addition, the population of NKT cells was reduced in response to chronic liver injury, rather due to an activation than to a decline in the NKT cell population. (223) In contrast to the study by Saiman et al., in which they used AMD3100 in chronic CCl_4 injury, we did not observe increased numbers of neutrophils. This could be attributed to the increased liver injury in their study rather than to a direct effect of CXCR4 inhibition. (193) On the other hand, while we found that the relative amount of B cells was increased in response to CCl_4, this accumulation was abrogated by NOX-A12. Similarly, Tsuchiya et al., observed a decrease in $CD19^+$ cells (i.e., B cells) in the liver of CCl_4-challenged *Cxcr4*-deficient mice compared to *Cxcr4*-competent mice. (194)

CD107a, also known as lysosomal-associated membrane protein-1 (LAMP-1), is highly abundant in the membranes of cytolytic granules and only appears on the cell surface, when granules fuse with the plasma membrane, as it occurs during degranulation. Therefore, surface CD107a serves as a marker of cytotoxicity. (224) Notably, while the total number of NK cells and CD8 T cells was unaffected, NOX-A12 reduced surface CD107a on NK and $CD8^+$ T cells, indicating a reduced cytotoxicity. Concomitantly, CD25 was elevated upon chronic CCl_4 treatment on $CD4^+$ T cells, but strongly reduced by NOX-A12.

Although CD25, a subunit of the IL-2 receptor, is highly abundant on Treg cells, it is also upregulated on activated $CD4^+$ T helper cells. Thus, the reduction of CD25 on $CD4^+$ T cells could both indicate an impaired T cell activation and a decrease in Treg response. Additional markers, such as Foxp3, CD127 or IL-10 would be necessary to clarify the identity of these cells. (15) Nevertheless, the importance of CXCL12/CXCR4 interactions for Treg recruitment and differentiation is well characterized, and a blockade of CXCL12 or CXCR4 is expected to reduce Tregs. (159-161) At the same time there is evidence that the CXCR4/CXCL12 axis does not only function as a chemoattractant for $CD8^+$ and $CD4^+$ T cells, (225-227) but is also involved in T cell activation. CXCR4 on $CD4^+$ T cells was shown to form heterodimers with the TCR and to cross-regulate cytokine responses (228) and to be recruited to the immunological synapse during crosstalk between APCs and $CD4^+$ T cells. (229) In addition, several reports have shown that co-stimulation with CXCL12 augments the proliferation and cytokine production of human $CD4^+$ T cells after CD3 activation. (226, 230, 231) A similar effect was also described for $CD8^+$ T cells. (232)

Regarding the role of CXCL12 in NK cell activation, there exists contradictory data. While Correia et al., reported that CXCL12 exposure induced NK cell quiescence and hence restrained their anti-tumor immunosurveillance, (132) another study reported that CXCL12 induced B7-H1 (PD-L1) expression on NK

cells. (233) Interestingly, engagement of PD-L1 on NK cells was shown to enhance their antitumor activity. (234)

On the contrary, NOX-A12 increased the cytotoxicity-associated marker CD107a on the cell surface of NK and CD8$^+$ T cells and the amount of CD25$^+$ CD4$^+$ T cells in mice fed the MCD diet, while the absolute numbers of T cells and NK cells were not changed. Data on the role of CXCL12 and its receptors in NAFLD/NASH is scarce. However, CXCR4 seems to have a crucial role in the recruitment of lymphocytes to the steatotic liver. Lymphocytes from mice and patients with NASH showed an increased migratory responsiveness to CXCL12 that was not caused by increased receptor expression and could be inhibited by AMD3100. (235, 236)

Despite evidence for a direct effect of CXCL12 on lymphocyte activation, we hypothesized that there were also indirect effects involved, caused by a change in the activation of APCs such as dendritic cells and macrophages. Previous studies demonstrated an involvement of CXCL12 in dendritic cell maturation and survival, however we found the number of dendritic cells only marginally affected. (219) Although CXCL12-HMGB1 heterodimers have been shown to be potent chemoattractants for monocytes, CXCL12 inhibition with NOX-A12 did not alter the total number of infiltrating MoMF in CCl$_4$-treated mice, but we did observed changes in MoMF subpopulations. (118)

Classical monocytes that have recently exited the bone marrow can be identified in mice by their high expression of Ly6C and low expression of MHC-II. Upon extravasation into tissues, they differentiate into MoMF, and upregulate MHC-II and other markers such as F4/80 and CD11c while gradually downregulating Ly6C. (32, 237, 238) Interestingly, in livers of chronically CCl$_4$-challenged mice we found the amount of CD11c$^+$MHC-II$^+$ MoMF decreased after treatment with NOX-A12, while the population of Ly6C$^+$MHCII$^-$ MoMF was expanded. Among the MHC-II$^+$ MoMF, the subset of Ly6C- MoMF was decreased indicating an influence of CXCL12 inhibition on macrophage differentiation and maturation.

In fact, the CXCL12/CXCR4/ACKR3 axis seems to influence macrophage activation and function. Exposure to CXCL12 increased the PRR CD14 and CD163 on human peripheral blood monocytes and induced the secretion of pro-angiogenic CCL1 and VEGF. (145) Another study reported that platelet derived CXCL12 stimulated phagocytosis of platelets by macrophages via CXCR4 and ACKR3. Co-culture of monocytes with platelets triggered upregulation of CD11c and the activation of monocytes into CD163$^+$ macrophages, which was attenuated upon CXCL12 inhibition. (239) On the other hand, siRNA-mediated knock-down of *Cxcr4* in RAW264.7 cells, a murine macrophage cell line, reduced IL-6 and TNF-α expression after LPS stimulation. (240) Altogether suggesting a role for CXCL12 in the modulation of both regenerative and immune responses.

Gating of Ly6G$^-$CD11b^{high}F4/80$^+$ cells is a commonly used strategy to differentiate MoMF from Ly6G$^-$CD11b^{low}F4/80^{high} Kupffer cells. (32, 239) Surprisingly, after chronic CCl$_4$ treatment, we noticed a large,

previously unappreciated population of SSC^{high} cells within this gate, which were identified as eosinophils by their positivity for SiglecF. (241)

In the CCl$_4$ model, eosinophils were reduced in the liver but increased in the blood of NOX-A12 treated mice, while the plasma level of CCL11, a crucial eosinophil chemoattractant (242) was unaltered, indicative of an involvement of the CXCL12 axis for the recruitment of eosinophils in the liver. Indeed, although peripheral eosinophils only weakly express CXCR4 in normal conditions, they upregulate CXCR4 in response to inflammatory cytokines such as TNF-α, IFNγ and TGF-β and efficiently migrate along CXCL12 gradients. (243, 244) Moreover, several studies reported that blockade of CXCR4 or CXCL12 could reduce eosinophil infiltration in different inflammatory settings. (244-246) Eosinophils are highly granulated, bone marrow-derived myeloid cells that are major cellular sources of IL-4 and IL-13 and thus mediate type 2 immune responses. (247, 248) Although eosinophils have mostly been implicated in the defense against parasites (249) and in allergic diseases (250), there is increasing evidence that eosinophils are important for liver regeneration and resolution of inflammation. (248, 251-253) Due to their high production of IL-4 and IL-13, eosinophils have been shown to maintain an anti-inflammatory phenotype in white adipose tissue macrophages. (254) However, to which extent eosinophils play a role in the polarization of hepatic macrophages remains to be determined.

Immune cells from MCD diet-fed mice responded differently to CXCL12 inhibition than in the CCl$_4$ model. In the liver from MCD-diet fed mice we did not observe changes on the amount of Ly6C$^+$ MHC-II$^-$ and MHC-II$^+$CD11c$^+$ macrophages and only subtle decrease in eosinophils after NOX-A12. On the other hand, the subset of MHC-II$^+$Ly6C$^+$ MoMF was highly expanded in this model, while the proportion of eosinophils was rather low. This could be due to different injury dynamics in this model – while the liver undergoes repeated cycles of injury with phases of regeneration in the CCl$_4$ model, in the MCD diet, the liver is subjected to continuous stress, which could suppress the impulse for inflammation resolution and regeneration. Moreover, the unique inflammatory microenvironment in NAFLD/NASH is known to profoundly influence the activation of monocytes and macrophages. (255, 256) It is tempting to speculate that this environment could impact the responsiveness of myeloid cells towards CXCL12, as it was already demonstrated for lymphocytes. (235, 236) In line with this hypothesis, Hart et al. suggested a pro-fibrogenic rather than a protective role for eosinophils in NASH. (257) However, the exact role of CXCL12 signaling in NAFLD/NASH remains unknown.

4.4 Consequences of CXCL12 inhibition on DEN-induced liver tumor growth

4.4.1 The impact of NOX-A12 on tumor growth

Surprisingly, application of NOX-A12 in DEN-induced, inflammation-driven models of HCC resulted in enhanced tumor growth. The CXCL12 chemokine axis is involved in the development and progression of primary liver tumors, acting through both ACKR3 and CXCR4 by directly inducing pro-survival and

proliferative effects and by shaping a pro-tumoral microenvironment. (138, 139, 147, 150-152, 159, 258-260) Using NOX-A12, we sought to investigate the anti-tumor potential of simultaneously disrupting both the tumor-promoting CXCR4 and ACKR3 signaling pathways and how this affects the tumor microenvironment in a model of DEN induced liver cancer which resembles alcohol-induced human HCC. (180) As described previously, the DEN model was combined with repetitive CCl_4 injections to mimic tumor growth in a fibrotic-inflamed environment or with WD to recapitulate tumor growth in a context of metabolic diseases. Unlike CCl_4, which induced large tumors after 16 weeks of treatment, WD only caused small neoplastic nodules. One reason for this difference might be the strong fibrosis caused by CCl_4, which is considered a crucial driver of HCC growth. (60)

Unexpectedly, we observed an increased tumor growth in response to CXCL12 inhibition with NOX-A12 with the most obvious difference between inhibitor and vehicle control in the DEN + WD model. In the DEN + CCl_4 model, a significant difference in tumor burden was present after 10 weeks of CCl_4 treatment, while after 16 weeks the tumor burden was too strong to assess differences in tumor number or size – still, the LBR was significantly increased after NOX-A12 compared to revNOX-A12 treatment indicating a higher tumor load. This contrasts with other studies targeting the CXCL12-CXCR4 axis in murine HCC models, in which inhibition of CXCR4 signaling by AMD3100 or other inhibitors either reduced tumor growth or had no adverse effect. (182, 261, 262) Similarly, in ectopic xenograft models in mice and rats, ACKR3 knockdown with short hairpin RNA (shRNA) was shown to attenuate tumor growth and metastasis, while ACKR3 overexpression promoted proliferation and invasiveness. (139, 140, 263) However, there is a lack of studies investigating ACKR3 inhibition in more physiological models of HCC that consider the influence of the immune system and the disease-specific microenvironment. On the other hand, there is increasing evidence that distinct inflammatory responses of different etiologies profoundly influence the tumor microenvironment and tumor response to therapies. (4)

CXCR4 inhibitors have been shown to synergize with anti-PD-1 treatment, and this combination is already tested in patients with colorectal or pancreatic cancer (NTC03168139). (182, 261, 264) Therefore, we tested in a small cohort of DEN + WD treated mice whether combination therapy of NOX-A12 and anti-PD1 could improve tumor control, but this approach did not appear to ameliorate the phenotype. This may be a disease-model dependent effect, as Pfister et al. showed that anti-PD-1 therapy exacerbated NASH-HCC by increasing a population of autoreactive CD8^{+} T cells. (265) Nevertheless, due to the high variance within the groups, a larger cohort would be needed to draw further conclusions. Overall, checkpoint inhibitor monotherapies appear to benefit only a small proportion of patients (approximately 15-20%). (4) In addition, phase III trials of anti-PD-1 monotherapies in HCC failed to demonstrate superiority over sorafenib. (4, 266, 267) Nevertheless, due to the large variance within the groups, a larger cohort would be needed to draw further conclusions.

4.4.2 The effect of CXCL12 inhibition on the tumor stroma and immune cells

Intrigued by these unexpected results, we further investigated changes in the tumor microenvironment that might provide a possible explanation for the increased tumor growth. Indeed, we found evidence that CXCL12 inhibition facilitates a tumorigenic microenvironment presumably by altering the macrophage activation phenotype and the immune cell composition and by promoting vascular remodeling (Figure 46). The development and progression of HCC in humans and mice is accompanied by drastic changes in the microvascular system. LSECs progressively lose their phenotype, resulting in a capilarized tumor endothelium that lacks fenestrations and LYVE-1 expression but instead produces increased levels of other markers such as CD34 and CD146. (268, 269) The CXCL12 chemokine axis plays an important role in tumor angiogenesis and inhibition of CXCR4 or ACKR3 was shown to reduce CD31$^+$ vessels in murine HCC models. (151, 152, 261) Using the pan-endothelial marker CD146, we did not observe differences in MVD in DEN + CCl$_4$ induced tumors upon CXCL12 inhibition. In advanced tumors, however, the proportion of LYVE-1$^+$ CD146$^+$ endothelium was found to be increased suggesting a reduced TEC capillarization. Concomitantly, we found Ang1 upregulated after NOX-A12 treatment. Ang1, mainly produced by pericytes, induces maturation of newly formed vessels and thus promotes vessel normalization. (61, 62)

Interestingly, CXCL12 inhibition strongly upregulated CXCR4 expression specifically in CD146$^+$ LYVE-1$^-$ endothelium, but not CD146$^+$ LYVE-1$^+$ endothelium. CXCR4 overexpression has been correlated with sinusoid-like microvessels and a distinct growth pattern of HCC, which was induced by macrophage derived TNF-α. (147, 152) However, we did not observe this growth pattern in connection with CXCR4$^+$ TECs in NOX-A12 treated tumors. Also, the TNF-α expression levels were not increased in tumors from NOX-A2 treated animals. Therefore, the cause and consequence of the CXCR4 upregulation remains to be determined.

In CCl$_4$ treated tumor-bearing livers, NOX-A12 facilitated the accumulation of CD8$^+$ cells, and reduced infiltration of MoMF (IBA1$^+$ CLEC4F$^-$) into tumors, in good agreement with a previous *in vitro* study with NOX-A12 (165) and *in vivo* studies using CXCR4 inhibitors. (182, 261) Moreover, we observed a pronounced reduction in eosinophils and B cells after NOX-A12 treatment. This was similar to what we observed in fibrosis models. Eosinophils have been shown to improve tumor control in several preclinical tumor models, including HCC. (270, 271) B cells on the other hand play a dual role in HCC. While B cells can produce antibodies against tumor antigens and activate T cells and thus play a role in anti-tumoral responses, plasma cells and especially anti-inflammatory regulatory B cells can also promote tumor growth. (272) Specifically, we found that mature and memory B cells were reduced by CXCL12 inhibition, while the number of CD1d$^+$CD138$^+$ B cells, which might represent regulatory B cells, was unaltered. (273)

Although pro-tumoral CD206$^+$ MoMF were reduced, the altered balance in immature Ly6C$^+$MHC-II$^-$ and differentiated CD11c$^+$MHC-II$^+$ MoMF could be indicative of an impaired antigen-presentation and phagocytosis, which is an important mechanism of tumor control. (76, 274) Kupffer cells on the other hand

were seemingly unaffected. Interestingly, B cells, differentiated macrophages, and eosinophils were also reduced in livers with overgrowing tumors, further highlighting their potential role in tumor surveillance.

Taken together, CXCL12 inhibition by NOX-A12 seems to impair tumor control by immune cells, which might counteract the limiting effects of CXCL12 inhibition on tumor proliferation, survival, angiogenesis and TAM accumulation, and partially explain the enhanced tumor growth with NOX-A12.

Surprisingly, CXCL12 inhibition appeared to have different effects on the microenvironment of WD-fed tumor-bearing mice. Similar to the CCl$_4$-treated groups, both long-term and therapeutic treatment with NOX-A12 resulted in a decreased the amount of CD11c$^+$MHC-II$^+$ MoMF as well as the expression of the anti-inflammatory markers CD301 and CD206, accompanied by a decrease in CD25$^+$ CD4$^+$ T cells, suggesting a less anti-inflammatory microenvironment. On the other hand, the number of eosinophils and B cells was unaffected. Strikingly, we found a drastic difference between the group that was treated long-term with NOX-A12 and the therapeutically treated group, reflected by a strong upregulation of *Cxcr4* and *Il-6*, evident both in non-tumor and tumor tissue. With this treatment regimen, we also observed an increased frequency of spontaneous fibrosis development.

Like in the CCl$_4$ model, NOX-A12 increased CXCR4 in TECs of some, however not all tumor nodules, highlighting an intertumoral variability also in DEN-induced NAFLD-associated tumors. This aspect of tumor heterogeneity, highlighted in our multiplex immunostaining-based, single tumor analysis, is sometimes overlooked. It is indeed particularly true that in mice, DEN-induced tumors, originating from random gene mutations, drastically differ from one another. This could certainly explain the high heterogeneity observed in this study. Future works should further take this into account, for instance by purposely studying tumor heterogeneity in larger, more numerous tissue sections for each research animal.

NAFLD/NASH is associated with a distorted, dysfunctional microvasculature (275, 276) and a pathological angiogenesis, characterized by increased levels of Ang2 (277), which was also reflected by our data. Moreover, we observed a drastic increase in the mRNA levels of Thrombospondin (*Thbs1*) in tumor tissues of revNOX-A12 treated mice. THBS1 is a matricellular protein that can be produced by fibroblasts, endothelial cells, TAMs, tumor cells and activated platelets. (50, 278-280) Historically, THBS1 is considered an important anti-angiogenic factor. (281, 282) However, there is increasing evidence that THBS1 plays a dual or even tumor promoting role in HCC, as it was shown to correlate with disease progression and angiogenesis. (278, 283) Interestingly, we observed a dramatic upregulation of *Thbs1* as well as *Vegfa* both in non-tumor and tumor tissue from mice that had been treated therapeutically with NOX-A12. Tumor tissue from these mice also showed a strong increase in other angiogenesis-related genes with opposite functions, such as *Cxcl12, Id1* and *Ang1,* indicating a highly dynamic vascular remodeling.

While the underlying reasons remain to be determined, potential reasons for this could be for example an increasingly hypoxic environment, which can induce both *Cxcr4*, *Cxcl12* and *Vegfa* expression (104),
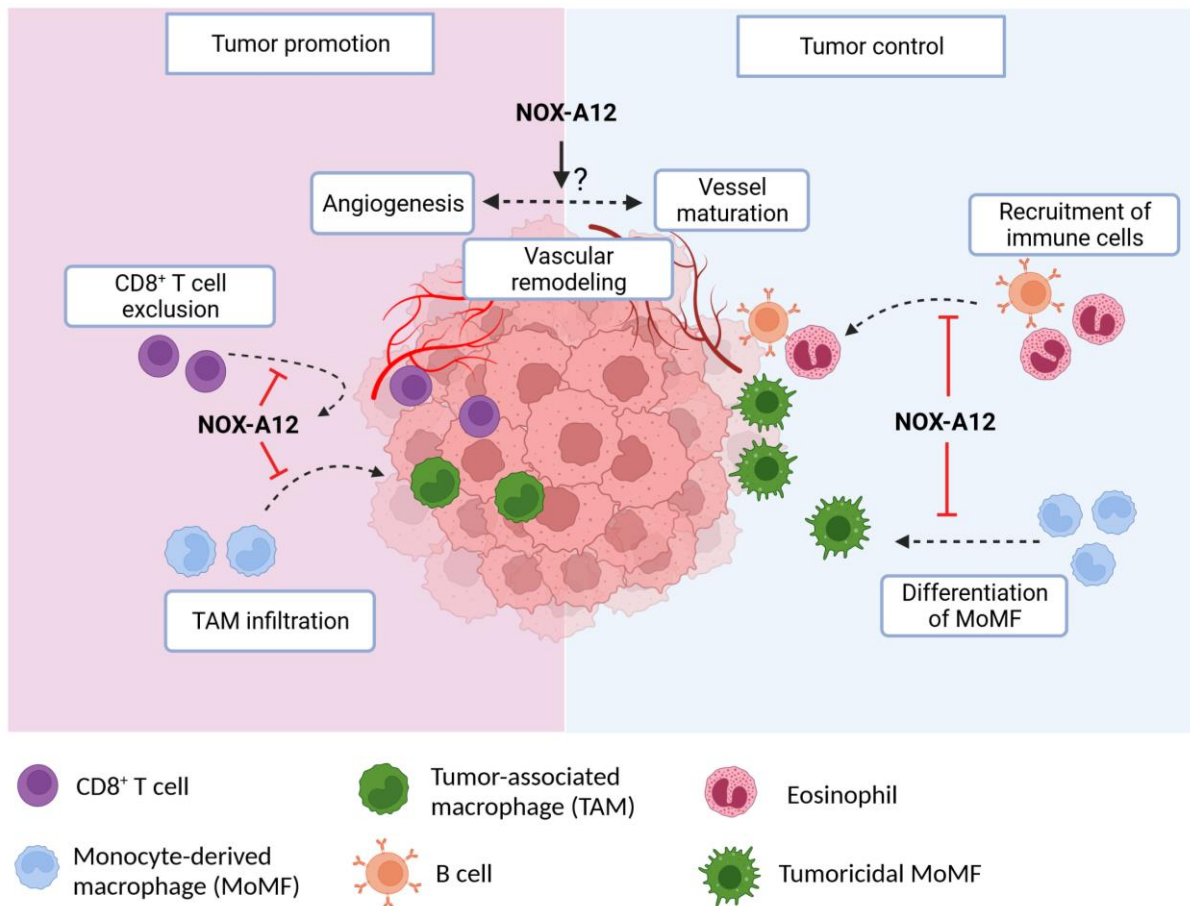
Figure 46: Overview over the proposed NOX-A12 induced changes in the tumor microenvironment. CXCL12 inhibition with NOX-A12 blocks both tumor-promoting and anti-tumorigenic mechanisms in the tumor microenvironment . NOX-A12 enhances CD8⁺ T cell infiltration to the tumor and reduces the infiltration of tumor-associated macrophages (TAM). On the other hand, NOX-A12 inhibits the recruitment of immune cells and the differentiation of immature monocyte-derived macrophages (MoMF) to tumoricidal MoMF and thus limits tumor control. Moreover, NOX-A12 increases the expression of both angiogenic and anti-angiogenic genes in tumors and therefore might increase remodeling of the tumor vasculature

heterodimerization and thus an altered affinity and function of CXCL12, CXCR4 or ACKR3 with another ligand/receptor or interactions of CXCR4 or ACKR3 with other ligands. (117) Indeed, Monnier et al., suggested an important role for the CXCL11/ACKR3 axis in HCC. (151) Moreover, although the study was conducted in immune compromised nude mice, ACKR3 was shown to promote hepatocellular tumor growth *in vivo* and to induce VEGFA as well as the pro-fibrotic protein Galectin-3. (140) Importantly, this upregulation in angiogenesis-related genes was not observed in the long-term (and thus preventive) treatment with NOX-A12, indicating a more complicated mechanism. However, more research is needed to explain these findings and unravel the intricate and contradictory role of CXCL12 in NAFLD. As NOX-A12 has been successfully and safely tested in pre-clinical and clinical trials in different malignancies, such as multiple myeloma, glioblastoma, as well as pancreatic and colorectal cancer, the observed effects are probably organ-specific. (190, 264, 284)

All in all, the results obtained in this thesis show a complex and highly context-dependent role for CXCL12 in liver diseases. Although CXCL12 is involved in many detrimental pathologies, blockade of CXCL12 might

change the activation of bystander cells or facilitate signaling through other ligands resulting in unfavorable side effects. Therefore, NOX-A12 seems not to be a suitable drug for liver diseases.

5. Conclusions

In this thesis, the role of CXCL12 in chronic liver inflammation and primary liver cancer was investigated. CXCL12 neutralization by NOX-A12 led to drastic but disease-specific changes of both circulating and hepatic immune cell populations, generally marked by higher numbers of myeloid cells in the circulation and a reduction of CD11c⁺MHCII⁺ MoMFs in the liver. Intriguingly, NOX-A12 further led to increased tumor burden in distinct models of HCC.

Importantly, this study demonstrates the multifaceted role of CXCL12 in primary liver cancer, uncovering pro-tumorigenic effects of pharmacological inhibition. Apart from promoting tumor survival, proliferation, and aggressiveness, as well as attracting pro-tumorigenic immune cells, this study suggests a pivotal function for CXCL12 in tumoral immune surveillance mechanisms. Although the reasons for this increased tumor load may be multifactorial, our data indicate that NOX-A12, along with redirecting immune cells toward tumorigenic or tumor permissive phenotypes, supports a differential activation of microvasculature that might be favorable for tumor growth (summarized in Figure 46). Importantly, the underlying fibrosis as the tumorigenic environment in chronic liver diseases is not affected by NOX-A12.

It will be important to further investigate the influence of CXCL12 inhibition on MoMF and liver endothelial cells, to identify and dissect the underlying mechanisms. For instance, the phagocytic activity of bone marrow derived macrophages and their ability to activate T cells in the presence of NOX-A12, could demonstrate whether NOX-A12 rather promotes a tumorigenic or prevents an anti-tumoral macrophage phenotype. Moreover, it would be of great interest to investigate how CXCL12 influences LSEC activation, especially in the context of steatotic liver diseases.

While our data do not support a therapeutic application of the CXCL12 inhibitor NOX-A12 in liver diseases and liver cancer, this study offers a detailed description of the immunological variations resulting from CXCL12 inhibition in very distinct mouse models. This emphasizes the importance of characterizing the immunological environment and monitoring tumor growth in several disease models in pre-clinical research. Further studies might unravel how such liver-specific mechanisms explain the different responses to NOX-A12 observed between distinct organs.

6. Literature

1.   Devarbhavi H, Asrani SK, Arab JP, Nartey YA, Pose E, Kamath PS. Global burden of liver disease: 2023 update. J Hepatol 2023;79:516-537.

2.   Tacke F, Weiskirchen R. Non-alcoholic fatty liver disease (NAFLD)/non-alcoholic steatohepatitis (NASH)-related liver fibrosis: mechanisms, treatment and prevention. Ann Transl Med 2021;9:729.

3.   Forner A, Llovet JM, Bruix J. Hepatocellular carcinoma. Lancet 2012;379:1245-1255.

4.   Llovet JM, Kelley RK, Villanueva A, Singal AG, Pikarsky E, Roayaie S, Lencioni R, et al. Hepatocellular carcinoma. Nat Rev Dis Primers 2021;7:6.

5.   Friedman SL, Pinzani M. Hepatic fibrosis 2022: Unmet needs and a blueprint for the future. Hepatology 2022;75:473-488.

6.   Crispe IN. The liver as a lymphoid organ. Annu Rev Immunol 2009;27:147-163.

7.   Kubes P, Jenne C. Immune Responses in the Liver. Annu Rev Immunol 2018;36:247-277.

8.   Jenne CN, Kubes P. Immune surveillance by the liver. Nat Immunol 2013;14:996-1006.

9.   Kamm DR, McCommis KS. Hepatic stellate cells in physiology and pathology. J Physiol 2022;600:1825-1837.

10.   Boyer JL. Bile formation and secretion. Compr Physiol 2013;3:1035-1078.

11.   Janeway CA, Jr., Medzhitov R. Innate immune recognition. Annu Rev Immunol 2002;20:197-216.

12.   Vivier E, Malissen B. Innate and adaptive immunity: specificities and signaling hierarchies revisited. Nat Immunol 2005;6:17-21.

13.   Medzhitov R. Recognition of microorganisms and activation of the immune response. Nature 2007;449:819-826.

14.   Kondo M. Lymphoid and myeloid lineage commitment in multipotent hematopoietic progenitors. Immunol Rev 2010;238:37-46.

15.   Muscate F, Woestemeier A, Gagliani N. Functional heterogeneity of CD4(+) T cells in liver inflammation. Semin Immunopathol 2021;43:549-561.

16.   Murphy K: Janeway's Immunobiology. In. 8th ed: Garland Science, Taylor & Francis Group, 2012; 214 - 215.

17.   Rahman AH, Aloman C. Dendritic cells and liver fibrosis. Biochim Biophys Acta 2013;1832:998-1004.

18.   Berg M, Wingender G, Djandji D, Hegenbarth S, Momburg F, Hammerling G, Limmer A, et al. Cross-presentation of antigens from apoptotic tumor cells by liver sinusoidal endothelial cells leads to tumor-specific CD8+ T cell tolerance. Eur J Immunol 2006;36:2960-2970.

19.   Patel AM, Liu YS, Davies SP, Brown RM, Kelly DA, Scheel-Toellner D, Reynolds GM, et al. The Role of B Cells in Adult and Paediatric Liver Injury. Front Immunol 2021;12:729143.

20.   Katikaneni DS, Jin L. B cell MHC class II signaling: A story of life and death. Hum Immunol 2019;80:37-43.

21.   Notas G, Kisseleva T, Brenner D. NK and NKT cells in liver injury and fibrosis. Clin Immunol 2009;130:16-26.

22.   Gomez Perdiguero E, Klapproth K, Schulz C, Busch K, Azzoni E, Crozet L, Garner H, et al. Tissue-resident macrophages originate from yolk-sac-derived erythro-myeloid progenitors. Nature 2015;518:547-551.

23.   Fogg DK, Sibon C, Miled C, Jung S, Aucouturier P, Littman DR, Cumano A, et al. A clonogenic bone marrow progenitor specific for macrophages and dendritic cells. Science 2006;311:83-87.

24.   Krenkel O, Tacke F. Liver macrophages in tissue homeostasis and disease. Nat Rev Immunol 2017;17:306-321.

25.   Sierro F, Evrard M, Rizzetto S, Melino M, Mitchell AJ, Florido M, Beattie L, et al. A Liver Capsular Network of Monocyte-Derived Macrophages Restricts Hepatic Dissemination of Intraperitoneal Bacteria by Neutrophil Recruitment. Immunity 2017;47:374-388 e376.

26.   Wen Y, Lambrecht J, Ju C, Tacke F. Hepatic macrophages in liver homeostasis and diseases-diversity, plasticity and therapeutic opportunities. Cell Mol Immunol 2021;18:45-56.

27.   Campana L, Esser H, Huch M, Forbes S. Liver regeneration and inflammation: from fundamental science to clinical applications. Nat Rev Mol Cell Biol 2021;22:608-624.

28.   Xu R, Huang H, Zhang Z, Wang FS. The role of neutrophils in the development of liver diseases. Cell Mol Immunol 2014;11:224-231.

29.   Marra F, Tacke F. Roles for chemokines in liver disease. Gastroenterology 2014;147:577-594 e571.

30. Turner MD, Nedjai B, Hurst T, Pennington DJ. Cytokines and chemokines: At the crossroads of cell signalling and inflammatory disease. Biochim Biophys Acta 2014;1843:2563-2582.

31. Kisseleva T, Brenner D. Molecular and cellular mechanisms of liver fibrosis and its regression. Nat Rev Gastroenterol Hepatol 2021;18:151-166.

32. Ramachandran P, Pellicoro A, Vernon MA, Boulter L, Aucott RL, Ali A, Hartland SN, et al. Differential Ly-6C expression identifies the recruited macrophage phenotype, which orchestrates the regression of murine liver fibrosis. Proc Natl Acad Sci U S A 2012;109:E3186-3195.

33. Bosurgi L, Cao YG, Cabeza-Cabrerizo M, Tucci A, Hughes LD, Kong Y, Weinstein JS, et al. Macrophage function in tissue repair and remodeling requires IL-4 or IL-13 with apoptotic cells. Science 2017;356:1072-1076.

34. Martinez FO, Sica A, Mantovani A, Locati M. Macrophage activation and polarization. Front Biosci 2008;13:453-461.

35. Kohlhepp MS, Liu H, Tacke F, Guillot A. The contradictory roles of macrophages in non-alcoholic fatty liver disease and primary liver cancer-Challenges and opportunities. Front Mol Biosci 2023;10:1129831.

36. Movahedi K, Laoui D, Gysemans C, Baeten M, Stange G, Van den Bossche J, Mack M, et al. Different tumor microenvironments contain functionally distinct subsets of macrophages derived from Ly6C(high) monocytes. Cancer Res 2010;70:5728-5739.

37. Christofides A, Strauss L, Yeo A, Cao C, Charest A, Boussiotis VA. The complex role of tumor-infiltrating macrophages. Nat Immunol 2022;23:1148-1156.

38. Peiseler M, Schwabe R, Hampe J, Kubes P, Heikenwalder M, Tacke F. Immune mechanisms linking metabolic injury to inflammation and fibrosis in fatty liver disease - novel insights into cellular communication circuits. J Hepatol 2022;77:1136-1160.

39. Ferreira-Gonzalez S, Rodrigo-Torres D, Gadd VL, Forbes SJ. Cellular Senescence in Liver Disease and Regeneration. Semin Liver Dis 2021;41:50-66.

40. Kobayashi T, Iwaki M, Nakajima A, Nogami A, Yoneda M. Current Research on the Pathogenesis of NAFLD/NASH and the Gut-Liver Axis: Gut Microbiota, Dysbiosis, and Leaky-Gut Syndrome. Int J Mol Sci 2022;23.

41. Hartmann P, Chen WC, Schnabl B. The intestinal microbiome and the leaky gut as therapeutic targets in alcoholic liver disease. Front Physiol 2012;3:402.

42. Wynn TA. Fibrotic disease and the T(H)1/T(H)2 paradigm. Nat Rev Immunol 2004;4:583-594.

43. Zhang M, Zhang S. T Cells in Fibrosis and Fibrotic Diseases. Front Immunol 2020;11:1142.

44. He Y, Hwang S, Ahmed YA, Feng D, Li N, Ribeiro M, Lafdil F, et al. Immunopathobiology and therapeutic targets related to cytokines in liver diseases. Cell Mol Immunol 2021;18:18-37.

45. Wehr A, Baeck C, Heymann F, Niemietz PM, Hammerich L, Martin C, Zimmermann HW, et al. Chemokine receptor CXCR6-dependent hepatic NK T Cell accumulation promotes inflammation and liver fibrosis. J Immunol 2013;190:5226-5236.

46. Mossanen JC, Kohlhepp M, Wehr A, Krenkel O, Liepelt A, Roeth AA, Mockel D, et al. CXCR6 Inhibits Hepatocarcinogenesis by Promoting Natural Killer T- and CD4(+) T-Cell-Dependent Control of Senescence. Gastroenterology 2019;156:1877-1889 e1874.

47. Wallace SJ, Tacke F, Schwabe RF, Henderson NC. Understanding the cellular interactome of non-alcoholic fatty liver disease. JHEP Rep 2022;4:100524.

48. Jaitin DA, Adlung L, Thaiss CA, Weiner A, Li B, Descamps H, Lundgren P, et al. Lipid-Associated Macrophages Control Metabolic Homeostasis in a Trem2-Dependent Manner. Cell 2019;178:686-698 e614.

49. Sun H, Feng J, Tang L. Function of TREM1 and TREM2 in Liver-Related Diseases. Cells 2020;9.

50. Giraud J, Chalopin D, Blanc JF, Saleh M. Hepatocellular Carcinoma Immune Landscape and the Potential of Immunotherapies. Front Immunol 2021;12:655697.

51. Schwabe RF, Luedde T. Apoptosis and necroptosis in the liver: a matter of life and death. Nat Rev Gastroenterol Hepatol 2018;15:738-752.

52. Rumgay H, Ferlay J, de Martel C, Georges D, Ibrahim AS, Zheng R, Wei W, et al. Global, regional and national burden of primary liver cancer by subtype. Eur J Cancer 2022;161:108-118.

53. Sung H, Ferlay J, Siegel RL, Laversanne M, Soerjomataram I, Jemal A, Bray F. Global Cancer Statistics 2020: GLOBOCAN Estimates of Incidence and Mortality Worldwide for 36 Cancers in 185 Countries. CA Cancer J Clin 2021;71:209-249.

54. Finn RS, Qin S, Ikeda M, Galle PR, Ducreux M, Kim TY, Kudo M, et al. Atezolizumab plus Bevacizumab in Unresectable Hepatocellular Carcinoma. N Engl J Med 2020;382:1894-1905.

55. Sia D, Villanueva A, Friedman SL, Llovet JM. Liver Cancer Cell of Origin, Molecular Class, and Effects on Patient Prognosis. Gastroenterology 2017;152:745-761.

56.   Yang JD, Hainaut P, Gores GJ, Amadou A, Plymoth A, Roberts LR. A global view of hepatocellular carcinoma: trends, risk, prevention and management. Nat Rev Gastroenterol Hepatol 2019;16:589-604.

57.   Hanahan D, Weinberg RA. Hallmarks of cancer: the next generation. Cell 2011;144:646-674.

58.   Anderson NM, Simon MC. The tumor microenvironment. Curr Biol 2020;30:R921-R925.

59.   Gunaydin G. CAFs Interacting With TAMs in Tumor Microenvironment to Enhance Tumorigenesis and Immune Evasion. Front Oncol 2021;11:668349.

60.   Filliol A, Saito Y, Nair A, Dapito DH, Yu LX, Ravichandra A, Bhattacharjee S, et al. Opposing roles of hepatic stellate cell subpopulations in hepatocarcinogenesis. Nature 2022;610:356-365.

61.   Vanderborght B, Lefere S, Vlierberghe HV, Devisscher L. The Angiopoietin/Tie2 Pathway in Hepatocellular Carcinoma. Cells 2020;9.

62.   Viallard C, Larrivee B. Tumor angiogenesis and vascular normalization: alternative therapeutic targets. Angiogenesis 2017;20:409-426.

63.   Zhu AX, Duda DG, Sahani DV, Jain RK. HCC and angiogenesis: possible targets and future directions. Nat Rev Clin Oncol 2011;8:292-301.

64.   Yang ZF, Poon RT. Vascular changes in hepatocellular carcinoma. Anat Rec (Hoboken) 2008;291:721-734.

65.   Bishayee A. The role of inflammation and liver cancer. Adv Exp Med Biol 2014;816:401-435.

66.   Yu LX, Ling Y, Wang HY. Role of nonresolving inflammation in hepatocellular carcinoma development and progression. NPJ Precis Oncol 2018;2:6.

67.   Zhao H, Wu L, Yan G, Chen Y, Zhou M, Wu Y, Li Y. Inflammation and tumor progression: signaling pathways and targeted intervention. Signal Transduct Target Ther 2021;6:263.

68.   Park EJ, Lee JH, Yu GY, He G, Ali SR, Holzer RG, Osterreicher CH, et al. Dietary and genetic obesity promote liver inflammation and tumorigenesis by enhancing IL-6 and TNF expression. Cell 2010;140:197-208.

69.   Binnewies M, Roberts EW, Kersten K, Chan V, Fearon DF, Merad M, Coussens LM, et al. Understanding the tumor immune microenvironment (TIME) for effective therapy. Nat Med 2018;24:541-550.

70.   Tanaka A, Sakaguchi S. Regulatory T cells in cancer immunotherapy. Cell Res 2017;27:109-118.

71.   Hinshaw DC, Shevde LA. The Tumor Microenvironment Innately Modulates Cancer Progression. Cancer Res 2019;79:4557-4566.

72.   Gabrilovich DI. Myeloid-Derived Suppressor Cells. Cancer Immunol Res 2017;5:3-8.

73.   Yeung OW, Lo CM, Ling CC, Qi X, Geng W, Li CX, Ng KT, et al. Alternatively activated (M2) macrophages promote tumour growth and invasiveness in hepatocellular carcinoma. J Hepatol 2015;62:607-616.

74.   Ehling J, Tacke F. Role of chemokine pathways in hepatobiliary cancer. Cancer Lett 2016;379:173-183.

75.   Eggert T, Wolter K, Ji J, Ma C, Yevsa T, Klotz S, Medina-Echeverz J, et al. Distinct Functions of Senescence-Associated Immune Responses in Liver Tumor Surveillance and Tumor Progression. Cancer Cell 2016;30:533-547.

76.   Mantovani A, Allavena P, Marchesi F, Garlanda C. Macrophages as tools and targets in cancer therapy. Nat Rev Drug Discov 2022;21:799-820.

77.   Biswas SK, Mantovani A. Macrophage plasticity and interaction with lymphocyte subsets: cancer as a paradigm. Nat Immunol 2010;11:889-896.

78.   Mantovani A, Marchesi F, Malesci A, Laghi L, Allavena P. Tumour-associated macrophages as treatment targets in oncology. Nat Rev Clin Oncol 2017;14:399-416.

79.   Mannino MH, Zhu Z, Xiao H, Bai Q, Wakefield MR, Fang Y. The paradoxical role of IL-10 in immunity and cancer. Cancer Lett 2015;367:103-107.

80.   Mulder K, Patel AA, Kong WT, Piot C, Halitzki E, Dunsmore G, Khalilnezhad S, et al. Cross-tissue single-cell landscape of human monocytes and macrophages in health and disease. Immunity 2021;54:1883-1900 e1885.

81.   Pu Y, Ji Q. Tumor-Associated Macrophages Regulate PD-1/PD-L1 Immunosuppression. Front Immunol 2022;13:874589.

82.   Kuang DM, Zhao Q, Peng C, Xu J, Zhang JP, Wu C, Zheng L. Activated monocytes in peritumoral stroma of hepatocellular carcinoma foster immune privilege and disease progression through PD-L1. J Exp Med 2009;206:1327-1337.

83.   Bronte V, Serafini P, Mazzoni A, Segal DM, Zanovello P. L-arginine metabolism in myeloid cells controls T-lymphocyte functions. Trends Immunol 2003;24:302-306.

84.   Kessenbrock K, Plaks V, Werb Z. Matrix metalloproteinases: regulators of the tumor microenvironment. Cell 2010;141:52-67.

85.   Peng D, Fu M, Wang M, Wei Y, Wei X. Targeting TGF-beta signal transduction for fibrosis and cancer therapy. Mol Cancer 2022;21:104.

86.   Song G, Shi Y, Zhang M, Goswami S, Afridi S, Meng L, Ma J, et al. Global immune characterization of HBV/HCV-related hepatocellular carcinoma identifies macrophage and T-cell subsets associated with disease progression. Cell Discov 2020;6:90.

87.   Lu Y, Yang A, Quan C, Pan Y, Zhang H, Li Y, Gao C, et al. A single-cell atlas of the multicellular ecosystem of primary and metastatic hepatocellular carcinoma. Nat Commun 2022;13:4594.

88.   Bartneck M, Schrammen PL, Mockel D, Govaere O, Liepelt A, Krenkel O, Ergen C, et al. The CCR2(+) Macrophage Subset Promotes Pathogenic Angiogenesis for Tumor Vascularization in Fibrotic Livers. Cell Mol Gastroenterol Hepatol 2019;7:371-390.

89.   Abou Khouzam R, Brodaczewska K, Filipiak A, Zeinelabdin NA, Buart S, Szczylik C, Kieda C, et al. Tumor Hypoxia Regulates Immune Escape/Invasion: Influence on Angiogenesis and Potential Impact of Hypoxic Biomarkers on Cancer Therapies. Front Immunol 2020;11:613114.

90.   Ruthenborg RJ, Ban JJ, Wazir A, Takeda N, Kim JW. Regulation of wound healing and fibrosis by hypoxia and hypoxia-inducible factor-1. Mol Cells 2014;37:637-643.

91.   Hirschhaeuser F, Sattler UG, Mueller-Klieser W. Lactate: a metabolic key player in cancer. Cancer Res 2011;71:6921-6925.

92.   Bogdanov A, Bogdanov A, Chubenko V, Volkov N, Moiseenko F, Moiseyenko V. Tumor acidity: From hallmark of cancer to target of treatment. Front Oncol 2022;12:979154.

93.   Mahoney KM, Freeman GJ. Acidity changes immunology: a new VISTA pathway. Nat Immunol 2020;21:13-16.

94.   Freemerman AJ, Johnson AR, Sacks GN, Milner JJ, Kirk EL, Troester MA, Macintyre AN, et al. Metabolic reprogramming of macrophages: glucose transporter 1 (GLUT1)-mediated glucose metabolism drives a proinflammatory phenotype. J Biol Chem 2014;289:7884-7896.

95.   Paul B, Lewinska M, Andersen JB. Lipid alterations in chronic liver disease and liver cancer. JHEP Rep 2022;4:100479.

96.   Luo X, Zheng E, Wei L, Zeng H, Qin H, Zhang X, Liao M, et al. The fatty acid receptor CD36 promotes HCC progression through activating Src/PI3K/AKT axis-dependent aerobic glycolysis. Cell Death Dis 2021;12:328.

97.   Wu H, Han Y, Rodriguez Sillke Y, Deng H, Siddiqui S, Treese C, Schmidt F, et al. Lipid droplet-dependent fatty acid metabolism controls the immune suppressive phenotype of tumor-associated macrophages. EMBO Mol Med 2019;11:e10698.

98.   Hughes CE, Nibbs RJB. A guide to chemokines and their receptors. FEBS J 2018;285:2944-2971.

99.   Griffith JW, Sokol CL, Luster AD. Chemokines and chemokine receptors: positioning cells for host defense and immunity. Annu Rev Immunol 2014;32:659-702.

100.   Bachelerie F, Ben-Baruch A, Burkhardt AM, Combadiere C, Farber JM, Graham GJ, Horuk R, et al. International Union of Basic and Clinical Pharmacology. [corrected]. LXXXIX. Update on the extended family of chemokine receptors and introducing a new nomenclature for atypical chemokine receptors. Pharmacol Rev 2014;66:1-79.

101.   Janssens R, Struyf S, Proost P. The unique structural and functional features of CXCL12. Cell Mol Immunol 2018;15:299-311.

102.   Mollica Poeta V, Massara M, Capucetti A, Bonecchi R. Chemokines and Chemokine Receptors: New Targets for Cancer Immunotherapy. Front Immunol 2019;10:379.

103.   Proudfoot AE, Handel TM, Johnson Z, Lau EK, LiWang P, Clark-Lewis I, Borlat F, et al. Glycosaminoglycan binding and oligomerization are essential for the in vivo activity of certain chemokines. Proc Natl Acad Sci U S A 2003;100:1885-1890.

104.   Bao S, Darvishi M, A HA, Al-Haideri MT, Patra I, Kashikova K, Ahmad I, et al. CXC chemokine receptor 4 (CXCR4) blockade in cancer treatment. J Cancer Res Clin Oncol 2023;149:7945-7968.

105.   Luker GD, Yang J, Richmond A, Scala S, Festuccia C, Schottelius M, Wester HJ, et al. At the Bench: Pre-clinical evidence for multiple functions of CXCR4 in cancer. J Leukoc Biol 2021;109:969-989.

106.   Murphy PM, Heusinkveld L. Multisystem multitasking by CXCL12 and its receptors CXCR4 and ACKR3. Cytokine 2018;109:2-10.

107.   Ma Q, Jones D, Borghesani PR, Segal RA, Nagasawa T, Kishimoto T, Bronson RT, et al. Impaired B-lymphopoiesis, myelopoiesis, and derailed cerebellar neuron migration in CXCR4- and SDF-1-deficient mice. Proc Natl Acad Sci U S A 1998;95:9448-9453.

108.   Zou YR, Kottmann AH, Kuroda M, Taniuchi I, Littman DR. Function of the chemokine receptor CXCR4 in haematopoiesis and in cerebellar development. Nature 1998;393:595-599.

109.	Gerrits H, van Ingen Schenau DS, Bakker NE, van Disseldorp AJ, Strik A, Hermens LS, Koenen TB, et al. Early postnatal lethality and cardiovascular defects in CXCR7-deficient mice. Genesis 2008;46:235-245.

110.	Heusinkveld LE, Yim E, Yang A, Azani AB, Liu Q, Gao JL, McDermott DH, et al. Pathogenesis, diagnosis and therapeutic strategies in WHIM syndrome immunodeficiency. Expert Opin Orphan Drugs 2017;5:813-825.

111.	Cambier S, Gouwy M, Proost P. The chemokines CXCL8 and CXCL12: molecular and functional properties, role in disease and efforts towards pharmacological intervention. Cell Mol Immunol 2023;20:217-251.

112.	Feng Y, Broder CC, Kennedy PE, Berger EA. HIV-1 entry cofactor: functional cDNA cloning of a seven-transmembrane, G protein-coupled receptor. Science 1996;272:872-877.

113.	Shi Y, Riese DJ, 2nd, Shen J. The Role of the CXCL12/CXCR4/CXCR7 Chemokine Axis in Cancer. Front Pharmacol 2020;11:574667.

114.	Wang J, Knaut H. Chemokine signaling in development and disease. Development 2014;141:4199-4205.

115.	Smit MJ, Schlecht-Louf G, Neves M, van den Bor J, Penela P, Siderius M, Bachelerie F, et al. The CXCL12/CXCR4/ACKR3 Axis in the Tumor Microenvironment: Signaling, Crosstalk, and Therapeutic Targeting. Annu Rev Pharmacol Toxicol 2021;61:541-563.

116.	Koenen J, Bachelerie F, Balabanian K, Schlecht-Louf G, Gallego C. Atypical Chemokine Receptor 3 (ACKR3): A Comprehensive Overview of its Expression and Potential Roles in the Immune System. Mol Pharmacol 2019;96:809-818.

117.	Pawig L, Klasen C, Weber C, Bernhagen J, Noels H. Diversity and Inter-Connections in the CXCR4 Chemokine Receptor/Ligand Family: Molecular Perspectives. Front Immunol 2015;6:429.

118.	Schiraldi M, Raucci A, Munoz LM, Livoti E, Celona B, Venereau E, Apuzzo T, et al. HMGB1 promotes recruitment of inflammatory cells to damaged tissues by forming a complex with CXCL12 and signaling via CXCR4. J Exp Med 2012;209:551-563.

119.	Bianchi ME, Mezzapelle R. The Chemokine Receptor CXCR4 in Cell Proliferation and Tissue Regeneration. Front Immunol 2020;11:2109.

120.	Wang S, Gao S, Li Y, Qian X, Luan J, Lv X. Emerging Importance of Chemokine Receptor CXCR4 and Its Ligand in Liver Disease. Front Cell Dev Biol 2021;9:716842.

121.	Chen H, Li G, Liu Y, Ji S, Li Y, Xiang J, Zhou L, et al. Pleiotropic Roles of CXCR4 in Wound Repair and Regeneration. Front Immunol 2021;12:668758.

122.	Garcia-Cuesta EM, Santiago CA, Vallejo-Diaz J, Juarranz Y, Rodriguez-Frade JM, Mellado M. The Role of the CXCL12/CXCR4/ACKR3 Axis in Autoimmune Diseases. Front Endocrinol (Lausanne) 2019;10:585.

123.	Santagata S, Ierano C, Trotta AM, Capiluongo A, Auletta F, Guardascione G, Scala S. CXCR4 and CXCR7 Signaling Pathways: A Focus on the Cross-Talk Between Cancer Cells and Tumor Microenvironment. Front Oncol 2021;11:591386.

124.	Ramachandran P, Dobie R, Wilson-Kanamori JR, Dora EF, Henderson BEP, Luu NT, Portman JR, et al. Resolving the fibrotic niche of human liver cirrhosis at single-cell level. Nature 2019;575:512-518.

125.	Liepelt A, Tacke F. Stromal cell-derived factor-1 (SDF-1) as a target in liver diseases. Am J Physiol Gastrointest Liver Physiol 2016;311:G203-209.

126.	Ding BS, Cao Z, Lis R, Nolan DJ, Guo P, Simons M, Penfold ME, et al. Divergent angiocrine signals from vascular niche balance liver regeneration and fibrosis. Nature 2014;505:97-102.

127.	DeLeve LD, Wang X, Wang L. VEGF-sdf1 recruitment of CXCR7+ bone marrow progenitors of liver sinusoidal endothelial cells promotes rat liver regeneration. Am J Physiol Gastrointest Liver Physiol 2016;310:G739-746.

128.	Lehwald N, Duhme C, Wildner M, Kuhn S, Furst G, Forbes SJ, Jonas S, et al. HGF and SDF-1-mediated mobilization of CD133+ BMSC for hepatic regeneration following extensive liver resection. Liver Int 2014;34:89-101.

129.	Hao NB, Li CZ, Lu MH, Tang B, Wang SM, Wu YY, Liang GP, et al. SDF-1/CXCR4 Axis Promotes MSCs to Repair Liver Injury Partially through Trans-Differentiation and Fusion with Hepatocytes. Stem Cells Int 2015;2015:960387.

130.	Terada R, Yamamoto K, Hakoda T, Shimada N, Okano N, Baba N, Ninomiya Y, et al. Stromal cell-derived factor-1 from biliary epithelial cells recruits CXCR4-positive cells: implications for inflammatory liver diseases. Lab Invest 2003;83:665-672.

131.	Hong F, Tuyama A, Lee TF, Loke J, Agarwal R, Cheng X, Garg A, et al. Hepatic stellate cells express functional CXCR4: role in stromal cell-derived factor-1alpha-mediated stellate cell activation. Hepatology 2009;49:2055-2067.

132. Correia AL, Guimaraes JC, Auf der Maur P, De Silva D, Trefny MP, Okamoto R, Bruno S, et al. Hepatic stellate cells suppress NK cell-sustained breast cancer dormancy. Nature 2021;594:566-571.

133. Saiman Y, Agarwal R, Hickman DA, Fausther M, El-Shamy A, Dranoff JA, Friedman SL, et al. CXCL12 induces hepatic stellate cell contraction through a calcium-independent pathway. Am J Physiol Gastrointest Liver Physiol 2013;305:G375-382.

134. Liu H, Li J, Tillman B, Morgan TR, French BA, French SW. TLR3/4 signaling is mediated via the NFkappaB-CXCR4/7 pathway in human alcoholic hepatitis and non-alcoholic steatohepatitis which formed Mallory-Denk bodies. Exp Mol Pathol 2014;97:234-240.

135. Neve Polimeno M, Ierano C, D'Alterio C, Simona Losito N, Napolitano M, Portella L, Scognamiglio G, et al. CXCR4 expression affects overall survival of HCC patients whereas CXCR7 expression does not. Cell Mol Immunol 2015;12:474-482.

136. Schimanski CC, Bahre R, Gockel I, Muller A, Frerichs K, Horner V, Teufel A, et al. Dissemination of hepatocellular carcinoma is mediated via chemokine receptor CXCR4. Br J Cancer 2006;95:210-217.

137. Li X, Li P, Chang Y, Xu Q, Wu Z, Ma Q, Wang Z. The SDF-1/CXCR4 axis induces epithelial-mesenchymal transition in hepatocellular carcinoma. Mol Cell Biochem 2014;392:77-84.

138. Gao PT, Ding GY, Yang X, Dong RZ, Hu B, Zhu XD, Cai JB, et al. Invasive potential of hepatocellular carcinoma is enhanced by loss of selenium-binding protein 1 and subsequent upregulation of CXCR4. Am J Cancer Res 2018;8:1040-1049.

139. Zheng K, Li HY, Su XL, Wang XY, Tian T, Li F, Ren GS. Chemokine receptor CXCR7 regulates the invasion, angiogenesis and tumor growth of human hepatocellular carcinoma cells. J Exp Clin Cancer Res 2010;29:31.

140. Lin L, Han MM, Wang F, Xu LL, Yu HX, Yang PY. CXCR7 stimulates MAPK signaling to regulate hepatocellular carcinoma progression. Cell Death Dis 2014;5:e1488.

141. Gok Yavuz B, Gunaydin G, Gedik ME, Kosemehmetoglu K, Karakoc D, Ozgur F, Guc D. Cancer associated fibroblasts sculpt tumour microenvironment by recruiting monocytes and inducing immunosuppressive PD-1(+) TAMs. Sci Rep 2019;9:3172.

142. Deng Y, Cheng J, Fu B, Liu W, Chen G, Zhang Q, Yang Y. Hepatic carcinoma-associated fibroblasts enhance immune suppression by facilitating the generation of myeloid-derived suppressor cells. Oncogene 2017;36:1090-1101.

143. Yamada K, Maishi N, Akiyama K, Towfik Alam M, Ohga N, Kawamoto T, Shindoh M, et al. CXCL12-CXCR7 axis is important for tumor endothelial cell angiogenic property. Int J Cancer 2015;137:2825-2836.

144. Sharma A, Seow JJW, Dutertre CA, Pai R, Bleriot C, Mishra A, Wong RMM, et al. Onco-fetal Reprogramming of Endothelial Cells Drives Immunosuppressive Macrophages in Hepatocellular Carcinoma. Cell 2020;183:377-394 e321.

145. Sanchez-Martin L, Estecha A, Samaniego R, Sanchez-Ramon S, Vega MA, Sanchez-Mateos P. The chemokine CXCL12 regulates monocyte-macrophage differentiation and RUNX3 expression. Blood 2011;117:88-97.

146. Bertran E, Crosas-Molist E, Sancho P, Caja L, Lopez-Luque J, Navarro E, Egea G, et al. Overactivation of the TGF-beta pathway confers a mesenchymal-like phenotype and CXCR4-dependent migratory properties to liver tumor cells. Hepatology 2013;58:2032-2044.

147. Meng YM, Liang J, Wu C, Xu J, Zeng DN, Yu XJ, Ning H, et al. Monocytes/Macrophages promote vascular CXCR4 expression via the ERK pathway in hepatocellular carcinoma. Oncoimmunology 2018;7:e1408745.

148. Singh S, Fujii LL, Murad MH, Wang Z, Asrani SK, Ehman RL, Kamath PS, et al. Liver stiffness is associated with risk of decompensation, liver cancer, and death in patients with chronic liver diseases: a systematic review and meta-analysis. Clin Gastroenterol Hepatol 2013;11:1573-1584 e1571-1572; quiz e1588-1579.

149. Cai X, Wang KC, Meng Z. Mechanoregulation of YAP and TAZ in Cellular Homeostasis and Disease Progression. Front Cell Dev Biol 2021;9:673599.

150. Yang N, Chen T, Wang L, Liu R, Niu Y, Sun L, Yao B, et al. CXCR4 mediates matrix stiffness-induced downregulation of UBTD1 driving hepatocellular carcinoma progression via YAP signaling pathway. Theranostics 2020;10:5790-5801.

151. Monnier J, Boissan M, L'Helgoualc'h A, Lacombe ML, Turlin B, Zucman-Rossi J, Theret N, et al. CXCR7 is up-regulated in human and murine hepatocellular carcinoma and is specifically expressed by endothelial cells. Eur J Cancer 2012;48:138-148.

152. Xu J, Liang J, Meng YM, Yan J, Yu XJ, Liu CQ, Xu L, et al. Vascular CXCR4 Expression Promotes Vessel Sprouting and Sensitivity to Sorafenib Treatment in Hepatocellular Carcinoma. Clin Cancer Res 2017;23:4482-4492.

153. Pitulescu ME, Schmidt I, Giaimo BD, Antoine T, Berkenfeld F, Ferrante F, Park H, et al. Dll4 and Notch signalling couples sprouting angiogenesis and artery formation. Nat Cell Biol 2017;19:915-927.

154. Li H. Angiogenesis in the progression from liver fibrosis to cirrhosis and hepatocelluar carcinoma. Expert Rev Gastroenterol Hepatol 2021;15:217-233.

155. Liang Z, Brooks J, Willard M, Liang K, Yoon Y, Kang S, Shim H. CXCR4/CXCL12 axis promotes VEGF-mediated tumor angiogenesis through Akt signaling pathway. Biochem Biophys Res Commun 2007;359:716-722.

156. Fang JH, Zhou HC, Zhang C, Shang LR, Zhang L, Xu J, Zheng L, et al. A novel vascular pattern promotes metastasis of hepatocellular carcinoma in an epithelial-mesenchymal transition-independent manner. Hepatology 2015;62:452-465.

157. Sugino T, Yamaguchi T, Ogura G, Saito A, Hashimoto T, Hoshi N, Yoshida S, et al. Morphological evidence for an invasion-independent metastasis pathway exists in multiple human cancers. BMC Med 2004;2:9.

158. Renne SL, Woo HY, Allegra S, Rudini N, Yano H, Donadon M, Vigano L, et al. Vessels Encapsulating Tumor Clusters (VETC) Is a Powerful Predictor of Aggressive Hepatocellular Carcinoma. Hepatology 2020;71:183-195.

159. Shen X, Li N, Li H, Zhang T, Wang F, Li Q. Increased prevalence of regulatory T cells in the tumor microenvironment and its correlation with TNM stage of hepatocellular carcinoma. J Cancer Res Clin Oncol 2010;136:1745-1754.

160. Meiron M, Zohar Y, Anunu R, Wildbaum G, Karin N. CXCL12 (SDF-1alpha) suppresses ongoing experimental autoimmune encephalomyelitis by selecting antigen-specific regulatory T cells. J Exp Med 2008;205:2643-2655.

161. Santagata S, Napolitano M, D'Alterio C, Desicato S, Maro SD, Marinelli L, Fragale A, et al. Targeting CXCR4 reverts the suppressive activity of T-regulatory cells in renal cancer. Oncotarget 2017;8:77110-77120.

162. Xu Y, Fang F, Jiao H, Zheng X, Huang L, Yi X, Zhao W. Activated hepatic stellate cells regulate MDSC migration through the SDF-1/CXCR4 axis in an orthotopic mouse model of hepatocellular carcinoma. Cancer Immunol Immunother 2019;68:1959-1969.

163. Hughes R, Qian BZ, Rowan C, Muthana M, Keklikoglou I, Olson OC, Tazzyman S, et al. Perivascular M2 Macrophages Stimulate Tumor Relapse after Chemotherapy. Cancer Res 2015;75:3479-3491.

164. Vianello F, Papeta N, Chen T, Kraft P, White N, Hart WK, Kircher MF, et al. Murine B16 melanomas expressing high levels of the chemokine stromal-derived factor-1/CXCL12 induce tumor-specific T cell chemorepulsion and escape from immune control. J Immunol 2006;176:2902-2914.

165. Zboralski D, Hoehlig K, Eulberg D, Fromming A, Vater A. Increasing Tumor-Infiltrating T Cells through Inhibition of CXCL12 with NOX-A12 Synergizes with PD-1 Blockade. Cancer Immunol Res 2017;5:950-956.

166. Stirling DR, Swain-Bowden MJ, Lucas AM, Carpenter AE, Cimini BA, Goodman A. CellProfiler 4: improvements in speed, utility and usability. BMC Bioinformatics 2021;22:433.

167. Schindelin J, Arganda-Carreras I, Frise E, Kaynig V, Longair M, Pietzsch T, Preibisch S, et al. Fiji: an open-source platform for biological-image analysis. Nat Methods 2012;9:676-682.

168. Berg S, Kutra D, Kroeger T, Straehle CN, Kausler BX, Haubold C, Schiegg M, et al. ilastik: interactive machine learning for (bio)image analysis. Nat Methods 2019;16:1226-1232.

169. Bankhead P, Loughrey MB, Fernandez JA, Dombrowski Y, McArt DG, Dunne PD, McQuaid S, et al. QuPath: Open source software for digital pathology image analysis. Sci Rep 2017;7:16878.

170. Slater TF, Cheeseman KH, Ingold KU. Carbon tetrachloride toxicity as a model for studying free-radical mediated liver injury. Philos Trans R Soc Lond B Biol Sci 1985;311:633-645.

171. Liedtke C, Luedde T, Sauerbruch T, Scholten D, Streetz K, Tacke F, Tolba R, et al. Experimental liver fibrosis research: update on animal models, legal issues and translational aspects. Fibrogenesis Tissue Repair 2013;6:19.

172. Bakiri L, Wagner EF. Mouse models for liver cancer. Mol Oncol 2013;7:206-223.

173. Uehara T, Pogribny IP, Rusyn I. The DEN and CCl(4) -Induced Mouse Model of Fibrosis and Inflammation-Associated Hepatocellular Carcinoma. Curr Protoc 2021;1:e211.

174. Vater A, Klussmann S. Turning mirror-image oligonucleotides into drugs: the evolution of Spiegelmer((R)) therapeutics. Drug Discov Today 2015;20:147-155.

175. Willems B, Tong L, Minh TDT, Pham ND, Nguyen XH, Zumbansen M. Novel Cytokine Multiplex Assay for Tear Fluid Analysis in Sjogren's Syndrome. Ocul Immunol Inflamm 2021;29:1639-1644.

176.   Vater A, Sahlmann J, Kroger N, Zollner S, Lioznov M, Maasch C, Buchner K, et al. Hematopoietic stem and progenitor cell mobilization in mice and humans by a first-in-class mirror-image oligonucleotide inhibitor of CXCL12. Clin Pharmacol Ther 2013;94:150-157.

177.   Neuman RE, Logan MA. The determination of hydroxyproline. J Biol Chem 1950;184:299-306.

178.   Junqueira LC, Bignolas G, Brentani RR. Picrosirius staining plus polarization microscopy, a specific method for collagen detection in tissue sections. Histochem J 1979;11:447-455.

179.   Guillot A, Kohlhepp MS, Bruneau A, Heymann F, Tacke F. Deciphering the Immune Microenvironment on A Single Archival Formalin-Fixed Paraffin-Embedded Tissue Section by An Immediately Implementable Multiplex Fluorescence Immunostaining Protocol. Cancers (Basel) 2020;12.

180.   Friemel J, Frick L, Unger K, Egger M, Parrotta R, Boge YT, Adili A, et al. Characterization of HCC Mouse Models: Towards an Etiology-Oriented Subtyping Approach. Mol Cancer Res 2019;17:1493-1502.

181.   Heymann F, Peusquens J, Ludwig-Portugall I, Kohlhepp M, Ergen C, Niemietz P, Martin C, et al. Liver inflammation abrogates immunological tolerance induced by Kupffer cells. Hepatology 2015;62:279-291.

182.   Chen Y, Ramjiawan RR, Reiberger T, Ng MR, Hato T, Huang Y, Ochiai H, et al. CXCR4 inhibition in tumor microenvironment facilitates anti-programmed death receptor-1 immunotherapy in sorafenib-treated hepatocellular carcinoma in mice. Hepatology 2015;61:1591-1602.

183.   D'Alterio C, Buoncervello M, Ierano C, Napolitano M, Portella L, Rea G, Barbieri A, et al. Targeting CXCR4 potentiates anti-PD-1 efficacy modifying the tumor microenvironment and inhibiting neoplastic PD-1. J Exp Clin Cancer Res 2019;38:432.

184.   Abel AM, Yang C, Thakar MS, Malarkannan S. Natural Killer Cells: Development, Maturation, and Clinical Utilization. Front Immunol 2018;9:1869.

185.   Kawai K, Tsuno NH, Matsuhashi M, Kitayama J, Osada T, Yamada J, Tsuchiya T, et al. CD11b-mediated migratory property of peripheral blood B cells. J Allergy Clin Immunol 2005;116:192-197.

186.   DeLeve LD, Maretti-Mira AC. Liver Sinusoidal Endothelial Cell: An Update. Semin Liver Dis 2017;37:377-387.

187.   Schrage A, Loddenkemper C, Erben U, Lauer U, Hausdorf G, Jungblut PR, Johnson J, et al. Murine CD146 is widely expressed on endothelial cells and is recognized by the monoclonal antibody ME-9F1. Histochem Cell Biol 2008;129:441-451.

188.   Sun HC, Tang ZY, Li XM, Zhou YN, Sun BR, Ma ZC. Microvessel density of hepatocellular carcinoma: its relationship with prognosis. J Cancer Res Clin Oncol 1999;125:419-426.

189.   Ninichuk V, Clauss S, Kulkarni O, Schmid H, Segerer S, Radomska E, Eulberg D, et al. Late onset of Ccl2 blockade with the Spiegelmer mNOX-E36-3'PEG prevents glomerulosclerosis and improves glomerular filtration rate in db/db mice. Am J Pathol 2008;172:628-637.

190.   Hoellenriegel J, Zboralski D, Maasch C, Rosin NY, Wierda WG, Keating MJ, Kruschinski A, et al. The Spiegelmer NOX-A12, a novel CXCL12 inhibitor, interferes with chronic lymphocytic leukemia cell motility and causes chemosensitization. Blood 2014;123:1032-1039.

191.   Darisipudi MN, Kulkarni OP, Sayyed SG, Ryu M, Migliorini A, Sagrinati C, Parente E, et al. Dual blockade of the homeostatic chemokine CXCL12 and the proinflammatory chemokine CCL2 has additive protective effects on diabetic kidney disease. Am J Pathol 2011;179:116-124.

192.   Chow LN, Schreiner P, Ng BY, Lo B, Hughes MR, Scott RW, Gusti V, et al. Impact of a CXCL12/CXCR4 Antagonist in Bleomycin (BLM) Induced Pulmonary Fibrosis and Carbon Tetrachloride (CCl4) Induced Hepatic Fibrosis in Mice. PLoS One 2016;11:e0151765.

193.   Saiman Y, Jiao J, Fiel MI, Friedman SL, Aloman C, Bansal MB. Inhibition of the CXCL12/CXCR4 chemokine axis with AMD3100, a CXCR4 small molecule inhibitor, worsens murine hepatic injury. Hepatol Res 2015;45:794-803.

194.   Tsuchiya A, Imai M, Kamimura H, Takamura M, Yamagiwa S, Sugiyama T, Nomoto M, et al. Increased susceptibility to severe chronic liver damage in CXCR4 conditional knock-out mice. Dig Dis Sci 2012;57:2892-2900.

195.   Seemann S, Lupp A. Administration of AMD3100 in endotoxemia is associated with pro-inflammatory, pro-oxidative, and pro-apoptotic effects in vivo. J Biomed Sci 2016;23:68.

196.   Ito C, Haraguchi R, Ogawa K, Iwata M, Kitazawa R, Takada Y, Kitazawa S. Demethylation in promoter region of severely damaged hepatocytes enhances chemokine receptor CXCR4 gene expression. Histochem Cell Biol 2023.

197.   Saini V, Marchese A, Majetschak M. CXC chemokine receptor 4 is a cell surface receptor for extracellular ubiquitin. J Biol Chem 2010;285:15566-15576.

198. Rajasekaran D, Groning S, Schmitz C, Zierow S, Drucker N, Bakou M, Kohl K, et al. Macrophage Migration Inhibitory Factor-CXCR4 Receptor Interactions: EVIDENCE FOR PARTIAL ALLOSTERIC AGONISM IN COMPARISON WITH CXCL12 CHEMOKINE. J Biol Chem 2016;291:15881-15895.

199. Tanegashima K, Suzuki K, Nakayama Y, Tsuji K, Shigenaga A, Otaka A, Hara T. CXCL14 is a natural inhibitor of the CXCL12-CXCR4 signaling axis. FEBS Lett 2013;587:1731-1735.

200. Schwartz V, Lue H, Kraemer S, Korbiel J, Krohn R, Ohl K, Bucala R, et al. A functional heteromeric MIF receptor formed by CD74 and CXCR4. FEBS Lett 2009;583:2749-2757.

201. Bernhagen J, Krohn R, Lue H, Gregory JL, Zernecke A, Koenen RR, Dewor M, et al. MIF is a noncognate ligand of CXC chemokine receptors in inflammatory and atherogenic cell recruitment. Nat Med 2007;13:587-596.

202. Jankauskas SS, Wong DWL, Bucala R, Djudjaj S, Boor P. Evolving complexity of MIF signaling. Cell Signal 2019;57:76-88.

203. Heinrichs D, Knauel M, Offermanns C, Berres ML, Nellen A, Leng L, Schmitz P, et al. Macrophage migration inhibitory factor (MIF) exerts antifibrotic effects in experimental liver fibrosis via CD74. Proc Natl Acad Sci U S A 2011;108:17444-17449.

204. Thavayogarajah T, Sinitski D, El Bounkari O, Torres-Garcia L, Lewinsky H, Harjung A, Chen HR, et al. CXCR4 and CD74 together enhance cell survival in response to macrophage migration-inhibitory factor in chronic lymphocytic leukemia. Exp Hematol 2022;115:30-43.

205. Van Loy T, De Jonghe S, Castermans K, Dheedene W, Stoop R, Verschuren L, Versele M, et al. Stimulation of the atypical chemokine receptor 3 (ACKR3) by a small-molecule agonist attenuates fibrosis in a preclinical liver but not lung injury model. Cell Mol Life Sci 2022;79:293.

206. Xiao Ling K, Peng L, Jian Feng Z, Wei C, Wei Yan Y, Nan S, Cheng Qi G, et al. Stromal Derived Factor-1/CXCR4 Axis Involved in Bone Marrow Mesenchymal Stem Cells Recruitment to Injured Liver. Stem Cells Int 2016;2016:8906945.

207. Zhang S, Lv C, Yang X, Han Z, Zhang S, Zhang J, Zong C, et al. Corticosterone mediates the inhibitory effect of restraint stress on the migration of mesenchymal stem cell to carbon tetrachloride-induced fibrotic liver by downregulating CXCR4/7 expression. Stem Cells Dev 2015;24:587-596.

208. Wilson GC, Freeman CM, Kuethe JW, Quillin RC, 3rd, Nojima H, Schuster R, Blanchard J, et al. CXC chemokine receptor-4 signaling limits hepatocyte proliferation after hepatic ischemia-reperfusion in mice. Am J Physiol Gastrointest Liver Physiol 2015;308:G702-709.

209. O'Brien PJ, Slaughter MR, Polley SR, Kramer K. Advantages of glutamate dehydrogenase as a blood biomarker of acute hepatic injury in rats. Lab Anim 2002;36:313-321.

210. Devine SM, Vij R, Rettig M, Todt L, McGlauchlen K, Fisher N, Devine H, et al. Rapid mobilization of functional donor hematopoietic cells without G-CSF using AMD3100, an antagonist of the CXCR4/SDF-1 interaction. Blood 2008;112:990-998.

211. Chong SZ, Evrard M, Devi S, Chen J, Lim JY, See P, Zhang Y, et al. CXCR4 identifies transitional bone marrow premonocytes that replenish the mature monocyte pool for peripheral responses. J Exp Med 2016;213:2293-2314.

212. Liu Q, Li Z, Gao JL, Wan W, Ganesan S, McDermott DH, Murphy PM. CXCR4 antagonist AMD3100 redistributes leukocytes from primary immune organs to secondary immune organs, lung, and blood in mice. Eur J Immunol 2015;45:1855-1867.

213. Devi S, Wang Y, Chew WK, Lima R, N AG, Mattar CN, Chong SZ, et al. Neutrophil mobilization via plerixafor-mediated CXCR4 inhibition arises from lung demargination and blockade of neutrophil homing to the bone marrow. J Exp Med 2013;210:2321-2336.

214. Nie Y, Waite J, Brewer F, Sunshine MJ, Littman DR, Zou YR. The role of CXCR4 in maintaining peripheral B cell compartments and humoral immunity. J Exp Med 2004;200:1145-1156.

215. Okada T, Ngo VN, Ekland EH, Forster R, Lipp M, Littman DR, Cyster JG. Chemokine requirements for B cell entry to lymph nodes and Peyer's patches. J Exp Med 2002;196:65-75.

216. Gallego C, Vetillard M, Calmette J, Roriz M, Marin-Esteban V, Evrard M, Aknin ML, et al. CXCR4 signaling controls dendritic cell location and activation at steady state and in inflammation. Blood 2021;137:2770-2784.

217. Roccaro AM, Sacco A, Purschke WG, Moschetta M, Buchner K, Maasch C, Zboralski D, et al. SDF-1 inhibition targets the bone marrow niche for cancer therapy. Cell Rep 2014;9:118-128.

218. Fu J, Lehmann CHK, Wang X, Wahlbuhl M, Allabauer I, Wilde B, Amon L, et al. CXCR4 blockade reduces the severity of murine heart allograft rejection by plasmacytoid dendritic cell-mediated immune regulation. Sci Rep 2021;11:23815.

219.   Kabashima K, Sugita K, Shiraishi N, Tamamura H, Fujii N, Tokura Y. CXCR4 engagement promotes dendritic cell survival and maturation. Biochem Biophys Res Commun 2007;361:1012-1016.

220.   Jung H, Mithal DS, Park JE, Miller RJ. Localized CCR2 Activation in the Bone Marrow Niche Mobilizes Monocytes by Desensitizing CXCR4. PLoS One 2015;10:e0128387.

221.   Zou Y, Kamada N, Seong SY, Seo SU. CD115(-) monocytic myeloid-derived suppressor cells are precursors of OLFM4(high) polymorphonuclear myeloid-derived suppressor cells. Commun Biol 2023;6:272.

222.   Lefere S, Puengel T, Hundertmark J, Penners C, Frank AK, Guillot A, de Muynck K, et al. Differential effects of selective- and pan-PPAR agonists on experimental steatohepatitis and hepatic macrophages(☆). J Hepatol 2020;73:757-770.

223.   Wilson MT, Johansson C, Olivares-Villagomez D, Singh AK, Stanic AK, Wang CR, Joyce S, et al. The response of natural killer T cells to glycolipid antigens is characterized by surface receptor down-modulation and expansion. Proc Natl Acad Sci U S A 2003;100:10913-10918.

224.   Aktas E, Kucuksezer UC, Bilgic S, Erten G, Deniz G. Relationship between CD107a expression and cytotoxic activity. Cell Immunol 2009;254:149-154.

225.   Nomura T, Hasegawa H, Kohno M, Sasaki M, Fujita S. Enhancement of anti-tumor immunity by tumor cells transfected with the secondary lymphoid tissue chemokine EBI-1-ligand chemokine and stromal cell-derived factor-1alpha chemokine genes. Int J Cancer 2001;91:597-606.

226.   Borge M, Nannini PR, Morande PE, Jancic C, Bistmans A, Bezares RF, Giordano M, et al. CXCL12 is a costimulator for CD4+ T cell activation and proliferation in chronic lymphocytic leukemia patients. Cancer Immunol Immunother 2013;62:113-124.

227.   Munk R, Ghosh P, Ghosh MC, Saito T, Xu M, Carter A, Indig F, et al. Involvement of mTOR in CXCL12 mediated T cell signaling and migration. PLoS One 2011;6:e24667.

228.   Kremer KN, Clift IC, Miamen AG, Bamidele AO, Qian NX, Humphreys TD, Hedin KE. Stromal cell-derived factor-1 signaling via the CXCR4-TCR heterodimer requires phospholipase C-beta3 and phospholipase C-gamma1 for distinct cellular responses. J Immunol 2011;187:1440-1447.

229.   Contento RL, Molon B, Boularan C, Pozzan T, Manes S, Marullo S, Viola A. CXCR4-CCR5: a couple modulating T cell functions. Proc Natl Acad Sci U S A 2008;105:10101-10106.

230.   Nanki T, Lipsky PE. Cutting edge: stromal cell-derived factor-1 is a costimulator for CD4+ T cell activation. J Immunol 2000;164:5010-5014.

231.   Suzuki Y, Rahman M, Mitsuya H. Diverse transcriptional response of CD4+ T cells to stromal cell-derived factor SDF-1: cell survival promotion and priming effects of SDF-1 on CD4+ T cells. J Immunol 2001;167:3064-3073.

232.   Nanki T, Lipsky PE. Stimulation of T-Cell activation by CXCL12/stromal cell derived factor-1 involves a G-protein mediated signaling pathway. Cell Immunol 2001;214:145-154.

233.   Saudemont A, Jouy N, Hetuin D, Quesnel B. NK cells that are activated by CXCL10 can kill dormant tumor cells that resist CTL-mediated lysis and can express B7-H1 that stimulates T cells. Blood 2005;105:2428-2435.

234.   Quatrini L, Mariotti FR, Munari E, Tumino N, Vacca P, Moretta L. The Immune Checkpoint PD-1 in Natural Killer Cells: Expression, Function and Targeting in Tumour Immunotherapy. Cancers (Basel) 2020;12.

235.   Bigorgne AE, Bouchet-Delbos L, Naveau S, Dagher I, Prevot S, Durand-Gasselin I, Couderc J, et al. Obesity-induced lymphocyte hyperresponsiveness to chemokines: a new mechanism of Fatty liver inflammation in obese mice. Gastroenterology 2008;134:1459-1469.

236.   Boujedidi H, Robert O, Bignon A, Cassard-Doulcier AM, Renoud ML, Gary-Gouy H, Hemon P, et al. CXCR4 dysfunction in non-alcoholic steatohepatitis in mice and patients. Clin Sci (Lond) 2015;128:257-267.

237.   Jakubzick CV, Randolph GJ, Henson PM. Monocyte differentiation and antigen-presenting functions. Nat Rev Immunol 2017;17:349-362.

238.   Bonnardel J, T'Jonck W, Gaublomme D, Browaeys R, Scott CL, Martens L, Vanneste B, et al. Stellate Cells, Hepatocytes, and Endothelial Cells Imprint the Kupffer Cell Identity on Monocytes Colonizing the Liver Macrophage Niche. Immunity 2019;51:638-654 e639.

239.   Chatterjee M, von Ungern-Sternberg SN, Seizer P, Schlegel F, Buttcher M, Sindhu NA, Muller S, et al. Platelet-derived CXCL12 regulates monocyte function, survival, differentiation into macrophages and foam cells through differential involvement of CXCR4-CXCR7. Cell Death Dis 2015;6:e1989.

240.   Tian X, Xie G, Xiao H, Ding F, Bao W, Zhang M. CXCR4 knockdown prevents inflammatory cytokine expression in macrophages by suppressing activation of MAPK and NF-kappaB signaling pathways. Cell Biosci 2019;9:55.

241.   Zhang M, Angata T, Cho JY, Miller M, Broide DH, Varki A. Defining the in vivo function of Siglec-F, a CD33-related Siglec expressed on mouse eosinophils. Blood 2007;109:4280-4287.

242.   Garcia-Zepeda EA, Rothenberg ME, Ownbey RT, Celestin J, Leder P, Luster AD. Human eotaxin is a specific chemoattractant for eosinophil cells and provides a new mechanism to explain tissue eosinophilia. Nat Med 1996;2:449-456.

243.   Nagase H, Miyamasu M, Yamaguchi M, Fujisawa T, Ohta K, Yamamoto K, Morita Y, et al. Expression of CXCR4 in eosinophils: functional analyses and cytokine-mediated regulation. J Immunol 2000;164:5935-5943.

244.   Hu JS, Freeman CM, Stolberg VR, Chiu BC, Bridger GJ, Fricker SP, Lukacs NW, et al. AMD3465, a novel CXCR4 receptor antagonist, abrogates schistosomal antigen-elicited (type-2) pulmonary granuloma formation. Am J Pathol 2006;169:424-432.

245.   Avniel S, Arik Z, Maly A, Sagie A, Basst HB, Yahana MD, Weiss ID, et al. Involvement of the CXCL12/CXCR4 pathway in the recovery of skin following burns. J Invest Dermatol 2006;126:468-476.

246.   Regenass P, Abboud D, Daubeuf F, Lehalle C, Gizzi P, Riche S, Hachet-Haas M, et al. Discovery of a Locally and Orally Active CXCL12 Neutraligand (LIT-927) with Anti-inflammatory Effect in a Murine Model of Allergic Airway Hypereosinophilia. J Med Chem 2018;61:7671-7686.

247.   Schmid-Grendelmeier P, Altznauer F, Fischer B, Bizer C, Straumann A, Menz G, Blaser K, et al. Eosinophils express functional IL-13 in eosinophilic inflammatory diseases. J Immunol 2002;169:1021-1027.

248.   Goh YP, Henderson NC, Heredia JE, Red Eagle A, Odegaard JI, Lehwald N, Nguyen KD, et al. Eosinophils secrete IL-4 to facilitate liver regeneration. Proc Natl Acad Sci U S A 2013;110:9914-9919.

249.   Klion AD, Nutman TB. The role of eosinophils in host defense against helminth parasites. J Allergy Clin Immunol 2004;113:30-37.

250.   Gleich GJ. Mechanisms of eosinophil-associated inflammation. J Allergy Clin Immunol 2000;105:651-663.

251.   Wang Y, Yang Y, Wang M, Wang S, Jeong JM, Xu L, Wen Y, et al. Eosinophils attenuate hepatic ischemia-reperfusion injury in mice through ST2-dependent IL-13 production. Sci Transl Med 2021;13.

252.   Xu L, Yang Y, Jiang J, Wen Y, Jeong JM, Emontzpohl C, Atkins CL, et al. Eosinophils protect against acetaminophen-induced liver injury through cyclooxygenase-mediated IL-4/IL-13 production. Hepatology 2023;77:456-465.

253.   Isobe Y, Kato T, Arita M. Emerging roles of eosinophils and eosinophil-derived lipid mediators in the resolution of inflammation. Front Immunol 2012;3:270.

254.   Wu D, Molofsky AB, Liang HE, Ricardo-Gonzalez RR, Jouihan HA, Bando JK, Chawla A, et al. Eosinophils sustain adipose alternatively activated macrophages associated with glucose homeostasis. Science 2011;332:243-247.

255.   Krenkel O, Hundertmark J, Abdallah AT, Kohlhepp M, Puengel T, Roth T, Branco DPP, et al. Myeloid cells in liver and bone marrow acquire a functionally distinct inflammatory phenotype during obesity-related steatohepatitis. Gut 2020;69:551-563.

256.   Puengel T, Liu H, Guillot A, Heymann F, Tacke F, Peiseler M. Nuclear Receptors Linking Metabolism, Inflammation, and Fibrosis in Nonalcoholic Fatty Liver Disease. Int J Mol Sci 2022;23.

257.   Hart KM, Fabre T, Sciurba JC, Gieseck RL, 3rd, Borthwick LA, Vannella KM, Acciani TH, et al. Type 2 immunity is protective in metabolic disease but exacerbates NAFLD collaboratively with TGF-beta. Sci Transl Med 2017;9.

258.   Garcia-Irigoyen O, Latasa MU, Carotti S, Uriarte I, Elizalde M, Urtasun R, Vespasiani-Gentilucci U, et al. Matrix metalloproteinase 10 contributes to hepatocarcinogenesis in a novel crosstalk with the stromal derived factor 1/C-X-C chemokine receptor 4 axis. Hepatology 2015;62:166-178.

259.   Tsai CN, Yu SC, Lee CW, Pang JS, Wu CH, Lin SE, Chung YH, et al. SOX4 activates CXCL12 in hepatocellular carcinoma cells to modulate endothelial cell migration and angiogenesis in vivo. Oncogene 2020;39:4695-4710.

260.   Wang Y, Yu H, Shan Y, Tao C, Wu F, Yu Z, Guo P, et al. EphA1 activation promotes the homing of endothelial progenitor cells to hepatocellular carcinoma for tumor neovascularization through the SDF-1/CXCR4 signaling pathway. J Exp Clin Cancer Res 2016;35:65.

261.   Song JS, Chang CC, Wu CH, Dinh TK, Jan JJ, Huang KW, Chou MC, et al. A highly selective and potent CXCR4 antagonist for hepatocellular carcinoma treatment. Proc Natl Acad Sci U S A 2021;118.

262.   Zheng N, Liu W, Li B, Nie H, Liu J, Cheng Y, Wang J, et al. Co-delivery of sorafenib and metapristone encapsulated by CXCR4-targeted PLGA-PEG nanoparticles overcomes hepatocellular carcinoma resistance to sorafenib. J Exp Clin Cancer Res 2019;38:232.

263.   Zhao ZW, Fan XX, Song JJ, Xu M, Chen MJ, Tu JF, Wu FZ, et al. ShRNA knock-down of CXCR7 inhibits tumour invasion and metastasis in hepatocellular carcinoma after transcatheter arterial chemoembolization. J Cell Mol Med 2017;21:1989-1999.

264.   Suarez-Carmona M, Williams A, Schreiber J, Hohmann N, Pruefer U, Krauss J, Jager D, et al. Combined inhibition of CXCL12 and PD-1 in MSS colorectal and pancreatic cancer: modulation of the microenvironment and clinical effects. J Immunother Cancer 2021;9.

265.   Pfister D, Nunez NG, Pinyol R, Govaere O, Pinter M, Szydlowska M, Gupta R, et al. NASH limits anti-tumour surveillance in immunotherapy-treated HCC. Nature 2021;592:450-456.

266.   Qin S, Chen Z, Fang W, Ren Z, Xu R, Ryoo BY, Meng Z, et al. Pembrolizumab Versus Placebo as Second-Line Therapy in Patients From Asia With Advanced Hepatocellular Carcinoma: A Randomized, Double-Blind, Phase III Trial. J Clin Oncol 2023;41:1434-1443.

267.   Yau T, Park JW, Finn RS, Cheng AL, Mathurin P, Edeline J, Kudo M, et al. Nivolumab versus sorafenib in advanced hepatocellular carcinoma (CheckMate 459): a randomised, multicentre, open-label, phase 3 trial. Lancet Oncol 2022;23:77-90.

268.   Geraud C, Mogler C, Runge A, Evdokimov K, Lu S, Schledzewski K, Arnold B, et al. Endothelial transdifferentiation in hepatocellular carcinoma: loss of Stabilin-2 expression in peri-tumourous liver correlates with increased survival. Liver Int 2013;33:1428-1440.

269.   Thomann S, Longerich T, Bazhin AV, Mier W, Schemmer P, Ryschich E. Selective targeting of liver cancer with the endothelial marker CD146. Oncotarget 2014;5:8614-8624.

270.   Carretero R, Sektioglu IM, Garbi N, Salgado OC, Beckhove P, Hammerling GJ. Eosinophils orchestrate cancer rejection by normalizing tumor vessels and enhancing infiltration of CD8(+) T cells. Nat Immunol 2015;16:609-617.

271.   Hollande C, Boussier J, Ziai J, Nozawa T, Bondet V, Phung W, Lu B, et al. Inhibition of the dipeptidyl peptidase DPP4 (CD26) reveals IL-33-dependent eosinophil-mediated control of tumor growth. Nat Immunol 2019;20:257-264.

272.   Milardi G, Lleo A. Tumor-Infiltrating B Lymphocytes: Promising Immunotherapeutic Targets for Primary Liver Cancer Treatment. Cancers (Basel) 2023;15.

273.   Oleinika K, Rosser EC, Matei DE, Nistala K, Bosma A, Drozdov I, Mauri C. CD1d-dependent immune suppression mediated by regulatory B cells through modulations of iNKT cells. Nat Commun 2018;9:684.

274.   Lecoultre M, Dutoit V, Walker PR. Phagocytic function of tumor-associated macrophages as a key determinant of tumor progression control: a review. J Immunother Cancer 2020;8.

275.   McCuskey RS, Ito Y, Robertson GR, McCuskey MK, Perry M, Farrell GC. Hepatic microvascular dysfunction during evolution of dietary steatohepatitis in mice. Hepatology 2004;40:386-393.

276.   Farrell GC, Teoh NC, McCuskey RS. Hepatic microcirculation in fatty liver disease. Anat Rec (Hoboken) 2008;291:684-692.

277.   Lefere S, Van de Velde F, Hoorens A, Raevens S, Van Campenhout S, Vandierendonck A, Neyt S, et al. Angiopoietin-2 Promotes Pathological Angiogenesis and Is a Therapeutic Target in Murine Nonalcoholic Fatty Liver Disease. Hepatology 2019;69:1087-1104.

278.   Poon RT, Chung KK, Cheung ST, Lau CP, Tong SW, Leung KL, Yu WC, et al. Clinical significance of thrombospondin 1 expression in hepatocellular carcinoma. Clin Cancer Res 2004;10:4150-4157.

279.   Jaffe EA, Ruggiero JT, Leung LK, Doyle MJ, McKeown-Longo PJ, Mosher DF. Cultured human fibroblasts synthesize and secrete thrombospondin and incorporate it into extracellular matrix. Proc Natl Acad Sci U S A 1983;80:998-1002.

280.   Baenziger NL, Brodie GN, Majerus PW. A thrombin-sensitive protein of human platelet membranes. Proc Natl Acad Sci U S A 1971;68:240-243.

281.   Lawler J. Thrombospondin-1 as an endogenous inhibitor of angiogenesis and tumor growth. J Cell Mol Med 2002;6:1-12.

282.   Hanahan D, Weinberg RA. The hallmarks of cancer. Cell 2000;100:57-70.

283.   Joo YY, Jang JW, Lee SW, Yoo SH, Kwon JH, Nam SW, Bae SH, et al. Circulating pro- and anti-angiogenic factors in multi-stage liver disease and hepatocellular carcinoma progression. Sci Rep 2019;9:9137.

284.   Liu SC, Alomran R, Chernikova SB, Lartey F, Stafford J, Jang T, Merchant M, et al. Blockade of SDF-1 after irradiation inhibits tumor recurrences of autochthonous brain tumors in rats. Neuro Oncol 2014;16:21-28.

7. List of Tables and Figures

7.1 List of Tables

7.2 List of Figures

8. List of publications

Poster Presentations

EASL NAFLD Summit 2022 in Dublin Ireland
Marlene Sophia Kohlhepp, Adrien Guillot, Marc Winkler, Milessa Silva Afonso, Abhishek Aggarwal, Hilmar Berger, David Lopez, Hanyang Liu, Jing Ma, Moritz Peiseler, Felix Heymann, Swetha Pendem, Sangeetha Mahadevan, Bin Gao, Lauri Diehl, Ruchi Gupta, Frank Tacke
Multiplex immunostaining identifies novel immune cell markers for non-alcoholic fatty liver disease and primary sclerosing cholangitis

Publications

Vucur M, Ghallab A, Schneider AT, Adili A, Cheng M, Castoldi M, Singer MT, Büttner V, Keysberg LS, Küsgens L, Kohlhepp M, Görg B, Gallage S, Barragan Avila JE, Unger K, Kordes C, Leblond AL, Albrecht W, Loosen SH, Lohr C, Jördens MS, Babler A, Hayat S, Schumacher D, Koenen MT, Govaere O, Boekschoten MV, Jörs S, Villacorta-Martin C, Mazzaferro V, Llovet JM, Weiskirchen R, Kather JN, Starlinger P, Trauner M, Luedde M, Heij LR, Neumann UP, Keitel V, Bode JG, Schneider RK, Tacke F, Levkau B, Lammers T, Fluegen G, Alexandrov T, Collins AL, Nelson G, Oakley F, Mann DA, Roderburg C, Longerich T, Weber A, Villanueva A, Samson AL, Murphy JM, Kramann R, Geisler F, Costa IG, Hengstler JG, Heikenwalder M, Luedde T. Sublethal necroptosis signaling promotes inflammation and liver cancer. Immunity. 2023 Jul 11;56(7):1578-1595.e8. doi: 10.1016/j.immuni.2023.05.017. Epub 2023 Jun 16. PMID: 37329888.

Guillot A, Kohlhepp MS, Tacke F. Multiplex Immunostaining to Spatially Resolve the Cellular Landscape in Human and Mouse Livers. Methods Mol Biol. 2023;2669:245-255. doi: 10.1007/978-1-0716-3207-9_15. PMID: 37247065.

Heymann F, Mossanen JC, Peiseler M, Niemietz PM, Araujo David B, Krenkel O, Liepelt A, Batista Carneiro M, Kohlhepp MS, Kubes P, Tacke F. Hepatic C-X-C chemokine receptor type 6-expressing innate lymphocytes limit detrimental myeloid hyperactivation in acute liver injury. Hepatol Commun. 2023 Mar 24;7(4):e0102. doi: 10.1097/HC9.0000000000000102. PMID: 36972392.

Kohlhepp MS, Liu H, Tacke F, Guillot A. The contradictory roles of macrophages in non-alcoholic fatty liver disease and primary liver cancer-Challenges and opportunities. Front Mol Biosci. 2023 Feb 10;10:1129831. doi: 10.3389/fmolb.2023.1129831. PMID: 36845555; PMCID: PMC9950415.

Guillot A, Winkler M, Silva Afonso M, Aggarwal A, Lopez D, Berger H, Kohlhepp MS, Liu H, Özdirik B, Eschrich J, Ma J, Peiseler M, Heymann F, Pendem S, Mahadevan S, Gao B, Diehl L, Gupta R, Tacke F. Mapping the hepatic immune landscape identifies monocytic macrophages as key drivers of steatohepatitis and cholangiopathy progression. Hepatology. 2023 Jul 1;78(1):150-166. doi: 10.1097/HEP.0000000000000270. Epub 2023 Jan 13. PMID: 36630995.

Knorr J, Kaufmann B, Inzaugarat ME, Holtmann TM, Geisler L, Hundertmark J, Kohlhepp MS, Boosheri LM, Chilin-Fuentes DR, Birmingham A, Fisch KM, Schilling JD, Loosen SH, Trautwein C, Roderburg C, Demir M, Tacke F, Hoffman HM, Feldstein AE, Wree A. Interleukin-18 signaling promotes activation of hepatic stellate cells in mouse liver fibrosis. Hepatology. 2023 Jun 1;77(6):1968-1982. doi: 10.1002/hep.32776. Epub 2022 Oct 12. PMID: 36059147; PMCID: PMC9984672.

Puengel T, Lefere S, Hundertmark J, Kohlhepp M, Penners C, Van de Velde F, Lapauw B, Hoorens A, Devisscher L, Geerts A, Boehm S, Zhao Q, Krupinski J, Charles ED, Zinker B, Tacke F. Combined Therapy with a CCR2/CCR5 Antagonist and FGF21 Analogue Synergizes in Ameliorating Steatohepatitis and

Fibrosis. Int J Mol Sci. 2022 Jun 15;23(12):6696. doi: 10.3390/ijms23126696. PMID: 35743140; PMCID: PMC9224277.

Günes Günsel G, Conlon TM, Jeridi A, Kim R, Ertüz Z, Lang NJ, Ansari M, Novikova M, Jiang D, Strunz M, Gaianova M, Hollauer C, Gabriel C, Angelidis I, Doll S, Pestoni JC, Edelmann SL, Kohlhepp MS, Guillot A, Bassler K, Van Eeckhoutte HP, Kayalar Ö, Konyalilar N, Kanashova T, Rodius S, Ballester-López C, Genes Robles CM, Smirnova N, Rehberg M, Agarwal C, Krikki I, Piavaux B, Verleden SE, Vanaudenaerde B, Königshoff M, Dittmar G, Bracke KR, Schultze JL, Watz H, Eickelberg O, Stoeger T, Burgstaller G, Tacke F, Heissmeyer V, Rinkevich Y, Bayram H, Schiller HB, Conrad M, Schneider R, Yildirim AÖ. The arginine methyltransferase PRMT7 promotes extravasation of monocytes resulting in tissue injury in COPD. Nat Commun. 2022 Mar 14;13(1):1303. doi: 10.1038/s41467-022-28809-4. PMID: 35288557; PMCID: PMC8921220.

Sonntag R, Penners C, Kohlhepp M, Haas U, Lambertz D, Kroh A, Cramer T, Ticconi F, Costa IG, Tacke F, Gassler N, Trautwein C, Liedtke C. Cyclin E1 in Murine and Human Liver Cancer: A Promising Target for Therapeutic Intervention during Tumour Progression. Cancers (Basel). 2021 Nov 13;13(22):5680. doi: 10.3390/cancers13225680. PMID: 34830835; PMCID: PMC8616292.

Conlon TM, John-Schuster G, Heide D, Pfister D, Lehmann M, Hu Y, Ertüz Z, Lopez MA, Ansari M, Strunz M, Mayr C, Angelidis I, Ciminieri C, Costa R, Kohlhepp MS, Guillot A, Günes G, Jeridi A, Funk MC, Beroshvili G, Prokosch S, Hetzer J, Verleden SE, Alsafadi H, Lindner M, Burgstaller G, Becker L, Irmler M, Dudek M, Janzen J, Goffin E, Gosens R, Knolle P, Pirotte B, Stoeger T, Beckers J, Wagner D, Singh I, Theis FJ, de Angelis MH, O'Connor T, Tacke F, Boutros M, Dejardin E, Eickelberg O, Schiller HB, Königshoff M, Heikenwalder M, Yildirim AÖ. Inhibition of LTβR signalling activates WNT-induced regeneration in lung. Nature. 2020 Dec;588(7836):151-156. doi: 10.1038/s41586-020-2882-8. Epub 2020 Nov 4. Erratum in: Nature. 2021 Jan;589(7842):E6. PMID: 33149305; PMCID: PMC7718297.

Bartneck M, Koppe C, Fech V, Warzecha KT, Kohlhepp M, Huss S, Weiskirchen R, Trautwein C, Luedde T, Tacke F. Roles of CCR2 and CCR5 for Hepatic Macrophage Polarization in Mice With Liver Parenchymal Cell-Specific NEMO Deletion. Cell Mol Gastroenterol Hepatol. 2021;11(2):327-347. doi: 10.1016/j.jcmgh.2020.08.012. Epub 2020 Sep 4. PMID: 32896623; PMCID: PMC7779787.

Guillot A, Kohlhepp MS, Bruneau A, Heymann F, Tacke F. Deciphering the Immune Microenvironment on A Single Archival Formalin-Fixed Paraffin-Embedded Tissue Section by An Immediately Implementable Multiplex Fluorescence Immunostaining Protocol. Cancers (Basel). 2020 Aug 28;12(9):2449. doi: 10.3390/cancers12092449. PMID: 32872334; PMCID: PMC7565194.

Puengel T, De Vos S, Hundertmark J, Kohlhepp M, Guldiken N, Pujuguet P, Auberval M, Marsais F, Shoji KF, Saniere L, Trautwein C, Luedde T, Strnad P, Brys R, Clément-Lacroix P, Tacke F. The Medium-Chain Fatty Acid Receptor GPR84 Mediates Myeloid Cell Infiltration Promoting Steatohepatitis and Fibrosis. J Clin Med. 2020 Apr 16;9(4):1140. doi: 10.3390/jcm9041140. PMID: 32316235; PMCID: PMC7231190.

Malehmir M, Pfister D, Gallage S, Szydlowska M, Inverso D, Kotsiliti E, Leone V, Peiseler M, Surewaard BGJ, Rath D, Ali A, Wolf MJ, Drescher H, Healy ME, Dauch D, Kroy D, Krenkel O, Kohlhepp M, Engleitner T, Olkus A, Sijmonsma T, Volz J, Deppermann C, Stegner D, Helbling P, Nombela-Arrieta C, Rafiei A, Hinterleitner M, Rall M, Baku F, Borst O, Wilson CL, Leslie J, O'Connor T, Weston CJ, Chauhan A, Adams DH, Sheriff L, Teijeiro A, Prinz M, Bogeska R, Anstee N, Bongers MN, Notohamiprodjo M, Geisler T, Withers DJ, Ware J, Mann DA, Augustin HG, Vegiopoulos A, Milsom MD, Rose AJ, Lalor PF, Llovet JM, Pinyol R, Tacke F, Rad R, Matter M, Djouder N, Kubes P, Knolle PA, Unger K, Zender L, Nieswandt B, Gawaz M, Weber A, Heikenwalder M. Platelet GPIbα is a mediator and potential interventional target for

NASH and subsequent liver cancer. Nat Med. 2019 Apr;25(4):641-655. doi: 10.1038/s41591-019-0379-5. Epub 2019 Apr 1. Erratum in: Nat Med. 2022 Mar;28(3):600. PMID: 30936549.

Mossanen JC, Kohlhepp M, Wehr A, Krenkel O, Liepelt A, Roeth AA, Möckel D, Heymann F, Lammers T, Gassler N, Hermann J, Jankowski J, Neumann UP, Luedde T, Trautwein C, Tacke F. CXCR6 Inhibits Hepatocarcinogenesis by Promoting Natural Killer T- and CD4+ T-Cell-Dependent Control of Senescence. Gastroenterology. 2019 May;156(6):1877-1889.e4. doi: 10.1053/j.gastro.2019.01.247. Epub 2019 Jan 30. PMID: 30710528.

Liepelt A, Wehr A, Kohlhepp M, Mossanen JC, Kreggenwinkel K, Denecke B, Costa IG, Luedde T, Trautwein C, Tacke F. CXCR6 protects from inflammation and fibrosis in NEMOLPC-KO mice. Biochim Biophys Acta Mol Basis Dis. 2019 Feb 1;1865(2):391-402. doi: 10.1016/j.bbadis.2018.11.020. Epub 2018 Nov 24. PMID: 30476545.
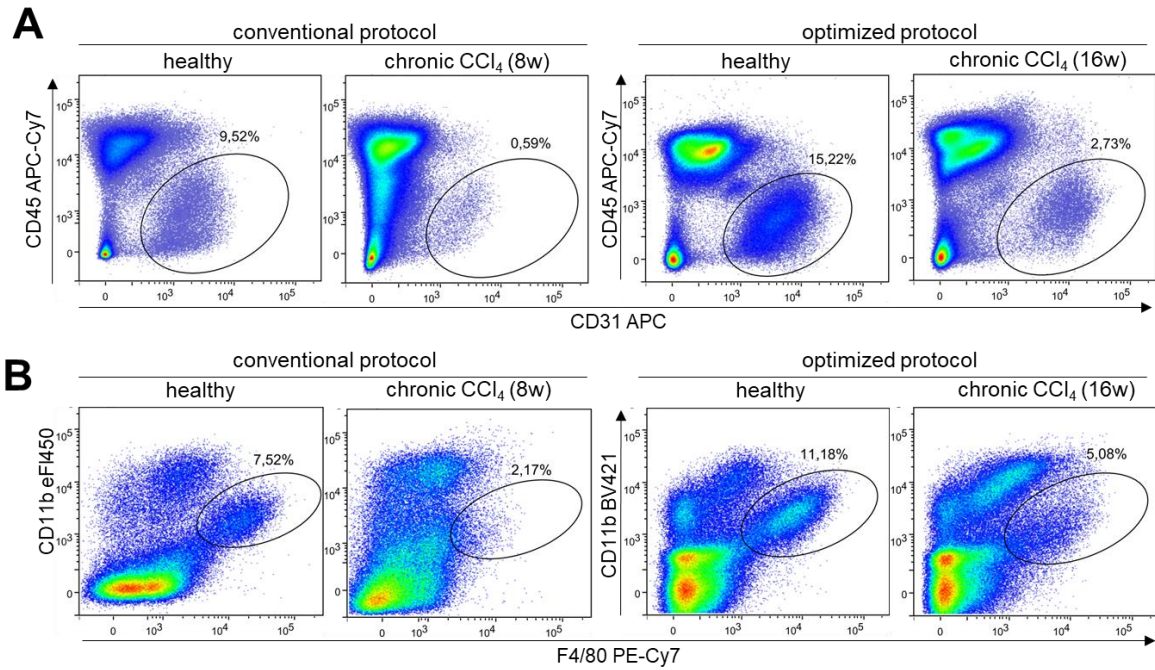
Krenkel O, Puengel T, Govaere O, Abdallah AT, Mossanen JC, Kohlhepp M, Liepelt A, Lefebvre E, Luedde T, Hellerbrand C, Weiskirchen R, Longerich T, Costa IG, Anstee QM, Trautwein C, Tacke F. Therapeutic inhibition of inflammatory monocyte recruitment reduces steatohepatitis and liver fibrosis. Hepatology. 2018 Apr;67(4):1270-1283. doi: 10.1002/hep.29544. Epub 2018 Feb 19. PMID: 28940700.

Puengel T, Krenkel O, Kohlhepp M, Lefebvre E, Luedde T, Trautwein C, Tacke F. Differential impact of the dual CCR2/CCR5 inhibitor cenicriviroc on migration of monocyte and lymphocyte subsets in acute liver injury. PLoS One. 2017 Sep 14;12(9):e0184694. doi: 10.1371/journal.pone.0184694. PMID: 28910354; PMCID: PMC5598992.

Heymann F, Niemietz PM, Peusquens J, Ergen C, Kohlhepp M, Mossanen JC, Schneider C, Vogt M, Tolba RH, Trautwein C, Martin C, Tacke F. Long term intravital multiphoton microscopy imaging of immune cells in healthy and diseased liver using CXCR6.Gfp reporter mice. J Vis Exp. 2015 Mar 24;(97):52607. doi: 10.3791/52607. PMID: 25866988; PMCID: PMC4401387.

Heymann F, Peusquens J, Ludwig-Portugall I, Kohlhepp M, Ergen C, Niemietz P, Martin C, van Rooijen N, Ochando JC, Randolph GJ, Luedde T, Ginhoux F, Kurts C, Trautwein C, Tacke F. Liver inflammation abrogates immunological tolerance induced by Kupffer cells. Hepatology. 2015 Jul;62(1):279-91. doi: 10.1002/hep.27793. Epub 2015 Apr 22. PMID: 25810240.

9.Supplementary Figures

Supplementary Figure 1: Identification of SSC^{hi} CD11b$^+$ cells as SiglecF$^+$ eosinophils in the blood and the liver of healthy mice, and mice that were repetitively injected with CCl$_4$ for 8 weeks and sacrificed 36 h after the last CCl$_4$ injection. **A)** Backgating of SiglecF$^+$ CD11b$^+$ Ly6G$^-$ blood leukocytes (highlighted in orange) identifies the Ly6G$^-$SSC^{hi}CD11b$^+$ cell population as SiglecF$^+$ eosinophils in healthy and CCl$_4$ treated mice. **B)** SiglecF staining on SSC^{hi} (2) and SSC^{low} (3) infiltrating myeloid cells (1) in healthy and chronically CCl$_4$ treated liver and percentage of SiglecF$^+$ cells (eosinophils) within the SSC^{hi} population
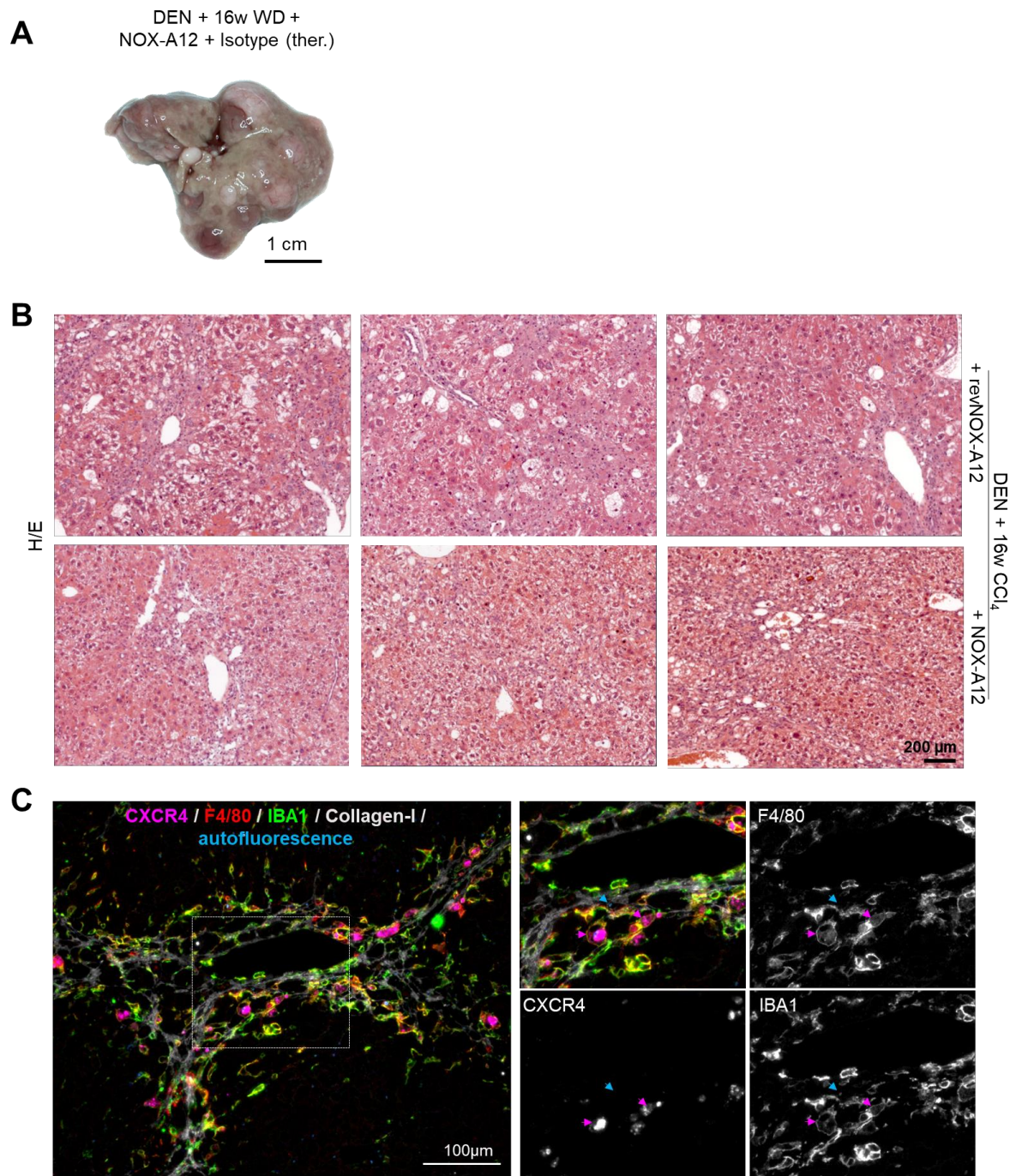
Supplementary Figure 2: Comparison of liver immune cell isolation protocols. Isolation of endothelial cells and Kupffer cells for flow cytometry analysis was conducted using the conventional and an optimized isolation protocol.
A) Endothelial cells, defined as $CD31^{+}CD45^{int/-}$ cells, isolated from healthy and fibrotic liver (chronic CCl_4). **B**) Kupffer cells ($CD45^{+}Ly6G^{-}CD11b^{int}F4/80^{high}$) isolated from healthy and fibrotic liver (chronic CCl_4).
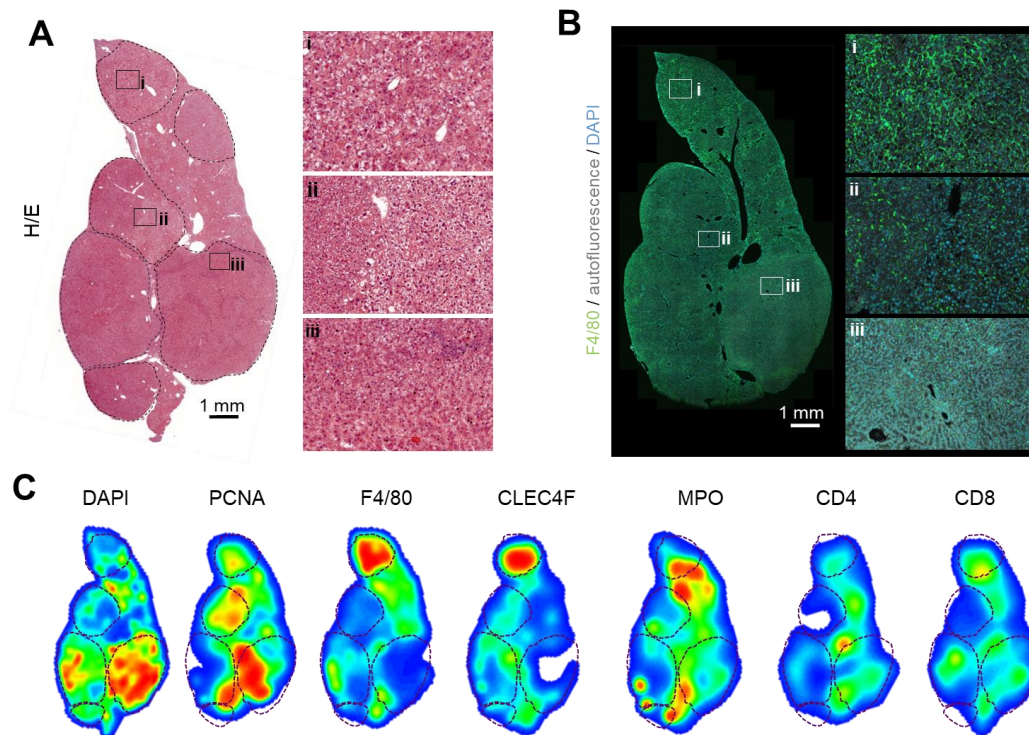
Supplementary Figure 3: **DEN + CCl$_4$ induced tumors are histologically and immunologically heterogenous.**
A) H/E staining of a representative liver section from a DEN + 16w CCl$_4$ + revNOX-A12 treated mouse. Scan of the entire section and enlarged images from different tumor regions. Tumors were circled manually (black dashes). **B**) A consecutive section of A) was stained for F4/80 by immunofluorescence. Whole section scan and enlarged regions from different tumors. **C**) A consecutive section of the same sample was subjected to sequential multiplex immunofluorescence staining for various immune cell markers. The heatmaps depict the densities of cells across the tissue. Tumor areas are indicated by black dashes. MPO = myeloperoxidase, PCNA= proliferating cell nuclear antigen.

A

DEN + 16w WD +
NOX-A12 + Isotype (ther.)

1 cm

B

H/E

+ revNOX-A12

DEN + 16w CCl₄

+ NOX-A12

200 µm

C

CXCR4 / F4/80 / IBA1 / Collagen-I / autofluorescence

F4/80

CXCR4

IBA1

100µm

Supplementary Figure 4: A) Representative fibrotic liver from a mouse that was subjected to DEN + 16w WD and treated for 8 weeks (therapeutically) with NOX-A12 + Isotype. **B**) Representative images of non-tumorous regions, stained with H/E from three different livers following DEN and 16 weeks of CCl₄ together with revNOX-A12 or NOX-A12. **B**) Representative picture of CXCR4 staining in macrophages (IBA1⁺ F4/80⁺) next to a vessel in fibrotic tissue in a liver exposed to DEN and 10 weeks CCl₄ and revNOX-A12. An autofluorescence channel was added to verify the specificity of the signal. Pink arrows: CXCR4 staining, blue arrows: tissue autofluorescence.